



# Fluorescence Imaging of Virus-Host Cell Interaction and Super-Resolution Imaging of Neuronal Cytoskeleton

## Citation

He, Jiang. 2016. Fluorescence Imaging of Virus-Host Cell Interaction and Super-Resolution Imaging of Neuronal Cytoskeleton. Doctoral dissertation, Harvard University, Graduate School of Arts & Sciences.

## Permanent link

<http://nrs.harvard.edu/urn-3:HUL.InstRepos:26718714>

## Terms of Use

This article was downloaded from Harvard University's DASH repository, and is made available under the terms and conditions applicable to Other Posted Material, as set forth at <http://nrs.harvard.edu/urn-3:HUL.InstRepos:dash.current.terms-of-use#LAA>

## Share Your Story

The Harvard community has made this article openly available.  
Please share how this access benefits you. [Submit a story](#).

[Accessibility](#)

# **Fluorescence imaging of Virus-Host Cell Interaction and Super-resolution Imaging of Neuronal Cytoskeleton**

A dissertation presented

By

Jiang He

to

The Department of Molecular and Cellular Biology

in partial fulfillment of the requirements

for the degree of

Doctor of Philosophy

in the subject of

Biochemistry

Harvard University

Cambridge, Massachusetts

August, 2015

© 2015 – Jiang He

All rights reserved.

# Fluorescence imaging of Virus-Host Cell Interaction and Super-resolution Imaging of Neuronal Cytoskeleton

## Abstract

To study biological molecules, pathways and processes, fluorescence microscope has become an indispensable tool in modern biology. The major advantages of using fluorescence microscope include its ability to achieve molecule-specific visualization for targets of interest, and the compatibility of live cell imaging. With the advent of super-resolution imaging techniques, fluorescent microscope, for the first time, allows researchers to study biological processes on the nanometer scale. In this dissertation, I present the application of fluorescence imaging to characterize the role of host factors in influenza virus infection, and super-resolution imaging to study the developmental mechanism and prevalence of a periodic membrane skeleton in neurons.

In Chapter 2 and 3, my colleagues and I studied the role of CD81 and COPI complex, two host factors identified in large-scale screens, for influenza infection. We found that CD81 regulates two distinct steps during influenza infection cycle: virus uncoating during entry and virus budding during egress. Depleting CD81 led to a significant defect in viral uncoating and viral gene replication during entry, while during virus egress, CD81 depletion resulted in virions that failed to detach from the plasma membrane and a marked decrease in progeny virus production. For COPI complexes, we found that COPI plays a direct role in viral membrane protein expression and assembly post-viral entry.



In Chapter 4 and 5, we used super-resolution imaging to study the developmental mechanism and prevalence of a newly discovered periodic membrane skeleton in axons, formed by actin, spectrin and associated molecules. We found that the periodic membrane skeleton is highly prevalent in different neuronal types. It forms early during neuronal development, and originates from regions closer to the cell body and propagates toward the distal ends of axons. The lattice structure further matures by recruiting additional molecular components and appears to be highly stable once formed. The local concentration of  $\beta$ II spectrin is a key determinant for the formation of this periodic membrane skeleton. In addition, we identified ankyrin B as a critical molecular component for the polarized distribution of  $\beta$ II spectrin in neurites.

# Table of Contents

Abstract.....	iii
Table of Contents.....	v
List of Figures .....	viii
Citations to previously published work.....	x
Acknowledgements.....	xi
Chapter 1: Introduction.....	1
1.1 Fluorescence imaging.....	2
1.2 Fluorescence imaging of virus-host cell interaction.....	3
1.3 Host factors in influenza virus infection.....	7
1.4 Super-resolution fluorescence microscopy.....	11
1.5 Actin cytoskeleton in neurons.....	14
1.6 Outline of chapters.....	19
Chapter 2: Dual function of CD81 in influenza virus uncoating and budding .....	22
2.1 Introduction.....	23
2.2 Results.....	24
2.2.1 CD81 is involved in both early and late stages of influenza virus infection.....	24
2.2.2 CD81 is not involved in virus binding, internalization or trafficking to early endosomes.....	29
2.2.3 Influenza virus particles are delivered to and fuse in CD81+ endosomes.....	30
2.2.4 CD81 is not involved in the expression or trafficking of viral proteins.....	34
2.2.5 CD81 is recruited to influenza virus budding sites on the plasma membrane.....	36
2.2.6 CD81 is incorporated at specific sub-viral locations and facilitates influenza virus budding.....	38
2.2.7 Distribution of CD81 in budding filamentous Udorn virus.....	42
2.3 Discussion.....	43
2.4 Materials and methods.....	47
Chapter 3: Dissecting the role of COPI complexes in influenza virus infection.....	58
3.1 Introduction.....	59
3.2 Results.....	61
3.2.1 COPI depletion inhibits influenza infection via an entry step at or prior to viral fusion.....	61
3.2.2 siRNA knockdown of COPI abrogates the internalization of influenza, as well as other clathrin-mediated endocytosis or macropinocytosis cargos.....	66

3.2.3 ARCNI knockdown cells exhibit impaired endosomal trafficking upon virus internalization.....	68
3.2.4 Rapid disruption of COPI vesicles with pharmacological inhibitors does not block viral entry....	70
3.2.5 Rapid disruption of COPI complex function decreases viral membrane protein expression and progeny virus production.....	74
3.3 Discussion.....	78
3.4 Materials and methods.....	83
Chapter 4: Developmental mechanism of the periodic membrane skeleton in axons.....	90
4.1 Introduction.....	91
4.2 Results.....	93
4.2.1 Early development and propagation of the periodic lattice structure in axons .....	93
4.2.2 The structural organization of $\beta$ II spectrin in dendrites.....	96
4.2.3 Actin dependence during the early developmental phase of the periodic membrane skeleton.....	98
4.2.4 Assembly of axon initial segment components into the periodic membrane skeleton during late development stages.....	100
4.2.5 Stability of the periodic membrane skeleton .....	104
4.2.6 Microtubule dependence of the periodic membrane skeleton .....	106
4.2.7 Role of Ankyrin B in the periodic membrane skeleton .....	107
4.2.8 Local $\beta$ II spectrin concentration regulates the formation of this periodic lattice structure and ankyrin B regulates the polarized distribution of $\beta$ II spectrin in neurites.....	111
4.3 Discussion.....	112
4.4 Materials and methods.....	116
Chapter 5: The prevalence of the periodic membrane skeleton in different neuronal types.....	123
5.1 Introduction.....	124
5.2 Results.....	124
5.2.1 The periodic membrane skeleton is present in inhibitory neurons from the hippocampus.....	124
5.2.2 The periodic membrane skeleton is present in neurons from central and periphery nervous system.....	126
5.2.3 The structural organization of $\beta$ II spectrin in glia cells.....	130
5.2.4 Myelination does not affect the formation of the periodic structure in cultured neurons.....	131
5.3 Discussion.....	133
5.4 Materials and methods.....	135
Chapter 6: Discussion and future directions.....	139
6.1 Host Factors in Influenza Virus Infection.....	140

6.2 The periodic membrane skeleton in neurons.....	143
References.....	146

# List of Figures

## Chapter 1: Introduction

Figure 1.1 Schematic of the different viral infection pathways.....	5
Figure 1.2 Influenza virus structure and virus infection cycle.....	8
Figure 1.3 The principle of STORM.....	13
Figure 1.4 Actin, spectrin-associated cytoskeletal structure in red blood cells.....	16
Figure 1.5 The actin, spectrin-based periodic membrane skeleton in axons.....	19

## Chapter 2: Dual Function of CD81 in Influenza Virus Uncoating and Budding

Figure 2.1 CD81 depletion efficiency with different siRNA constructs.....	25
Figure 2.2 CD81 is involved in both early and late stages of influenza virus infection.....	27
Figure 2.3 CD81 is not required for virus binding, internalization or delivery into early endosomes....	30
Figure 2.4 A major fraction of viruses are trafficked to and fuse in CD81-positive endosomes.....	31
Figure 2.5 CD81 depletion does not affect viral protein expression and transport.....	35
Figure 2.6 CD81 is recruited to the virus budding sites.....	37
Figure 2.7 CD81 is enriched at specific sub-viral sites of budding virions and CD81 knockdown impairs virus scission.....	39
Figure 2.8 CD81 is enriched in the budding WSN virions and CD81-knockdown impairs scission of the X-31 virus.....	41
Figure 2.9 Scattered distribution of CD81 along budding filamentous Udorn virus.....	42

## Chapter 3: Dissecting the role of COPI complexes on influenza virus infection

Figure 3.1 COPI depletion blocks viral infection and cells are sufficiently healthy for subsequent experiments.....	63
Figure 3.2 ARCN1 knockdown cells exhibit a defect in viral entry at or prior to fusion, but not at binding.....	65
Figure 3.3 ARCN1 knockdown cells exhibit defective internalization of influenza and other cargoes.....	67
Figure 3.4 Defective endosomal trafficking of internalized influenza particles in ARCN1 depleted cells.....	69
Figure 3.5 Pharmacological disruption of COPI complexes does not block virus entry.....	72
Figure 3.6 Functional COPI complex recruitment to cis-golgi is required for viral membrane protein expression.....	75
Figure 3.7 Disruption of COPI complexes with inhibitors inhibits assembly of progeny virions.....	77

## Chapter 4: Developmental mechanism of the periodic membrane skeleton in axons

Figure 4.1 $\beta$ II spectrin structure in a DIV 10 neuron .....	94
Figure 4.2 Early development and propagation of the periodic lattice structure in axons.....	95
Figure 4.3 Distributions of dendritic $\beta$ II and $\beta$ III spectrin .....	97
Figure 4.4 The periodic structure of $\beta$ II spectrin depends on actin during early development .....	99
Figure 4.5 Recruitment of adducin into the periodic lattice structure during development .....	100
Figure 4.6 Assembly of AIS components into the periodic lattice structure during late developmental stages .....	101
Figure 4.7 The formation of the periodic $\beta$ IV spectrin structure in the AIS is dependent on $\beta$ II spectrin .....	103
Figure 4.8 The periodic lattice structure is stable in live neurons .....	105
Figure 4.9 The periodic structure of $\beta$ II spectrin relies on intact microtubules .....	106
Figure 4.10 The $\beta$ II spectrin structure in axons of ankyrin B KO neurons .....	107
Figure 4.11 Role of ankyrin B in the regulation of the periodic lattice structure .....	108
Figure 4.12 Formation of the periodic lattice structure in dendrites of ankyrin B knockout neurons depends on $\beta$ II spectrin .....	110
Figure 4.13 Local $\beta$ II spectrin concentration determines the formation of the periodic lattice structure.....	112

## Chapter 5: The prevalence of the periodic membrane skeleton in different neuronal types

Figure 5.1 $\beta$ II spectrin is organized into a periodic structure in inhibitory neurons from the hippocampus.....	126
Figure 5.2 The periodic lattice structure is present in both excitatory and inhibitory neurons from the cortex and middle brain.....	128
Figure 5.3 The periodic structure is highly prevalent in different neuronal types from the central and periphery nervous system.....	129
Figure 5.4 $\beta$ II spectrin is largely irregular in the processes of different glia cells.....	131
Figure 5.5 Myelination does not affect the formation of the periodic membrane skeleton.....	133

## Citations to previously published work

### Chapter 2 has been previously published with minor changes as:

J. He, E. Sun, M.V. Bujny, D. Kim, M.W. Davidson, X. Zhuang, “Dual Function of CD81 in influenza virus uncoating and budding”. *Plos Pathogens*. (2013) e1003701.

### Chapter 3 has been previously published with minor changes as:

E. Sun, J. He, X. Zhuang, “Dissecting the role of COP1 complexes on influenza virus infection”, *Journal of Virology*. (2013) 87:5 2673-2685.

### Chapter 4 has been previously published with minor changes as:

G. Zhong\*, J. He\*, R. Zhou, D.N. Lorenzo, H. Babcock, V. Bennett, X. Zhuang. “Developmental mechanism of the periodic membrane skeleton in axons”, *eLife* (2014), 10.7554/eLife.04581.

### Other publications related to the dissertation:

E. Sun\*, J. He\*, X. Zhuang, “Live cell imaging of viral entry”, *Current Opinions in Virology*. (2013) 3:34-43.

A. M. Avalos, A.M. Bilate, M.D. Witte, A.K. Tai, J. He, M.P. Fruschicheva, P.D. Thill, F. Meyer-Wentrup, C.S. Theile, A.K. Chakraborty, X. Zhuang, H.L. Ploegh, “Monovalent engagement of the BCR activates ovalbumin-specific transnuclear B Cells”. *Journal of Experimental Medicine*, (2014) 211:365-7910.

S. Jones, S. Shim, J. He, X. Zhuang, “Fast, three-dimensional super-resolution imaging of live cells”. *Nature Methods*. (2011) 8: 499-508.

D.N. Lorenzo, A. Badea, J.Q. Davis, J. Hostettler, J. He, G. Zhong, X. Zhuang, V. Bennett, “A PIK3C3/Ankyrin-B/Dynactin pathway promotes axonal growth and multi-organelle transport” *Journal of Cell Biology*, (2014) 207:735-752.

\* Authors contributed equally to these manuscripts.

## Acknowledgements

Throughout graduate school, I received generous help from many people inside and outside the lab. First and foremost, I want to express my sincere gratitude to my thesis advisor Dr. Xiaowei Zhuang. I felt extremely fortunate to join her lab and team with a group of brilliant scientists for my thesis work. Xiaowei's insights for research, her passion for science, and attitude for vigorous and critical thinking has taught me how to become a good scientist. Without her guidance and support, this thesis could have never been materialized. Xiaowei always encourages me to think big and work on problems that have big impact. Whenever I presented my hypothesis or new research directions to her, she always makes me think thoroughly about the experimental design and sketch a broader and deeper picture of the project, while at the same time, challenges me with insightful and detailed comments. Her way of pursuing science has truly made me grow rapidly.

I want to thank my thesis and DAC committee members Dr. Joshua Sanes, Victoria D'Souza, Nir Hacohen, Raymond Erikson, Michael Farzan, David Sabatini, and David Knipe for their advice and generous support over the years. All of them are all incredibly busy, yet whenever I approached them for advice, they always made themselves available and gave me insightful suggestions. Their feedback and encouragements have helped tremendously in shaping my research projects.

In the Zhuang lab, I have been fortunate to work with a group of phenomenal scientists. I want to thank Dr. Sara Jones and Sanghee Shim for introducing me to the lab during my rotation, and for always being there to give me advice. For influenza virus related work, I worked closely with Dr. Eileen Sun, Miriam Bujny and Doory Kim. I want to particularly thank Dr. Eileen Sun, who is not only my close collaborator for several projects, but also a close friend in lab. Her passion and dedication for work has always been an inspiration, and I learned an incredibly lot from her during our conversations. For the neuronal work, I worked closely with Dr. Guisheng Zhong, Ruobo Zhou, Guiping Wang. I feel extremely grateful for Guisheng for introducing me into the exciting field of neuroscience and quickly preparing me for the



work on the periodic membrane skeleton. I want to thank Ruobo and Guiping for the great scientific discussions and help on experiments. The Zhuang lab has been an amazing and fun place for me to work in. I feel grateful for all of the current and past lab members I interacted with. In particular, I want to thank Wenqin Wang, William Huang, Joshua Vaughan, John Wu, Sebastian Deindl, George Hao, Alistair Boettiger, Pallav Kosuri, Jeff Moffitt, Colenso Speer, Siyuan Wang for offering their help and stimulating conversations over the years.

Outside the lab, I want to thank my classmates in MCB program for their friendship and support, and for organizing so many cool and fun events. In particular I want to thank Kyle McElroy for being such an amazing roommate and genuine friend. The Chinese graduate student community has made me feel at home while in school, and I have met many wonderful friends over the years. I was fortunate to be affiliated with Lowell House for the past three years. I want to thank Professor Diana Eck and Dorothy Austin for bringing me into the house, and introducing me into the undergraduate community. Harvard has been an incredible place for me to grow professionally as well as personally. I want to acknowledge Professor Niall Ferguson from the history department for inspiring me to think my personal stories from a broader perspective, and supporting me to put the stories into words. Professor Vicki Sato from HBS has been a wonderful mentor, and I feel tremendously grateful for her encouragements and advice over the years.

Finally, I want to thank my parents for being so supportive and understanding of their son, even though they know little of what I have been doing. My brother for standing by my side and cheering for me. Their love and support has made all that I have been doing possible, to which I always feel grateful.

*Dedicated to my parents.*

# **Chapter 1: Introduction**

## 1.1 Fluorescence imaging

Biological processes are intrinsically dynamic and complex, and happen at length scales that span several orders of magnitude. To study biological molecules, pathways and processes in living cells, tissues or animals, biologists need tools to probe into these processes and light microscope has become an invaluable tool for modern biology. From the discovery of neurons by Ramon y Cajal a century ago[1], to the visualization of motor proteins walking along the cytoskeleton[2], light microscope has made countless significant contributions to modern biology and transformed our understanding of many biological questions. One attribute that makes light microscope so powerful in biology is its capability to visualize targets of interest specifically [3-5]. Various biological entities, including protein, DNA, and RNA have all been extensively characterized and studied under light microscope [3-5]. The availability of dyes at different spectrum not only makes it possible to visualize the target of interest specifically, but also permits the labeling of multiple targets simultaneously, further enabling the study of interactions among different biological entities [6-11]. As light is relatively non-invasive, light microscope is compatible with, and has been well-adapted for studying biological processes in living cells and live animals [3-5]. This feature gives light microscope an exceptional capability to study dynamics of various biological processes, making it possible to directly visualize the biological processes in real time.

Among various light microscopes, fluorescence microscope is perhaps one of the most widely used techniques in modern cell biology. As the name indicates, fluorescence microscope relies on the detection of emitted fluorescence from targets of interest. Light excitation of fluorophores can emit photons characterized by a specific wavelength [3]. The unexcited non-fluorescence state is called ground state. After absorbing the light energy from the excitation light, the fluorophore quickly transits to an excited state (fluorescence state), and then returns to the ground state by shedding off the energy through vibrational relaxation or fluorescence excitation [3]. The wavelength of emitted light is longer than that of excited light. By using a filter to block the excitation light while allowing emission light to pass, it enables the visualization of fluorescence from targets of interest.

There are a large repertoire of synthetic fluorophores and genetically encoded fluorescent proteins, with excitation and emission spectrum spanning from UV to far red [6-11]. Synthetic fluorophores are usually credited for their brightness and photo-stability[11]. Quantum dots, a group of synthetic nano-sized particles made from semiconductor materials, is particularly well known for their exceptional brightness and low photo-bleaching property [12]. However, synthetic fluorophores are usually non-cell permeable, making it difficult to use for live cell studies [11]. Compared with synthetic fluorophores, fluorescent proteins are intrinsically compatible with live cell imaging [8, 10, 11]. Since the initial discovery and clone of green fluorescent protein (GFP) in jellyfish, many variants of fluorescent proteins have been developed and used in fluorescence imaging [8, 10, 11]. Because the fluorophore is encoded genetically, any protein of interest inside a cell can be tagged specifically by fusing its gene sequence with that of fluorescent proteins [8]. With modifications of labeling methods, DNA and RNA transcripts can be specifically labeled by fluorescent proteins as well [8, 10, 11, 13, 14].

To date, fluorescence imaging has been widely used in biological research for decades. Its capability to provide spatial, temporal and functional information makes it one of the most popular tools in biology, and has generated many significant insights for different biological questions. The dissertation presents the development and application of different fluorescence imaging techniques for the study of various biological questions, including virus-host cell interaction and super-resolution imaging of the developmental mechanism of a novel periodic membrane skeleton in axons.

## **1.2 Fluorescence imaging of virus-host cell interaction**

As microscopic Trojan horses, viruses usurp host cell machinery to deliver their genome into the cell for initiating productive infection [15]. Viral infection is extremely dynamic and consists of multiple steps. The process begins with virion attachment to the cell surface, typically via low affinity electrostatic interactions with the glycocalyx, followed by specific binding to receptors. Receptor engagement allows viruses to either directly release their genome into the cell at the plasma membrane, or to enter cells through endocytosis. Endocytosed virus particles typically traffick through endosomal vesicles by actin-

and/or microtubule-dependent transport to rapidly navigate through the dense cytoplasm. Specific environmental cues then trigger either fusion of enveloped virus with the endosome, or membrane penetration by capsid proteins for non-enveloped viruses, allowing viral genetic material to be released into the cytoplasm [15]. For DNA viruses and a few RNA viruses, nuclear import of the viral genome precedes viral replication, protein expression, and assembly. For most RNA viruses however, subsequent steps of the infection cycle follow immediately after viral genome release (Figure 1.1) [15, 16]. After viral replication, protein expression, all the viral components are brought to the virus assembly site for successful virus egress, and subsequently start another infection cycle [15].

Given the dynamic and multi-step nature of viral infection, many questions can benefit from studying viral entry and replication through imaging. To allow successful detection, viruses and relevant cellular components can be labeled with fluorescent probes. A number of different imaging modalities such as confocal, TIRF and epifluorescence microscopy have been used. Furthermore, development of image analysis algorithms has enabled researchers to track a large number of viral entry events in three-dimensions with high speed and precision [17-21].

Fluorescence imaging offers a powerful tool for studying these important events in live and fixed cells. For example, several viruses such as human immunodeficiency virus (HIV), vesicular stomatitis virus (VSV), vaccinia virus (VV), hepatitis C virus (HCV), and herpes simplex virus-1 (HSV-1) have been shown by live cell imaging to navigate along the cell body in an actin-dependent manner after attachment [22-27]. For these viruses, attachment is followed by transport along microvilli or filopodia toward the cell at a speed consistent with the actin retrograde flow [22, 24-27]. After viral binding to specific receptors, virus-induced clustering of receptors can either trigger conformational changes in the receptor-bound viral protein that prime viral genome release directly at the plasma membrane, or more commonly, transduce intracellular signaling to initiate endocytosis [15].

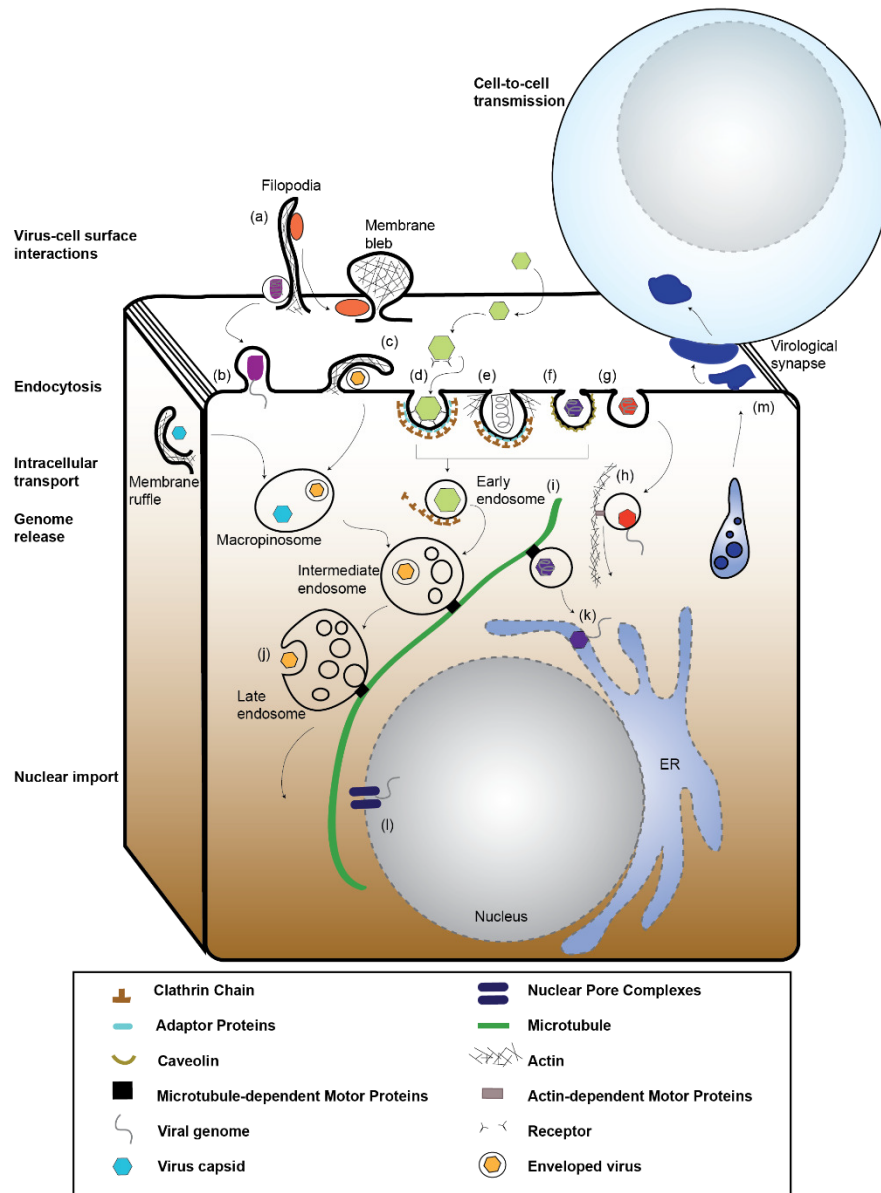


**Figure 1.1. Schematic of the different viral infection pathways.** Viral entry encompasses the following steps: virus - cell surface interactions, endocytosis, intracellular transport, genome release, and in some cases, nuclear import. To begin an infection, virus particles absorb directly onto the cell surface or onto filopodia (a). Cell surface interactions are typically characterized by low electrostatic interactions with the glycocalyx prior to specific binding with cellular receptors. Virus binding to receptors may directly lead to genome release at the plasma membrane (b). More commonly, however, virus-receptor engagement induces downstream signaling events, resulting in internalization through one or more of the following pathways: macropinocytosis (c), clathrin-mediated endocytosis (d and e), caveolin-dependent endocytosis (f), or alternative, less characterized uptake pathways (g). Upon endocytosis, viruses hijack either the actin cytoskeleton (h) or microtubule network (i) to navigate through the dense cytoplasm. In addition to relying on the cytoskeleton for transport, viruses also utilize compartment-specific environmental cues, such as low pH or enzymatic cleavage, to trigger genome release through viral fusion for enveloped viruses or membrane penetration for non-enveloped viruses (j and k). For DNA viruses and a few RNA

**Figure 1.1. (continued)** viruses, genome translocation into the nucleus (l) precedes subsequent replication steps, while all other viruses replicate within the cytoplasm immediately after uncoating. After viral replication, some viruses such as HIV have the capability of mediating direct transfer of virions from the infected cell to another neighboring, uninfected cell (m). Figure from reference [28]

Viruses hijack different cellular endocytotic pathways for internalization, among which clathrin-mediated endocytosis is most commonly used. Many viruses also internalize through other pathways such as macropinocytosis, caveolar/raft-dependent endocytosis, and clathrin- caveolin/raft-independent pathways. Multicolor live cell imaging offers a powerful tool to probe the orchestrated recruitment of endocytic machinery during the virus internalization process. Using this technique, researchers found that influenza virus, reovirus, and VSV induce *de novo* assembly of clathrin machinery [29-32], rather than diffusing into nascent assembling clathrin-coated pits. HCV, Dengue virus (DenV), and VSV internalize cells exclusively through clathrin-mediated endocytosis [26, 29, 30, 33, 34], while Simian Virus 40 (SV40) may enter cells through a clathrin and caveolin-independent pathways [35-37]. A number of viruses, including adenovirus, VV, Ebola, and influenza internalize through macropinocytosis [24, 38-44].

The internalized viruses are usually sorted into endosomal vesicles and transported toward the perinuclear region along microtubules. As shown by live and fixed cell imaging studies, viruses including VSV and respiratory syncytial virus (RSV) undergo viral uncoating within early endosomes [30, 45, 46]. Many other viruses, such as influenza, Ebola, DenV, semliki forest virus (SFV), and Uukuniemi virus (UUKV), require trafficking from early to maturing or late endosomes before uncoating [34, 43, 47-50]. For delivery of viral genome into the nucleus, viruses can hijack the host cell machinery to reach its destination. For example, HIV-1 complexes sequentially exhibit four distinct stages of movement inside a cell: (1) microtubule-dependent transport, (2) actin-directed trafficking, (3) confined mobility upon docking at the nuclear membrane, and (4) diffusive intranuclear movement [51].

Fluorescence imaging has substantially improved our understanding on viral infection, and has been used to study virtually every major step of virus infection cycle. The aforementioned examples are just a tip of iceberg for the insights garnered by fluorescence imaging for the study of virus-host cell interactions. Readers interested in this topic are referred to a comprehensive review of literature on this



topic [28, 52]. For the first part of this dissertation (Chapter 2 and 3), specifically, I will present the use of fluorescence imaging, in combination with other biochemical assays, to study the role of host factors in influenza virus infection.

### **1.3 Host factors in influenza virus infection**

Influenza virus is the major causal agent for flu, and has historically led to pandemic infections, such as the 1918 Spanish flu that killed an estimated 50 million people worldwide. It is an enveloped, negatively-sensed RNA virus. The virus envelope contains three viral membrane proteins: hemagglutinin (HA), neuraminidase (NA) and the protein channel M2. Enclosed within the viral envelope is a protein matrix made of M1 proteins, and a segmented genome, comprised of eight single-stranded RNAs packed into ribonucleoprotein complexes (vRNPs) with individual polymerase PA, PB1 and PB2 (Figure 1.2) [15].

As an obligatory pathogen that only encodes 13 viral proteins, influenza virus must hijack host cell machinery for productive infection. Influenza infection begins with virus binding to sialic acid on the plasma membrane [53], which triggers virus internalization through multiple endocytic routes including clathrin-mediated endocytosis and a clathrin-independent pathway [44, 54-57]. Internalized virus particles are first sorted into early endosomes, then low pH late endosomes, where viral fusion between the viral and endosomal membranes occurs to allow the release of viral genome into the cytoplasm. vRNPs are subsequently imported into the nucleus to initiate viral replication [15, 28, 58, 59]. As replication proceeds, viral mRNAs are exported out of the nucleus for protein translation, and different viral components are trafficked and assembled at the plasma membrane to form progeny virions (Figure 1.2) [60].

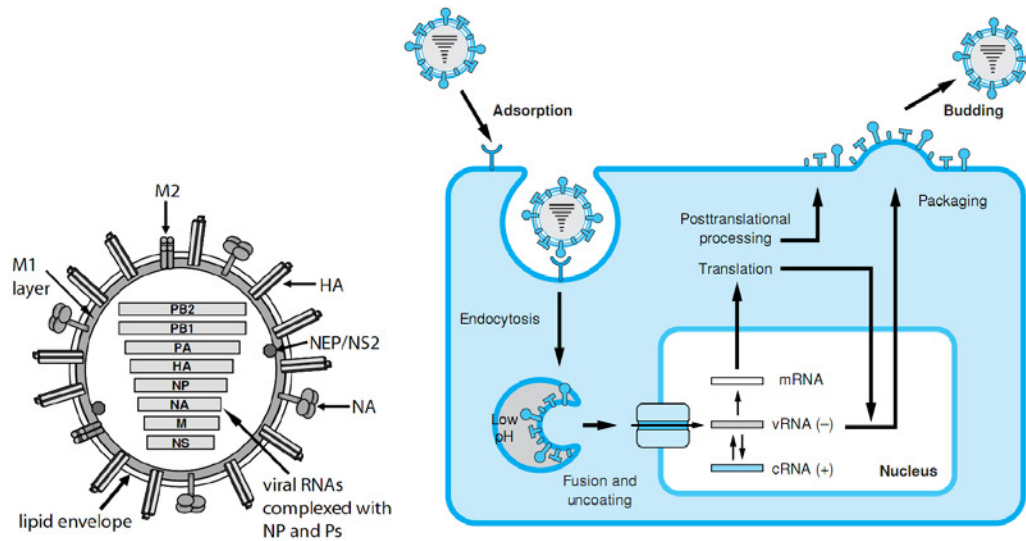


**Figure 1.2. Influenza virus structure and virus infection cycle** (Figures from reference [15])

To dissect the molecular and cellular mechanisms for influenza infection, it is of paramount importance to understand the interaction between the virus and host cell factors. In the past decade or so, live cell imaging has generated many important insights on influenza virology [52]. By tracking individual labeled-viruses during infection, for example, it has been shown that influenza enters the cell through three stages of active transport process: actin-dependent surfing in the cell periphery, a rapid microtubule-dependent unidirectional transport toward the perinuclear region, and an intermittent microtubule-dependent bidirectional transport before viral fusion [48]. Influenza virus is internalized through multiple endocytic pathways [44, 54-57], and can induce de novo assembly of clathrin machinery during clathrin-mediated endocytosis [56]. Inhibiting clathrin-mediated endocytosis for influenza shunts the virus to the alternative pathway, but does not affect overall infectivity [61]. By tracking individual virus trajectories that lead to successful infection, it was found that epsin 1, an adaptor protein for clathrin-mediated endocytosis, is recruited in synchrony with clathrin at influenza entry sites, while viruses that enter through the alternative pathway do not require epsin 1 [61]. Depleting epsin 1 or overexpressing a dominant-negative mutant only affects the clathrin-dependent entry pathway, with most of the virus particles routed through a clathrin-independent pathway [61].

After internalization, influenza virus hijacks the endocytic pathway to reach low-pH endosomes for successful viral uncoating. Live-cell tracking of Rab5 (early endosome marker) and Rab7 (late endosome marker) shows that early endosomes consist of two populations: a dynamic population that rapidly matures into late endosomes and a static population with much slower kinetics [62]. Interestingly, influenza virus and other degradative cargoes, primarily sort into the dynamic population of early endosomes, while recycling cargoes such as transferrin non-discriminately sorts into both populations [62]. The study revealed that sorting signals can come from the plasma membrane rather than beginning at the early endosomes. Furthermore, tracking influenza within the dynamic population revealed that viral fusion occurs within Rab5+ and Rab7+ endosomes [62]. Macropinocytosis has also been characterized by live cell imaging as an important entry pathway for influenza [44], although it remains unclear whether influenza virus can undergo fusion directly within macropinosomes, or whether influenza in macropinosomes eventually are sorted into degradative, low pH endosomal compartments for uncoating.

To further investigate the molecular pathways for influenza virus infection, several large scale siRNA screens and proteomic analyses have been performed recently and successfully identified hundreds of candidate genes involved in influenza infection [63-68]. Between different screen studies, relatively low overlap was observed for the candidate genes, perhaps due to the difference of reagents and cells used in these studies. However, among five large scale siRNA screens, CD81 and COPI complex emerged as top candidates for early virus infection, with COPI complex identified in four screens [63, 64, 66, 67], and CD81 in two screens [66, 67]. Additionally, CD81 was identified as a host cell component specifically incorporated into newly assembled virions through mass spectrum analysis of purified virions coming from infected cell [69]. The exact role played by CD81 and COPI complex in influenza infection, however, has not been elucidated thus far.

CD81 belongs to the family of tetraspanins, a family of evolutionally conserved proteins that are expressed in almost every cell type. There are over 32 members of tetraspanins in mammals, and they associate with each other and tetraspanin-interacting proteins to form tetraspanin-enriched microdomains

[70-72]. Like other tetraspanins, CD81 consists of three distinct domains: an extracellular domain with small extracellular loop and large extracellular loop; transmembrane domain and cytosolic domain. It is expressed on both the plasma and endosomal membranes [70, 73, 74]. Together with other tetraspanin family proteins, CD81 regulates many cellular processes such as cell adhesion, cell signaling, cell migration, and protein trafficking [70, 74-77]. Tetraspanins are known to play important roles in different steps of viral infection [78]. For example, CD81 functions as a co-receptor for hepatitis C virus (HCV) [79-82]. CD81 interacts with HCV glycoprotein E2 to prime the virus for low-pH dependent fusion during entry [79, 83, 84]. In addition to mediating viral entry, CD81 is also potentially involved in viral assembly. CD81 is one of the cell-derived components incorporated into purified influenza virus particles [69]. For HIV infection, CD81 and other tetraspanins have been previously identified as exit gateways for HIV budding, and CD81 colocalizes with HIV envelope proteins on the plasma membrane [85]. Relatively little is known about how CD81 regulates different steps during influenza virus infection.

COPI proteins form complexes that coat vesicles essential for intracellular trafficking. There are nine different COPI complex subunits— $\alpha$ ,  $\beta 1$ ,  $\beta 2$ ,  $\delta$ ,  $\epsilon$ ,  $\gamma 1$ ,  $\gamma 2$ ,  $\zeta 1$ , and  $\zeta 2$  [86-88], and multiple components of COPI complex are identified as host factors required for influenza infection. Each COPI complex contains a single copy of  $\alpha$ ,  $\beta 1$ ,  $\beta 2$ ,  $\delta$ , and  $\epsilon$  subunits, in addition to one of the following isoform combinations:  $\gamma 1/\zeta 1$ ,  $\gamma 1/\zeta 2$ , or  $\gamma 2/\zeta 1$ , to form a coatmer [86-88]. The coatmers are recruited to the vesicle membrane by activated ADP-ribosylation factor 1 (Arf1), which cycles between an activated GTP and inactivated GDP state [89]. Once formed, COPI coated vesicles mediate retrograde trafficking between Golgi apparatus and the ER, as well as between the Golgi stacks. In addition, COPI complexes have been suggested to play a role in endocytic tracking, multivesicular body formation and/or membrane trafficking [90-95]. COPI complexes have been shown to play important roles for virus infection such as VSV [45]. Disruption of COPI complex through  $\epsilon$ -COPI depletion inhibits VSV virus binding and internalization. On the other hand, short-term Brefeldin A (BrefA) treatment, an inhibitor that prevents GDP to GTP exchange of ARF1, leads to a specific decrease in VSV gene expression [45]. Influenza is a

different virus than VSV, it is thus unclear how COPI proteins are involved in each step of influenza virus infection.

#### **1.4 Super-resolution fluorescence microscopy**

Fluorescence microscopy has a resolution limit due to the diffraction of light. First recognized by Ernst Abbe in 1873, the resolution limit, or Abbe limit, defines the minimal distance between two objects that can be resolved by light microscopy [96]. The diffraction limit is calculated as  $\lambda/2n\sin\theta$ , where  $\lambda$  is the wavelength of light,  $n$  is the refraction index of the imaging medium, and  $\theta$  is the angle that the light converges to form a spot [96].  $n\sin\theta$  is also called the numerical aperture (NA). The intensity profile of a point of light source after passing through an object is known as point spread function (PSF). The resolution limit is approximately calculated as the full width at half maximum (FWHM) of the PSF [97]. For a fluorescence microscope equipped with an objective of  $\sim 1.4$  NA, and light source at visible spectrum, the lateral resolution is usually around 200 nm and the axial resolution is around 500 nm. The resolution limit presents as a major drawback to study sub-cellular organizations and molecular interactions on the nanometer scale. Significant advancements have been made in fluorescence imaging to push the boundary of resolution limit in recent years. Super-resolution fluorescence microscopy, a class of newly developed light microscopy, completely shatters the resolution limit and allows the study of nanoscopic biological processes [98-101].

There are two major categories of super-resolution imaging techniques: the first category relies on the use of patterned illumination to spatially modulate and confine a diffraction-limited fluorescent spot. The methods include stimulated emission depletion (STED) microscopy [102, 103], related RESOLFT microscopy [101], and saturated structured-illumination microscopy (SSIM) [104]. The second category of techniques relies on the precise localization of single molecules and reconstruction of measured positions from individual fluorophores. The methods include stochastic optical reconstruction microscopy (STORM) [105], photoactivated localization microscopy (PALM) [106], and fluorescence photoactivated localization microscopy (FPALM) [107]. Readers interested in a general overview of

super-resolution fluorescence microscopy are referred to excellent reviews [98-101]. In the following paragraphs, STORM, a method primarily used in this dissertation, will be described in more detail.

STORM, PALM and fPALM are conceptually similar techniques and they all rely on the detection and localization of single molecules [98, 99]. A single fluorophore appears as a diffraction-limited spot on a camera. However, the centroid position of the fluorophore can be determined with much higher accuracy [108, 109]. During STORM imaging, each photon can be counted as an independent measurement of the fluorophore's position. The uncertainty of finding the centroid position is inversely related to the number of photon ( $N$ ) collected, scaling approximately with its inverse square root ( $\sim 1/\sqrt{N}$ ) [98, 99]. Localization precision of less than one nanometer has been achieved with synthetic fluorophores that emit millions of photons [108].

A direct translation of high-precision localization information to super-resolution image, however, is still challenging if two fluorophores within the diffraction limit emit the photons at the same time. STORM overcomes this challenge by a sequential localization of photo-switchable fluorescent probes [98, 99]. To perform STORM imaging on a biological sample, a target of interest is first labeled with photo-switchable fluorescent probes that convert between an on (bright state) and off (dark state or another fluorescent state) state. Each imaging round, only a small subset of non-overlapping fluorophores are activated to the on state, and their localization can be accurately determined. After recording their positions, these fluorophores are switched to the off state, and a different subpopulation of fluorophores are switched to the on state. By repeating this process for many rounds, all the measured localizations can be superimposed to reconstruct a high-resolution image (Figure 1.3) [98, 99]. Using Alexa 647, a synthetic dye that emits over 5000 photons, a lateral resolution of less than 25 nm can be achieved through STORM [105].

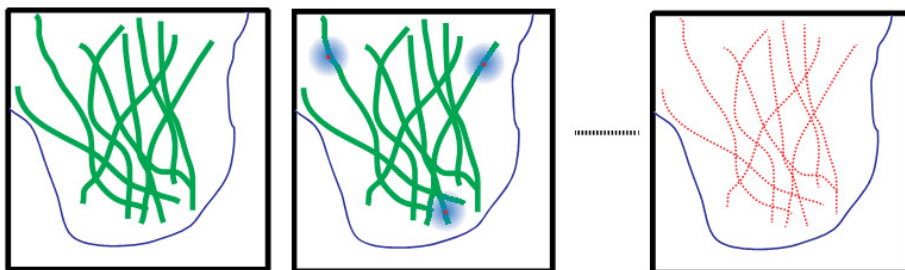


**Figure 1.3. The principle of STORM.** For a densely labeled cellular structure (green lines in the left image), during each imaging round, only a small subset of non-overlapping fluorophores are activated to the on state (blue circle in the middle image), and their localization can be accurately determined (red dot at the center of blue circle). After recording their positions, these fluorophores are switched to the off state, and a different population of fluorophores are switched to the on state. By repeating this process for many times, all the measured localizations can be superimposed to reconstruct a high-resolution image (red dotted line in the right image). Figure modified from reference [105].

STORM is compatible with multi-color and 3D imaging. There are several approaches for multi-color imaging: reporter-based and activator-based approach. The reporter-based approach is conceptually straightforward: fluorophores with different emission spectrum are used to label targets of interest, and images from different color channel are constructed from the photons emitted from that specific fluorophore [110]. For activator-based approach, dye-pairs capable of switching between the on and off state are used. In each dye pair, there is a reporter fluorophore that undergoes photoswitching and an activator fluorophore that excites the reporter from off to on state. The color is distinguished by the activation wavelength used to excite the activator and shuffle its paired reporter to the on state [111].

For 3D imaging, a cylindrical lens is inserted at the detection path before the camera to introduce astigmatism into the PSF [112]. With the cylindrical lens, fluorophores on the focal plane will have a circular PSF, while those above or below have an elliptical PSF. The degree of ellipticity is related to the axial position of the fluorophore. Using a single objective and Alexa 647, 3D STORM imaging with a lateral resolution of 25 nm and axial resolution of 50 nm has been demonstrated previously [112].

STORM imaging can be done in live cells. A spatial resolution of 25nm and time resolution of 0.5 second has been achieved for 2D STORM image. For live cell 3D imaging, a frame can be imaged as fast as 1-2 second while maintaining a lateral resolution of ~30 nm and axial resolution of ~50 nm [113,

114]. The image resolution for STORM can be further improved by collecting more photons. In dual-objective STORM, for example, two objectives collect the photons emitted from the sample sandwiched in between, and a lateral resolution of 7 nm and axial resolution of 15 nm has been achieved [115]. A separate approach uses fluorophore caging to generate photoswitchable probes with high photon yield, and also improves the resolution of STORM to sub-ten nanometer [116].

## **1.5 Actin cytoskeleton in neurons**

Neurons are one of the most polarized cell types with their somatodendritic regions receiving synaptic inputs and axons propagating electrical signal output to target cells. The shape and mechanical properties of a neuron is critically dependent on cytoskeletal proteins; many neuronal functions are also supported by the cytoskeleton [117-120]. Specifically, cytoskeletal structures are essential for the establishment of neuronal polarity, the growth and stabilization of axons and dendrites, the trafficking of cargos to specific neurites, as well as the plasticity of synapses [121-126]. There are three types of cytoskeletal proteins in neurons: microtubules, neurofilament and actin. Each cytoskeletal protein can oligomerize and form a distinctive ultrastructure, and regulate many important cellular functions [127].

Like in other eukaryotic cells, microtubules in a neuron are assembled from heterodimers of  $\alpha$  and  $\beta$  tubulin to form a hollow tubular structure with an outer diameter of 25 nm [120]. Tubulin dimers exhibit two distinct states by binding with GTP or GDP, and the conversion between these two states is closely related to the assembly and disassembly of microtubules. Briefly, GTP-associated tubulins are incorporated into the fast-growing end of microtubule (plus end), while GDP-associated tubulins more easily dissociate from the microtubule, and they mark the minus end of microtubule [120]. In neurons, microtubule filaments have a more uniform orientation inside axons with the plus end extending away from the cell body, contrasting from the mixed orientations of microtubules in dendrites [119]. Tubulins inside axons also exhibit a higher rate of acetylation than that of dendrites, a post-translation modification that stabilizes microtubule filaments [119]. Microtubules are organized as bundled filaments inside



neurites and regulate many neuronal functions such as cargo transport and establishment of neuronal polarity [118].

Five types of intermediate filaments (IF) exist in eukaryotic cells, including Type I, II, III, IV, and V IFs [120]. In neurons, the most abundant types are Type III and IV IFs, and they are generally named as neurofilament (NF) [127]. Like all the other IFs, NFs organize into a solid ropelike fiber, with a diameter of around 8-12 nm. They differ from other IFs by having an extended sidearm that projects out from the fiber surface. NFs are stable cytoskeletal structure and exhibit distinctive cellular distribution. They provide general mechanical support for the cell and help to maintain neuronal morphology [127]. Entangled NFs are often observed as a hallmark for many neurodegenerative diseases such as Alzheimer Disease (AD) and Amyotrophic Lateral Sclerosis (ALS) [127].

Among the three type of cytoskeletal proteins, actin filament is the thinnest, with actin monomers oligomerizing into two strings of intertwined fibers of around 7 nm in diameter [120]. Monomeric actin is generally called globular actin (G-actin), whereas the polymerized form is called filamentous actin (F-actin). Like microtubules, actin filaments also display an asymmetric orientation, with a plus end exhibiting fast polymerization and a minus end showing slow dynamics. Individual actin filaments often associate with each other to form actin bundles, such as stress fibers; or they crosslink with each other and form a dense meshwork beneath the cell membrane [120].

A variety of proteins have been found to interact with actin, including actin polymerization factors, nucleation factors, motor proteins, actin capping protein, anchoring proteins, spectrin, etc [117]. Among these proteins, the distribution and general function of spectrin in neurons have been well characterized. Spectrin is an actin-interacting protein initially identified in red blood cells. There are two subunits for spectrin,  $\alpha$  and  $\beta$  spectrin. Two  $\alpha$  ( $\alpha$ I and  $\alpha$ II) and five  $\beta$  subunits ( $\beta$ I– $\beta$ V) have been cloned in mammals [128].  $\alpha$  and  $\beta$  spectrin associate laterally to form an antiparallel heterodimer, which are joined head to head to form a rod-shaped heterotetramer with a length around 200 nm [129]. In red blood cells,  $\alpha$  and  $\beta$  spectrin bind with actin and actin-associated proteins to form a 2D pentagonal and

hexagonal structure beneath the plasma membrane (Figure 1.4) [130, 131]. This structure is further anchored to the plasma membrane by ankyrin through the ankyrin-binding domain of spectrin [128, 132]. Depleting spectrin or ankyrin leads to a significant change of membrane plasticity in red blood cells, indicating the actin-spectrin associated membrane skeleton is essential for providing mechanical support for a cell [129].

In neurons, the major subunits of spectrin are  $\alpha$ II,  $\beta$ II,  $\beta$ III and  $\beta$ IV spectrin.  $\alpha$ II and  $\beta$ II are expressed in many neuronal types [133, 134], while  $\beta$ III spectrin is more enriched in Purkinje cells [135-137].  $\beta$ IV spectrin, on the other hand, is predominantly found in axonal initial segment (AIS) regions [128, 138]. Together, spectrin, actin and associated molecules make up a membrane skeleton beneath the plasma membrane in neurons.

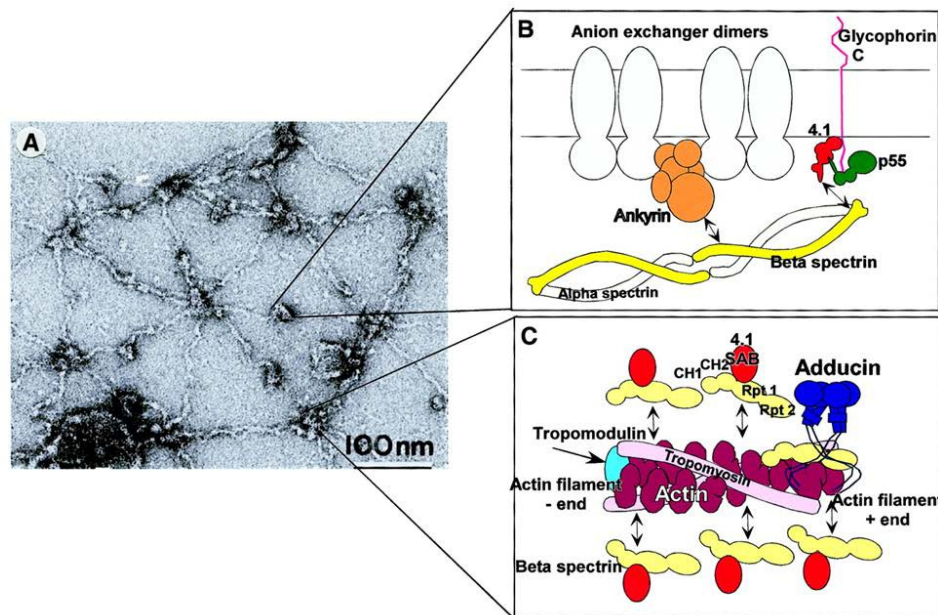


**Figure 1.4. Actin, spectrin-associated cytoskeletal structure in red blood cells.** A) Electron microscopy of the membrane skeleton in erythrocytes. Spectrin tetramers are cross-linked at nodes with actin and associated molecules to form a 2D pentagonal and hexagonal structure beneath the plasma membrane. B) Spectrin is attached to the plasma membrane through interaction with ankyrin and protein 4.1. C) Short actin filament interacts with tropomodulin at the minus end, and adducin at the plus end, whereas tropomyosin lies along the filament. Actin also binds with the N terminal domain of  $\beta$ -spectrin. (Figure from reference [128]).

Actin and actin-associated cytoskeletal proteins play crucial role in determining the shape of the cells, as well as in supporting many important cellular functions [117]. In neurons, actin filaments are particularly enriched in the growth cones, dendritic spines and presynaptic terminals [125]. Electron microscopy imaging has shown that actin forms a dense meshwork-like structure beneath the cell membrane [139]. During neuronal development, actin filaments exhibit high dynamics within the growth cone, spine or presynaptic terminal [125]. The retrograde flow of actin in the growth cone is essential for axonal growth and path finding, whereas the high actin dynamics at the tip of neurite is important for the establishment of neuronal polarity [122, 140, 141]. Increasing evidence also suggests important roles for spectrin in the maintenance of neuronal polarization, as well as the development and stabilization of axons [134, 142].  $\alpha$ II and  $\beta$ II spectrin are mainly located in axons, and are both involved in maintaining the compartmental domains of axons [133, 134]. Mice lacking either  $\alpha$ II or  $\beta$ II spectrin are embryonically lethal [134, 143, 144], whereas knocking down  $\alpha$ II or  $\beta$ II spectrin leads to a loss of AIS without affecting axon specification [134]. In *C elegans*, spectrin participates in the mechanical sensing in sensory neurons [145], and provides the mechanical stability for the growing axons [142]. Axons more easily break in *C elegans* lacking spectrin [142], highlighting the crucial function of spectrin in providing mechanical support for neurons. Dysfunctions in actin and associated molecules have been implicated in various neurodegenerative diseases, such as AD, Parkinson's disease (PD), and ALS [146-148].

Despite its importance, our understanding of actin structures in neurons---particularly in axonal shafts regions---is limited due to its high density in neuronal processes and the difficulty to resolve with conventional imaging methods. The challenge mainly lies in the fact that neurites are often sub-micrometer in diameter but contain a high density of different types of cytoskeletal filaments, such as microtubules and neurofilaments [139]. Under electron microscopy, these cytoskeletal proteins entangle with each other, making the tracing of individual protein challenging [139]. Resolving the organization of actin and spectrin in the axons and dendrites requires imaging tools with both high spatial resolution and molecular specificity.

Given its impressive resolution and molecular specificity, super-resolution fluorescence microscopy is a powerful tool to study the ultrastructural organization of actin and associated molecules in axons. Using STORM, the Zhuang lab recently discovered a strikingly ordered submembrane skeleton in axons [149]. Three molecular components of this novel membrane skeleton, actin, spectrin and adducin were identified. STORM imaging of actin in cultured hippocampal neurons revealed ring-like structure of actin that were wrapped around axonal circumference and evenly spaced with 180-190 nm periodicity along the axonal shaft (Figure 1.5). This periodic structure spans the entire axon shaft starting from the axon initial segment. In stark contrast, dendrites appear to be dominated by long actin filaments that run along the dendritic shaft. Two-color STORM images of actin and the center region of spectrin tetramer showed highly regular, alternating patterns of actin and spectrin in axons, indicating adjacent actin rings are connected by spectrin tetramers (Figure 1.5). In addition, adducin also forms periodic ring-like structure that colocalizes with the actin rings. Given that adducin caps one end of actin filaments, this result suggests that the ring-like actin structures are made of capped, short actin filaments aligned along the circumferential direction of the axon, probably facilitated by actin-binding or actin-crosslinking proteins [149].

The results described above suggest a crude structural model of the axonal submembrane cytoskeleton (Figure 1.5) [149]: short actin filaments, capped by adducin at one end, align into ring-like structures wrapping around the circumference of the axon; spectrin tetramers connect the adjacent actin/adducin rings along the axon, creating a quasi-one-dimensional periodic lattice structure. Interestingly, this periodic lattice places sodium channels into a periodic pattern along the axon initial segments, suggesting the ability of this submembrane cytoskeleton to organize molecular components of the axonal membrane, which is critical for action potential generation and propagation, as well as for other signaling processes in axons [149]. These observations suggest important functional roles of this novel cytoskeletal structure, but little is known about this new form of molecular assembly.

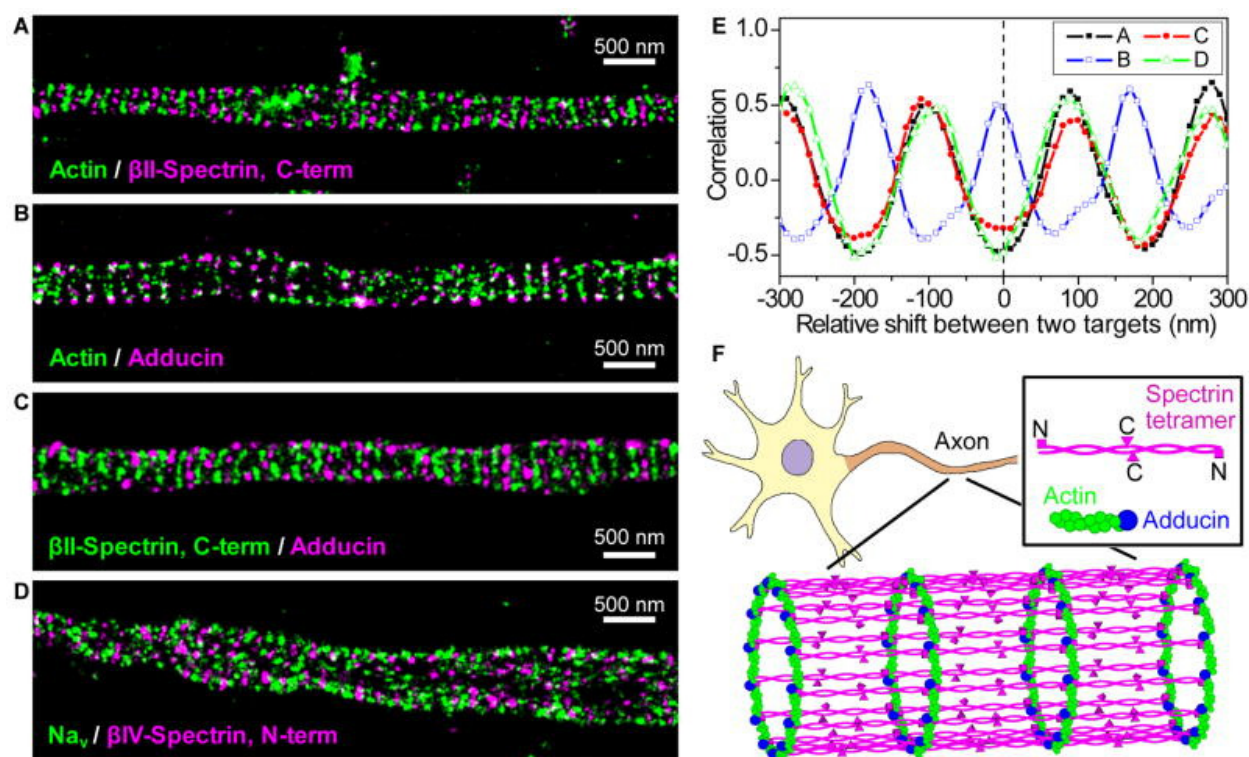


**Figure 1.5. The actin, spectrin-based periodic membrane skeleton in axons.** A) Two-color STORM image of actin (green) and  $\beta$ II-spectrin C-terminus (magenta). B) Two-color STORM image of actin (green) and adducin (magenta). C) Two-color STORM image of  $\beta$ II-spectrin (green) and adducin (magenta). D) Two-color STORM image of sodium channels (green) and  $\beta$ IV-spectrin N-terminus (magenta). E) Spatial correlations between actin and  $\beta$ II-spectrin C-terminus (A, black), between actin and adducin (B, blue), between adducin and  $\beta$ II-spectrin C-terminus (C, red), and between sodium channels and  $\beta$ IV-spectrin N-terminus (D, green) to show the periodic distribution of these molecules with a periodicity of  $\sim 180$ – $190$  nm. F) A model for the periodic membrane skeleton. Actin filaments (green) form a ring-like structure around the circumference of the axon. Actin filaments are capped by adducin (blue), and adjacent actin rings are connected by spectrin tetramer (magenta) (Figure from reference [149]).

## 1.6 Outline of chapters

The dissertation reports the application of fluorescence imaging to study the role of host factors in influenza virus infection, and super-resolution imaging to the characterization of developmental mechanism of the periodic membrane skeleton.

In Chapter 2, my colleagues and I examined the effect of CD81 depletion on the major steps of influenza infection. CD81 primarily affected virus infection at two stages: viral uncoating during entry and virus budding. Using single-virus tracking, CD81 was found to mark a specific endosomal population

and about half of the fused influenza virus particles underwent fusion within the CD81-positive endosomes. Depletion of CD81 resulted in a substantial defect in viral fusion and subsequent viral infection, without impacting virus binding, internalization or trafficking into early endosomes. During virus assembly, CD81 was recruited to virus budding site on the plasma membrane, and in particular, to specific sub-viral locations. In spherical and slightly elongated influenza virus, CD81 was localized at both the growing tip and the budding neck of the progeny viruses. CD81 depletion resulted in elongated budding virions that failed to detach from the plasma membrane and a marked decrease in progeny virus production. Taken together, these findings demonstrate an important dual function of CD81 in both entry and budding of influenza viruses.

In Chapter 3, my colleagues and I conducted a comprehensive study to characterize the role of COPI complex in influenza virus infection. We found that prolonged exposure to COPI complex disruption through siRNA resulted in significant defects in virus internalization and trafficking to late endosomes. Acute inhibition of COPI complex with pharmacological compounds, however, failed to recapitulate the same entry defects as observed with the COPI-depleted cells, but did result in specific decreases in viral membrane protein expression, assembly and progeny virion production. Our findings suggest that COPI complexes likely function indirectly in influenza virus entry but play direct roles in viral membrane protein expression and assembly.

In Chapter 4, my colleagues and I focused on using super-resolution imaging to study the developmental mechanism of the periodic membrane skeleton. Specifically, we addressed the question of how the periodic membrane skeleton develops during neuronal polarization, and why it is primarily formed in axons instead of dendrites. We found that formation of the periodic membrane skeleton initiated early during neuronal development, and originated from regions closer to the cell body and propagated to the distal ends of axons. The lattice structure further matured by recruiting additional molecular components, and the matured membrane skeleton was highly stable. Multiple molecular factors played roles in regulating the formation of this structure. The lattice structure depended on intact

microtubules. The high local concentration of  $\beta$ II spectrin in axons was the key determining factor for the specific formation of the lattice structure in axons, and artificially increasing the concentration of  $\beta$ II spectrin in dendrites was sufficient to induce the formation of the periodic lattice structure in dendrites. Remarkably, ankyrin B was important for the polarized distribution of  $\beta$ II spectrin in neurites; in ankyrin B knockout mice,  $\beta$ II spectrin was evenly distributed in axons and dendrites, giving rise to a highly regular, periodic membrane skeleton in both dendrites and axons.

As the initial discovery was made primarily in hippocampal neurons, in Chapter 5, my colleagues and I examined the prevalence of the periodic membrane skeleton in different neuronal types. We found that the periodic lattice structure is highly prevalent in different neuronal types from the central and periphery nervous system. The periodic skeleton predominantly existed in axons for all the neurons we imaged, while dendrites only contained isolated patches of the lattice structure. Moreover, we found that myelination does not impact the formation of this lattice structure in vitro.

In Chapter 6, I summarize the findings presented in Chapter 2 to 5, and present a discussion on the future directions for these studies.

## **Chapter 2: Dual Function of CD81 in Influenza Virus Uncoating and Budding**

Work in this chapter was performed in collaboration with Dr. Eileen Sun, Miriam Bujny, and Doory Kim. Most of the results from this work are published in [150].



## 2.1 Introduction

Influenza virus, the major causal agent of flu, is an enveloped, negative-sense RNA virus containing three viral membrane proteins: hemagglutinin (HA), neuraminidase (NA), and M2 proton channel. Encapsulated within the viral envelope is a layer of matrix protein (M1) and a segmented genome. The eight single-stranded RNAs package into viral ribonucleoprotein complexes (vRNPs), each attached to a RNA-dependent RNA polymerase complex with three subunits: PA, PB1, and PB2 [15].

As an obligatory pathogen that encodes only 13 viral proteins, influenza virus must rely on host proteins and cellular machinery to complete its infection cycle. Influenza infection begins with virus binding to sialic acids on the plasma membrane [53]. Virus-receptor interaction subsequently triggers viral entry through multiple endocytic routes including clathrin-mediated endocytosis, a clathrin/caveolin-independent pathway, and macropinocytosis [44, 54-57]. Upon internalization, virus particles are trafficked from early endosomes to maturing endosomes, where fusion between the virus and endosomal membranes results in release of vRNPs into the cytoplasm followed by nuclear import of the vRNPs [15, 28, 58, 59]. As replication proceeds, viral mRNAs are exported out of the nucleus for protein translation, and viral components are trafficked to the plasma membrane, the site of virus assembly and progeny virion egress [60].

Recently, several genome-wide siRNA screens identified host factors exploited by influenza virus [63-67]. CD81 emerged as a top candidate in two screens and was found to regulate early viral entry steps [66, 67]. CD81 belongs to the family of tetraspanins and is expressed on both plasma and endosomal membranes [70, 73, 74]. It associates with other tetraspanins and tetraspanin-interacting proteins to form tetraspanin-enriched microdomains [70-72]. Together, these proteins regulate many cellular processes such as cell adhesion, cell signaling, cell migration, and protein trafficking [70, 74-77]. Tetraspanins are known to play an important role in different steps of viral infection [78]. For example, CD81 functions as a co-receptor for hepatitis C virus (HCV) [79-82]. CD81 interacts with HCV glycoprotein E2 to prime the virus for low-pH dependent fusion during entry [79, 83, 84]. In addition to mediating viral entry, CD81 is

also potentially involved in viral assembly. CD81 is one of the cell-derived components incorporated into purified influenza virus particles [69]. It is however unknown how CD81 facilitates influenza viral entry, or whether CD81 plays a functional role in influenza virus assembly.

We conducted a comprehensive study from viral entry to egress to examine the effect of CD81 depletion on influenza infection. Upon dissecting each of the major steps in influenza infection pathway, we found that CD81 was required for productive viral infection and that CD81 primarily functions at two stages: viral fusion within endosomes and virus budding. About half of the influenza virus particles that fused in cells underwent fusion within CD81+ endosomes, and CD81 depletion led to a decrease in virus fusion and infection. CD81 was highly enriched in the virus budding zones and recruited to specific sub-viral locations. During virus assembly, CD81 initially formed small clusters at the growing tip of assembling virus, and then localized at both the growing tip and budding neck of spherical or slightly elongated virions. CD81 depletion led to an increase in the propensity of budding virions to remain attached to the plasma membrane and a reduction in progeny virus production. These findings demonstrate a dual function of CD81 in both entry and budding of influenza viruses.

## **2.2 Results**

### **2.2.1 CD81 is involved in both early and late stages of influenza virus infection**

To elucidate the role of CD81 in influenza virus infection, we used CD81 knockdown by siRNA to probe the effect on three different influenza A virus strains: influenza A/WSN/33 (H1N1), a lab-adapted strain that mainly produces spherical virus particles; influenza A X-31, A/Aichi/68 (H3N2) which has a slightly elongated shape [151]; and influenza A/Udorn/72 (H3N2), which can produce long filamentous virus [152-155]. We screened six CD81 siRNA constructs, including several previously reported ones [66, 67], and found that CD81 siRNA 1 gave the highest knockdown efficiency (Figure 2.1A, B and Figure 2.2A, B). After 48 hours, siRNA 1 yielded 80-85% CD81 knockdown (Figure 2.1C). Treatment with siRNA 1 specifically depleted CD81, whereas the expression levels of several known

CD81-associating proteins, including CD9, CD82, CD63, integrin  $\beta 1$  (ITGB1), EGFR, and EWIF, were not affected (Figure 2.1D). In subsequent experiments, we used siRNA 1 to deplete CD81 in A549 lung carcinoma cells.

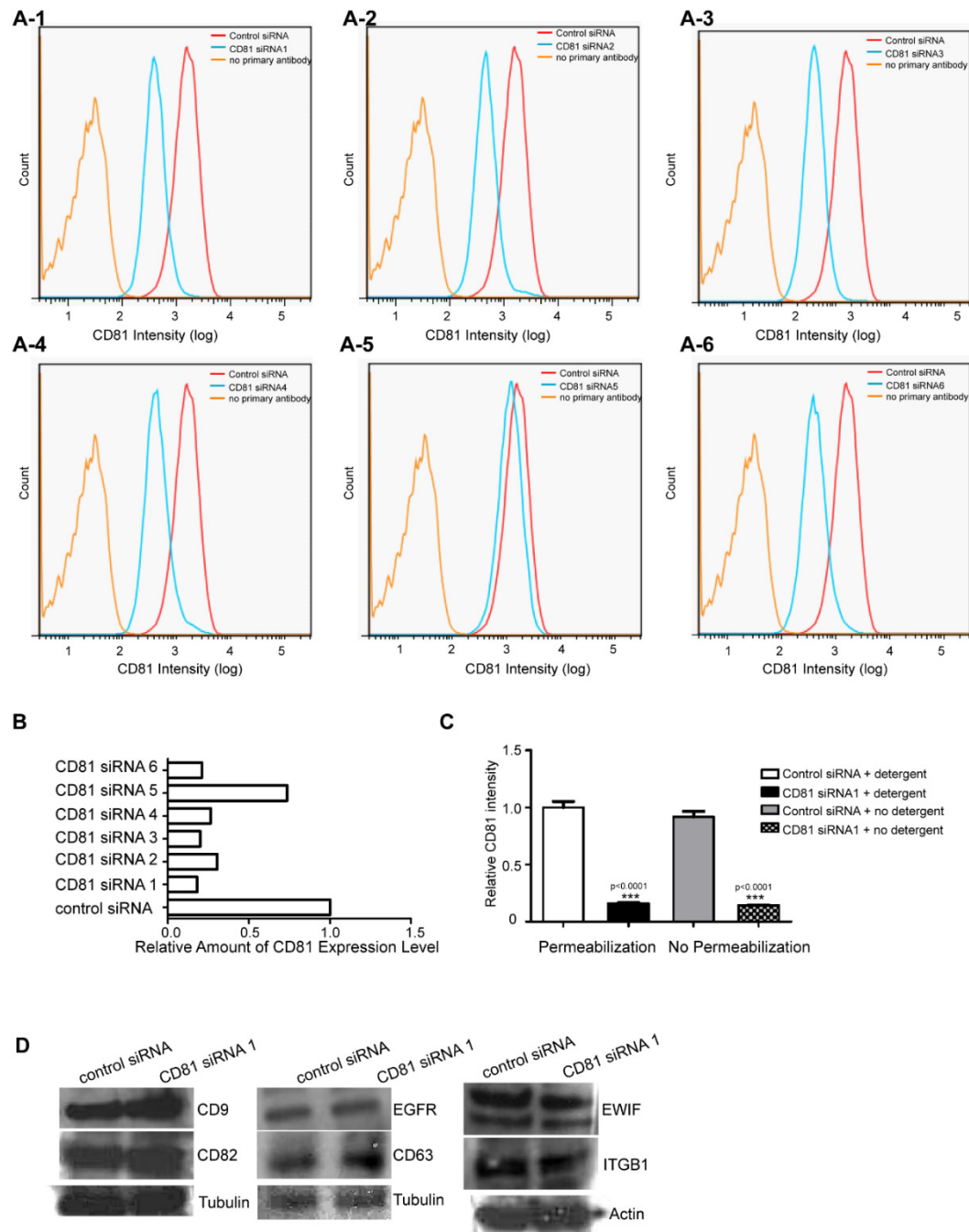


**Figure 2.1. CD81 depletion efficiency with different siRNA constructs.** A) Six different siRNA constructs were tested for CD81-knockdown efficiency after 48 hours of electroporation. CD81 expression was measured by flow cytometry following staining with anti-CD81 primary antibody and

**Figure 2.1. (continued)** fluorescently labeled secondary antibody. At least 10,000 cells were measured for each condition. The orange, blue and magenta curves correspond to the intensity profiles measured for cells without addition of the primary antibody, control (non-targeting) siRNA treated cells immunostained for CD81, and CD81 siRNA treated cells immunostained for CD81, respectively. B) Quantitative summary of the measurements from (A). CD81 siRNA 1 was selected for subsequent studies. C) A549 cells were treated with control or CD81 siRNA 1 for 48 hours. Cells were either permeabilized with detergent or not permeabilized to detect the total amount of CD81 in cells or the amount of CD81 on the cell surface, respectively. The intracellular CD81 level was then calculated by subtracting the amount of CD81 on the cell surface from the total amount of CD81. Based on the quantification, the cell-surface and intracellular CD81 fractions were ~92% and 8% in control cells, respectively. The partition is similar in CD81-knockdown cells (87% versus 13% for cell-surface and intracellular CD81, respectively). A two-tailed *t-test* was performed in each case and the *p* values were provided. D) CD81 knockdown does not affect the expression of CD81-associating proteins. A549 cells were treated with control or CD81 siRNA for 48 hours. Cells were harvested for western blotting with indicated antibodies. Actin and tubulin were used as loading controls.

To assay the effect of CD81 depletion on the production of infectious viral progeny, siRNA-treated A549 cells were infected with WSN, X-31 or Udorn virus at a MOI of <0.1 for 36 hours. The virus titer of the supernatant was determined using plaque assays. Compared to the non-targeting control siRNA treated cells, the CD81-knockdown cells exhibited a substantial decrease in virus titer: ~90% decrease for WSN, ~75% decrease for X-31, and ~70% decrease for Udorn (Figure 2.2C). These results are consistent with the previously published data [66, 67], and indicate that multiple different influenza strains require CD81 for infection.

Next, we proceeded to determine which stage(s) of the multi-step influenza-infection process is CD81-dependent. To test whether CD81 affects early infection, we infected siRNA-treated A549 cells and measured the expression of NP, the first viral protein expressed in influenza-infected cells [66, 67, 156]. We assayed the fraction of cells that express NP (NP+) as well as the level of NP expression in each NP+ cell using flow cytometry. For all three viral strains, CD81-knockdown cells had ~50% fewer NP+ cells, as compared to non-targeting siRNA treated control cells (Figure 2.2D). Among the NP+ cells, the NP expression level was similar between control and CD81-knockdown cells (data not shown). These results suggest that CD81 is involved in early infection either at the step of or prior to viral protein expression.

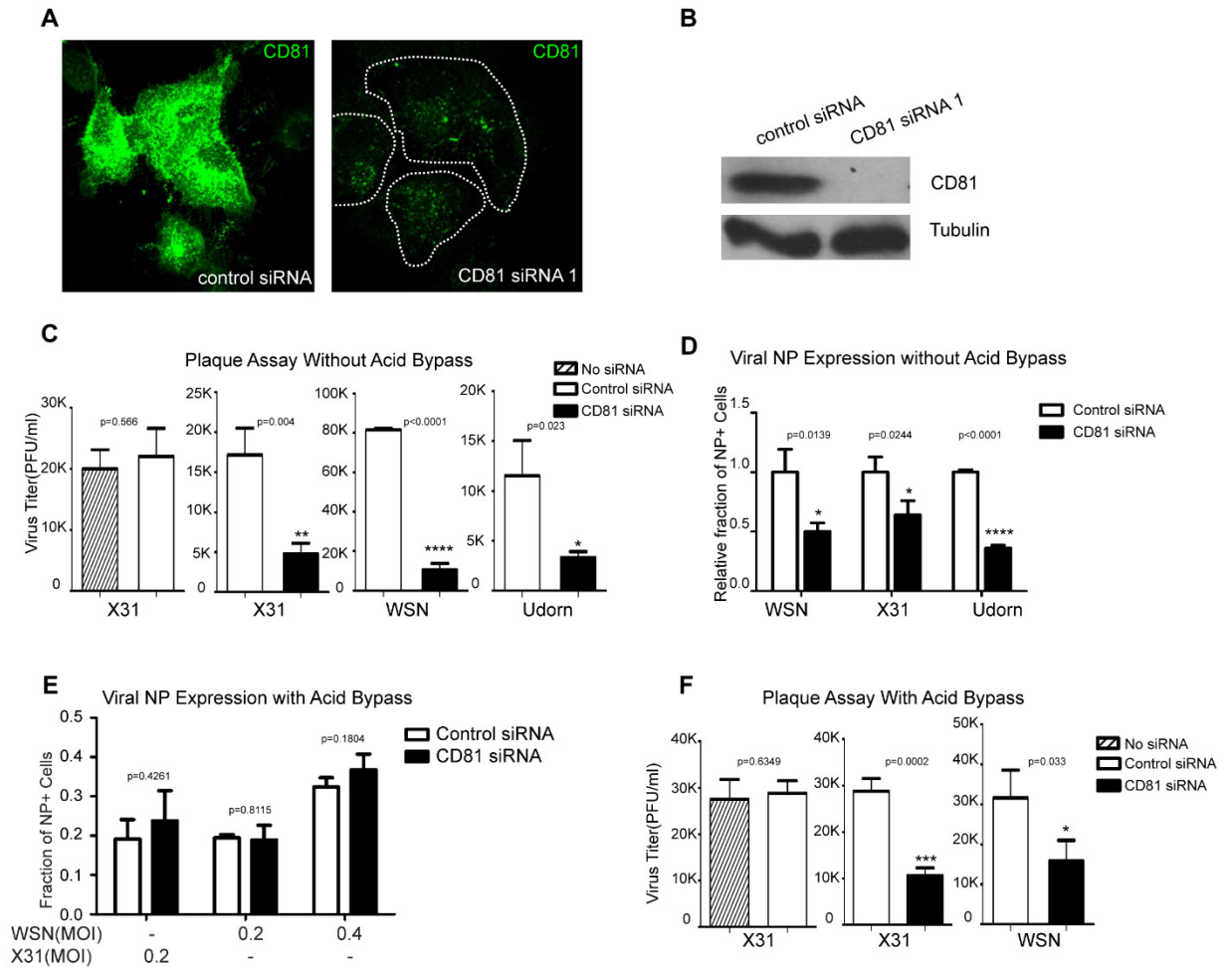


**Figure 2.2. CD81 is involved in both early and late stages of influenza virus infection.** **A)** A549 cells were treated with non-targeting control siRNA, or CD81 siRNA1 for 48 hours and immunostained with anti-CD81 antibody. Images are maximum projections of confocal z-stacks. **B)** A549 cells were treated with control or CD81 siRNA for 48 hours. Cells were harvested for western blotting with indicated antibodies. Tubulin was used as a loading control. **C)** Influenza virus infection is impaired by CD81 depletion. A549 cells were treated with siRNAs or mock treated for 48 hours and subsequently infected with X-31, WSN, or Udorn at a MOI of <0.1 for 36 hours. The viral titer in the supernatant was determined by plaque assays. The shaded bar indicates the infectivity measured in cells mock treated with a transfection solution that contains no siRNA; the hollow bars indicated the infectivity measured in cells treated with control, non-targeting siRNA; the black solid bars indicate the infectivity measured in cells treated with CD81 siRNA. **D)** The number of infected cells expressing viral NP is reduced by about 50% upon CD81- knockdown. siRNA-treated A549 cells were infected with WSN, X-31, or Udorn viruses with a MOI of <0.1 for 8 hours without acid bypass and the fraction of cells expressing NP was measured through flow cytometry. **E)** Viral NP expression is unaffected upon CD81 knockdown when influenza infection is induced by the acid-bypass treatment to eliminate the entry defect. siRNA-treated A549 cells were allowed to bind with WSN or X-31 virus on ice for 1 hour, treated with warm low pH PBS buffer (pH 4.5) for 2 minutes. After 8 hours, cells were collected and stained against NP for flow cytometry analysis. **F)** Virus titer in the supernatant is reduced by ~50% or more in CD81-knockdown cells infected by influenza viruses through the acid-bypass treatment. Briefly virus was allowed to bind with control or CD81-knockdown cells on ice for 1 hour. Unbound virus particles were washed out and low pH buffer was added in for 2 minutes to trigger virus fusion at the plasma membrane. At 17 hours post infection,

**Figure 2.2. (continued)** supernatant was collected and the viral titer was assayed by plaque assay. For figure 2.2C-F, the error bars are standard deviation derived from three independent experiments. A two-tailed student *t-test* was performed for all of the numerical data, and the p value of the data is shown. A p value smaller than 0.05 indicates there is a statistically significant difference.

In order to test whether CD81 directly affects viral protein expression, we next induced viral fusion (uncoating) at the plasma membrane through an acid-bypass treatment: treatment with a buffer of pH below 5, the pH value required for HA-induced membrane fusion. We then probed the expression of NP in these samples. The fraction of NP+ cells and the level of NP expression were similar between control and CD81-knockdown cells infected by the virus using the acid-bypass treatment (Figure 2.2E and data not shown). These results suggest that CD81 is not directly involved in the viral protein expression, and the inhibition of virus infection by CD81 knockdown was most likely due to inhibition of viral uncoating in endosomes or any step prior to uncoating. It is worth noting that this acid-bypass assay overcame the entry defect for the WSN and X-31 strain, but a similar acid bypass treatment did not work for the Udorn strain, likely because low pH causes fragmentation of filamentous influenza viruses [57].

To probe whether CD81 plays additional roles beyond viral uncoating, we induced influenza viral fusion at the plasma membrane using the acid-bypass treatment to overcome the entry defect, and determined the virus titer of the supernatant 17 hours post-infection. Notably, as compared to control siRNA treated cells, the virus titer was decreased by more than 50% in the CD81-knockdown cells (Figure 2.2F). This defect did not result from a decrease in viral gene expression, as the percent of viral protein expressing cells and the expression level at 17 hours post-infection were unaffected upon CD81 knockdown (Figure 2.2E and data shown later). These results suggest that CD81 affects another step post viral gene expression.

Taken together, the above results indicate that CD81 is important for two distinct stages of the influenza infection cycle: one during the early infection at or prior to viral uncoating and one during late infection after viral gene expression. In the following experiments, we aimed to identify the specific roles of CD81 in influenza virus infection.

### **2.2.2 CD81 is not involved in virus binding, internalization or trafficking to early endosomes.**

To identify the CD81-dependent entry step(s), we conducted a series of experiments to examine the effect of CD81 on virus binding, internalization, transport into early endosomes, and fusion. siRNA-treated A549 cells were first incubated with fluorescently labeled X-31 virus for 30 minutes at 4 °C, a temperature that inhibits endocytosis. The amount of surface-bound virus was analyzed through flow cytometry. CD81-knockdown cells exhibited no defect in binding with influenza viruses when compared to control cells treated by non-targeting siRNA (Figure 2.3A). Next, influenza virus infection was allowed to proceed for 30 minutes at 37 °C, and the number of internalized virus particles was quantified. As shown in Figure 2.3B, the number of internalized viruses per cell was similar between control and CD81-knockdown cells. Moreover, virus particles in both control and CD81-knockdown cells were delivered into early endosomes after internalization at 37 °C. At 20 minutes post infection, the mean fraction of virus particles colocalized with early endosomes (marked by EEA1) was ~50% and ~53% for control and CD81-knockdown cells, respectively (Figure 2.3C). These results suggest that CD81 does not affect trafficking of influenza virus to early endosomes.

Additionally, we tested the effect of CD81 depletion on two other viruses: respiratory syncytial virus (RSV) and GFP-encoding pseudotyped murine leukaemia virus (MLV), which are known to undergo virus fusion in early endosomes in a pH-independent manner [157, 158]. Pseudotyped MLV infected cells express GFP, but cannot produce complete virions, allowing the quantification of MLV entry through measuring the GFP expression. For RSV, we measured the expression level of the fusion protein (F protein) after 24 hours of infection. As shown in Figure 2.3D, the fraction of infected cells was similar between control and CD81-knockdown cells with MLV and RSV infection. This data further corroborates the notion that CD81 does not affect virus trafficking into early endosomes.

Taken together, the results presented above indicate that CD81 is not involved in influenza virus binding, internalization, or trafficking into early endosomes.

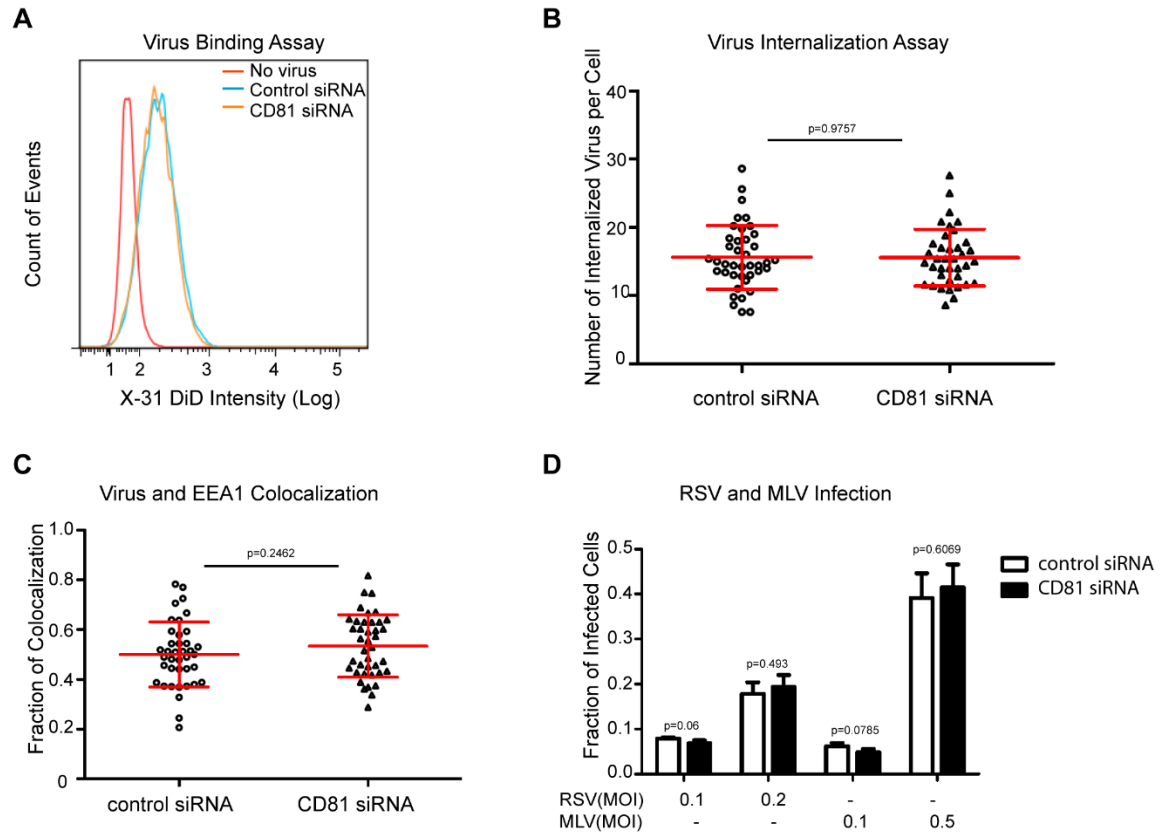


**Figure 2.3. CD81 is not required for virus binding, internalization or delivery into early endosomes**

A) CD81-knockdown does not affect virus binding, as measured by flow cytometry. The magenta, blue and orange curves correspond to the intensity profiles measured for cells without adding viruses, control cells after influenza virus binding, and CD81-knockdown cells after influenza virus binding, respectively.

B) The number of virus particles internalized is not affected by CD81 knockdown. The number of internalized virus particles was shown in a dot plot, with the middle line representing the mean value, and top/bottom line representing standard deviation. At least 40 randomly chosen cells were analyzed for each condition.

C) The percent of virus particles colocalizing with early endosome is not affected by CD81 knockdown. Early endosomes were immunostained with anti-EEA1 antibody. Data was plotted similarly as in (B). At least 40 randomly chosen cells were analyzed for each condition.

D) CD81 depletion does not affect RSV or pseudo-typed MLV infection. siRNA-treated A549 cells were infected with different doses of RSV and pseudo-typed MLV virus for 24 hours. For RSV virus infection, RSV fusion protein expression was quantified by flow cytometry, while for pseudo-typed MLV virus, the GFP signal was analyzed. A two-tailed student *t-test* was performed for all of the numerical data, and the *p* value of the data is shown.

### 2.2.3 Influenza virus particles are delivered to and fuse in CD81+ endosomes

Next, we probed the role of CD81 in virus fusion. Influenza virus is trafficked from early endosomes to maturing endosomes, in which the low pH environment triggers conformational changes in HA that mediate viral fusion with the endosomal membrane [50, 53, 59]. In addition to being distributed on the plasma membrane, CD81 also showed substantial colocalization with early and maturing



endosomes, which are Rab5 positive (Rab5+) (Figure 2.4A) [50]. About 30-35% Rab5+ endosomes contained CD81 (Figure 2.4A), suggesting that CD81 is enriched in a sub-population of these endosomes. To probe whether influenza virus particles are delivered into CD81+ endosomes, we allowed Alexa Fluor 647-labeled X-31 to internalize for 15 minutes and immunostained the cells for CD81. As shown in Figure 2.4B, a substantial fraction (~54%) of virus colocalized with CD81+ endosomes.

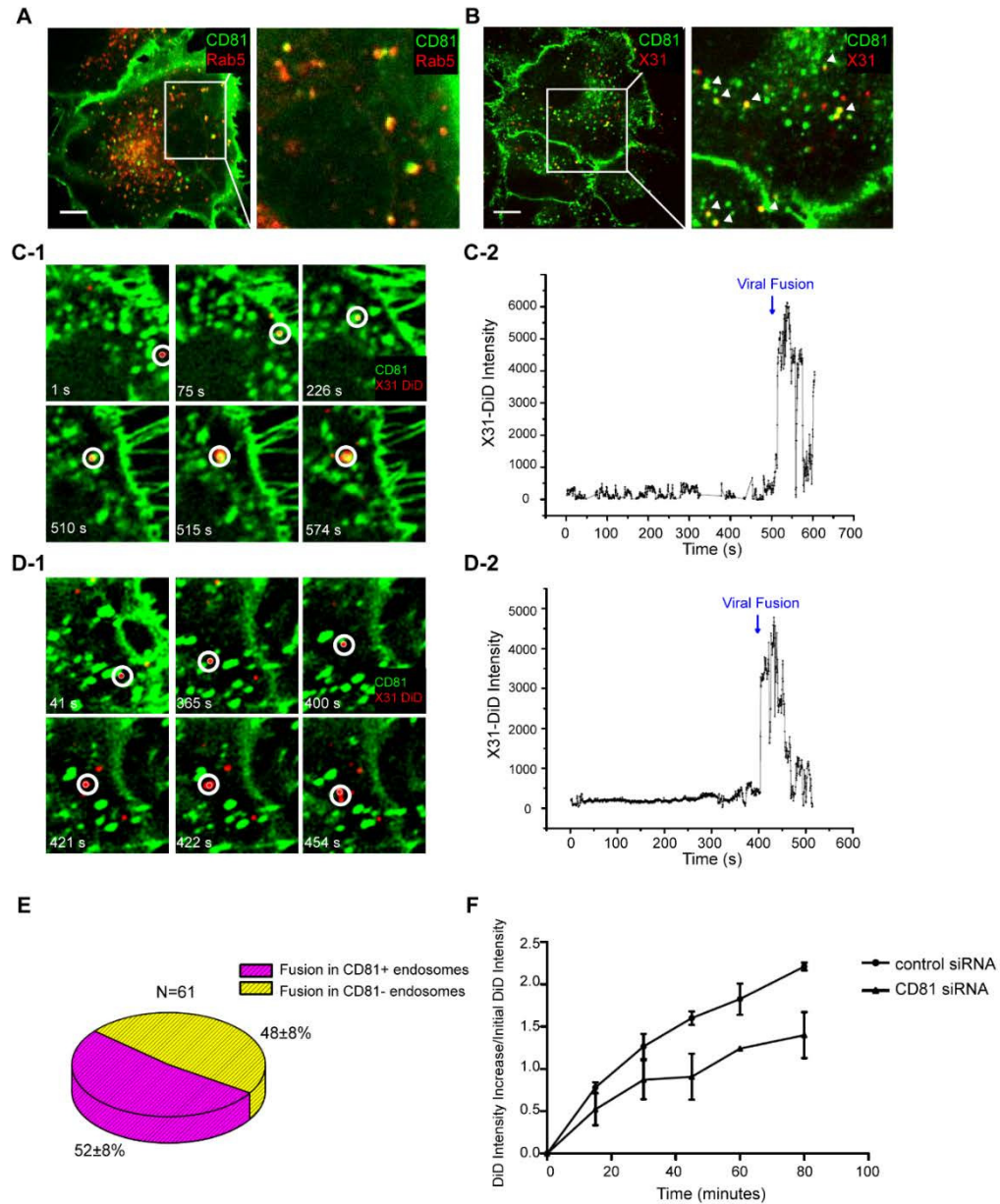


**Figure 2.4. A major fraction of viruses are trafficked to and fuse in CD81-positive endosomes. A)** CD81 substantially colocalizes with Rab5. A549 cells were electroporated with CD81-mEmerald and

**Figure 2.4. (continued)** RFP-Rab5. At 24 hours, the cells were fixed and imaged. An enlarged image of the boxed region is shown on the right. Scale bar: 10  $\mu$ m. B) Influenza virus particles traffick into CD81+ endosomes. A549 cells were cold bound with Alexa Fluor 647-labeled X-31 virus (red) on ice for 30 minutes and then chased for 15 minutes at 37 °C. The samples were fixed and immunostained against CD81 (green). An enlarged image of the boxed region is shown on the right. All of the images are confocal XY cross sections. Scale bar: 10  $\mu$ m. C) An influenza virus particle enters and fuses within a CD81-positive endosome after entry. Live-cell confocal imaging of DiD-labeled X-31 added *in situ* to CD81-mEmerald expressing A549 cells maintained at 37 °C. The images were collected with a 0.5 s interval. C-1) Several snapshots taken at different time points with the virus indicated by the white circles. C-2) The fluorescence signal of the indicated DiD-labeled virus as a function of time. Note that there is a sudden increase of DiD signal at 515 s, which indicates a viral fusion event. D) Influenza virus can also fuse in a CD81-negative endosome. D-1) Several snapshots taken at different time points with the virus indicated by the white circles. D-2) The fluorescence signal of the indicated DiD labeled virus as a function of time. The virus particle fused at 422 s. E) Among 61 virus particles tracked from binding to fusion,  $52 \pm 8\%$  enter and fuse within CD81+ endosomes whereas the remaining  $48 \pm 8\%$  fuse in CD81- endosomes. The results are taken for four independent experiments, and the  $\pm$ error indicates the standard deviation derived from these experiments. F) Virus fusion is impaired upon CD81 depletion. DiD-labeled X-31 was allowed to bind with A549 cells on ice for 30 minutes, and then chased for the indicated times at 37 °C. Cells were trypsinized and fixed immediately, and analyzed by flow cytometry. The increase in the DiD intensity versus the initial DiD intensity is plotted. The error bars are standard deviation derived from duplicate experiments.

We then tracked individual influenza virus particles in living cells, a technique that has been previously established [28, 50, 56, 61, 159], to examine whether influenza viruses fuse in CD81+ endosomes. To this end, we expressed CD81-mEmerald in A549 cells. Similar to endogenous CD81, CD81-mEmerald was localized on both plasma and endosomal membranes and the expression of CD81-mEmerald did not affect the fraction of endosomes that are CD81+ (data not shown). Moreover, the expression of CD81 also did not affect influenza viral fusion or infectivity (data not shown).

To facilitate tracking of individual virus particles, X-31 viruses were labeled with a saturating amount of DiD, a lipophilic dye, such that the fluorescence emission from the DiD molecules was low due to a self-quenching effect between neighboring dyes. Fusion between the virus envelope and endosomal membrane should lead to an increase in fluorescent intensity (dequenching), due to the diffusion of dyes from the virus into the lipid bilayer of the endosomes [159]. We added labeled viruses to the CD81-mEmerald expressing cells *in situ* at 37 °C. The virus particles typically show restricted movement immediately after binding to the cell, followed by rapid and directed movement once the virus particles are internalized, similar to our previous observations [50, 56, 159]. We observed a proportion of

virus particles entering into CD81+ endosomes soon after internalization, as illustrated by the example shown in Figure 2.4C. These viruses remained colocalized with CD81 and eventually fused with the CD81+ endosomes, as reflected by the sudden increase of DiD fluorescence, presumably after the endosomes matured to acquire a sufficiently low pH (Figure 2.4C). Among the 61 virus particles that we tracked from binding to fusion, about  $52 \pm 8\%$  underwent viral fusion within CD81+ endosomes (Figure 2.4E). The remaining  $48 \pm 8\%$  of virus particles fused in endosomes lacking CD81 (Figures 2.4D and 2.4E). To confirm that the fusion events indeed occurred in endosomes, we tracked individual DiD-labeled influenza virus particles in cells expressing RFP-Rab5. Similar to previous observations [50], nearly 90% of the viral fusion events occurred in Rab5+ endosomes (data not shown).

To investigate whether CD81 affects viral fusion, we next monitored the DiD fluorescent intensity in control and CD81-knockdown cells that were infected with DiD-labeled X-31 virus. In these experiments, cells were first incubated with DiD-labeled virus at 4 °C and then the temperature was increased to 37 °C to initiate viral entry. At specific time points after the temperature shift, infected cells were collected and the DiD fluorescence from these cells was quantified with flow cytometry. As expected, there was a consistent increase of DiD fluorescence with time due to viral fusion (Figure 2.4F). Notably, compared to control cells, CD81-knockdown cells exhibited a significant reduction in viral fusion (Figure 2.4F), suggesting that CD81 facilitates viral fusion. Most of the remaining viral fusion events in CD81-knockdown cells still occurred in Rab5+ endosomes (data not shown). The reduction in viral fusion was, however, incomplete (Figure 2.4F), consistent with the observation that only about half of the virus particles fuse in CD81+ endosomes (Figure 2.4E), though the incomplete inhibition of viral fusion could also be in part due to the incomplete knockdown of CD81 (Figure 2.1).

These data indicate that CD81 marks a specific population of Rab5+ endosomes that are responsible for half of viral fusion events. Because CD81-knockdown cells reduced viral infection (Figure 2.2C) and exhibited a higher reduction in virus titer when infected without acid bypass than when infected

with acid bypass (Figures 2.2C and 2.2F), viral fusion within CD81+ endosomes likely leads to productive influenza infection.

Taken together, our results indicate that half of virus particles are trafficked to and undergo viral fusion in CD81+ endosomes. CD81 could facilitate viral fusion by organizing endosomal membrane to assist viral fusion or helping virus traffick to fusion-competent endosomal compartments.

#### **2.2.4 CD81 is not involved in the expression or trafficking of viral proteins**

In the subsequent experiments, we aimed to determine which post-entry step(s) of the viral infection process are CD81 dependent. To this end, we examined the effect of CD81 on viral protein expression, viral protein trafficking, and the assembly and egress of progeny viruses. Our initial results in Figure 2.2E suggested that CD81 knockdown did not directly affect viral NP expression. This was further substantiated by infecting cells with various viral doses across different time points using the acid-bypass treatment. As shown in Figure 2.5A, the fraction of NP+ cells and NP expression level increased with the viral dose and infection time, while there was no significant difference between control and CD81-knockdown cells. To further validate the finding, we measured the expression of another cytosolic viral protein, M1. Similar to the results on NP, CD81-knockdown cells infected by influenza viruses using the acid-bypass treatment did not exhibit a difference in the fraction of M1+ cells or the level of M1 protein expression, when compared to the control cells (Figure 2.5B). These data suggest that CD81 does not play a role in viral gene expression for cytosolic viral proteins.

To determine whether CD81 affects viral membrane protein expression, we probed M2 expression with acid bypass treatment. The fraction of M2+ cells and the M2 expression level in M2+ cells were similar between control and CD81-knockdown cells (Figure 2.5C). Furthermore, by only probing the surface M2 protein without permeabilizing the cells, we found that there was no difference in surface M2 protein expression level either (Figure 2.5D), indicating that CD81 knockdown also did not

affect the trafficking of M2 to the cell surface. Similarly, the expression and trafficking of another viral membrane protein, NA, were also not affected upon CD81 depletion (Figure 2.5E).

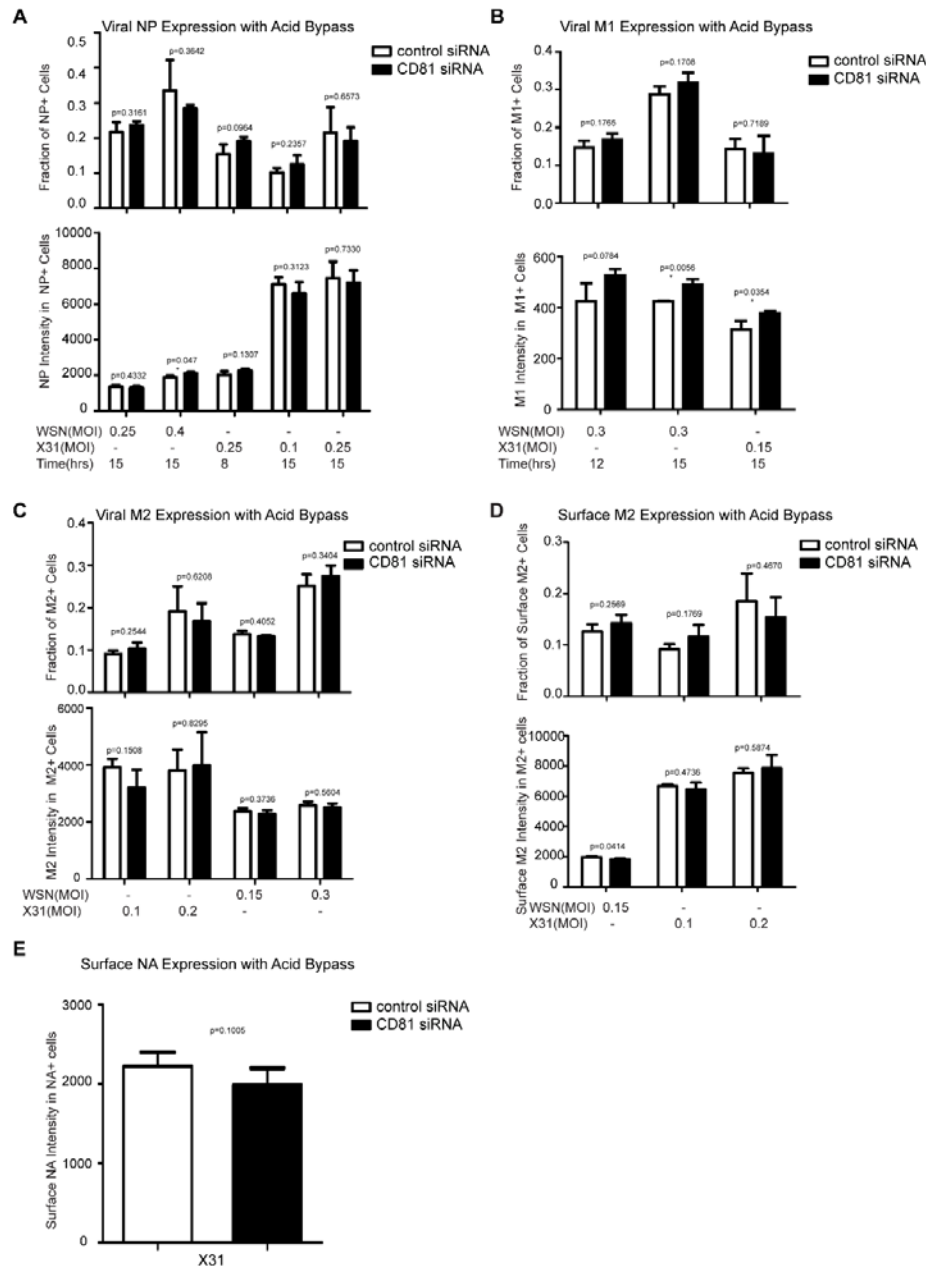


**Figure 2.5. CD81 depletion does not affect viral protein expression and transport.** A) CD81 knockdown does not affect the expression of viral NP protein in cells infected by influenza viruses with the acid-bypass treatment. Experiments were performed similarly as in 1E) except that the expression levels are evaluated at different time point post infection and with different dose of viruses. The percent of NP-expression cells and the NP expression level in NP+ cells are plotted. B) CD81 knockdown does not affect the expression of viral M1 protein in cells infected by influenza viruses with the acid-bypass treatment. Experiments were performed similarly as in (A) except cells were immunostained for M1. The

**Figure 2.5. (continued)** percent of M1+ cells and the M1 expression level in the M1+ cells are plotted. C) CD81 knockdown does not affect the expression of viral M2 protein in cells infected by influenza viruses with the acid-bypass treatment. Experiments were performed similarly as in (A) except cells were immunostained for M2. The percent of M2+ cells and the M2 expression level in the M2+ cells are plotted. D) CD81 knockdown does not affect the amount of M2 protein trafficked to the cell surface in cells infected by influenza viruses with the acid-bypass treatment. Experiments were performed similarly as in (C) except cells were stained for M2 without permeabilization. The percent of M2+ cells and the surface M2 expression level in M2+ cells are plotted. E) CD81 knockdown does not affect the amount of NA protein trafficked to the cell surface in cells infected by influenza viruses with the acid-bypass treatment. The NA expression level was estimated from confocal images in control or CD81 siRNA treated cells infected by X-31 virus. A two-tailed student *t-test* was performed for all of the numerical data, and the p value of the data is shown.

Taken together, these data indicate that CD81 does not play a direct role in the expression of influenza viral proteins or the trafficking of influenza membrane proteins to the plasma membrane.

### **2.2.5 CD81 is recruited to influenza virus budding sites on the plasma membrane**

Next, we probed the role of CD81 in virus assembly. To test whether CD81 is present at the viral assembly sites, A549 cells were infected with the three influenza strains and immunostained for CD81 and the viral protein. Notably, with X-31 infection, CD81 was mostly localized to a site concentrated with multiple viral proteins (Figures 2.6A and data not shown). In contrast to uninfected cells, which showed a uniform distribution of CD81 on the plasma membrane, X-31-infected cells exhibited marked redistribution of CD81 into concentrated patches. All of the X-31 proteins that we could obtain specific immunofluorescence staining for, including PB1, NA and M2, were present in these patches. The CD81 patches were formed on the plasma membrane, as confirmed by immunofluorescence of non-permeabilized cells (data not shown). We note that there was only a modest decrease of CD81 expression upon viral infection (data not shown). For Udorn-infected cells, CD81 was enriched along the budding virus filaments marked by PB1 (Figure 2.6B). PB1 is a good filament marker that colocalized with Udorn HA and M2 in the budding filamentous virions (data not shown). We have also directly observed colocalization between CD81 and other Udorn proteins including HA, NA and an anti-Udorn serum (data not shown). Remarkably, upon siRNA treatment, which depleted 80~85% of the endogenous CD81, the remaining CD81 was all concentrated in the budding viral filaments, whereas the cell body had little CD81 signal (Figures 2.6C). The average amount of CD81 per virus filament in the CD81-knockdown

cells was reduced by more than 60% compared to that in control cells. Although our lack of WSN antibodies made it difficult to perform similar immunofluorescence experiments on WSN-infected cells, our EM images with CD81 labeled by immunogold showed that CD81 was also recruited to the WSN virus budding zones (data shown later in Figure 2.8A). Taken together, these results indicate that CD81 is specifically recruited to the influenza virus assembly and budding sites.

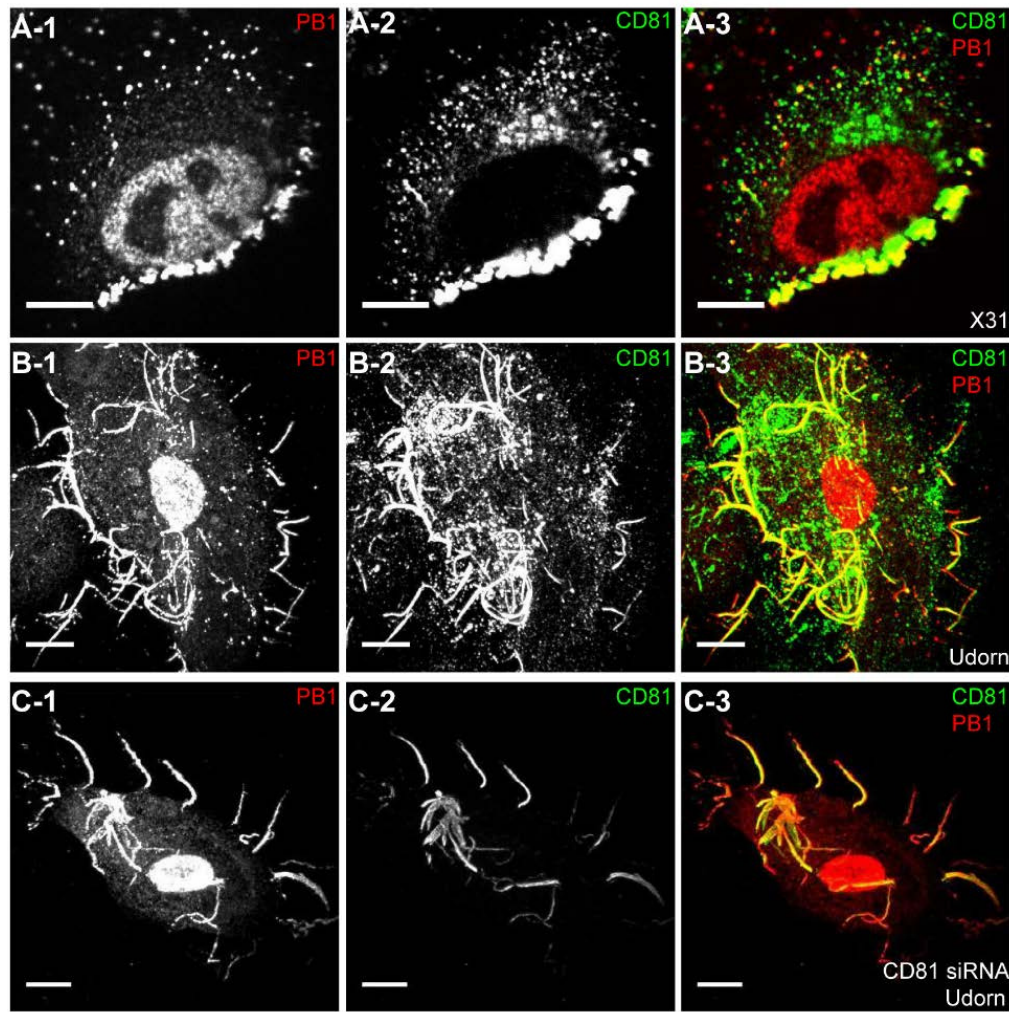


**Figure 2.6. CD81 is recruited to the virus budding sites.** A) CD81 is recruited to the virus budding zone in X-31 infected cells. A549 cells were infected with X-31 for 16 hours. Cells were stained with anti-CD81 antibody (green) and anti-PB1 antibody (red). Images are confocal XY cross-sections. Scale bar: 10  $\mu$ m. B) CD81 is incorporated into budding filamentous virions of Udorn-infected cells. A549 cells were infected with Udorn virus for 16 hours, and stained with anti-CD81 antibody and anti-PB1 antibody. Scale bar: 10  $\mu$ m. C) Remaining CD81 in CD81-knockdown cells is incorporated into budding filamentous viruses of Udorn infected cells. Similar to (B) except that CD81-knockdown cells were used. The CD81 expression level in Udorn-infected cells was calculated based on confocal images of more than

**Figure 2.6. (continued)** 100 cells, and was found to be decreased by ~88% upon CD81 depletion as compared to control cells. The amount of CD81 per viral filament was reduced by 63% compared to that in untreated cells. Scale bar: 10  $\mu$ m.

To probe which viral component may be responsible for recruiting CD81, we turned to a plasmid-based system that expresses only specific viral envelope proteins in cells [160]. We transiently transfected the plasmid containing HA or NA in A549 cells and immunostained the cells with CD81 and HA or NA. Interestingly, HA tends to form clusters on the cell surface even when expressed alone in A549 cells and CD81 accumulated substantially in the HA clusters (data not shown). About 46% of HA clusters colocalized with CD81. In contrast, NA when expressed alone did not form clusters but was distributed largely uniformly across the plasma membrane and there was no appreciable correlation between the CD81 distribution and NA distribution (data not shown). Mock transfection with plasmid that did not contain HA or NA did not yield any appreciable HA or NA staining (data not shown). These results suggest that HA is likely responsible for recruiting CD81 to the viral budding sites.

## **2.2.6 CD81 is incorporated at specific sub-viral locations and facilitates influenza virus budding**

Although we observed a ~50% or more decrease in virus titer in CD81-knockdown cells after acid-bypass treatment to overcome the CD81-dependent entry defects (Figure 2.2F), it remained unknown whether the defect in viral titer stems from a decrease in the number of budding virions assembled on the cell, the number of progeny virus particles released from the cell, or the specific infectivity per released virus particle. To distinguish between these possibilities, we first infected cells using the acid-bypass treatment and then quantified the number of budding virions attached to the cells using transmission electron microscopy. After quantifying more than 250 cell cross-sections per condition, we performed statistical analysis and found no statistically significant difference in the number of assembling virus particles per cell cross-section in the control versus CD81-knockdown cells (Figure 2.7A).

Next, we infected cells with WSN using the acid-bypass treatment, collected the virus particles in the supernatant, and then quantified the amount of viral matrix protein M1 using an ELISA assay and the number of released virus particles positive of both M1 and HA using an imaging assay (Figure 2.7B).



Notably, compared to control cells treated by non-targeting siRNA, CD81-knockdown cells exhibited 50% or more decrease in both the amount of viral M1 and the number of M1+ and HA+ virus particles released into the supernatant. These results suggest that the CD81-knockdown-induced reduction in viral titer in cells infected by the acid-bypass treatment stems from a defect in virus release. Given that the reduction in viral titer (Figure 2.2F) was similar to the reduction in the amount of released viral proteins or viral particles (Figure 2.7B), we did not further probe the change in specific infectivity per virus particle.

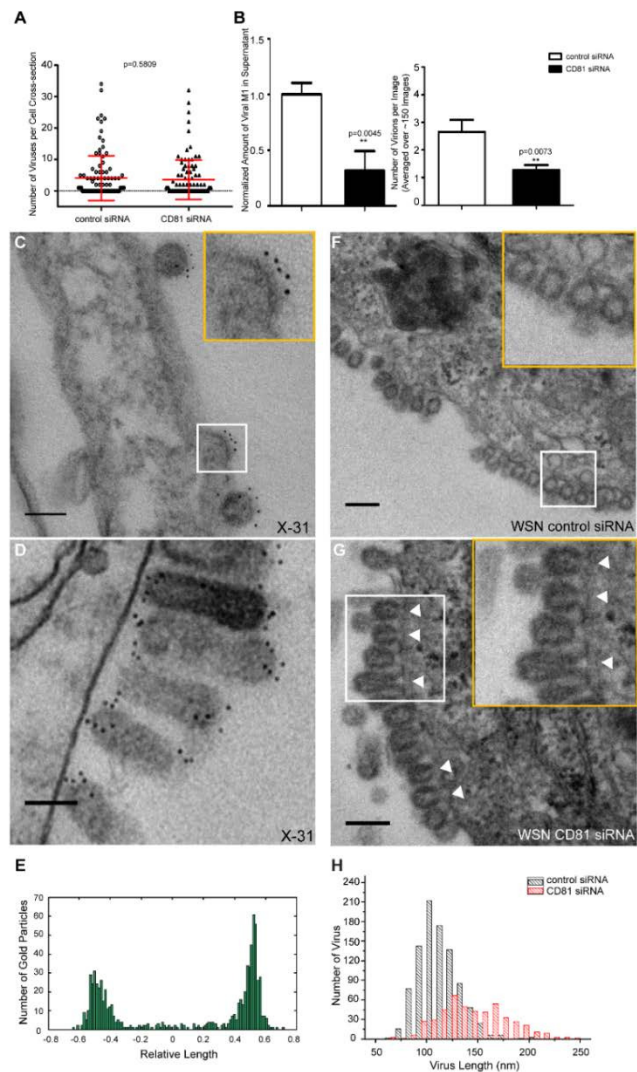


**Figure 2.7. CD81 is enriched at specific sub-viral sites of budding virions and CD81 knockdown impairs virus scission.** A) CD81 knockdown does not change the number of budding virions attached to infected cells. siRNA-treated cells were infected with WSN virus with the acid-bypass treatment for 15 hours. Cells were directly fixed for transmission electron microscopy and the number of budding virus

**Figure 2.7. (continued)** particles per cell cross-section is quantified for over 250 sections, and presented in the dot plot. A two-tailed student *t-test* was performed and the p value is provided. B) CD81 knockdown causes a substantial reduction in the number of released virus particles. siRNA-treated cells were infected with WSN virus with the acid-bypass treatment for 17 hours. The amount of viral M1 protein in the supernatant was probed with ELISA. The number of M1 positive and HA positive virus particles in the supernatant was counted using immunofluorescence imaging. The error bar is standard deviation from three independent measurements. C) CD81 localizes at the tip of growing X-31 viruses during the early budding stages. Cells were infected with X-31 for 12 hours and CD81 was immunogold labeled for electron microscopy. An enlarged image of the area in the white box is shown in the upper right corner. Scale bar: 100 nm. D) CD81 mainly localizes at the tip and budding neck of the X-31 viruses during late budding stages. Similar to (C) except the infection time was 16 hours. Scale bar: 200 nm. E) Distribution of gold particles in budding X-31 viruses at 16 hour post infection. To align the virus particles, the length of each virus is normalized to 1, with its middle point assigned with coordinate value of 0. For individual gold particles on the budding virus, their coordinate values were calculated based on their relative distance to the middle point. Coordinates with negative values correspond to positions close to the plasma membrane. A total of 105 budding viruses were analyzed. F) Budding WSN viruses exhibit a spherical morphology with fully enclosed membrane envelope in control siRNA-treated cells. A549 cells were infected with virus with the acid-bypass treatment for 13 hours. The region in the white box is magnified and shown in the upper right corner. Scale bar: 200 nm. G) Budding WSN viruses are more elongated in CD81 siRNA treated A549 cells. A substantial fraction of budding viruses have an open membrane neck connected to the plasma membrane (indicated by arrowheads). The region in the white box is magnified and shown in the upper right corner. Scale bar: 200 nm. H) Budding WSN viruses are elongated upon CD81 depletion, as shown by the distribution of budding virus length in control or CD81-knockdown cells.

To examine how CD81 may facilitate release of progeny virus particles, we next probed the distribution of CD81 within individual budding virions using immunogold electron microscopy. In X-31-infected cells, CD81 was readily observed in budding virions (Figure 2.7C and 2.7D). During early assembly stages, CD81 clusters located at the growing tip of budding virions (Figure 2.7C). Interestingly, when viruses grew into a mature, slightly elongated shape [151], CD81 was not only found on the growing tip, but also on the neck of budding virions (Figure 2.7D). The elongated morphology of X-31 allowed us to quantitatively analyze the CD81 distribution in virions by aligning the long axis of the virus particles and normalizing the position of immunogold-labeled CD81 to the total length of the virus. Remarkably, CD81 is highly enriched at the two ends of the budding virions (Figure 2.7D and 2.7E).

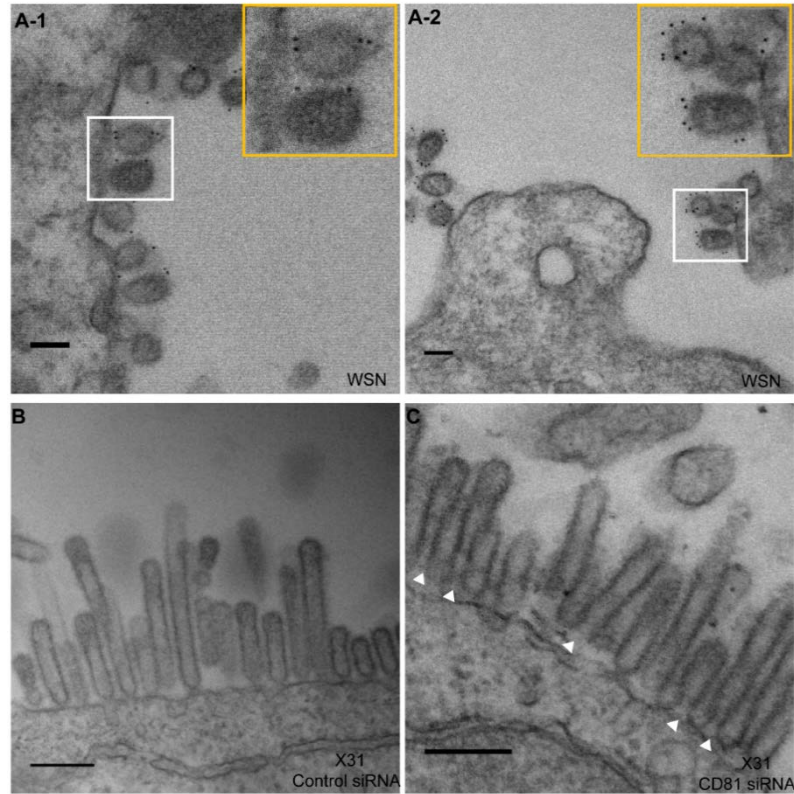


**Figure 2.8. CD81 is enriched in the budding WSN virions and CD81-knockdown impairs scission of the X-31 virus.** A) CD81 is incorporated in budding WSN viruses. Cells were infected with WSN for 15 hours, and CD81 was immunogold labeled for electron microscopy. An enlarged image of the area in the white box is shown on the upper right. Scale bar: 100 nm. B) EM image of budding X-31 virus in control cells. A549 cells were infected with X-31 virus with the acid-bypass treatment for 16 hours. Scale bar: 200 nm. C) Budding X-31 viruses in CD81-knockdown cells. A549 cells were infected with X-31 virus with the acid-bypass treatment for 16 hours. Note that a substantial fraction of budding viruses have their open membrane neck connected to the plasma membrane (arrowheads). Scale bar: 200 nm.

Similarly, we also found CD81 to be enriched in budding WSN virus particles, but the quantity of immunogold detected per WSN virus is substantially lower than that in X-31 viruses, which made it difficult to determine the CD81 distribution in these viruses (Figure 2.8A). However, the nearly perfectly spherical shape of the WSN virus allowed us to detect an interesting morphological defect of budding viruses in CD81-knockdown cells. When we examined budding virions in cells infected by WSN, we found that most budding WSN viruses were spherical and completely enclosed by viral envelope in control cells treated by non-targeting siRNA (Figure 2.7F). In stark contrast, budding WSN virus in CD81-knockdown cells appeared much more elongated (Figure 2.7G). The average length of budding virions in control and CD81-knockdown cells was ~100 nm and ~150 nm, respectively (Figure 2.7H).

Furthermore, many budding viruses in CD81-knockdown cells did not have a fully enclosed envelope but remain attached to the plasma membrane through an open membrane neck (indicated by arrowheads in Figure 2.7G). We performed similar experiments with the X-31 strain. Again, we consistently observed many budding X-31 virions with the open budding neck defect upon CD81 depletion (Figure 2.8B and 2.8C), though characterizing whether the budding virions were further elongated was difficult due to the large variation of the virion length of the pleomorphic X-31.

Taken together, the specific enrichment of CD81 at the neck of the budding virions, the defect in budding neck closure in CD81-knockdown cells, and the reduction in the number of released virus particles but not in the number of assembling virions upon CD81 knockdown suggests that CD81 plays a role in a late stage of the virus budding process, likely at the final scission step. CD81 may facilitate viral scission by directly participating in the scission process, by recruiting host or viral scission proteins, or by organizing the lipid domains and making it conducive to viral scission.

### 2.2.7 Distribution of CD81 in budding filamentous Udorn virus

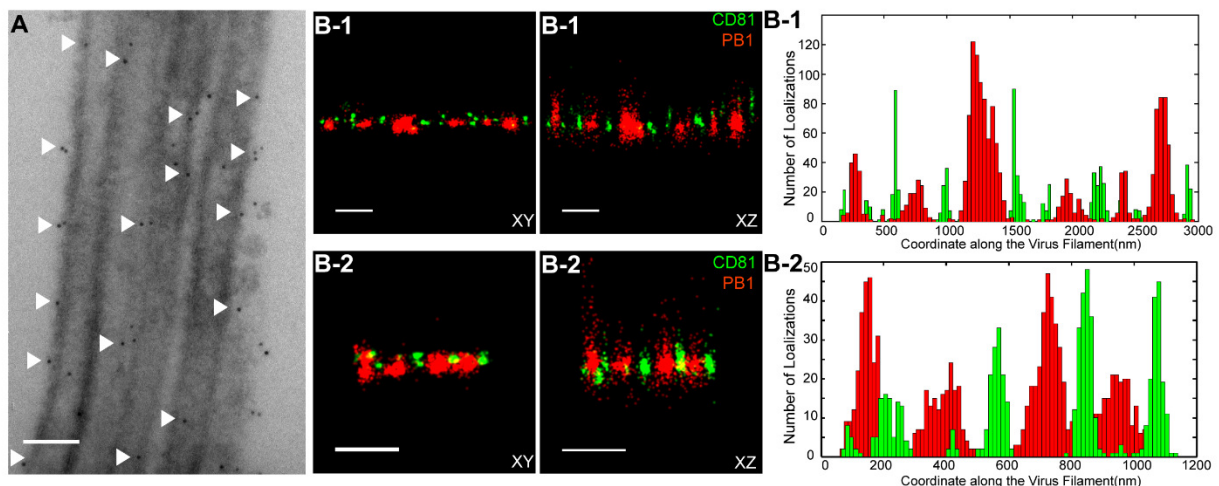


**Figure 2.9: Scattered distribution of CD81 along budding filamentous Udorn virus.** A) CD81 localizes along the filament of budding Udorn viruses. A549 cells were infected with Udorn virus for 18 hours and CD81 was immunogold labeled for electron microscopy. Shown here is a bundle of virus filament budding from the cell (the cell is not shown in order to magnify the virus filaments). Scale bar: 200 nm. B) CD81 and viral PB1 proteins appear to take an alternating distribution along filamentous Udorn virus. A549 cells were infected with Udorn virus for 16 hours and immunostained with anti-CD81 (green) and anti-PB1 (red) antibodies. CD81 was further probed with Alexa Fluor 405/Alexa Fluor 647-conjugated secondary antibody while PB1 was labeled with Atto 488 conjugated antibody for two-color 3D STORM imaging. Two example filamentous viruses were shown in B-1) and B-2). Left: xy projection

**Figure 2.9. (continued)** images. Middle) xz projection images. Right) Localization distribution of CD81 and PB1 along the filament long axis. Scale bar: 500 nm.

Unlike WSN and X-31 strain, Udorn virus infection typically produces filaments that can reach 2 to 20  $\mu\text{m}$  long [60, 153, 161, 162]. We visualized immunogold-labeled CD81 distribution in A549 cells infected by Udorn virus with electron microscopy and observed CD81 clusters in budding viral filaments. Notably, CD81 appeared to be distributed along the entire Udorn filament (Figure 2.9A).

As an alternative approach, we used a super-resolution fluorescence imaging technique, Stochastic Optical Reconstruction Microscopy (STORM), to measure the distribution of CD81 on the budding filament. STORM overcomes the diffraction limit of light microscopy by sequentially activating, imaging and localizing individual fluorescent photoswitchable molecules at high precision, thereby reconstituting images from the molecular localizations with nano-meter scale resolution [163, 164]. Here, we used a single-objective detection geometry and photoswitchable Alexa Fluor 647 and Atto 488 dyes to obtain a lateral resolution of 20-30 nm and axial resolution of 50-100 nm [110, 164]. To visualize the localization of CD81 in filamentous Udorn, we immunostained CD81 and viral PB1, and performed two-color 3D STORM imaging. Consistent with the results from electron microscopy (Figure 2.9A), we found that CD81 formed small clusters evenly distributed along the entire filament (Figure 2.9B). Adjacent CD81 clusters were usually separated by about 150~200 nm. Curiously, CD81 appeared to be enriched between clusters of viral PB1 proteins (Figure 2.9B), but the significance of this alternating pattern is unclear.

## 2.3 Discussion

CD81, a cellular tetraspannin protein, is critical for influenza viral infection [66, 67]. The infectivity of various strains of influenza viruses is strongly inhibited when cellular CD81 is depleted (Figure 2.2). In this work, we dissected the roles of CD81 on individual steps along the infection pathway from virus entry to egress. We found that CD81 plays functional roles in two separate steps of viral infection: viral fusion and virus budding.

## **The role of CD81 in viral entry**

The specific role of CD81 during influenza viral entry was determined using a series of independent assays. First, knocking down CD81 by siRNA led to ~50% decrease in the percent of infected cells expressing viral proteins. The defect was not due to direct regulation of viral protein expression by CD81, since viral protein expression remained unchanged upon CD81 knockdown when influenza infection was induced by the acid-bypass treatment (Figure 2.2 and Figure 2.5). These results suggest that CD81 mediates influenza virus entry prior to viral gene expression. Next, CD81 knockdown did not affect virus binding, internalization or trafficking to early endosomes (Figure 2.3), but led to a significant defect in viral fusion (Figure 2.4). Furthermore, single-virus tracking experiments showed that half of internalized virus particles were trafficked into CD81-positive endosomes and underwent viral fusion within these endosomes, whereas the remaining half fused in CD81-negative endosomes (Figure 2.4). Notably, the fraction of viral fusion events occurring within CD81-positive endosomes correlated well with the 50% reduction in the percent of infected cells expressing viral proteins upon depletion of CD81, suggesting a role of CD81 in productive viral uncoating. Altogether, these results indicate that CD81 plays a role in influenza viral fusion. CD81 marks an endosomal route for productive virus uncoating process, though a parallel CD81-independent route also exists.

Interestingly, the role of CD81 in influenza virus entry appears to differ from the role of CD81 previously observed in HCV and HIV entry. As an essential co-receptor for HCV, CD81 is important for the endocytosis of HCV [80, 81, 165, 166]. Furthermore, CD81 interacts with HCV glycoprotein E2 and helps prime its fusogenic activity for low-pH dependent viral fusion [79, 83]. Moreover, CD81 negatively regulates HIV-cell fusion [167]. Incorporation of CD81 and CD81-associated tetraspanins suppresses the HIV-mediated cellular fusion processes [167, 168]. On the other hand, CD81 unlikely functions as a co-receptor or attachment factor for influenza viruses because the internalization of influenza viruses into cells does not require CD81. Influenza viral fusion does not need to be primed by CD81 either, as acid treatment is sufficient to trigger viral uncoating at the plasma membrane in CD81-depleted cells. Instead,

our results suggest a role of CD81 in facilitating influenza virus fusion in endosomal compartments. Given that CD81 and CD81-associating proteins can organize membrane domains [70, 71, 73, 74], CD81 may help organize the endosomal membrane for assisting influenza viral fusion. Alternatively, CD81 may play a role in trafficking influenza to fusion competent endosomal compartments. CD81 is highly enriched in multivesicular bodies (MVBs), an intermediate endosomal organelle on the maturation pathway of late endosomes and lysosomes [169]. CD81 depletion may inhibit the maturation of endosomes and thus compromise influenza virus fusion with endosomes.

### **The role of CD81 in viral assembly**

In addition to its role in virus uncoating, CD81 also plays a functional role in a later stage of influenza infection post viral fusion. The requirement of CD81 in a post-fusion stage was evident from the finding that CD81 depletion led to a significant decrease in virus titer even when the acid-bypass treatment was used to induce viral uncoating at the plasma membrane, thereby eliminating entry defects (Figure 2.2F). The decrease did not result from a defect in expression of viral proteins or trafficking of viral proteins to the plasma membrane (Figure 2.5), suggesting that the perturbation likely occurred at the virus assembly stage. Furthermore, the average number of budding virions attached to each infected cell did not change upon CD81 knockdown, whereas the number of virus particles released into the supernatant markedly decreased (Figure 2.7A and 2.7B). These results further narrowed the involvement of CD81 to a relatively late stage of the budding process, likely the scission step that severs the virus particle from the host cells. Supporting this notion, CD81 was specifically recruited to viral budding sites (Figure 2.6), and among the viral proteins, HA is likely important for recruiting CD81 to the virus budding sites. Interestingly, CD81 was specifically enriched at the tip and budding neck of the spherical and slightly elongated viruses (Figure 2.7 C-E). Upon CD81 knockdown, the budding spherical viruses exhibited a consistent change in morphology: the budding virions appeared substantially elongated compared to their counterparts in control cells and failed to detach from the plasma membrane. Many budding viruses did not have their budding neck closed, indicating a defect in the final scission process

(Figure 2.7 F-H). Taken together, our observations indicate a role of CD81 in scission process that severs the budding virions from the plasma membrane. CD81 could be directly participating in the scission process, recruiting other host or viral scission proteins for this purpose, or organizing the membrane domain at the budding site and making it conducive for viral scission.

It is interesting to compare the role of CD81 in the assembly of influenza virus with that of other viruses. Previous studies have shown that HIV envelope proteins associate with a few tetraspanins, including CD81, and that HIV buds from the tetraspanin-enriched microdomains [85, 170, 171]. However, the exact role of CD81 in HIV egress remains unclear [168, 172-175]. One study reports that HIV infection is significantly impaired upon CD81 depletion or treatment with anti-CD81 antibodies [175], whereas two other papers report that depletion of tetraspanins does not affect the efficiency of HIV release whereas overexpression of tetraspanins results in decreased infectivity in released virions [168, 173]. Tetraspanins have also been proposed to facilitate cell-to-cell transmission of HTLV-1 infection [78]. The role of CD81 in the egress of influenza virus appears different from these previously reported roles of tetraspanins in HIV and HTLV-1 infection in that CD81 positively regulate viral scission.

It has been previously shown that influenza virus scission is dependent on viral M2 protein [176]. During virus budding, M2 is localized at the neck of budding viruses and mutation of its amphiphilic tail at the C-terminus leads to a marked defect in virus budding [176]. Interestingly, M2 is known to localize at the interface between lipid rafts and non-rafts region, while CD81 is partitioned into tetraspanin-enriched microdomains, a platform that resembles lipid rafts [70]. Thus, it is possible that CD81 facilitates the recruitment of M2 to the budding neck of the viruses. Future studies on the interaction between CD81 and M2 during the viral scission process would be of interest to further elucidate the mechanistic role of CD81. CD81 associates with tetraspanins and other tetraspanin-interacting proteins to form tetraspanin-enriched microdomains on cellular membranes [70, 71]. CD9, a tetraspanin that interacts with CD81, was previously identified in the purified virus particles [69]. Our preliminary results revealed that other tetraspanin family proteins were also incorporated into budding viruses (data not shown).



Whether and how different components within the tetraspanin-enriched microdomains cooperate with each other in facilitating influenza virus budding remains an interesting question for future investigations.

## 2.4 Materials and methods

*Cell culture, viruses and reagents.* A549 lung carcinoma cells (ATCC) were cultured in high glucose Dulbecco's modified Eagle medium (DMEM; Invitrogen) containing 10% fetal bovine serum (Serum International), and antibiotics (ATCC; 25U/ml penicillin and 25 µg/ml streptomycin), and maintained in humidified, 5% CO<sub>2</sub> environment at 37°C. For siRNA knockdown experiments, A549 cells were electroporated with 100 pmol siRNA constructs using program X-001 of Amaxa Lonza Nucleofector with Kit-T (Lonza, VVCA-1002). Experiments were performed 48 hours post electroporation. siGENOME non-targeting siRNA #1(Thermo Scientific) was used as a control siRNA. Six CD81 siRNA constructs were designed with the following sequences: CD81 siRNA 1: CACCU UCUAU GUAGG CAUCU A dTdT(Thermo Scientific); CD81 siRNA 2: AAGGA ACAUC AGGCA UGCUA A dTdT(Thermo Scientific); CD81 siRNA 3: GGAAC AUCAG GCAUG CUAATT (Qiagen); CD81 siRNA 4: CCUUC UAUGU AGGCA UCUATT(Qiagen); CD81 siRNA 5: GCCCA ACACC UUCUA UGUATT (Ambion); CD81 siRNA 6: CCACC UCAGU GCUCA AGAATT (Ambion). Note that CD81 siRNA 1 and CD81 siRNA 2 have been confirmed previously not to cause interferon-induced response [67]. For plasmid expression, 2 µg plasmids were electroporated with a similar procedure. The following plasmids were used in this study: CD81-mEmerald (human tetraspanin CD81 was cloned into the C terminal of mEmerald, with a 10 amino acid linker between mEmerald and CD81), RFP-Rab5 (gift from Professor Ari Helenius, Addgene, 14437 [177]), EYFP-Rab7 [50]), pCAGGS-HA/Ud and pCAGGS-NA/Ud (gifts from Professor Michael Farzan, Scripps Institute, FL).

The following viruses were used in this study: influenza virus X-31 was purchased from Charles River Laboratories; WSN and Udorn virus strains were gifts from Professor Robert Lamb (Northwestern University, Evanston, IL). Respiratory syncytial virus was purchased from Virapur. Pseudo-typed MLV virus was a gift from Professor Nir Hacohen (Broad Institute, Cambridge, MA).

The following primary antibodies were used in this study: mouse anti-CD81 antibody (BD Biosciences, 555675), FITC-conjugated anti-CD81 antibody (BD Bioscience, 551108), mouse anti-EEA1 (BD Biosciences, 610457), rabbit anti-EEA1 (Cell signaling, 3288s), rabbit anti-CD82 (Santa Cruz, c-16, SC-1087), mouse anti-CD63 (Abcam, ab8219), rabbit anti-EWIF (Fitzgerald, 70R-13159), mouse anti-ITGB1 (Millipore, MAB2253), mouse anti-tubulin (Sigma, T5076), mouse anti-EGFR (BD bioscience, 610016), rabbit anti-actin (Abcam, ab8227), rabbit anti-CD9 (Santa Cruz, H-110, sc-9148), goat anti-Udorn serum (gift from Professor Robert Lamb (Northwestern University, Evanston, IL)), mouse anti-M1 antibody (AbD Serotec, MCA401), goat anti-M1 antibody (Abcam, ab20910), mouse anti-influenza virus M2 antibody [14C2] (Abcam, ab5416), mouse anti-influenza virus NP antibody [AA5H] (Abcam, ab20343), mouse anti-Alexa Fluor 647 (Sigma, C1117), mouse anti-RSV fusion protein (AbD serotec, MCA490), goat anti-influenza virus PB1 antibody (Santa Cruz, vK-20), mouse anti-influenza virus HA antibody (Lifespan, LS-C58889), rabbit anti-influenza virus NA (gift from Professor Gillian Air (University of Oklahoma, Oklahoma, OK) ).

The following secondary antibodies were used for immunofluorescence with conventional light microscopy or immunogold electron microscopy: Alexa Fluor 647 donkey anti-mouse (Jackson ImmunoResearch, 715-605-150), Cy3 donkey anti-mouse (Jackson ImmunoResearch, 715-165-150), Alexa Fluor 488 donkey anti-mouse (Jackson ImmunoResearch, 715-545-150), Alexa Fluor 488 donkey anti-rabbit (Jackson ImmunoResearch, 711-545-152), Cy3 donkey anti-rabbit (Jackson ImmunoResearch, 711-165-152), Alexa Fluor 647 bovine anti-goat (Jackson ImmunoResearch, 805-605-180), Alexa Fluor 488 bovine anti-goat (Jackson ImmunoResearch, 805-545-180), 6 nm gold conjugated goat anti-mouse IgG (Jackson ImmunoResearch, 115-195-146).

The following secondary antibodies were used for immunofluorescence with STORM: donkey anti-mouse (Jackson ImmunoResearch, 715-005-150) labeled with Atto 488 or Alexa Fluor 405 and Alexa Fluor 647, Bovine anti-goat (Jackson ImmunoResearch, 805-005-180) labeled with Atto 488 or Alexa Fluor 405 and Alexa Fluor 647. To label antibodies with Alexa Fluor 405 and Alexa Fluor 647, 80

μl antibody (1.3 mg/ml) were mixed with 10 μl 1M NaHCO<sub>3</sub>, 8 μg Alexa Fluor 405 and 1.2 μg Alexa Fluor 647 dissolved in DMSO for 30 minutes. To label antibodies with Atto 488, the conditions were similar except 1.6 μg Atto 488 was used for the labeling reaction. The mixture was then filtered through a NAP-5 gel filtration column (GE Healthcare) to collect labeled antibody. Atto 488 emitted about 1100~1300 photons per switching cycle, which is significantly lower than that of Alexa Fluor 647 (4000~5000 photons per switching cycle) [110].

*Virus infection.* For virus infection, A549 cells were first inoculated with different doses of viruses diluted in DMEM (without serum) for 90 minutes at 37 °C. Cells were washed with PBS twice to remove unbound viruses, and subsequently incubated with pre-warmed full DMEM medium and maintained at 37 °C. For measuring the influenza virus titer (X-31, WSN, and Udorn) without using the acid-bypass treatment, a total of 36 hours were allowed for virus infection before collecting the supernatant for the plaque assay as described below. For RSV virus infection, A549 cells were infected with RSV for 24 hours, followed by immunostaining with anti-fusion protein (F protein) antibodies and analysis by flow cytometry. For pseudo-typed MLV virus infection, a 24-hour was allowed for infection and cells were directly fixed to assay the GFP fluorescent intensity by flow cytometry.

To ensure equal amounts of viral entry in control and CD81 siRNA treated cells for post-entry studies, an acid-bypass treatment was conducted to induce viral fusion at the plasma membrane. siRNA treated A549 cells were allowed to bind with influenza virus at 4 °C for one hour. After extensive washes with cold PBS, a pre-warmed low pH buffer (PBS, pH 4.5) was added in for two minutes. The low pH buffer was then neutralized with culture medium and cells were placed with pre-warmed fresh culture medium afterwards. For measuring the influenza virus titer (X-31 and WSN) with the acid-bypass treatment, a total of 17 hours were allowed for virus infection before collecting the supernatant for the plaque assay.

*Plaque assay.* Cells were infected with influenza virus for indicated amounts of time as described above and supernatant was collected to assay the virus titer at the end of each time point. Serial dilutions

of the supernatant were used to inoculate MDCK-Texas cells (Kind gift from Robert Lamb) seeded in 6-well plates for 90 minutes at 37°C. After washing with PBS twice, a 3 ml agar overlay of DMEM containing 30% Noble agar (Affymetrix), antibiotics and 2 µg/ml acetylated trypsin (Sigma) was placed on cells. The plates were incubated at 37 °C. After about two days, the agar disks were removed carefully and cells were immediately stained with crystal violet solution (1:1,000 V/W crystal violet, 30% ethanol in water) for 10 to 15 minutes, which allowed for an easy quantification of the number of plaques. Virus titer (PFU/mL) = number of plaques / (dilution factor × inoculation volume (mL)). For each condition, samples were tested with triplicates.

*Influenza virus labeling.* Influenza virus X-31 was either labeled with lipophilic dye DiD (Invitrogen, D7757) or Alexa Fluor 647 (Invitrogen, A-20006) as previously described [159]. For the labeling reaction, 100 µl of the original virus stock (2 mg/ml protein concentration) was incubated with either 3 µl of 25mM DiD or 3 µg Alexa Fluor 647 dissolved in DMSO for two hours or one hour respectively with gentle vortexing in the dark at room temperature. Unincorporated dye was removed by buffer exchange into the Hepes 145 buffer (50mM Hepes, pH 7.4, 145mM NaCl) by using NAP-5 gel filtration columns (GE Healthcare). The labeled virus was aliquoted, snap-frozen in liquid nitrogen, and stored at -80°C. Immediately before experiments, the labeled virus was thawed and filtered through a 0.2 µm pore size syringe filter (Supor membrane, Pall) to remove viral aggregates. Labeled viruses are infectious, as confirmed with standard plaque assays (data not shown).

*Virus binding assay.* Control or CD81-knockdown A549 cells were allowed to bind with DiD-labeled X-31 diluted in DMEM (without serum) for 30 minutes at 4°C. After extensive washes with cold PBS to remove unbound viruses, cells were trypsinized and immediately fixed with 2% paraformaldehyde (PFA) for 20 minutes at room temperature. After washing PFA away with PBS, the DiD fluorescent intensity was measured by a flow cytometer (BD bioscience). At least 10,000 cells were quantified for each measurement. The data was analyzed via FlowJo.

*Virus internalization assay.* Control or CD81-knockdown A549 cells were allowed to bind with  $3 \times 10^4$  PFU/ml Alexa Fluor 647-labeled X-31 virus diluted in DMEM (without serum) on ice for 30 minutes at 4°C. After extensive washes with cold PBS to remove unbound viruses, pre-warmed full culture medium was added in and the virus was allowed to internalize at 37 °C for indicated amounts of time. At the end of each time point, cells were washed with PBS, directly fixed with 4% PFA for 20 minutes at room temperature. In order to distinguish the surface-bound versus internalized virus particles, a non-permeablizing immunofluorescence in the absence of detergents was performed by using a mouse anti-Alexa Fluor 647 primary antibody (Sigma, C1117), followed by staining with an Alexa Fluor 555-conjugated donkey anti-mouse secondary antibody (Invitrogen, A31570). The samples were imaged using a custom-built spinning disk confocal microscope. Non-internalized virus particles were stained with both Alexa Fluor 647 and Alexa Fluor 555, while the internalized virus particles—inaccessible to the antibodies—exhibited only the Alexa Fluor 647 signal. To quantify the number of particles internalized per cell, we used the maximum z-projection of the confocal z-stacks, and counted both the total number of virus particles (with Alexa Fluor 647 signal) and the number of non-internalized virus particles (with both Alexa Fluor 647 and Alexa Fluor 555 signals), and the number of internalized particles (with Alexa Fluor 647 but not Alexa Fluor 555 signal). A low enough number of virus particles (~15 particles) was internalized each cell to minimize the possibility of multiple virus particles sorting into the same vesicle. Statistical analysis was performed using a two-tailed student t-test.

*Western Blotting.* Cell lysate samples were prepared with Laemmli sample buffer (Bio-Rad, 161-037) and run on a 4-15% Tris-HCL polyacrylamide gel (Bio-Rad). After transferring the protein onto Hybond polyvinylidene difluoride membranes (GE Healthcare), the membrane was blocked with 5% nonfat-milk in TBS-Tween for 1 hour, followed with incubation of primary antibody overnight at 4 °C, a three 10 minutes wash step with TBS-Tween, and a one hour incubation of HRP-conjugated secondary antibody at room temperature. The signal was detected with TMA-6 (TMA-100, Lumigen) and developed to Kodak films. Note that CD81 and CD63 could only be detected under non-reducing conditions.

*Flow Cytometry.* For flow cytometry analysis, the procedures were similar to what was previously described [178]. Briefly, for measuring total protein expression level (CD81 or viral proteins), cells were collected and fixed with 2% PFA for 20 minutes. After washing with PBS once, cells were permeablized with buffer P (0.075% Saponin, 10% BSA in PBS) for 20 minutes at room temperature. Cells were incubated with primary antibodies diluted in buffer P (1:1,000) for 1 hour and washed with buffer P three times before incubating with secondary antibodies for another 45 minutes. Secondary antibodies were also diluted with buffer P (1: 1,000). After washing with buffer P, cells were resuspended with PBS and then analyzed by flow cytometry. The data was analyzed by FlowJo. Cells were gated based on FSC and SSC scattering, and a histogram was generated based on the fluorescence intensity profile. For cells that were infected with influenza virus, a second gate was set based on comparison of fluorescence intensity of uninfected versus infected cells. The population that falls into the second gate corresponds to the percent of infected cells in each sample, from which the mean fluorescence intensity was analyzed to infer the viral protein expression level. To probe surface protein expression, all steps were similar except detergent was excluded.

*Immunofluorescence.* For imaging-based experiments, A549 cells seeded in Lab-Tek 8 well glass dishes were fixed with 4% PFA for 20 minutes at room temperature. Unless specified, fixed cells were permeablized with 0.1% Triton-X100 in PBS for 5 minutes, washed with PBS twice and incubated with blocking buffer PBSA (3% BSA in PBS, or 5% bovine serum in PBS) for 30 minutes. Cells were then incubated with primary antibodies diluted in PBSA (1:500) for 1 hour. Followed by three PBS washes (5 minutes each), secondary antibodies were added for another 1 hour. Afterwards, cells were washed with PBS for three times again before imaging. For STORM, a post-fixation step was followed with 3% PFA and 0.1% glutaraldehyde (GA) in PBS for 20 minutes. For immunostaining surface protein only, permeablization was not performed after fixation. When antibody species conflict existed, labeled primary antibodies (CD81-FITC, BD Bioscience; HA-Alexa Fluor 647) were used as needed.

To quantify the colocalization ratio between internalized virus and cellular proteins (EEA1 and CD81), samples were prepared similarly as in virus internalization assay. After probing the surface-bound virus particles with anti-Alexa Fluor 647 antibody, cells were permeabilized with 0.1% Triton-X100 in PBS, and a subsequent indirect immunofluorescence was performed to stain against each protein. Images were acquired by confocal microscopy and at least 40~100 randomly chosen cells were analyzed manually for each condition. Only internalized virus particles were used to quantify the fraction of viruses colocalized with CD81 or EEA1.

*ELISA.* Cells were infected with influenza virus with acid bypass for 17 hours and the supernatant was collected to assay the total amount of viral protein in the released virus particles. M1 was chosen due to its abundance in the virus to maximize signal. Nunc 96 well plates (eBioscience, 44-2404-21) were incubated with capture antibody (Goat anti-M1, Abcam, 1:1000 diluted in 0.2 M sodium carbonate/bicarbonate buffer, pH 9.4) at room temperature for 2 hours. After three 5 minutes wash with PBST (0.05% Tween in PBS), the plates were blocked with PBSA (2% BSA in PBST) for 1 hour. The supernatant was mixed with RIPA buffer (1:2 dilution), and added in each well for overnight incubation at 4 °C. The samples were washed three times with PBST, and incubated with detection antibody (Mouse anti-M1, AbD Serotec, 1:600 dilution in PBSA) for 1 hour at room temperature, washed three times, and further incubated with HRP-conjugated goat anti-Mouse antibody (Bio-Rad, 172-1011, 1:5,000) for 1 hour. TMB substrate (Thermo Scientific, N301) was used to detect HRP activity, and the reaction was stopped by 0.18 M sulfuric acid before measuring the absorbance at 450 nm. The experiment was performed with triplicate samples from independent infections, with three measurements for each sample. To confirm the efficiency of detection, purified X-31 virus (Charles River laboratory) was used as a standard sample (data not shown).

*Quantification of the Number of Released Virions.* Control and CD81 siRNA treated cells were infected with influenza virus by acid bypass treatment. At 17 hours post infection, supernatant was collected to assay for the number of released virions through immunofluorescence. Briefly, the

supernatant was absorbed on poly-lysine coated Lab-Tek 8 well glass dishes at 4 °C overnight. After washing away unbound virions with PBS twice, the sample was fixed with 4% PFA for 15 minutes, blocked with 3% PBSA buffer, immunostained with anti-HA and anti-M1 antibody, and then imaged by confocal microscopy. More than 150 randomly selected regions were imaged, and the number of particles positive for HA and M1 staining was quantified (with more than 600 virus particles).

*Single particle tracking.* The single-particle tracking experiment has been described in detail previously [50, 56, 61, 159]. Briefly, A549 cells were nucleofected with CD81-mEmerald or RFP-Rab5 plasmids 24 hours prior to single virus tracking experiments. After washing the cells with pre-warmed PBS twice,  $2.6 \times 10^4$  PFU/ml DiD-labeled X-31 virus diluted in imaging buffer (9 parts DMEM without phenol red, 1 part pH8 Hepes buffer, supplemented with oxygen scavenge system: 0.8 mg/ml dihydroxybenzoic acid (PCA, Sigma, 37580), 0.5U/ml protocatechuate 3,4- dioxygenase (PCD, Sigma, P8279) ) was added to the cells. The objective and stage of the microscope were heated to maintain the temperature at 37 °C for the cells. Image acquisition began immediately after adding DiD-labeled virus *in situ*. To obtain a simultaneous imaging of DiD-labeled virus and cellular protein, DiD was excited with a 647 nm krypton laser (Coherent) while mEmerald and RFP was excited with a 488 nm argon ion laser (Coherent) and a 561 nm solid state laser (CrystaLaser) respectively. Fluorescence emissions from DiD and mEmerald/RFP were separated by a 630 nm long-pass dichroic, filtered with bandpass filters (705/40 for 647 channel, 525/40 for 488 channel, and 605/70 for 561 channel) and imaged on a EMCCD camera (Andor) with 0.5 second exposure time. The imaging analysis was performed as described previously [56]. Briefly, for each image, the fluorescence signal collected from the DiD channel was convolved with a Gaussian spatial filter to remove background and noise. To identify the virus peaks, the algorithm performs recursive integration over bright regions connected to each local maximum. The centroid of each fluorescent peak was computed to determine the virus particle position, and the trajectories were obtained by reconstructing paired peaks between adjacent frames with similar proximity and intensity. The fluorescence intensity of DiD was plotted versus time.



*Bulk viral fusion assay.* Control or CD81-knockdown A549 cells seeded in Lab-Tek 8 well glass dishes were rinsed with cold PBS first, and then incubated with  $2 \times 10^4$  PFU/ml DiD-labeled X-31 diluted in DMEM (without serum) for 45 minutes at 4°C. After washing away unbound viruses with cold PBS twice, pre-warmed full culture medium was added in and cells were maintained at 37°C for indicated amounts of time. At the end of each time point, cells were trypsinized and immediately fixed with 2% PFA for 20 minutes. Afterwards, cells were washed and resuspended with PBS. DiD-fluorescent intensity was measured through a flow cytometer. At least 10,000 cells were measured for each measurement with duplicates for each condition. The data was analyzed with FlowJo. The normalized viral fusion extent (mean DiD intensity at each time point-initial mean DiD intensity)/Initial mean DiD intensity) was plotted.

*STORM.* STORM experiments were performed as previously described on an Olympus IX71 inverted optical microscope [113]. Three lasers were used in this study for STORM: 657 nm (RCL-300-656; Crystalaser), 488 nm (Sapphire 460-10; Coherent) and 405 nm (CUBE 405-50C; Coherent). A high-numerical-aperture (NA) oil-immersion objective (100X UPlanSapo, NA1.4; Olympus) was used to collect the fluorescence emission, which is imaged onto a back-illuminated electron-multiplying charge-coupled device (EMCCD) camera (iXON DU-897; Andor). For two-color 3D imaging of Alexa Fluor 647 and Atto 488, two imaging laser beams (488 nm and 657 nm) and an activation laser beam (405 nm) were reflected by a custom-designed polychroic mirror (z488/647/780rpc; Chroma). Fluorescence emission from Alexa Fluor 647 and Atto 488 were separated by a 630 nm long-pass dichroic mounted on a commercial beamsplitting device (3D Dual-View with a cylindrical lens, 100 cm focal length; Photometrics). Two bandpass filters: FF01-535/50 (Semrock) and ET705/72m (Chroma) were used to filter for the short-wavelength and long-wavelength channel independently. In addition to the bandpass filters, a double-notch filter (NF01-488/647; Semrock) was added before the Dual-View (Photometrics) to block the two excitation laser beams. STORM imaging for each channel was performed at 60 Hz sequentially and each channel was imaged onto  $256 \times 256$  pixels in the EMCCD camera (iXON DU-897).

STORM images were generated using similar methods as previously described [113]. The STORM images in the Alexa Fluor 647 and Atto 488 channels were aligned by a third-order polynomial warping map in three dimensions obtained from calibration images of 100-nm Tetraspeck fluorescent beads. The residual alignment error was ~7 nm in x-y and ~20 nm in z dimensions. To correct for the sample drift during imaging acquisition, we relied on the correlation function of imaging itself to correct for the lateral and axial drift, as previously described [164]. Since the imaging acquisition was performed sequentially with the longer wavelength channel first, 647 channel was drift-corrected to the last frame of the 647 nm acquisition while 488 channel was drift-corrected to the first frame of the 488 nm acquisition. The spatial resolution measured was 20~30 nm laterally and 50~60 nm axially for Alexa Fluor 647; while Atto 488 gives a lateral resolution of 30~40 nm and axial resolution of ~100nm.

*Electron microscopy.* A549 cells were infected with influenza viruses at a MOI of 2. Infection was allowed to proceed for a total of 15 hours before fixing with 2.5% PFA/GA in 0.1M sodium cacodylate buffer, pH 7.4 (Electron Microscopy Sciences, 15949) at room temperature for at least 1 hour. The cells were post-fixed for 30 minutes in 1% Osmium tetroxide (OsO<sub>4</sub>)/1.5% potassium ferrocyanide (K<sub>4</sub>Fe(CN)<sub>6</sub>), washed in water three times and incubated in 1% aqueous uranyl acetate for 30 minutes followed by two washes in water and subsequent dehydration in grades of alcohol (5 minutes each; 50%, 70%, 95%, 2x 100%). Cells were removed from the dish in propyleneoxide, pelleted at 3000 rpm for 3 minutes and infiltrated for 2 hours in a 1:1 mixture of propyleneoxide and TAAB Epon (Marivac Canada Inc. St. Laurent, Canada). The samples subsequently embedded in TAAB Epon and polymerized at 60 °C for 48 hours. Ultrathin sections (about 60 nm) were cut on a Reichert Ultracut-S microtome, transferred onto copper grids stained with lead citrate and examined in a TecnaiG<sup>2</sup> Spirit BioTWIN and images were recorded with an AMT 2k CCD camera.

For immunogold electron microscopy, at the end of indicated time points of virus infection, cells were rinsed with PBS once, fixed with 4% PFA for 15 minutes, and blocked with PBSA (3% BSA in PBS) for 30 minutes. Primary antibodies diluted in PBSA (1:500) were incubated with cells for overnight at 4

°C. After three washes with PBS, cells were treated with 6 nm gold-conjugated secondary antibodies (1:40) for four hours, post-fixed with 2.5% PFA/GA in 0.1 M sodium cacodylate buffer for at least one hour. The sample were embedded and sectioned as described above for transmission electron microscope imaging.

## **Chapter 3: Dissecting the Role of COPI Complexes in Influenza Virus Infection**

Work in this chapter was performed in collaboration with Dr. Eileen Sun.  
Most of the results from this work are published in [178].

### 3.1 Introduction

Influenza virus is a negative-sense stranded RNA, enveloped virus that contains eight segmented genomes, which encode 13 viral proteins. The influenza virion envelope is derived from the infected cell's plasma membrane and contains three integral viral membrane proteins: M2 proton channel, hemagglutinin (HA), and neuraminidase (NA). Encapsulated within the viral envelope is a coat of matrix protein 1 (M1), which also forms contacts with each of the viral ribonucleoprotein complexes (vRNP). Each of the vRNPs consists of a strand of vRNA, which is bound to viral nucleoprotein (NP). In addition, each vRNP is bound to a RNA-dependent RNA polymerase complex containing three proteins: PA, PB1, and PB2 [15].

Influenza A virus is the causative agent of seasonal flu, and historically has led to pandemic infections, such as the 1918 Spanish influenza outbreak that killed an estimated 50 million people worldwide [15]. At a cellular level, influenza virus infection starts with virion attachment to cell surface sialylated glycoproteins or glycolipids [53]. The virus particle then triggers endocytosis through clathrin-dependent and clathrin-independent pathways [44, 54-56]. Productive entry requires the virus to traffick to low pH endosomes (pH ~ 5.0), at which point HA mediates fusion between the viral envelope and the lipid bilayer of the endosome [15, 54, 159, 179, 180]. Upon pH-mediated fusion, the vRNPs release into the cytoplasm and subsequently transport into the nucleus to initiate viral replication and viral protein translation [181]. Infected cells produce progeny virions by assembling viral proteins and vRNP complexes at the plasma membrane. Viral NA cleaves cell surface sialic acids, to allow assembled virions to bud and release from the infected cell's membrane, and thereby initiate another infection cycle in neighboring uninfected cells [15].

As obligate pathogens encoding only 13 viral proteins, influenza hijacks host proteins and cellular compartments/organelles in order to harbor infection and produce progeny virus. Recently, four genome-wide knockdown screens, one in drosophila cells and three in human cells [63, 64, 66, 67], identified host proteins important for influenza virus infection. One group of host dependency proteins identified in all

influenza screens included subunits of the COPI complex [63, 64, 66, 67]. There are nine different COPI-complex subunits— $\alpha$ ,  $\beta 1$ ,  $\beta 2$ ,  $\delta$ ,  $\epsilon$ ,  $\gamma 1$ ,  $\gamma 2$ ,  $\zeta 1$ , and  $\zeta 2$ . Each COPI complex contains a single copy of  $\alpha$ ,  $\beta 1$ ,  $\beta 2$ ,  $\delta$ , and  $\epsilon$  subunits, in addition to one of the following isoform combinations:  $\gamma 1/\zeta 1$ ,  $\gamma 1/\zeta 2$ , or  $\gamma 2/\zeta 1$  [86-88]. Together, COPI complexes form a vesicle coat that traffick contents between golgi stacks, as well as cargoes between the golgi apparatus and the endoplasmic reticulum (ER) [86, 88, 182]. In addition, several studies have reported a role for COPI complexes in the endocytic pathway, since perturbation of these complexes lead to defects in endosomal sorting, multivesicular body (MVB) formation, and/or membrane trafficking [90-95].

Previous studies indicate that COPI may play a role in influenza virus entry. König and colleagues have reported that  $\delta$ -COPI (ARCN1)-knockdown inhibits vRNP nuclear import [67]. Given the roles of COPI proteins in the endocytic pathway, König and colleagues hypothesized that the block in vRNP nuclear import may be due to defects in endosomal trafficking. However, viral entry is a multi-step process and it remains unclear which step or whether any of those steps is ARCN1-dependent.

Recently, Cureton and colleagues reported that disruption of COPI complexes differentially affects Vesicular Stomatitis Virus (VSV) entry versus viral gene expression [45]. The authors used a temperature sensitive CHO cell line (IdIF), which degrades  $\epsilon$ -COPI at 40°C [95], to show that  $\epsilon$ -COPI depletion inhibits virus binding and internalization, as well as transferrin (Tfn) uptake. However, these results were only recapitulated after prolonged treatment with Brefeldin A (BrefA), an inhibitor that prevents GDP to GTP exchange of ARF1, an essential step for membrane recruitment of COPI to the golgi apparatus [89]. Acute (short-term) treatment of BrefA did not lead to the same effect in viral entry as observed with the IdIF cells incubated at 40 °C, but did cause a specific decrease in VSV gene expression.

The results from Cureton and colleagues suggest that indirect effects caused by long term inactivation of COPI lead to general defects in the clathrin-mediated endocytosis pathway [45]. VSV exclusively uses clathrin-mediated endocytosis for infection [29, 183-186]. Influenza virus, on the other

hand, can productively infect cells in the absence of clathrin-mediated endocytosis. Indeed, several reports have shown that depleting key components of the clathrin complex fails to block influenza virus entry and infection because alternative productive endocytic pathways such as macropinocytosis can be hijacked by influenza [44, 55, 56, 61]. Moreover, influenza requires lower pH compartments for viral fusion than VSV [54, 184, 187]. Therefore, how COPI proteins are involved in each of the steps of influenza virus entry and infection remains unclear.

Here, we dissect the different steps of the influenza virus infection cycle—entry, replication, trafficking, and assembly—in order to identify the steps COPI proteins affect. We found that the first major entry block in COPI knockdown cells occurs at virus internalization. In addition, COPI-depleted cells also exhibited defects in early endosome to intermediate/late endosome trafficking for virus particles that did manage to internalize these cells. The entry block was not limited to influenza virus, but also for other cargoes (Tfn, EGF, and dextran) that internalize through either clathrin-mediated endocytosis or macropinocytosis. Given the large defect in viral entry upon siRNA silencing of COPI, we used pharmacological inhibitors — BrefA and Golgicide A (GCA) — to acutely disrupt the COPI complexes. With the inhibitor treatment, we found that COPI complexes were not directly required for influenza viral entry. However, disruption of functional COPI complexes directly inhibited viral membrane protein expression, assembly of viral components at the plasma membrane, and production of infectious progeny virus.

## **3.2 Results**

### **3.2.1 COPI depletion inhibits influenza infection via an entry step at or prior to viral fusion**

To confirm previously published results showing that COPI proteins are required for influenza virus infection, we used siRNA to deplete one of the essential subunits of the COPI complex,  $\delta$ -COPI (ARCN1). We were able to achieve efficient ARCN1 depletion after 48 hours, as shown with western blotting (Figure 3.1A). To test the effect of siRNA treatment on influenza infection, supernatant from influenza A/Aichi/1968 (H3N2) (X31) or influenza A/WSN/1933 (H1N1) (WSN)- infected A549 cells

was collected and the viral titer was measured with plaque assays. Relative to the non-targeting siRNA control, the viral titers of supernatant from ARCN1 knockdown cells was decreased by 78%  $\pm$  3% for X31 and 90%  $\pm$  1% for WSN infection (Figure 3.1B). Furthermore, ARCN1 knockdown cells exhibited a defect in virus infection prior to viral progeny production. After 8.5 hpi with X31 or WSN, we quantified the fraction of NP-positive (NP+) cells with flow cytometry. Relative to the control cells, the ARCN1 knockdown cells had 93%  $\pm$  0.01% and 82%  $\pm$  2% fewer NP+ expressing cells for X31 and WSN infection, respectively (Figure 3.1C). Amongst the cells that expressed NP, the NP expression level was similar between control and ARCN1 knockdown cells (data not shown).

In addition, we checked for potential siRNA-mediated off-target effects: cytotoxicity and interferon induction. Compared to the control cells, the ARCN1 knockdown cells— after 24 and 48 hours siRNA treatment— exhibited ~25% decrease in cell viability (Figure 3.1D), a minor increase in cytotoxicity (Figure 3.1E), and a correspondingly slight decrease in cell growth (Figure 3.1F). Furthermore, siRNA treatment did not stimulate interferon induction [188] (Figure 3.1G). Given that the COPI complex is required for influenza virus infection and that the cells were largely healthy, we conducted experiments to dissect which steps of the influenza infection cycle COPI proteins mediate.



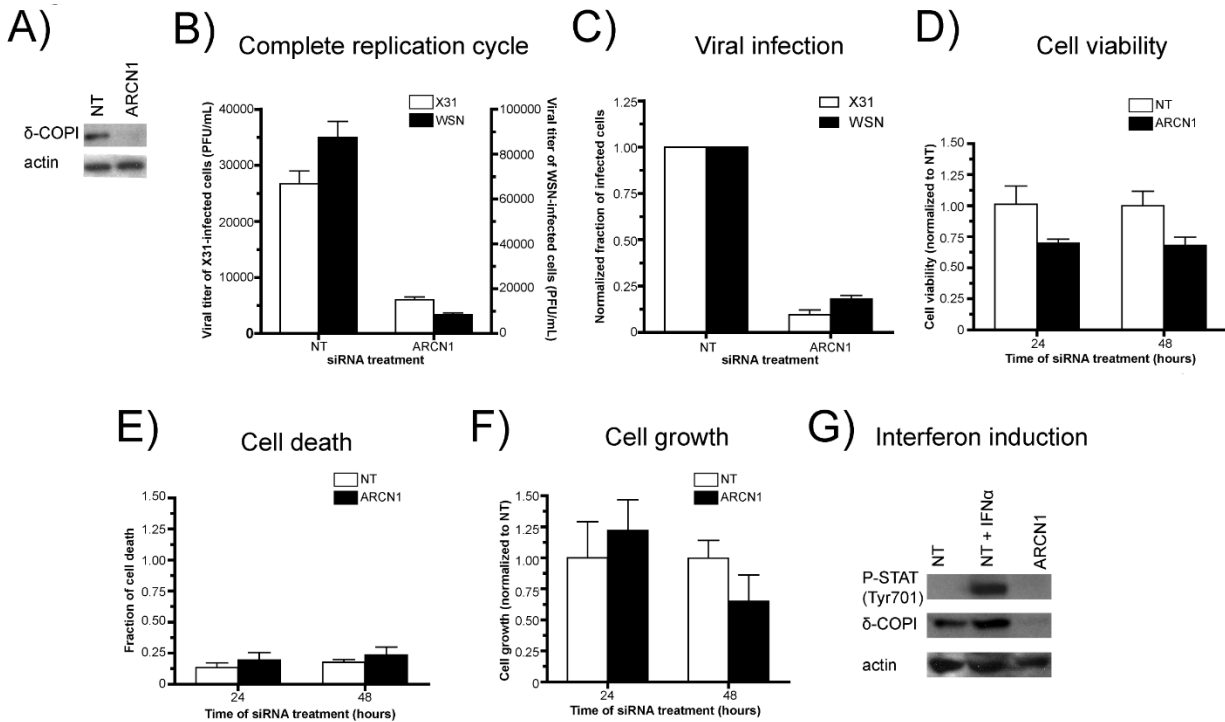


**Figure 3.1. COPI depletion blocks viral infection and cells are sufficiently healthy for subsequent experiments.** A) A western blot probing  $\delta$ -COP1 expression in non-targeting (NT) or ARCNI siRNA treated cells after 48 hours knockdown. B) Plaque assay results measuring the viral titer of released virions from X31 or WSN infected siRNA treated cells after 24 hours post infection (hpi). The mean viral titers and standard deviations from duplicate experiments. C) Normalized fraction of NP-expressing cells in X31 or WSN infected siRNA treated cells after 8.5 hpi. D) Calcein AM and ethidium homodimer staining was used to measure cell viability and cytotoxicity, respectively, in siRNA treated cells at 24 and 48 hours after siRNA electroporation. Calcein AM is a standard indicator for cell viability: living cells contain esterases that can cleave the non-fluorescent, cell-permeable calcein-AM dye, resulting in a bright green fluorescence signal. Means represent the average of six different samples with the corresponding standard deviation. Results are normalized to the non-targeting control for each treatment condition. E) The cell-impermeable dye, ethidium homodimer, binds to nucleic acids and emits a red fluorescence in dead cells or cells with compromised membrane integrity. The fraction of cell death was measured by taking the ratio of ethidium homodimer readings from siRNA treated cells before and after saponin treatment. Means represent the average of six different samples with the corresponding standard deviation. F) Relative cell growth was measured by obtaining the ratio of ethidium homodimer fluorescence in permeabilized non-targeting siRNA treated and ARCNI knockdown cells. Live siRNA treated cells were permeabilized with saponin, stained with ethidium homodimer, and analyzed with a Typhoon fluorescence scanner. The signal measured correlates with the total number of cells within each well. The measured fluorescence signal in the ARCNI knockdown cells was normalized to the average fluorescence signal from the non-targeting control cells at 24 or 48 post siRNA treatment. G) The presence of intracellular dsRNA can induce an interferon anti-viral response, propagated by downstream signaling events such as STAT phosphorylation. Western blots were used to detect P-STAT (Tyr 701),  $\delta$ -COP1, and actin expression for cell lysates collected from non-targeting, non-targeting + 10,000 U/mL interferon alpha (IFN $\alpha$ ) for 4 hrs (to directly stimulate interferon induction), and ARCNI-depleted cells after 48 hours siRNA treatment.

We first probed the effect of COPI depletion on viral fusion using a fluorescence dequenching assay. To detect viral fusion, we incorporated a saturating amount of a lipophilic dye, DiDC18(5) (DiD), into enveloped viruses such that the detected fluorescent signal from the virus particles becomes partially quenched due to intermolecular dye interaction. For DiD-labeled viruses, pH-mediated fusion results in dramatic increase in fluorescent signal (de-quenching) stemming from the diffusion of DiD molecules from the viral envelope into the endosomal membrane [159, 189]. To measure the amount of viral fusion on a population level, we incubated siRNA treated cells with DiD-labeled X31 on ice, allowed the virus to infect the cells at 37°C for different amounts of time, and quantified the DiD fluorescent intensity using a flow cytometer. As shown in Figure 3.2A, we observed an enhancement in fluorescent intensity with increasing incubation time at 37°C for the non-targeting siRNA control cells. By 60 minutes post infection (mpi), the control cells exhibited a 5.70 +/- 0.02 fold increase in DiD signal. In stark contrast, the signal enhancement in ARCN1 knockdown cells was only 24% +/- 0.03%. In addition, we tested COPE, COPG1, and COPZ1 knockdown cells with the bulk DiD fusion assay to determine whether depletion of other COPI subunits also resulted in similar viral fusion defects. Indeed, knockdown of these COPI subunits also exhibited significant defects in viral fusion, albeit the effect due to COPE depletion appeared to be weaker (data not shown). Collectively, these results show that COPI subunit knockdown blocks a virus entry step(s) at or before viral fusion.

We next tested the amount of Alexa Fluor 647-conjugated X31 (AF647-X31) virus bound to control and ARCN1 knockdown cells using flow cytometry. The largest difference in binding was observed with the lowest virus dose tested, in which ARCN1 knockdown cells bound to 20% +/- 3% less virus than the non-targeting control (Figure 3.2B). We also quantified the level of  $\alpha(2,6)$ -linked sialic acids presented on the surface of the siRNA treated cells by measuring the amount of FITC-conjugated elderberry lectin (SNA-FITC) bound to non-permeabilized fixed cells. We found that the ARCN1 knockdown cells bound 17% +/- 1% less elderberry lectin than the control cells (Figure 3.2C). We validated the elderberry lectin binding assay with A549 cells treated with different sialidase A units

followed by SNA-FITC staining: exposure to higher units of sialidase A resulted in a dose dependent decrease in SNA-FITC binding (Figure 3.2D). Because X31 and SNA can still bind to ARCN1-depleted cells, siRNA-mediated COPI complex disruption unlikely leads to a general defect in sialylation or presentation of glycoproteins or glycolipids at the cell surface. Therefore, siRNA depletion of COPI inhibits viral infection and replication through an entry block post virus binding, but prior to or at viral fusion.

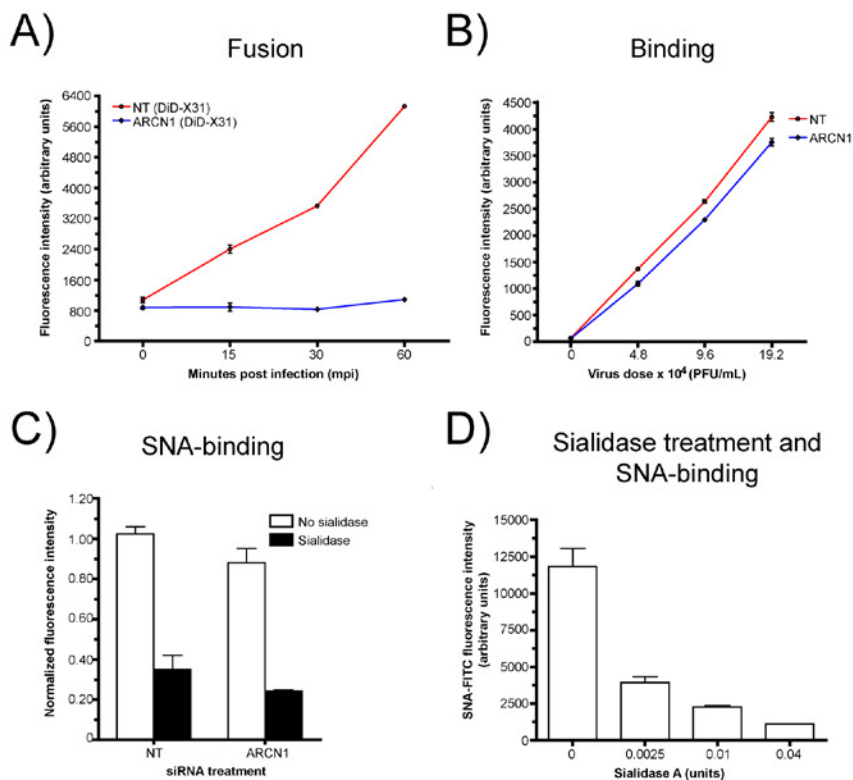


**Figure 3.2. ARCN1 knockdown cells exhibit a defect in viral entry at or prior to fusion, but not at binding.** A) Quantification of DiD fluorescence dequenching using flow cytometry. Non-targeting and ARCN1 knockdown cells were cold bound with DiD-labeled X31 (DiD X31), and allowed to internalize for different amounts of time at 37°C. The fold fluorescent signal increase from the DiD was monitored at each time point to measure the amount of viral fusion. B) Quantification of AF647-X31 binding in siRNA treated cells using flow cytometry. C) Binding of FITC-conjugated elderberry lectin (SNA-FITC)—a protein that binds to  $\alpha(2,6)$ -linked sialic acids on glycoproteins or glycolipids—to non-targeting and ARCN1 siRNA treated cells with and without treatment with 0.01 U sialidase A. The data for each independent experiment was normalized to the non-sialidase treated, non-targeting control. Each condition was tested in duplicate in two independent experiments. D) Flow cytometry-based quantification of A549 cells treated with different sialidase A units prior to SNA-FITC staining.

### **3.2.2 siRNA knockdown of COPI abrogates the internalization of influenza, as well as other clathrin-mediated endocytosis or macropinocytosis cargos**

The small defects in virus binding could not explain the dramatic decrease in viral fusion in the COPI-depleted cells. Therefore, we subsequently tested the effect of COPI depletion on influenza virus internalization by quantifying the fraction of internalized AF647-X31 in the siRNA treated cells after 30 minutes post infection (mpi). The cells were fixed, and labeled with SNA-FITC to delineate the plasma membrane. In addition, to confidently assign the virus particles close to the plasma membrane as being internalized or non-internalized, we performed non-permeabilizing immunofluorescence to stain for surface bound, non-internalized virus with an antibody specific for AF647 (Figure 3.3A). The ARCN1 knockdown cells exhibited a significant ( $p < 0.0001$ ) defect in virus uptake when compared to the control cells. Specifically, the mean internalization fraction in non-targeting siRNA control cells and ARCN1 knockdown cells was 0.58 and 0.19, respectively (Fig 3.3B). In addition, we report a ratio, representing the sum of internalized particles divided by the total number of virus particles amongst all cells. The ratio for the non-targeting and ARCN1 knockdown cells was 0.58 and 0.22, respectively (Figure 3.3B, top left corner).

Given the substantial defect in influenza virus internalization in the ARCN1 knockdown cells, we tested whether other cargoes of endocytic pathways previously described as productive influenza entry pathways— clathrin-mediated endocytosis and macropinocytosis — were also inhibited. Tfn, EGF, and dextran were used as representative markers of clathrin-mediated endocytosis and macropinocytosis, respectively. The cargoes were allowed to internalize for different amounts of time at 37°C, and surface bound cargoes were stripped off the cell using a low pH buffer (pH 2.5) prior to fixation and imaging. We applied the assay to the siRNA treated cells, and found that uptake of not only dextran, but also Tfn and EGF were significantly impaired (Figure 3.3C-E). The largest defects observed in internalization were the earlier time points tested: 15 minutes for dextran, and 10 minutes for Tfn and EGF. EGF uptake was

relatively less perturbed than Tfn uptake because it has been previously shown that EGF may internalize through a clathrin-independent pathway at high concentrations [190-192].

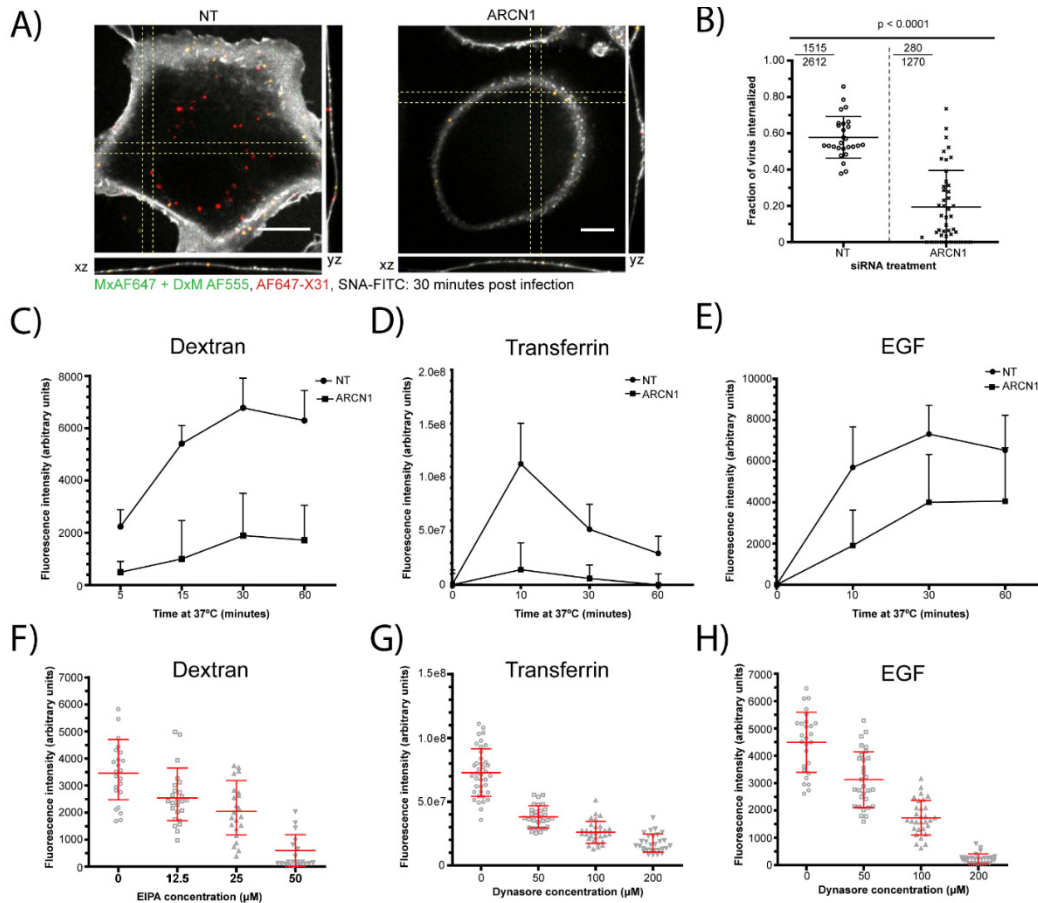


**Figure 3.3. ARC1 knockdown cells exhibit defective internalization of influenza and other cargoes.**

A) Representative confocal xy, yz, and xz cross section images of AF647-X31 (red) infected siRNA treated cells after 30 minutes post infection (mpi). The plasma membrane was labeled using SNA-FITC (white). Non-permeabilizing immunofluorescence with an antibody specific for AF647 (green) was also performed to differentiate plasma membrane-proximal particles as being non-internalized (yellow) or internalized (red) (10  $\mu$ m scale bars). B) The fraction of virus internalized out of the total number of virus particles per cell was counted. The internalized virus fraction was counted for more than 30 cells per siRNA treatment condition, and graphed in a form of a dot plot. Statistical analysis was performed using a one-sided student t-test. Furthermore, for each siRNA treatment, a ratio is presented on the top left corner, in which the numerator denotes the total particles internalized, and the denominator represents the total number of particles counted amongst all cells. C-E) Quantification of TMR-dextran, AF568-Tfn, and AF647-EGF uptake in non-targeting and ARC1 siRNA treated cells from at least 18 different confocal z-stacks per time point. To quantify the amount of TMR-dextran, AF568-Tfn or AF647-EGF uptake of 15 to 20 different confocal z-stacks per time point were analyzed. F) Quantification of AF647-dextran uptake in DMSO or EIPA treated cells. G and H) AF647-Tfn and AF647-EGF uptake in DMSO or dynasore treated cells. For all three experiments, at least 25 randomly selected fields of view per treatment condition were analyzed.

We validated our analysis method by quantifying the amount of cargo internalized upon treatment of known, well-established inhibitors for macropinocytosis and dynamin-dependent endocytosis. To verify our algorithm for macropinocytosis, we treated A549 cells with different concentrations of EIPA prior to allowing for fluid phase uptake, while for dynamin-dependent endocytosis, we treated A549 cells with different doses of dynasore prior to Tfn or EGF uptake [193, 194]. For all three cargoes tested, we observed a dose dependent decrease in measured cargo uptake with increasing concentration of inhibitor treatment (Figure 3.3F-H).

Collectively, our results show that COPI depletion blocks influenza virus internalization, which in part contributes to the defect in viral fusion as shown in Figure 3.2A. However, other representative cargoes of two different productive entry pathways for influenza—clathrin-mediated endocytosis and macropinocytosis [44, 54-56] —also exhibited defects in internalization in ARCN1 depleted cells.

### **3.2.3 ARCN1 knockdown cells exhibit impaired endosomal trafficking upon virus internalization**

We next tested whether ARCN1 knockdown leads to any post internalization defects. Upon internalization, influenza enters into Rab5+ endosomes near the cell periphery, and then sorts into Rab7+ endosomes towards the perinuclear region, which is late endosome/lysosome dense [50]. Upon exposure to pH ~5.0, the influenza envelope fuses with the endosomal membrane, releasing the vRNP into the cytoplasm for nuclear import [59, 195].

To test whether ARCN1 knockdown cells exhibit any defects in trafficking to intermediate/late endosomes, we cold bound AF647-X31 onto siRNA treated cells, and incubated the samples at 37°C for 90 minutes. The cells were then fixed, and immunostained for an intermediate/late endosome marker, lysobisphosphatidic acid (LBPA) [196]. We found a significant ( $p < 0.0001$ ) decrease in AF647-X31 colocalization with LBPA+ vesicles, with a mean colocalization fraction for individual cells of 0.42 for the non-targeting control versus 0.10 for the ARCN1 knockdown cells. In addition, we report the ratio of the sum of colocalized particles to the total number of internalized particles amongst all analyzed cells.

The ratio for non-targeting and ARCNI siRNA treated cells was 0.62 and 0.11, respectively (Figure 3.4A, and 3.4B, upper left corners). Regardless of the type of measurement, these findings strongly suggest that virus particles exhibit a defect trafficking to intermediate/late endosomes in ARCNI siRNA treated cells.

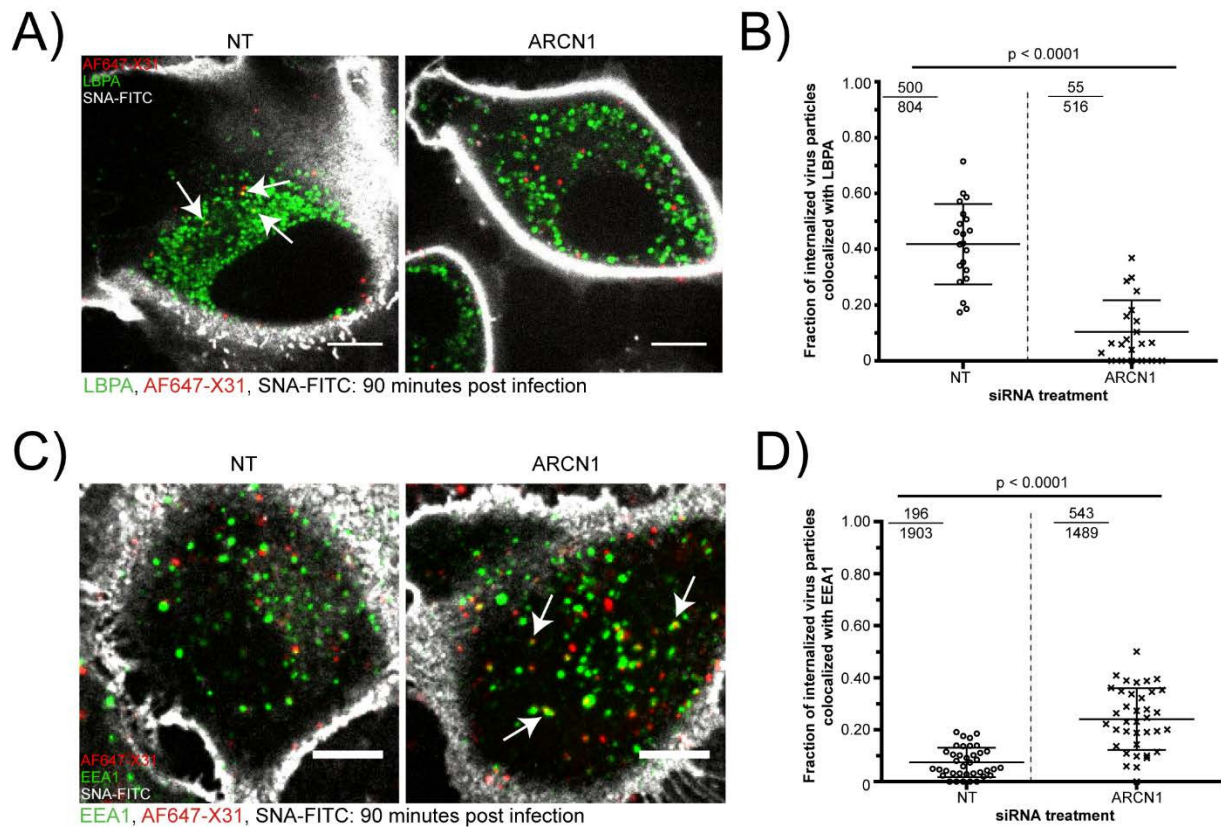


**Figure 3.4. Defective endosomal trafficking of internalized influenza particles in ARCNI depleted cells.** A) Representative spinning disk confocal images of non-targeting and ARCNI siRNA treated cells infected with AF647-X31 for 90 minutes. The plasma membrane was stained with SNA-FITC and the late endosomes were immunostained with LBPA (10  $\mu$ m scale bars). B) The fraction of internalized particles that colocalize with LBPA, a late endosome marker, was counted for at least 20 cells per siRNA treatment. Note that the dot plot average line represents the mean colocalization fraction of the analyzed cells, in which each dot within the plot is the colocalized fraction from an individual cell. Statistical analysis was performed using a one-sided student t-test. In addition, for each siRNA treatment, a ratio is presented on the top left corner, in which the numerator denotes the total number of internalized particles colocalized with LBPA, and the denominator represents the total number of internalized virus particles amongst all cells. On the top left corner we report the sum of colocalized particles divided by the total number of internalized particles for all analyzed cells. These two values are not necessarily equal to each other especially in the presence of substantial cell-to-cell variation. C) Representative spinning disk confocal images of non-targeting and ARCNI siRNA treated cells infected with AF647-X31 for 90 minutes, plasma membrane stained with SNA-FITC, and immunostained with EEA1, an early endosome marker (10  $\mu$ m scale bars). D) Quantification of the internalized particles that colocalize with EEA1 at 90 minutes post infection (mpi) was performed as in Figure 3.4B for more than 35 cells per siRNA treatment. Statistical analysis was performed using a one-sided student t-test.

Given the large defect observed in trafficking to LBPA+ vesicles, we tested whether the ARCN1 knockdown cells were accumulating the AF647-X31 in early endosomes. Indeed, after 90 mpi, the ARCN1 knockdown cells exhibited a significant ( $p < 0.0001$ ) increase the mean colocalization fraction, which was 0.24 for the ARCN1 knockdown cells and 0.07 for the non-targeting control (Figure 3.4C and 3.4D). The sum of colocalized particles divided by the total number of internalized particles for all non-targeting and ARCN1 siRNA treated cells was 0.1 and 0.36, respectively.

Previous studies have reported that COPI proteins may be important for endosomal trafficking [90, 94]. However, it remains unclear thus far whether COPI vesicles directly mediate sorting of influenza between different types of endosomes. To test whether AF647-X31 trafficks within COPI vesicles, we transiently expressed GFP-tagged  $\epsilon$ -COPI (COPE-GFP) in A549 cells. Of the GFP-fusion COPI subunit constructs tested,  $\epsilon$ -COP-GFP minimized the disruption of golgi architecture. After several rounds of live cell imaging experiments with A549 cells expressing COPE-GFP and infected with AF647-X31, we found only one example of COPE-GFP colocalized with AF647-X31 out of many virus particles tracked (data not shown). Though this does not completely negate that COPI proteins play a specific role in endosomal trafficking between MVBs and late endosomes, our data suggests that the effect of COPI in transporting the influenza virus from early to late endosome is likely indirect.

#### **3.2.4 Rapid disruption of COPI vesicles with pharmacological inhibitors does not block viral entry**

The results described thus far help explain why several of the COPI subunits emerged as important host proteins in influenza virus infection in the siRNA genome-wide knockdown screens [64, 66, 67]. However, efficient siRNA depletion can take a few days, thus potentially leading to the accumulation of siRNA mediated indirect effects due to long-term depletion of critical host proteins. In order to test whether we could recapitulate the observations in the siRNA treated cells, and therefore to determine whether there is a direct role for COPI during the influenza virus infection cycle, we conducted experiments using pharmacological inhibitors that rapidly disrupt COPI vesicle formation.



The conversion of inactive, cytosolic ADP ribosylation factor 1 (ARF1)-GDP to the activated ARF1-GTP form triggers its attachment to the golgi membrane, and subsequent recruitment of COPI complexes [86-88]. Two pharmacological inhibitors—BrefA and GCA—prevent exchange of ARF1-GDP to ARF1-GTP via different mechanisms. BrefA binds to the protein-protein interface of ARF1 and several different BrefA-sensitive guanine nucleotide exchange factors (GEFs) to prevent exchange of GDP with GTP [89, 197]. Therefore, treatment with BrefA not only inhibits COPI membrane recruitment, but also other ARF1-GTP dependent vesicular trafficking processes, such as AP1-dependent *trans*-golgi network (TGN) trafficking to endosomal compartments [86, 87]. A more specific inhibitor of COPI complex vesicle formation is GCA, which binds to GBF1, a COPI-specific ARFGEF [198].

We confirmed that the DMSO control treated cells exhibit a compact COPI perinuclear stain reminiscent of the golgi-apparatus. In stark contrast, the BrefA or GCA treated cells exhibit a dispersed  $\beta$ -COPI staining, indicative of the inability for COPI complex recruitment to the golgi apparatus [198] (data not shown). To test whether the drug treatment also inhibits viral fusion as observed for siRNA COPI knockdown, we performed the viral fusion assay, as described in Figure 3.2A. Viral fusion was measured in A549 cells pre-treated and incubated with 10  $\mu$ g/mL BrefA, 10  $\mu$ M GCA, or 0.1% V/V DMSO (as a control for the total amount of DMSO added in the BrefA or GCA treated cells) during the entire experiment. In contrast to the results from Figure 3.2A, we found that inhibition of COPI complex vesicle formation does not affect viral fusion (Figure 3.5A).

Because internalization and transport to late endosomes comprised the two major blocks in viral entry for ARCN1 knockdown cells, we tested whether BrefA and GCA treatment could also recapitulate those same defects. Using the same immunofluorescence-based internalization assay as described in Figure 3.3A and 3B, we found that the mean internalization fraction was 0.58, 0.56, and 0.57 for DMSO, BrefA, and GCA treated cells, respectively (Figure 3.5B). Furthermore, we tested whether inhibitor treatment affects trafficking to intermediate/late endosomes by measuring the fraction of internalized AF647-X31 within Rab7-GFP endosomes. The mean colocalization fraction between the virus and Rab7

in the DMSO, BrefA, and GCA treated cells was 0.74, 0.67, and 0.61, respectively (Figure 3.5C). Our AF647-X31 internalization and Rab7-GFP colocalization results were consistent with the viral fusion results: only minor differences were observed upon BrefA and GCA treatment, indicating that rapid disruption of COPI vesicles unlikely results in an entry defect.

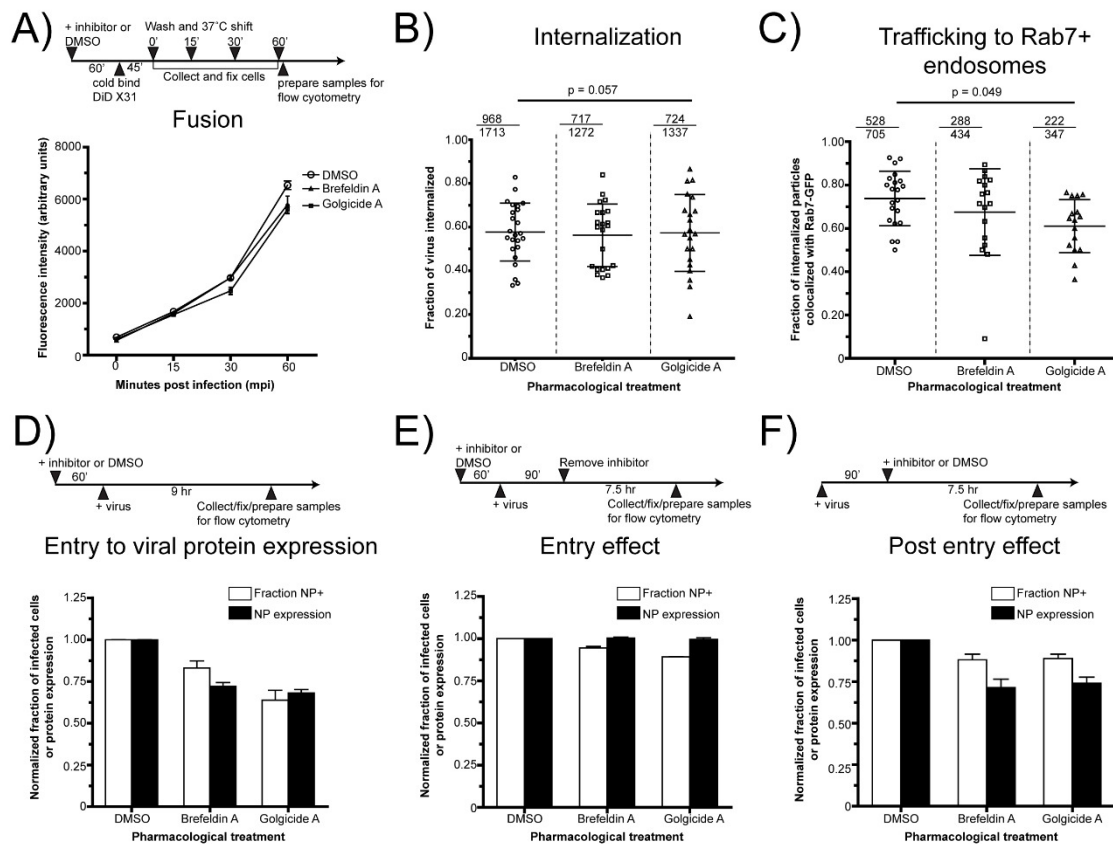


**Figure 3.5. Pharmacological disruption of COPI complexes does not block virus entry.** A) Representative flow cytometry-based quantification of DiD dequenching from three independent experiments. DiD signal was measured at different time points post DiD-X31 infection in A549 cells treated with 0.1% V/V DMSO, 10  $\mu$ g/mL BrefA, or 10  $\mu$ M GCA. Standard deviations represent duplicate samples for each time point. B) Quantification of the fraction of internalized AF647-X31 particles at 30 mpi, upon treatment with inhibitors or DMSO using the same immunofluorescence-based internalization assay in Figure 3.3A. At least 17 different cells were quantified for virus internalization. Statistical analysis was performed using a one-way analysis of variance (ANOVA). C) Quantification of the fraction of AF647-X31 particles colocalized with Rab7-GFP endosomes at 90 mpi in A549 cells treated with 0.1% V/V DMSO, 10  $\mu$ g/mL BrefA, or 10  $\mu$ M GCA. At least 16 different cells were quantified. On the top left corner, we report a ratio, representing the sum of all AF647-X31 particles colocalized Rab7 versus the total number of internalized virus particles for all cells quantified. Statistical analysis was performed using a one-way ANOVA. D) Flow cytometry-based quantification of the percent of NP-positive (NP+) cells and the NP expression levels of the NP-positive cells for A549 cells treated with 0.1% V/V DMSO, 10  $\mu$ g/mL BrefA, or 10  $\mu$ M GCA during the entire infection with X31 (MOI ~ 1). E) Flow

**Figure 3.5. (continued)** cytometry-based quantification of the percent of NP-positive (NP+) cells and the NP expression levels of the NP-positive cells for A549 cells infected with X31 (MOI ~ 1.5) and exposed to 0.1% V/V DMSO, 10 µg/mL BrefA or 10 µM GCA only during entry. F) Flow cytometry-based quantification of the percentage of NP-positive (NP+) cells and the NP expression levels of the NP-positive cells for A549 cells infected with X31 (MOI ~ 1.5) and exposed to 0.1% V/V DMSO, 10 µg/mL BrefA, or 10 µM GCA only after 90 mpi. In (D-F), the bar chart represents the average from two independent experiments (consisting of three replicate samples for each inhibitor or DMSO treatment), with the corresponding SEM.

Next, to test whether BrefA or GCA treatment affects influenza infection, we pre-treated A549 cells with 0.1% DMSO (as a control), 10 µg/mL BrefA, or 10 µM GCA for 60 minutes, allowed X31 to infect cells at an MOI of ~1 for nine hours, and measured NP expression with a flow cytometer. In stark contrast to the results from Figure 3.1C, we found that disruption of COPI complexes resulted in a moderate decrease in infection: relative to the DMSO control, BrefA or GCA treatment reduced the percent of NP-expressing cells by 21.3% +/- 7.9% or 40.6% +/- 1.3%, respectively. In addition, we found a moderate decrease in the NP expression level for the NP+ cells relative to the DMSO control: 31.1% +/- 1.2% and 35.3% +/- 3.6%, in the BrefA and GCA treated cells, respectively (Figure 3.5D). However, it remains unclear whether these defects resulted from an entry or post entry exposure to BrefA or GCA.

To assess whether exposure to BrefA or GCA during entry affects productive influenza virus infection, we pre-treated with the inhibitors for 60 minutes, followed by X31 infection in the presence of the compounds for 90 minutes. Afterwards, the compounds were removed, and the infection was continued for an additional 7.5 hours before processing for flow cytometry. We found that treatment of BrefA or GCA during entry alone did not affect the percent NP+ cells or the NP expression levels (Figure 3.5E). However, when BrefA and GCA were added and maintained only after 90 mpi, a moderate decrease in NP expression was again observed (Figure 3.5F), indicating that the effects on viral gene expression upon BrefA or GCA treatment originate from post entry steps.

Collectively, these results indicate that functional COPI vesicle recruitment to cellular membranes is not required for influenza virus internalization, endosomal trafficking, or viral fusion, but has a moderate effect on viral NP expression.

### **3.2.5 Rapid disruption of COPI complex function decreases viral membrane protein expression and progeny virus production**

To test whether COPI complex disruption inhibits viral membrane protein expression, we infected A549 cells with X31 (MOI ~ 1.5). At 90 mpi, we added 0.1% DMSO (as a control), 10  $\mu$ g/mL BrefA, or 10  $\mu$ M GCA to the virus infected cells. At nine hpi, we fixed the cells, and performed sequential immunostaining against M2 without and with permeabilization to detect surface and total M2. We also immunostained against  $\beta$ -COPI, and confirmed that COPI vesicle formation and concentration within the golgi apparatus was perturbed in both the BrefA and GCA treated cells. By nine hpi, M2 readily trafficked to the plasma membrane in the DMSO control cells. In stark contrast, no M2 was detected on the plasma membrane of BrefA treated cells, while some M2 was trafficked to the cell surface and some trapped within intracellular vesicles within GCA treated cells (Figure 3.6A).

To test whether BrefA or GCA treatment also impaired plasma membrane targeting of another influenza membrane protein, we performed the experiment as described above, except we fixed the cells at a total of 12 hpi, and then immunostained for surface and total NA. In contrast to the minor M2 trafficking defects, GCA treatment strongly inhibited NA transport to the cell surface (Figure 3.6B).

To quantify the defect in M2 protein expression and plasma membrane transport, we performed the experiment as described for Figure 3.6A, except at nine hpi, we collected, fixed, immunostained for M2, and analyzed the samples with a flow cytometer. Immunostaining the X31 infected cells for M2 in the presence of detergents allowed detection of total M2 expression. When compared to the results on post entry effect of BrefA and GCA on NP expression in Figure 3.5F, M2 expression was more substantially perturbed upon treatment with BrefA or GCA, relative to the DMSO control. Furthermore, consistent with the immunofluorescence results from Figure 3.6A, BrefA treatment inhibited M2 plasma membrane transport, and only minor M2 trafficking defects were measured in GCA treated cells (Figure 3.6C).

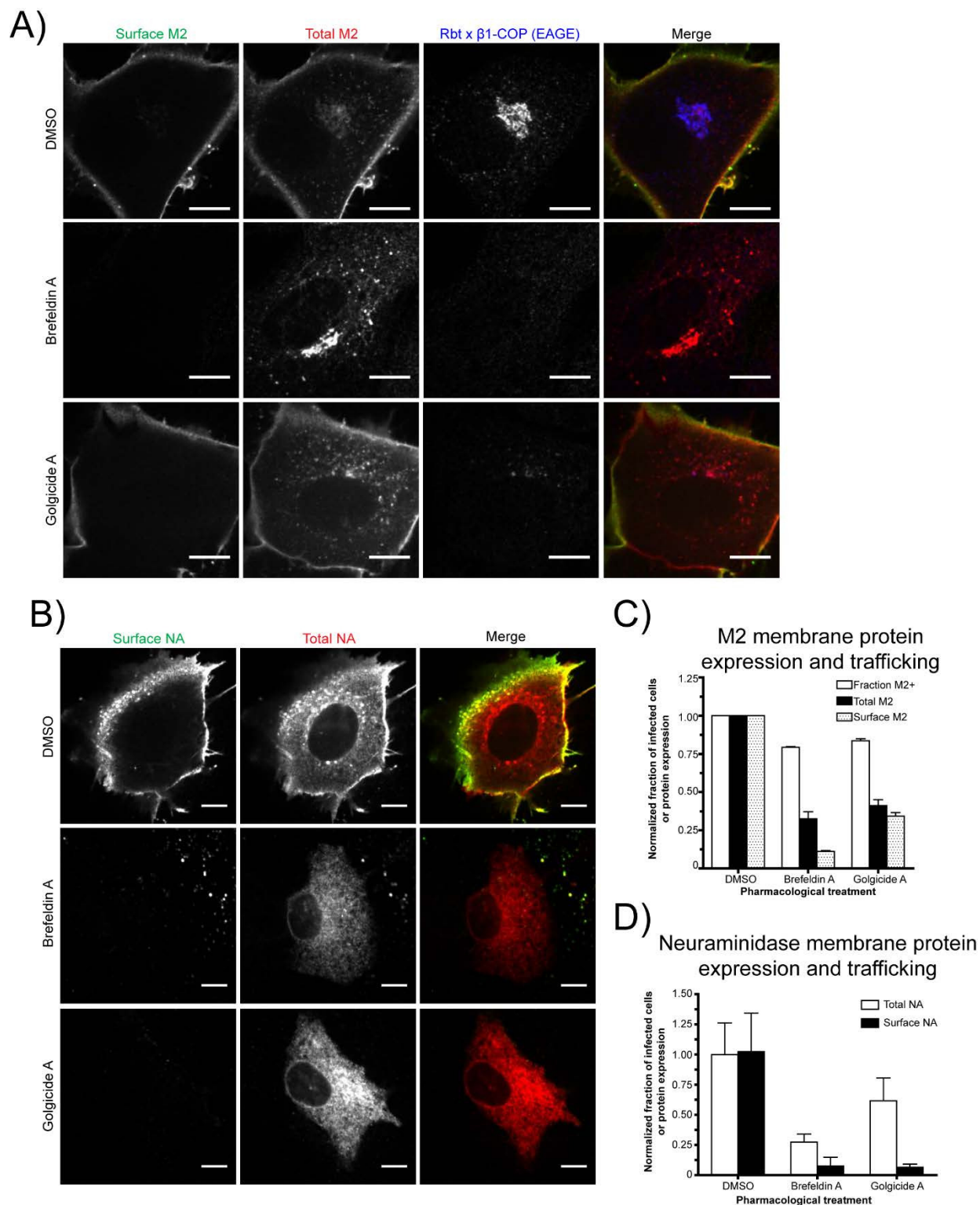


**Figure 3.6. Functional COPI complex recruitment to *cis*-golgi is required for viral membrane protein expression.** A) Representative spinning disk confocal xy cross-sections of X31 infected A549 cells treated with 0.1% V/V DMSO, 10  $\mu$ g/mL BrefA or 10  $\mu$ M GCA, and then immunostained to detect surface M2 (left most panels, or green in the right most panels), total M2 (second left panels, or red in the

**Figure 3.6. (continued)** right most panels), and  $\beta$ 1-COPI (second right panels, or blue in the right most panels) (10  $\mu$ m scale bars). B) X31 infected cells were stained for surface NA (left most panels, or red in right panels) and total NA (second left panels, or green in right panels) (10  $\mu$ m scale bars). C) Flow cytometry-based quantification of the percent of M2-positive (M2+) cells and the M2 expression levels in the M2-positive cells for A549 cells infected with X31 (MOI ~ 1.5) and exposed to 0.1% V/V DMSO, 10  $\mu$ g/mL BrefA, or 10  $\mu$ M GCA only after 90 mpi. Immunofluorescence was performed either in the presence of saponin to detect total M2 expression, or absence of detergent to detect surface M2. The bar chart represents the average from two independent experiments (consisting of three replicate samples for each inhibitor or DMSO treatment), with the corresponding SEM. D) Quantification of the relative surface or total NA expression based on the acquired confocal images (error bars indicate standard deviation of at least 18 images per treatment condition).

We also quantified the effect of BrefA and GCA treatment on NA expression and plasma membrane transport. In contrast to the M2 trafficking in Figure 3.6A and 3.6C, both BrefA and GCA treatment inhibited NA trafficking to the plasma membrane (Figure 3.6D). The discrepancy between M2 and NA plasma membrane trafficking in GCA treated cells suggests that the two membrane proteins may exhibit different transport requirements.

It remains unclear whether BrefA and GCA treatment leads to additional perturbations in the assembly of viral components at the plasma membrane. Influenza assembly is initiated by HA and NA recruitment to cholesterol-enriched plasma membrane domains. M1 is believed to interact with the cytoplasmic tails of HA and NA, and M1 interaction with vRNP facilitates the incorporation of the viral genomes into the budding virions [60]. The vRNPs can be detected with PB1-specific antibodies. The PB1 patches are sites enriched with assembling virus particles, or budding zones. To determine whether functional COPI vesicle formation is essential for viral assembly, we immunostained X31 infected cells treated with DMSO, BrefA, or GCA with M2 (to detect infected cells) and PB1 (Figure 3.7A). We found that 38% of infected, DMSO-treated cells contained budding zones enriched with PB1 at 18 hpi. In stark contrast, only 1% and 2% of BrefA and GCA treated cells infected by X-31, respectively, had the budding zones (Figure 3.7B). The inability to traffick NA (and to some extent M2) to the plasma membrane in either the BrefA or GCA treated cells may help to explain the large defect in assembly and the failure to concentrate progeny virions at budding zones within infected cells.

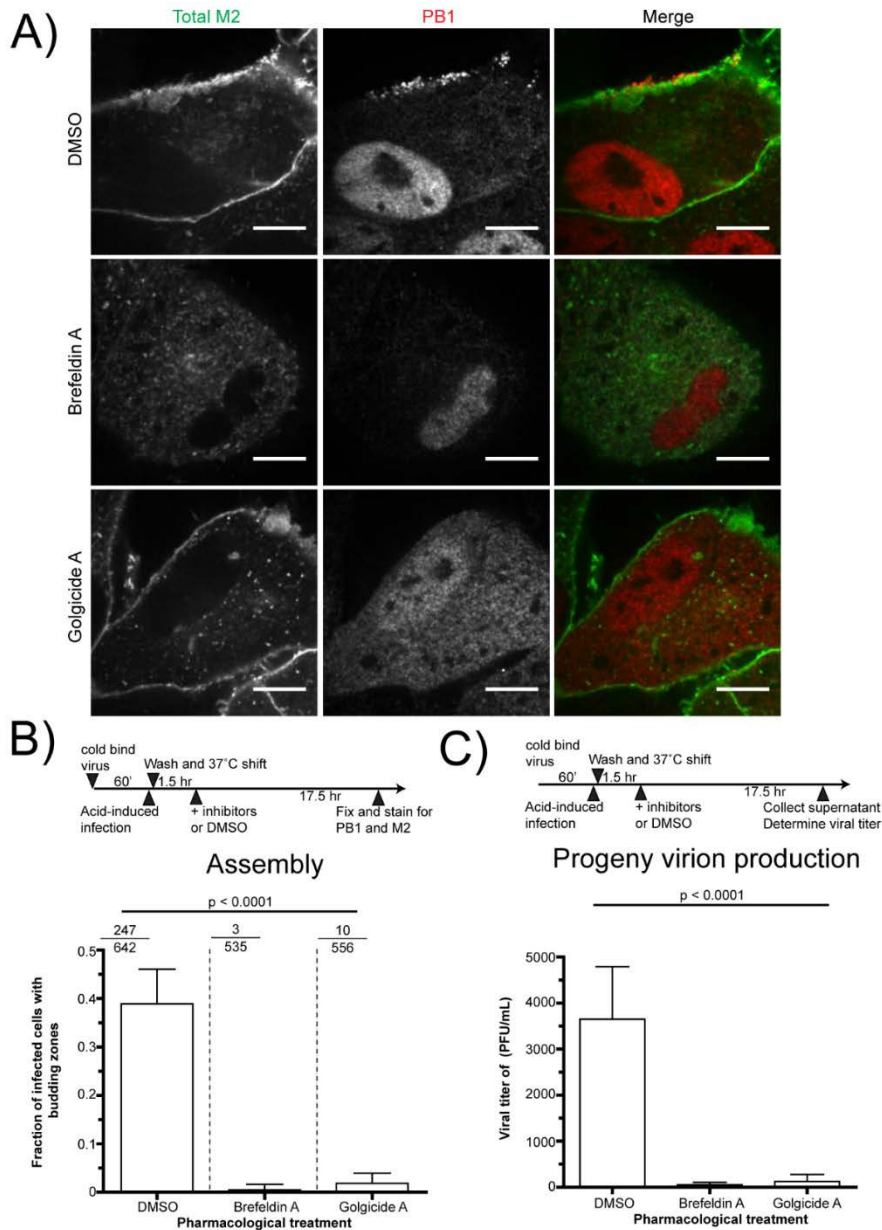


**Figure 3.7. Disruption of COPI complexes with inhibitors inhibits assembly of progeny virions.** A) Representative spinning disk confocal xy cross-sections of X31 infected A549 cells treated with 0.1% V/V DMSO, 10  $\mu$ g/mL BrefA or 10  $\mu$ M GCA, and then fixed and immunostained with antibodies against M2 (left panels, or green in the right panels) and PB1 (middle panels, or red in the right panels) (10  $\mu$ m scale bars). B) Quantification of the fraction of infected, 0.1% V/V DMSO, 10  $\mu$ g/mL BrefA, or 10  $\mu$ M GCA treated cells that contain budding zones at the cell periphery. The fraction on the top left corner represents that number of cells with the budding zone (numerator) relative to the total number of virus-infected cells (denominator) for all cells counted. C) Viral titer of supernatant collected from X31 infected, 0.1% V/V DMSO, 10  $\mu$ g/mL BrefA, or 10  $\mu$ M GCA -treated A549 cells after 18 hpi measured with plaque assays (Materials and Methods). The bar chart represents the SD from samples tested in quadruplicate.

To assess whether the defects in assembly was important for progeny virus production, the supernatant of the virus-infected cells was collected after 18 hpi and the viral titer was measured with standard plaque assays. We found that the presence of either BrefA or GCA reduced viral titers by about two orders of magnitude relative to the DMSO control (Figure 3.7C).

In summary, the results from the pharmacological inhibitors strongly suggest that inactivation of COPI vesicle formation does not result in an entry defect, but does specifically inhibit viral membrane protein expression, plasma membrane transport, assembly, and infectious progeny virion production.

### **3.3 Discussion**

As an obligate pathogen encoding 13 viral proteins, influenza virus requires host factors and compartments to mediate productive infection. Recently, genome-wide knockdown screens identified host dependency proteins important for influenza virus infection. Despite the relatively little overlap in identified host dependency proteins amongst the screens, all of them found subunits of the COPI complex, as critical host proteins in mediating productive virus infection. COPI proteins form complexes, which oligomerize to coat vesicles. These coated vesicles mediate retrograde trafficking between the golgi apparatus and the ER, as well as between the golgi stacks. Previous studies have also identified a role for COPI proteins in endosomal trafficking. Given that COPI proteins mediate trafficking between different cellular compartments both in the synthesis and endosomal trafficking pathways, it remained unclear which steps in the influenza virus infection cycle COPI proteins regulate.

Identification of host dependency proteins through siRNA depletion can result from four general outcomes: (1) siRNA-induced cytotoxicity, (2) off-target effects (e.g. interferon-induction or siRNA sequence overlap with other mRNA sequences), (3) direct effects of siRNA-mediated depletion of the gene of interest, or (4) indirect effects mediated by long term depletion of the target of interest. We confirmed that within our experimental window frame, siRNA-mediated cytotoxicity did not play a dominant role in our studies. No difference was observed in cell viability with minor changes to



cytotoxicity and concomitantly cell growth. Based on the control experiments, we believe that the defects in influenza virus infection upon ARCN1-depletion result in either direct or indirect effects specific to siRNA-mediated silencing. In order to differentiate whether the COPI depletion results in direct or indirect effects, we used both siRNA silencing and rapid COPI vesicle disruption via BrefA or GCA treatment to analyze how these two methods of perturbation affect different steps in the influenza virus infection cycle: binding, internalization, transport into late endosomes, fusion, viral protein expression, trafficking, assembly, and progeny virion production.

Previously, König and colleagues identified ARCN1, an essential subunit of the COPI complex, as a critical host protein for influenza virus infection [67]. Upon further analysis, the authors also provided evidence that ARCN1 depletion affects influenza virus entry. Because of the data suggesting a role for ARCN1 in mediating influenza virus entry and because ARCN1 is known to be an essential component of the COPI vesicle complex, we decided to focus our studies on understanding the role of ARCN1 on influenza virus infection, as a representative subunit for the COPI complex. After conducting a systematic dissection of the different entry steps, we found that ARCN1-depleted cells do exhibit a significant defect in viral fusion. The abrogation of viral fusion in ARCN1 depleted cells likely explains why König and colleagues observed a significant defect in vRNP accumulation in the nucleus when compared to the non-targeting control cells. Consistent with the viral fusion data, we found that ARCN1 knockdown cells exhibited a ~66% decrease in internalization, ~76% decrease in colocalization of the virus with a late endosome marker, LBPA, and ~90% decrease in virus infection relative to the non-targeting siRNA control cells. Taken together, our results show that COPI depletion leads to defects in virus internalization and transport to late endosomes, and viral fusion, the latter effect is likely a consequence of the former two effects.

Cureton and colleagues showed that COPI depletion also lead to defects in VSV entry, though there are differences in which particular steps are perturbed between the two viruses. Cureton and colleagues found that COPI depletion results in a decrease in viral fusion due to a ~40% decrease in VSV

binding and a decreased rate of VSV internalization. However, the VSV particles that do manage to internalize the COPI-depleted cells can still traffick to early endosomes and undergo vRNP release, indicating that the endosome trafficking of VSV is not perturbed. On the other hand, our findings show that COPI depletion did not perturb influenza virus binding, but did inhibit virus internalization and transport to late endosomes.

Treatment of cells with two pharmacological compounds—BrefA and GCA— that rapidly prevent the recruitment of COPI complexes to the golgi apparatus, resulted in strikingly different results from the siRNA experiments. Specifically, we did not observe any significant difference in influenza virus fusion, or colocalization with a late endosome marker when cells were treated with the DMSO, BrefA, or GCA. Substantiating the results from BrefA and GCA treatment, no extensive colocalization was observed between GFP-tagged  $\epsilon$ -COPI, another essential component of the COPI complex, and AF647-labeled influenza virus in live cells during entry. Combining the siRNA, pharmacological inhibitor, and live cell imaging results, we conclude that functional COPI complex vesicle formation is not directly required for influenza virus entry, though ARCN1 depletion leads to indirect effects that result in a defect in influenza virus internalization, trafficking to late endosomes, and consequently viral fusion.

Functional COPI complex formation and COPI vesicles mediate trafficking between the golgi apparatus and ER as well as between the different golgi stacks. The golgi-derived vesicles then traffick contents from the golgi apparatus to other locations within the cell including late endosomes, lysosomes, and the plasma membrane [87, 88]. Defects in golgi vesicular trafficking over an extended period of time, such as during siRNA depletion, could result in improper trafficking of membrane proteins or lipids. Changes in protein or lipid compositions [199] at the plasma membrane and endosomes may provide an explanation to the significant defect observed in viral, internalization, trafficking, and fusion. The potential changes in protein and lipid compositions is, however, not reflected in the amount of  $\alpha(2,6)$ -

linked sialic acids—the attachment factor for influenza— presented on the surface of cells, consistent with the observation that viral binding is not substantially affected by ARCN1 knockdown.

The severely compromised uptake of general clathrin-mediated endocytosis and macropinocytosis cargoes in the ARCN1 knockdown cells does suggest that protein and/or lipid compositions at the cell surface may be altered during the course of siRNA depletion. ARCN1 knockdown cells internalized ~60% less virus by 30 mpi relative to the non-targeting control. Other cargoes of clathrin-mediated endocytosis (Tfn and EGF) and macropinocytosis (dextran) also exhibited significant internalization defects in ARCN1 knockdown cells relative to the non-targeting siRNA treated cells. Consistent with our findings, Cureton and colleagues have found that only after prolonged, but not short exposure of COPI-disruption inhibitors, were VSV and Tfn uptake perturbed [45].

Another phenomenon that may be related to the defect in trafficking of influenza virus to late endosomes is the anomalous LBPA+ late endosome staining pattern as observed in Figure 3.4A. In contrast to the dense perinuclear LBPA+ late endosome staining observed with the non-targeting control cells, we observed a reproducible dispersion of late endosomes—with no apparent aberrant changes to the early endosome organization— in ARCN1 knockdown cells. This observation is consistent with previous reports that show COPI subunit depletion alters the late endosome trafficking pattern [200]. It has also been found that inhibition of endosomal trafficking by blocking the uptake pathways lead to a loss of lysosomal acidification and perinuclear localization [201]. We also note that the shape of the ARCN1 knockdown cells sometimes appeared different from the non-targeting control cells, though it remains unclear what is the underlying mechanism for the change in cell morphology. It is possible that the change in the spatial distribution of late endosomes and the cell morphology may also be related to the inhibition of viral entry.

Together, these above results show that prolonged exposure to siRNA depletion of an essential COPI subunit results in an indirect effect of compromised cargo endocytosis. On the other hand, inhibiting COPI complex recruitment to the golgi apparatus by acute pharmacological treatment directly

affects viral protein expression and infectious progeny virus production. Disruption of COPI complexes by BrefA and GCA only had a moderate effect on NP expression. However, BrefA and GCA treatment inhibited M2 and NA expression, suggesting that COPI complex formation is specifically required for at least some membrane protein expression. The inhibition could perhaps be due to retention of proteins within the ER from defective trafficking between the ER and golgi apparatus. Alternatively, treatment may also cause re-routing of golgi contents to alternative endosomal populations rather than intended target sites such as the plasma membrane [202].

We also observed that BrefA and GCA treated cells exhibited a defect in progeny virion assembly and production. Previous studies have found that NA, but not M2 associates with lipid rafts [60]. For GCA treated cells, transport of M2 to the plasma membrane was modestly affected, while both the plasma membrane targeting of NA and progeny virus assembly were strongly impaired. These results suggest that the large assembly defect in GCA treated cells may stem from inhibition of the trafficking of lipid-raft associated membrane proteins to the plasma membrane, which are critical for initiating virus budding and subsequent assembly steps.

In summary, upon dissection of the influenza virus infection cycle with both siRNA silencing and pharmacological compound perturbation, we have identified which steps of influenza viral infection are direct or indirectly dependent on functional COPI complex formation. Long-term siRNA COPI depletion in cells leads to indirect effects on viral entry through defective cargo uptake and vesicular trafficking to late endosomes, while acute treatment with COPI complex inhibitors impaired viral membrane protein expression and assembly, suggesting a direct role of COPI complexes in these later steps of infection. It has been recently found that COPI proteins mediate many additional effects beyond the well studied trafficking roles within the synthesis and secretory pathways, including lipid droplet formation and lipid metabolism, autophagosome formation, and endocytosis of EGF and Tfn [199, 200, 203, 204], which could potentially be related to the observed indirect effects of COPI depletion on viral entry. Future studies on how COPI siRNA treatment affects protein or lipid expression, modification, and transport to

different cellular compartments should be helpful in understanding how COPI proteins regulate such diverse cellular processes, as well as how these effects may lead to the observed defects of viral infection in COPI-depleted cells.

### **3.4 Materials and methods**

*Antibodies for immunofluorescence or western blotting analysis.* We used the following primary antibodies (vendor, catalog number, and dilution stated in parentheses) for this study: rabbit anti-coatomer subunit delta antibody (Abcam, ab96725, 1:1,000), mouse anti-influenza A virus nucleoprotein antibody [AA5H] (Abcam, ab20343, 1:1000), mouse anti-nucleoprotein (Santa Cruz biotechnology, sc-57882, 1:100), rabbit anti- $\beta$ -COPI (generously donated by James Rothman, 1:1000), rabbit anti- COPZ1 (Sigma, SAB4500896, 1:1,000), rabbit anti-  $\gamma$ 1-COP1 (generously donated by Felix Wieland, 1:10,000), rabbit anti-COPE (Abcam, ab88824, 1:1,000), mouse anti-beta actin antibody - loading control (Abcam, ab8227, 1:1,000), rabbit-anti phospho-STAT1 Tyr701 (Cell Signaling, 9167, 1:1,000), mouse anti-Cy5/AF647 (Sigma, C1117, 1:1,000), mouse anti-EEA1 (BD Transduction Laboratories, 610457, 1:500), ( mouse anti-LBPA antibody (Echelon, Z-PLBPA-50ug, 1:500), mouse anti-influenza A virus M2 protein antibody [14C2] (Abcam, ab5416, 1:1,000), rabbit anti-neuraminidase (kind gift of Gillian Air, 1:5000) and mouse anti-PB1 (Santa Cruz biotechnology, sc-17601, 1:100). We used the following secondary antibodies for this study: Alexa Fluor 647 donkey anti-mouse (Molecular probes, A31571, 1:1,000), Alexa Fluor 555 donkey anti-mouse (Molecular probes, A31570, 1:1,000), Alexa Fluor 488 donkey anti-mouse (Molecular probes A-21202, 1:1000), Alexa Fluor 568 donkey anti-rabbit (Molecular probes, A-100042, 1:1,000), ECL donkey anti-rabbit IgG, HRP-Linked (GE Healthcare, NA934, 1:5,000), and ECL sheep anti-mouse (GE Healthcare, NXA931, 1:5,000).

*Cell culture.* A549 lung carcinoma cells (ATCC) were cultured in Dulbecco's modified Eagle medium (DMEM; Invitrogen) supplemented with 10% fetal bovine serum (Serum International), 1 mM nonessential amino acids (ATCC), and antibiotics (ATCC; 25 U/ml penicillin and 25  $\mu$ g/ml streptomycin), and maintained in humidified, 5% CO<sub>2</sub> environment at 37°C.

For siRNA knockdown experiments, A549 cells were electroporated with 100 pmols of specified COPI siGENOME SMARTpool siRNA (Dharmacon) or AllStars Negative Control siRNA (Qiagen) using an Amaxa Lonza Nucleofector with kit -T (Lonza, VVCA-1002) and program X-001. Experiments were performed on the siRNA treated A549 cells 48 hours after electroporation. For plasmid expression, A549 cells were electroporated with 2 µg of either COPE-GFP (Origene) or Rab7-GFP (generous gift from Qing Zhong [205]) plasmid using kit-T and Nucleofector program X-001. Experiments using these plasmids were performed within 24 hours after electroporation of these plasmids.

LIVE/DEAD Viability/Cytotoxicity kit (Invitrogen, L-3224) was used according to vendor instructions to measure cell viability, death, and growth. Stimulation of the interferon response in A549 cells was achieved with 10,000 U/mL IFN $\alpha$  for three hours (PBL Biomedical Laboratories, 11101-1) prior to collecting cell lysate.

*Spinning disk confocal imaging.* Spinning disk confocal z-stacks were taken with a custom built confocal microscope, which was previously described in detail [206]. Briefly, multi-color fluorescent fixed cell imaging was achieved using an Okogawa spinning disk confocal scan head attached to an Olympus IX-71 microscope (Olympus, Center Valley, PA) with an Olympus 60 $\times$ , 1.35 NA oil-immersion objective. A 561 nm crystal laser, 647 nm krypton ion laser, and/or 457/488/514 nm argon laser were used to image the samples onto an Andor 885 electron-multiplying charge coupled device camera.

*Cargo uptake assays and data analysis.* siRNA treated A549 cells were rinsed extensively with PBS, and cold bound with Alexa Fluor 568-transferrin (AF568-Tfn, Invitrogen, T23365) and Alexa Fluor 647-epidermal growth factor (AF647-EGF, Invitrogen, E35351) for 30 minutes at 4°C. Unbound AF568-Tfn and AF647-EGF was removed with extensive cold PBS washes, and incubated in warm DMEM with antibiotics for different amounts of time at 37°C. For fluid phase uptake, serum starved A549 cells were incubated with 5 mg/mL TMR-dextran (Invitrogen, D-1868) in warm DMEM with antibiotics for different amounts of time at 37°C.

At the indicated time points, surface bound cargo was removed with acid buffer (PBS, adjusted to pH 2.6 with acetic acid) for 2 minutes, fixed with 3.2% paraformaldehyde (PFA, Electron microscopy sciences), and imaged using a spinning disk confocal microscope. Confocal z-stacks were taken for each field of view, which contained about nine to ten cells per image. For analyzing Tfn, EGF or dextran internalization, a Matlab script based on k-clustering analysis was used to threshold the images to differentiate the background pixels from the signal pixels. Briefly, the optimized thresholding value was determined for each maximum z-projection image by an iterative thresholding algorithm that found the maximum difference between the mean background pixels and the mean signal pixels. The mean signal intensity of 15 to 20 maximum z-projection images per time point was calculated and averaged.

To test the known effect of amiloride on macropinocytosis, A549 cells were treated with different concentrations (specified in the figure) of 5-(N-ethyl-N-isopropyl) amiloride (EIPA) (Sigma, A3085) in DMEM without P/S or FBS for 60 minutes. The cells were then incubated with 0.2 mg/mL AF647-Dextran for 30 minutes at 37°C prior to low pH PBS wash, followed by PFA fixation. Additionally, inhibition of dynamin-dependent endocytosis was tested by treatment with different doses of dynasore (Sigma, D7693) in DMEM without P/S or FBS for 30 minutes, prior to cold binding 1µg/mL AF647-Tfn or 1:1000 AF647-EGF for 30 minutes. Unbound cargo was replaced with warmed inhibitor containing DMEM without FBS or P/S, and incubated at 37°C for 10 minutes prior to low pH PBS wash, followed by PFA fixation. For dextran, Tfn, and EGF uptake experiments, images of the samples and analysis were performed as described in the above paragraph.

*Virus labeling. Non-specific amine-reactive labeling of virus:* 50 µL of 1 mg/mL purified influenza A X31, A/Aichi/68 (H3N2) (Charles River Laboratories) was mixed with 47 µL 0.1 M freshly prepared carbonate buffer (pH ~8 to 9) and 6 µg Alexa fluor 647 carboxylic acid, succinimidyl ester (Invitrogen, A-20106) dissolved in DMSO. The mixture was gently mixed in the dark for 60 minutes. A Nap5 size exclusion column (GE Healthcare) was used to separate free dyes from labeled virus using Hepes 145 elution buffer (50 mM Hepes pH 7.4, 145 mM NaCl). The excess AF647-labeled X31 was

aliquoted, snap frozen, and stored at -80°C [159]. No significant difference in infectivity was observed between labeled and unlabeled X31 (data not shown).

*X31 membrane labeling:* 100 µL of 1 mg/mL purified X31 was mixed with 3 µL 25 mM 1,1'-Diocadecyl-3,3,3',3'-Tetramethylindodicarbocyanine, 4-Chlorobenzenesulfonate Salt ('DiD' solid; DiIC<sub>18</sub>(5) solid) (Invitrogen, D-7757) dissolved in DMSO. The mixture was gently vortexed in the dark for 2 hours. A Nap5 size exclusion column was used to separate free dyes from labeled virus using Hepes 145 elution buffer. The excess DiD-labeled X31 was aliquoted, snap frozen, and stored at -80°C. Prior to using the DiD-labeled X31 for the experiments, the virus was filtered through a 0.2 µm filter [61]. We confirmed with plaque assays that the DiD-labeled X31 remained infectious.

*Bulk viral fusion assay.* For the pharmacological compound-treated cells, all steps during the fusion assay before trypsinization—except the PBS washes—included the compounds. A549 siRNA or pharmacological compound-treated cells seeded in Lab-tek 8 well glass dishes were rinsed extensively with PBS and cold bound with  $2 \times 10^4$  PFU/mL DiD-X31 for 45 minutes on ice. Unbound virus was removed with extensive PBS washes, and incubated with DMEM for different amounts of time at 37°C. Afterwards, the cells were washed once with PBS, and trypsinized. The trypsin was neutralized with PBS supplemented with 10% FBS and 30 mM sodium azide, and the cells were collected and placed on ice to prevent any further fusion. Cells were fixed with 2% PFA for 20 minutes, washed once with PBS, and analyzed immediately with a flow cytometer (BD Biosciences Fortessa). The data was interpreted using FlowJo software.

*Virus binding or Elderberry lectin binding assays.* After 48 hours siRNA knockdown, A549 cells were washed extensively with PBS, and cold bound with different concentrations of AF647-X31 in DMEM for 45 minutes. Unbound virus was removed through PBS washes, and the cells were immediately trypsinized. The trypsin was neutralized with PBS supplemented with 10% FBS and 30 mM



sodium azide. Cells were collected and fixed with 2% PFA for 20 minutes, washed once with PBS, and analyzed immediately with a flow cytometer.

For the elderberry lectin binding assays, siRNA treated cells were trypsinized and fixed with 2% PFA. The cells were then treated with or without different doses of sialidase A (Prozyme) in PBS (pH ~5) for one hour at 37°C. The pH was raised to ~pH 7 to stop the sialidase A reaction, and cells were stained with 1:1000 FITC-conjugated *S. nigra* (elderberry bark, SNA-FITC) lectin (Vector laboratories) for one hour. After three PBS washes, the samples were immediately analyzed by flow cytometry.

*Immunofluorescence for flow cytometry.* siRNA or pharmacological compound-treated A549 cells were infected with influenza virus at 37°C for nine or 12 hours. Infected cells were trypsinized and fixed in 2% PFA in PBS for 20 minutes at room temperature, and washed once to remove the fixation buffer. The cells were permeabilized in buffer P (PBS containing 10% FBS and 0.075% Saponin) for 5 minutes. The samples were incubated with mouse anti-influenza NP or anti-influenza M2 (1:1000 dilution in buffer P) for 60 minutes, washed three times with buffer P, incubated with Alexa Fluor 647 donkey anti-mouse (1:1000 dilution in buffer P) for 30 minutes, washed three times with buffer P, washed once with PBS, and analyzed by flow cytometry.

*Immunofluorescence with endosomal markers.* To delineate the cell membrane, fixed A549 cells were first stained with SNA-FITC without permeabilization. For colocalization studies between influenza virus and EEA1, fixed A549 cells were blocked and permeabilized with 3% bovine serum albumin (Jackson laboratories) and 0.1% Triton X-100 for 30 minutes at room temperature (blocking buffer). The cells were incubated with mouse anti-EEA1 in blocking buffer for one hour at room temperature, rinsed with PBS, stained with Alexa Fluor 555 donkey anti-mouse in blocking buffer for 30 minutes, and washed with PBS.

For colocalization studies between influenza virus and LBPA, fixed A549 cells were blocked and permeabilized with 3% bovine serum albumin (Jackson laboratories) and 0.075% (W/V) Saponin for 30

minutes at room temperature (blocking buffer). All subsequent wash and antibody incubations were performed with the blocking buffer, unless state. The sample was incubated with mouse anti-LBPA for one hour at room temperature, washed, stained with Alexa Fluor 555 donkey anti-mouse for 30 minutes, washed, and rinsed with PBS.

All samples were imaged on a customized spinning disk confocal microscope, which is described briefly above and previously in more detail [206]. ImageJ software was used to visualize the fluorescent confocal z-stacks, and the fraction of internalized virus particles that also colocalized with the respective endosomal marker was counted.

*Pharmacological compounds.* The following pharmacological compounds were used in this study with the vendor, catalog number, and concentration or dilution used in the experiments stated in parentheses: Dimethyl sulfoxide (DMSO) (Sigma, D2650; 1:1000), Brefeldin A (Sigma, B7651; 10  $\mu$ g/mL), and Golgicide A (EMD, 345862; 10  $\mu$ M). Brefeldin A and Golgicide A were both dissolved in DMSO, and incubations were performed in DMEM supplemented with 10% fetal bovine serum, 1 mM non-essential amino acids, and antibiotics. The final amount of DMSO did not exceed 0.1% V/V. Specific incubation times for each of the experiments are described in the figures and figure legends.

*Plaque assays.* We collected the supernatant from influenza-infected cells at 18 or 24 hpi. Serial dilutions of the virus-containing supernatant was used to inoculate a ~80% confluent monolayer of Texas-MDCK cells (generous gift from Robert Lamb) or Vero cells (ATCC) grown in 6-well dishes for ~1.5 to 2 hours at 37°C. The cells were washed with PBS, coated with 3 mL of 30% Noble Agar (Affymetrix) in DMEM containing antibiotics and 2  $\mu$ g/mL acetylated trypsin (Sigma), and then incubated at 37°C.

Two different detection methods were used to determine the viral titer. For immuno-detection of infected cell colonies (fluorescent foci), the noble agar disks were removed after ~36 hpi, and the cells were fixed with 100% methanol for 8 to 10 minutes at -20°C. The cells were rinsed with PBS, blocked and permeabilized with 3% BSA and 0.1% Triton X-100 in PBS for 30 minutes, immunostained against

NP in blocking buffer for 60 minutes, washed three times with PBS, incubated with Alexa fluor 488 donkey anti-mouse in blocking buffer for 30 minutes, and washed three times with PBS. The fluorescent foci were visualized and quantified using a Typhoon fluorescent scanner (GE Healthcare).

The second detection method to determine the viral titer was to count the number of plaques observed after 2.5 days post infection. To detect the plaques, the agar disks were removed and the cells were immediately fixed and stained with a solution containing 1:1000 V/W crystal violet with 30% ethanol in water. The number of plaques for each condition was counted. The viral titer was determined with the following equation: (number of foci or plaques)/(dilution \* inoculation volume in mL). Samples were tested in quadruplicate.

*Western blotting.* Cell lysates were diluted in Laemmli sample buffer (Bio-rad, 161-0737) containing DTT to achieve the same amount of protein for all samples. The samples were loaded and ran on a 4-15% Tris-HCL polyacrylamide gel (Bio-rad). The separated proteins from the gel were transferred onto Hybond PVDF membranes (GE Healthcare), blocked with 5% non-fat milk in TBS-tween, incubated with the specified primary antibodies (reported in the figure legends with product information listed above) for overnight at 4°C, washed with TBS-tween, incubated in HRP-conjugated secondary antibodies for 60 minutes at room temperature, washed with TBS-tween, detected with Lumigen TMA-6 (Lumigen, TMA-100), and exposed/developed onto high sensitivity Kodak film.

## **Chapter 4: Developmental Mechanism of the Periodic Membrane Skeleton in Axons**

Work in this chapter was performed in collaboration with Dr. Guisheng Zhong, Ruobo Zhou, Damaris Lorenzo, and Hazen Babcock. Most of the results from this work are published in [207].

## 4.1 Introduction

Neurons are highly polarized cells with their somatodendritic regions receiving synaptic inputs and axons propagating electrical signals and sending synaptic outputs to target cells. Cytoskeletal proteins are important for maintaining the polarity of neurons. For example, actin and microtubules are essential for the growth and stabilization of axons, the trafficking of cargos to specific neurites, and the stabilization and plasticity of synapses [121-126]. Transient destabilization of actin at the tip of a neurite is sufficient to induce a dendrite to become an axon [140]. Increasing evidence also suggests an important role for spectrin in the maintenance of neuronal polarization, as well as the development and stabilization of axons [134, 142].  $\alpha$ II and  $\beta$ II spectrin are enriched in axons [133, 134]. Spectrin is known to be important for providing the mechanical stability for axons [142] and protecting them from mechanical stress [145], for axon path finding [208], for the stabilization of presynaptic terminals [209], and for maintaining specific membrane domains in axons [210]. Mice lacking either  $\alpha$ II or  $\beta$ II spectrin die in the embryo, highlighting the crucial function of these proteins [134, 143, 144]. Spectrin has also been shown to play a role in human neurological diseases [146, 147].

Recently, the Zhuang lab discovered a periodic submembrane lattice structure made of actin, spectrin and other associated molecules preferentially formed in the axons of mammalian neurons [149]. In this membrane skeleton, actin filaments form a ring-like structure that wraps around the circumference of axons. These actin rings are evenly spaced along the axon shaft with a period of ~190 nm and show a remarkably long-range order. Actin filaments in the rings are capped by adducin. Adjacent actin rings are connected by spectrin, likely in the form of  $\alpha$ II- $\beta$ II-spectrin heterotetramers, given the observations that the periodic  $\beta$ II spectrin rings alternate with the actin-adducin rings along axons and that the observed 190 nm period matches the length of the spectrin tetramer. The ultrastructural organization of this quasi-one-dimensional, periodic lattice structure is different from the previously observed, two-dimensional polygonal membrane skeletal structure found in red blood cells [129-131], whereas an erythrocyte-like polygonal membrane skeletal was observed in the axon terminals at the *Drosophila* neuromuscular

junction [211]. Interestingly, this periodic structure forms preferentially in axons, with the actin in dendrites primarily adopting the form of long filaments running along the dendrite shaft [149]. In *C. elegans* that lack  $\beta$  spectrin or carry a  $\beta$  spectrin mutant, axons break more easily during animal movement [142] and exhibit impaired touch sensation [145], suggesting that this structure may be important for the mechanical stability of axons and for sensing mechanical stimuli. This periodic lattice also organizes the axonal membrane by placing important membrane proteins, such as the voltage-gated sodium channels, into a periodic distribution [149].

However, it is unknown how this highly regular membrane skeleton structure develops and how its formation is regulated. For example, it is unclear whether the periodic lattice develops during early or late stages of axon differentiation. Although protein factors previously identified to be important for axon differentiation tend to be enriched and function at the growing tips of axons [123, 124, 212, 213], it is unknown whether the actin-spectrin lattice also initiates at the distal ends of axons, or instead forms first in the proximal region near the cell body. Finally, the molecular mechanism that regulates the preferential formation of this periodic structure in axons remains a mystery. In this study, we addressed these important questions concerning the development of this newly discovered neuronal structure. We found that the periodic membrane skeleton initiated early during axon differentiation. The lattice structure originated in the axonal region adjacent to the cell body and propagated to the distal ends of axons. The lattice structure further matured by recruiting other components and the matured membrane skeleton was highly stable. The periodic structure formed preferentially in axons with long-range order, but appeared only in a small fraction of dendrites and they often appeared as isolated patches of periodic structures. Multiple molecular factors played roles in regulating the formation of this structure. The lattice structure depended on intact microtubules. The high local concentration of  $\beta$ II spectrin in axons was the key determining factor for the preferential formation of the lattice structure in axons and artificially increasing the concentration of  $\beta$ II spectrin in dendrites was sufficient to induce the formation of the periodic lattice structure in dendrites. Remarkably ankyrin B was important for the polarized distribution of  $\beta$ II spectrin

in neurites; in ankyrin B knockout mice,  $\beta$ II spectrin was evenly distributed in axons and dendrites, giving rise to a highly regular, periodic membrane skeleton in both dendrites and axons.

## **4.2 Results**

### **4.2.1 Early development and propagation of the periodic lattice structure in axons**

Neurons exhibit distinct developmental stages with different morphological characteristics during polarization [123, 212-214]. In dissociated hippocampal neuronal culture, neurons first display intense lamellipodial protrusive activity in stage 1, which then leads to the emergence of multiple immature neurites in stage 2 (~1 Day in Vitro (DIV)). In stage 3 (DIV 2-4), one of these neurites breaks the symmetry and extends rapidly to become an axon. The other neurites then gradually acquire dendritic properties in stage 4 (DIV 4-7). In stage 5 (> DIV 7), neurons continue to mature and form axon initial segments, dendritic spines and synapses. In order to determine the developmental course of the periodic membrane skeletal structure, we fixed dissociated neurons at different developmental stages, immunostained for  $\beta$ II spectrin, and imaged using stochastic optical reconstruction microscopy (STORM), a super-resolution imaging method that relies on switching and localizing single molecules to acquire sub-diffraction limit images [105-107, 112].

To illustrate how we systematically imaged and quantified this periodic structure in axons, we first imaged a neuron at DIV 10. Consistent with our previous findings [149],  $\beta$ II spectrin adopted a highly regular, periodic pattern in all regions of the axonal shaft (Figure 4.1). Both Fourier transform and autocorrelation analyses showed that the  $\beta$ II spectrin adopted a periodic distribution with a period of ~190 nm (Figure 4.1). Similarly, actin filaments exhibited a highly periodic distribution along axon shafts (data not shown). Depolymerizing the actin filaments with latrunculin A (LatA) disrupted the periodic distribution of  $\beta$ II spectrin, and knocking down  $\beta$ II spectrin using shRNA led to a loss of the periodic actin distribution (data not shown). These results indicate that the periodic organizations of actin and

spectrin are interdependent, consistent with the model that adjacent actin rings are connected by the spectrin tetramers.

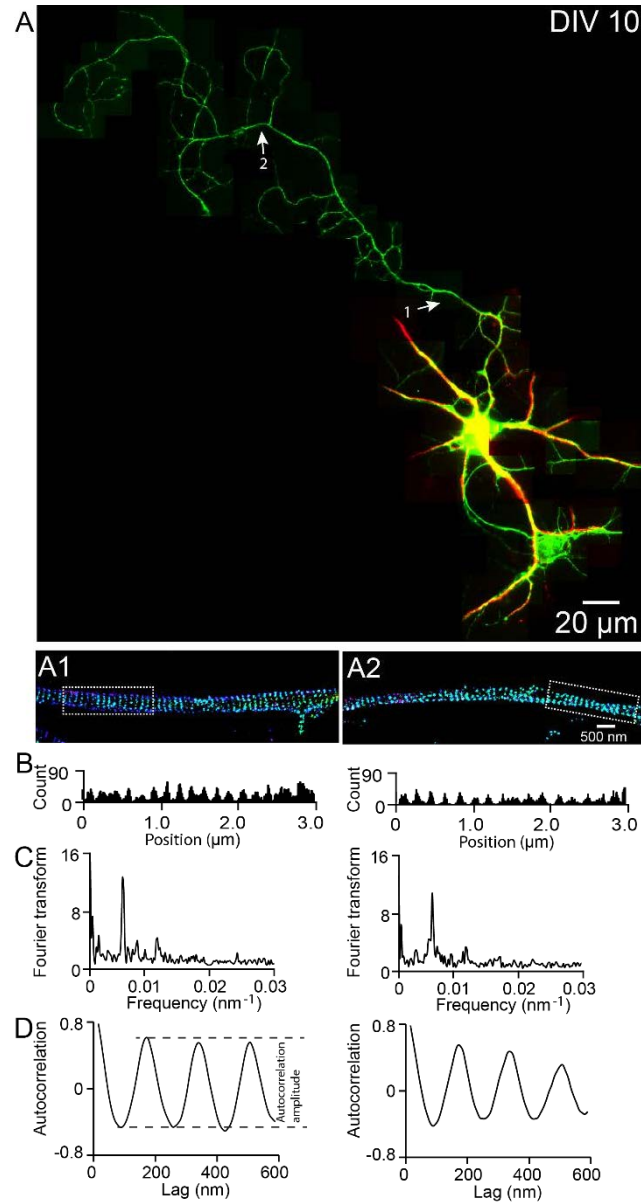


**Figure 4.1.  $\beta$ II spectrin structure in a DIV 10 neuron.** A) A DIV 10 neuron was immunostained for  $\beta$ II spectrin (green) and Map2 (red) and imaged by conventional fluorescence and 3D STORM microscopy. STORM images of the two arrow-indicated regions along the axon are shown below. B) Histograms of the  $\beta$ II spectrin localizations from the boxed regions in STORM images. C) Fourier transform analyses of the  $\beta$ II spectrin localizations from the boxed regions. D) Autocorrelation analyses of the  $\beta$ II spectrin localizations from the boxed regions.



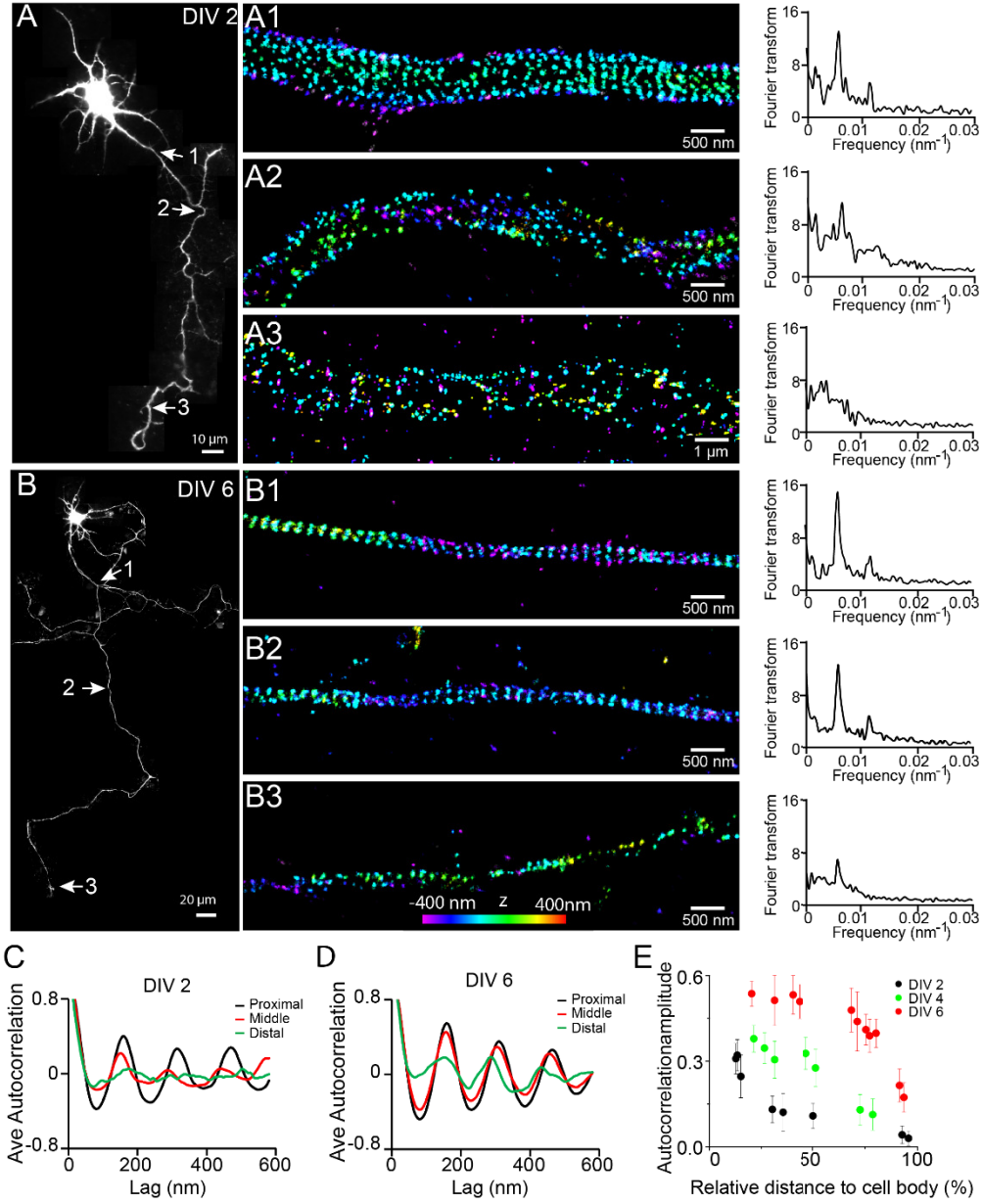


**Figure 4.2. Early development and propagation of the periodic lattice structure in axons.** A) A DIV 2 neuron was stained with  $\beta$ II spectrin antibody and imaged by 3D STORM. The single long process from the cell is the axon. A1, A2 and A3 are 3D STORM images taken from arrow-indicated regions from A. The Fourier transform analyses of the  $\beta$ II spectrin distribution along the axon shaft are shown on the right. B) Similar to A) but for a DIV 6 neuron. C-D) Autocorrelation analysis of  $\beta$ II spectrin distributions of DIV 2 (C) or DIV 6 (D) neurons at the proximal, middle and distal regions of axons. Shown are the averaged autocorrelation from multiple segments of axons for each condition. E) The average amplitude of autocorrelation analysis for different axonal regions of DIV 2, 4 and 6 neurons. The amplitude was measured as the difference between the first peak and the average of two first valleys of the autocorrelation curve. Error bars are standard deviation from measurements of multiple neurons ( $n = 7$  neurons for DIV2;  $n = 6$  neurons for DIV4;  $n = 9$  neurons for DIV6; from 3 independent experiments at each DIV). The color bar for 3D STORM image indicates the z-depth of the image, and is the same for all of our STORM images.

Next, we quantified the distribution of  $\beta$ II spectrin at earlier developmental stages in DIV 2, 4 and 6 neurons (Figure 4.2). Figure 4.2A shows a typical stage 3 neuron at DIV 2, with one neurite outgrowing the others and becoming an axon. Interestingly, the periodic pattern of  $\beta$ II spectrin has already formed in the proximal region of this axon near the cell body, as shown by both Fourier transform and autocorrelation analyses of the STORM image (Figure 4.2A, C). However, the periodic distribution did not extend far - the middle and distal parts of the same axon did not exhibit the periodic pattern (Figure 4.2A, C). Similar results were observed for other stage 3 neurons that we imaged. As neurons continued to mature, the periodic  $\beta$ II spectrin distribution extended to more distal regions of axons. By DIV 6, the periodic  $\beta$ II spectrin distribution extended for nearly the entire length of the axon, except for the very distal region (Figure 4.2B, D). Using the autocorrelation amplitude at the first peak ( $\sim 190$  nm) to quantify the degree of periodicity for the  $\beta$ II spectrin distributions, we found that the periodicity degraded quickly along axons in DIV 2 neurons, but gradually extended to the distal end of the axon in later developmental stages until the structure eventually occupied nearly the entire axon (Figure 4.2E). Taken together, these results demonstrate that the periodic membrane skeleton forms early during development, originates in proximal axon regions close to the cell body, and propagates toward the distal end of the axon.

#### **4.2.2 The structural organization of $\beta$ II spectrin in dendrites**

The periodic membrane skeleton was initially discovered in axons [149]. To test whether the lattice structure could be extended to other neurites, we examined the distribution of  $\beta$ II spectrin in dendrites of neurons at different developmental stages. DIV2, 5, 10 and 14 neurons were immunostained for  $\beta$ II spectrin and  $\beta$ II spectrin in the dendrites were imaged by STORM. As shown in Figure 4.3, during early developmental stages (DIV2 and DIV5),  $\beta$ II spectrin is largely irregular in dendrites, in contrast to the high periodic distribution in axons of the same neurons (Figure 4.3A and 4.3B). As neurons mature, however,  $\beta$ II spectrin adopted a periodic form in a small fraction of dendrites during later developmental stages (DIV14) (Figure 4.3 C-E). In these dendrites, isolated patches of periodic  $\beta$ II spectrin patterns

could be readily observed (Figure 4.3E). However, unlike in axons, these patches did not form a cohesive lattice structure with a long-range order. Quantitatively, the average autocorrelation analysis showed much smaller amplitudes in dendrites than those in axons (Figure 4.3G), indicating a much poorer regularity of the structure in dendrites. Similar results were observed for  $\beta$ III spectrin (Figure 4.3F, H), an isoform of  $\beta$  spectrin that is enriched in dendrites instead of axons [135-137]. Recently, D'Este and colleagues used SiR-Actin, a newly developed fluorescent probe, to label actin, and studied the periodic structure in live neurons using STED imaging. Consistent with our findings, they also found that the lattice structure could be identified in all axons but only in a small fraction (~25%) of dendrites [215].

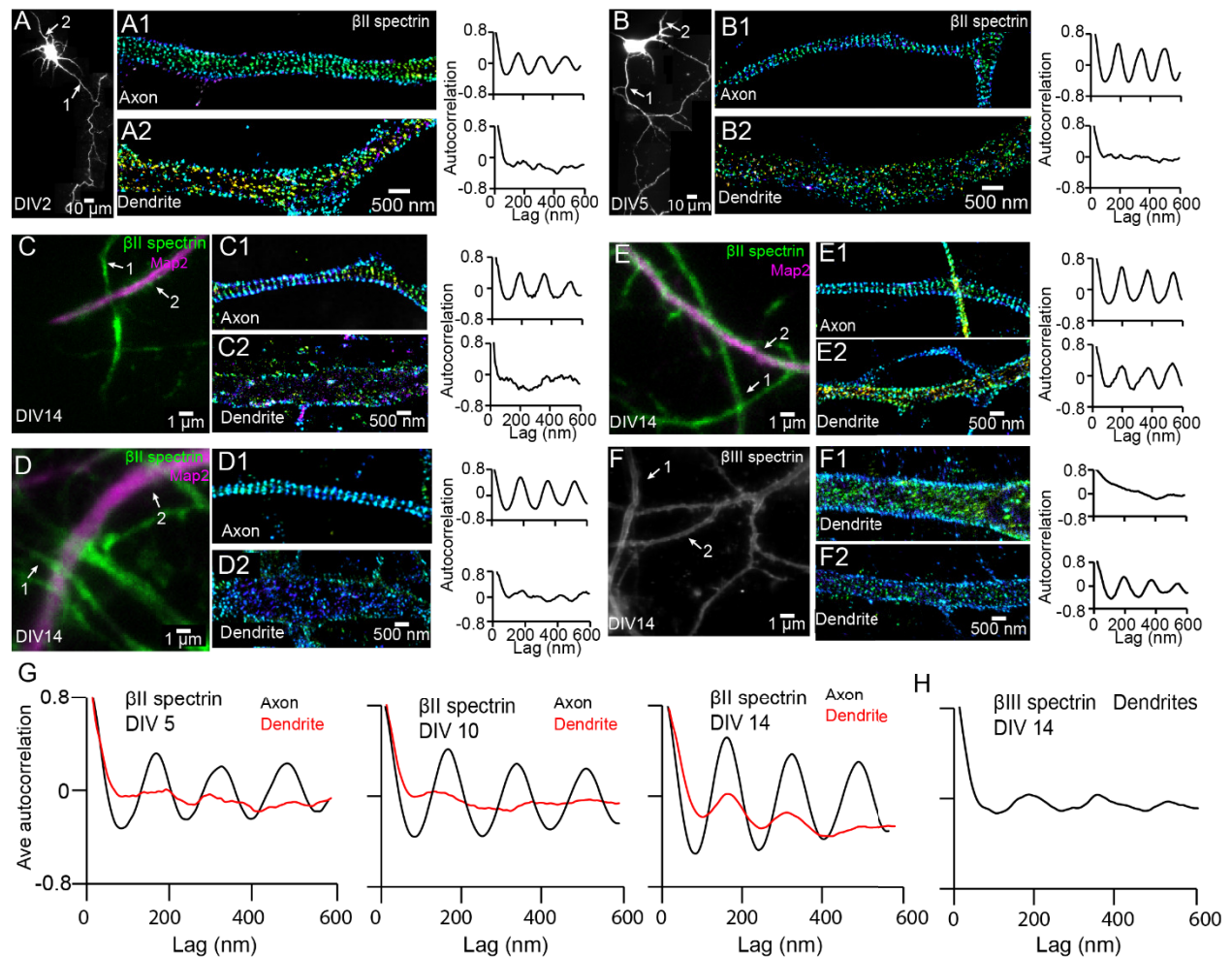


**Figure 4.3. Distributions of dendritic  $\beta$ II and  $\beta$ III spectrin.** A-B) DIV 2 and DIV 5 neurons were immunostained with  $\beta$ II spectrin, and both axonal and dendritic processes were imaged by 3D STORM. The reconstructed neuron image, 3D STORM images of axon and dendrite from indicated regions (arrows), and autocorrelation analyses are shown. C-E) DIV 14 neurons were immunostained with  $\beta$ II

**Figure 4.3. (continued)** spectrin and a dendritic marker Map2, and the  $\beta$ II spectrin was imaged by 3D STORM. The conventional images, 3D STORM images of axons and dendrites from indicated regions (arrows), and autocorrelation analyses are shown. F) DIV 14 neurons were immunostained with  $\beta$ III spectrin. The conventional image, STORM images of  $\beta$ III spectrin from two indicated dendritic regions, and autocorrelation analyses are shown.  $\beta$ III spectrin only stains for dendrites and we did not observe detectable  $\beta$ III spectrin in axons. G) Average autocorrelation analyses of  $\beta$ II spectrin in axons and dendrites of neurons at DIV 5, DIV 10 and DIV 14 (n =14 neurons for DIV5; n = 11 neurons for DIV 10; n = 16 neurons for DIV14; from at least 3 independent experiments at each DIV). H) Average autocorrelation analysis of  $\beta$ III spectrin of DIV 14 neurons (n = 12 neurons, from 4 independent experiments).

#### 4.2.3 Actin dependence during the early developmental phase of the periodic membrane skeleton

Similar to the lattice structure in mature axons, the periodic pattern of  $\beta$ II spectrin depended on actin during early development. Treatment of neurons with actin-depolymerizing drugs, cytochalasin D (CytoD) or LatA, disrupted the periodicity of  $\beta$ II spectrin in DIV 3 neurons (Figure 4.4 A-E). The effect of actin-depolymerizing drugs set in quickly with the periodic  $\beta$ II spectrin distribution substantially disrupted after several minutes of LatA treatment (Figure 4.4F and 4.4G), consistent with the drug acting directly on the lattice structure. These results indicate that actin is involved in the lattice structure during early neuronal development. The form of actin, however, appeared to be different during the early developmental stages as compared to that in mature axons. We have previously shown that the periodic pattern of actin was not directly observed in the STORM images during DIV 1-4. In DIV 5, the periodic actin pattern begins to appear in some neurons, and become robustly observed in neurons at DIV 7 [149]. Similar results were observed here (data not shown). One possible interpretation is that actin existed in a less stable form during the early developmental stages and was not preserved by our sample treatment (fixation and extraction) prior to imaging. Consistent with the notion that actin filaments in the lattice structure were less stable during early developmental stages, the periodic structure of  $\beta$ II spectrin was more quickly disrupted by LatA treatment during early development than in older neurons (Figure 4.4G).

We also observed a relatively slow developmental time course for the periodic pattern of adducin, an actin-capping protein [216]. The periodic pattern of adducin was not observed in axons at DIV 2 or DIV 4 (Figure 4.5). A periodic pattern began to appear at ~DIV 6 and became obvious after DIV 7 (Figure 4.5). The lack of adducin capping may have contributed to the lower stability of actin during early

development stages, although it is also possible that the lower stability of actin during the early development stages made it difficult to maintain the adducin pattern during cell fixation and extraction. Finally, it is formally possible that actin and adducin are not present in the periodic lattice structure during early developmental stages. However, we consider such a scenario to be less likely as it is difficult to imagine how spectrin tetramers themselves could self-assemble into a periodic lattice structure without the help of actin to crosslink multiple spectrin tetramers.

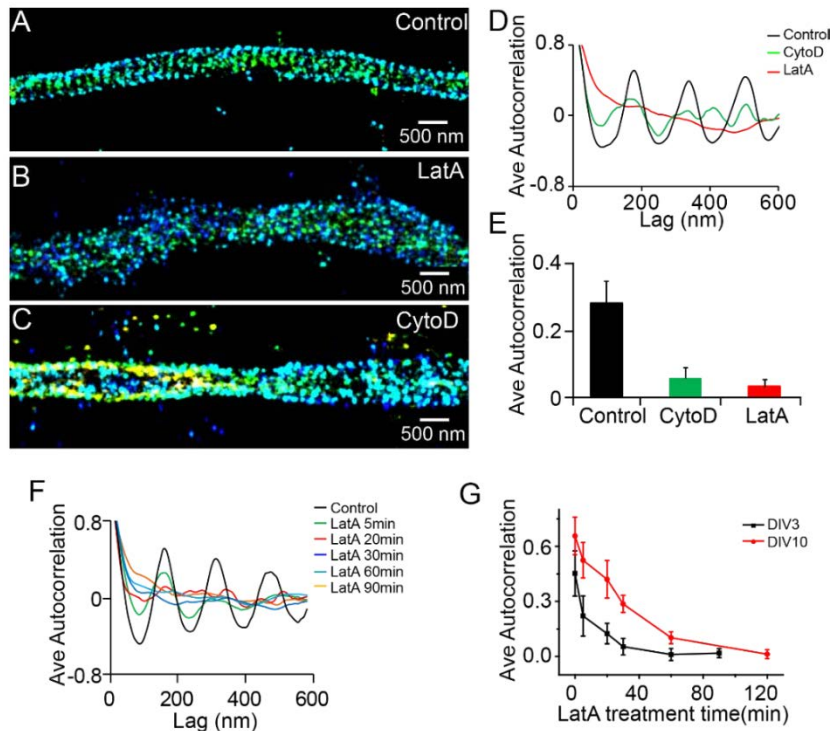


**Figure 4.4. The periodic structure of  $\beta$ II spectrin depends on actin during early development.** A-C) DIV 3 neurons were either untreated or treated with latrunculin A (LatA, 20  $\mu$ M) or cytochalasin D (CytoD, 50 $\mu$ M) for 1 hour, and subsequently immunostained with  $\beta$ II spectrin antibody for 3D STORM imaging. Shown here are representative images of  $\beta$ II spectrin in proximal axonal regions from control (A), LatA-treated (B) and CytoD-treated (C) neurons. D) Average autocorrelation analyses of  $\beta$ II spectrin from multiple axon segments of control, LatA-treated, and CytoD-treated DIV 3 neurons ( $n = 6$  neurons for control;  $n = 7$  neurons for LatA-treated;  $n = 7$  neurons for CytoD-treated conditions; from at least 3 independent experiments for each condition). E) The average autocorrelation amplitudes from control, LatA-treated, and CytoD-treated DIV 3 neurons. F) Average autocorrelation analyses of  $\beta$ II spectrin from multiple axon segments of control and LatA-treated DIV 3 neurons at different treatment time ( $n > 5$  neurons from 3 independent experiments for each condition). The axon segments are taken from the proximal axonal regions near the cell bodies. G) DIV 3 and DIV 10 neurons were treated with 20  $\mu$ M LatA for indicated amount of time, and the average autocorrelation amplitude of  $\beta$ II spectrin from these neurons are shown. Error bars are standard deviation from measurements of multiple neurons ( $n = 6$  neurons for DIV 3;  $n = 8$  neurons for DIV 10; from 4 independent experiments at each DIV).

Together, the above results indicate that the periodic membrane skeleton continued to mature after formation. Consistent with this notion, the auto-correlation amplitudes of the periodic  $\beta$ II spectrin distribution also continued to increase with time as the neuron matured (Figure 4.2E).

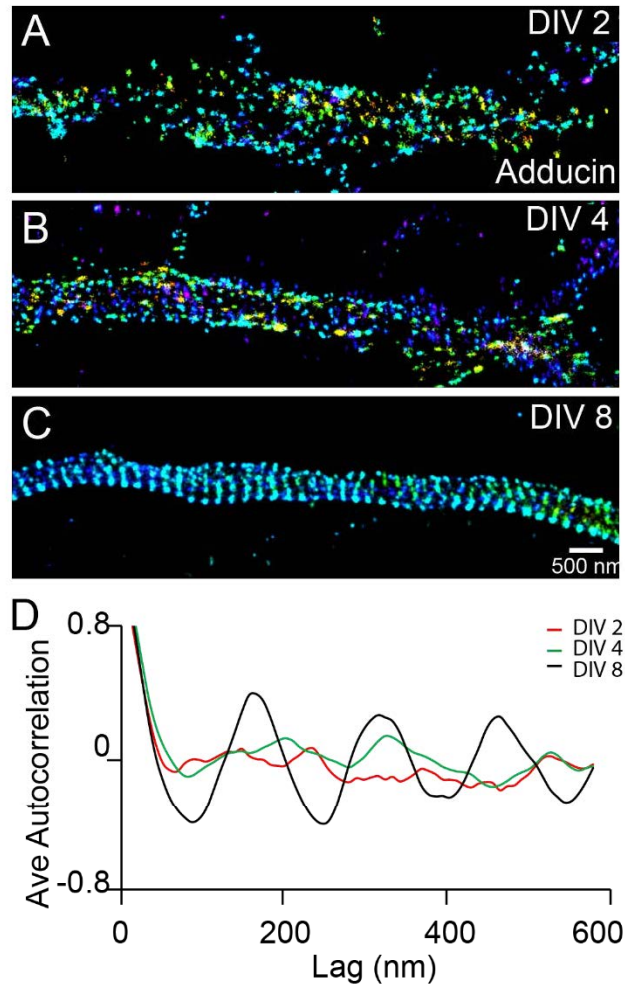


**Figure 4.5. Recruitment of adducin into the periodic lattice structure during development.** A-C) Neurons were immunostained for adducin and imaged by 3D STORM. Shown here are representative images of adducin at proximal axonal regions from DIV 2, 4 and 8 neurons. D) Average autocorrelation analyses of adducin at proximal regions of axons near the cell body. The autocorrelation curves are averaged from multiple neurons ( $n = 5$  neurons for DIV 2;  $n = 7$  neurons for DIV 4;  $n = 6$  neurons for DIV 8; from 3 independent experiments at each DIV).

#### 4.2.4 Assembly of axon initial segment components into the periodic membrane skeleton during late development stages

As neurons further mature, axon initial segment (AIS) starts to assemble at the axonal region proximal to the cell body. Ankyrin G is the master regulating protein for AIS assembly, and recruits other



molecular components such as  $\beta$ IV spectrin and sodium channels to the AIS [132, 217, 218]. Next, we examined whether  $\beta$ IV spectrin and ankyrin G were also recruited to the periodic membrane skeleton and, if so, during which developmental stage these components were incorporated.

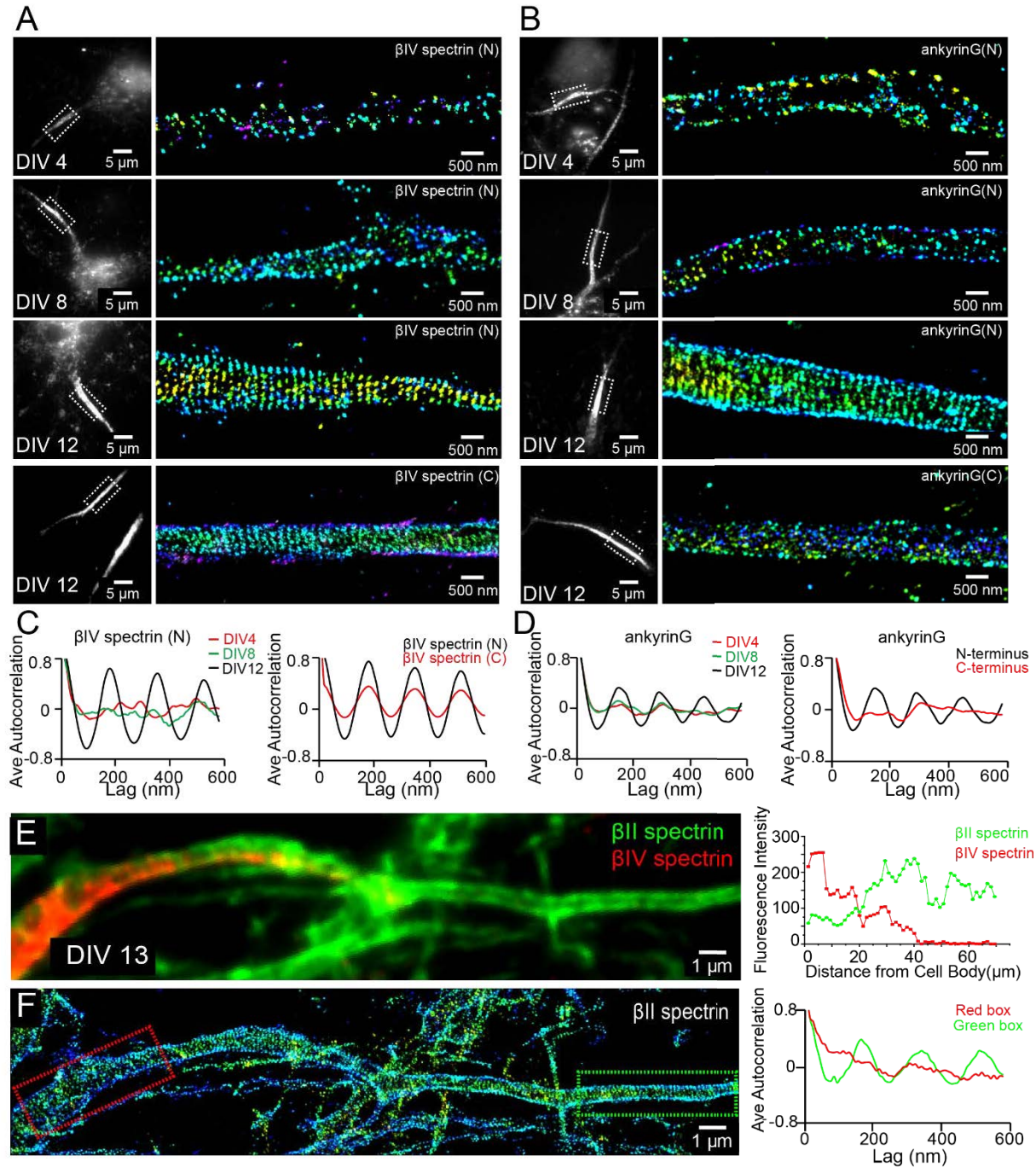


**Figure 4.6. Assembly of AIS components into the periodic lattice structure during late developmental stages.** A, B) Neurons were immunostained with antibodies against  $\beta$ IV spectrin N-

**Figure 4.6. (continued)** terminus ( $\beta$ IV spectrin (N)),  $\beta$ IV spectrin C-terminus ( $\beta$ IV spectrin (C)), ankyrin G spectrin-binding domain (ankyrin G (N)), or ankyrin G C-terminus (ankyrin G (C)), and imaged at various DIVs by 3D STORM. Representative conventional images and STORM images from the boxed region at different developmental stages are shown. C) Left: Average autocorrelation analyses of  $\beta$ IV spectrin N-terminus from neurons at different developmental stages ( $n = 9$  neurons for DIV 4;  $n = 12$  neurons for DIV 8;  $n = 16$  neurons for DIV 12; at least 3 independent experiments at each DIV). Right: Average autocorrelation analyses of  $\beta$ IV spectrin N-terminus and C-terminus of DIV 12 neurons ( $n = 13$  neurons for N-terminus and  $n = 15$  neurons for C-terminus, 3 independent experiments). D) Left: average autocorrelation analyses of ankyrin G spectrin-binding domain (near N-terminus) from neurons at different developmental stages ( $n = 12$  neurons for DIV4;  $n = 15$  neurons for DIV 8;  $n = 14$  neurons for DIV 12; at least 3 independent experiments at each DIV). Right: Average autocorrelation analysis of ankyrin G N-terminus and C-terminus of DIV 12 neurons ( $n = 9$  neurons for N-terminus and  $n = 10$  neurons for C-terminus, 3 independent experiments). E, F) A DIV 13 neuron was immunostained with  $\beta$ IV and  $\beta$ II spectrin antibodies.  $\beta$ II spectrin was subjected for 3D STORM imaging. E) Left: conventional image of  $\beta$ II and  $\beta$ IV spectrin in axon. Right: fluorescent intensity profile of  $\beta$ II and  $\beta$ IV spectrin along the axon. F) Left: STORM image of  $\beta$ II spectrin in the same region. Right: autocorrelation analyses of  $\beta$ II spectrin from red and green boxed-regions.

We labeled ankyrin G using an antibody against its spectrin-binding domain near the N-terminus, and  $\beta$ IV spectrin using an antibody against its N-terminal domain. Both ankyrin G and  $\beta$ IV spectrin signals were weak during early developmental stages, and the signals became stronger in the proximal region of axons at DIV 8 (data not shown). Notably, the expression level of  $\beta$ II spectrin remained high throughout the axons during this time (data not shown). At this time, the distributions of ankyrin G and  $\beta$ IV spectrin were not periodic (Figure 4.6A-D), in contrast to the highly periodic  $\beta$ II spectrin in the proximal region of axons (Figure 4.2). Over time, both ankyrin G and  $\beta$ IV spectrin signals further increased in the proximal region of axons, and by DIV 12, the N-terminal domains of both ankyrin G and  $\beta$ IV spectrin adopted highly periodic distributions, indicating that these molecules were incorporated into the periodic lattice structure (Figure 4.6A-D). Interestingly, the periodicity was substantially less pronounced for the C-terminal domain of  $\beta$ IV spectrin and undetectable for the C-terminal domain of ankyrin G (Figure 4.6A-D). These results suggest that the N-terminal regions of these molecules were tightly incorporated in the periodic lattice structure, but their C-terminal regions were likely hanging off from the lattice structure and moving relatively freely. Notably, as ankyrin G and  $\beta$ IV spectrin became incorporated into the periodic lattice, we observed a decrease in the local concentration of  $\beta$ II spectrin at the AIS (Figure 4.6 E and data not shown). The decrease of the  $\beta$ II spectrin concentration was associated



with a loss of periodicity for  $\beta$ II spectrin at AIS (Figure 4.6F), suggesting that as  $\beta$ IV spectrin was incorporated into the periodic structure in the AIS region,  $\beta$ II spectrin was displaced.

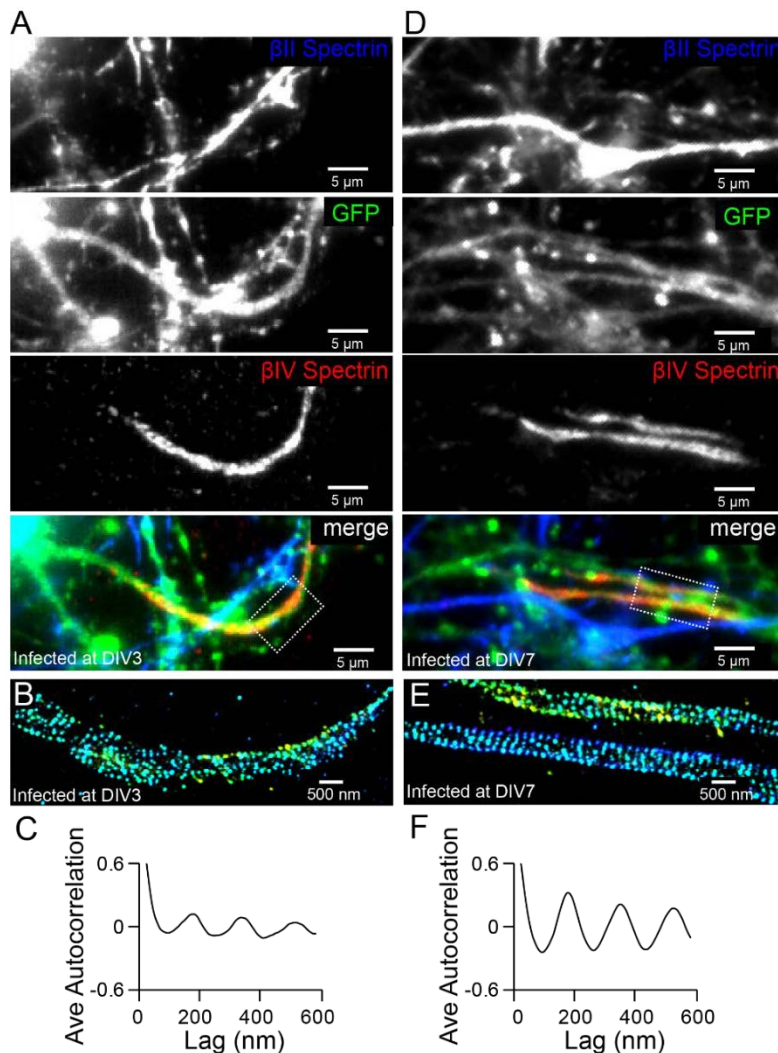


**Figure 4.7. The formation of the periodic  $\beta$ IV spectrin structure in the AIS is dependent on  $\beta$ II spectrin.** A) Neurons were infected with  $\beta$ II spectrin-shRNA expressing adenovirus at DIV 3, and subsequently stained for  $\beta$ II spectrin and  $\beta$ IV spectrin at DIV 12.  $\beta$ IV spectrin was subjected for STORM imaging. Infected neurons have a GFP signal. The conventional images of  $\beta$ II spectrin, GFP and  $\beta$ IV spectrin and the overlay image are shown. Efficient knockdown is demonstrated by lack of  $\beta$ II spectrin in GFP-positive process. B) STORM image of  $\beta$ IV spectrin from boxed region in A). C) Average autocorrelation analysis of  $\beta$ IV spectrin from  $\beta$ II spectrin knockdown neurons ( $n = 11$  neurons, 3 independent experiments). D-F) Similar to A-C) except that the virus was added at DIV 7 ( $n = 9$  neurons, 4 independent experiments).

To test whether the assembly of  $\beta$ IV spectrin into the periodic structure may rely on  $\beta$ II spectrin, we knocked down  $\beta$ II spectrin at various DIVs using a shRNA-expressing adenovirus, which also

expressed GFP, and subsequently imaged  $\beta$ IV spectrin at DIV12. The efficiency of knockdown was demonstrated by a lack of  $\beta$ II spectrin signal in virus-infected, GFP-positive neurons (Figure 4.7). When infected by the virus at DIV 3, the enrichment of  $\beta$ IV spectrin in the AIS region appeared partially impaired by  $\beta$ II spectrin knockdown, though at least 60% of the neurons still exhibited enrichment of  $\beta$ IV spectrin in AIS. For these neurons, the periodicity of  $\beta$ IV spectrin was also partially disrupted in the  $\beta$ II spectrin-depleted neurons (Figure 4.7A-C), indicating that  $\beta$ II spectrin is important for the periodic assembly of  $\beta$ IV spectrin. On the other hand, when neurons were infected with the virus at DIV 7,  $\beta$ IV spectrin remained periodic even though  $\beta$ II spectrin was depleted (Figure 4.7 D-F). Because it takes several days for pre-existing  $\beta$ II spectrin molecules to degrade [219], it is likely that  $\beta$ IV spectrin was already incorporated into the periodic lattice before the eventual depletion of  $\beta$ II spectrin when the virus was added late.

#### **4.2.5 Stability of the periodic membrane skeleton**

We next probed the dynamics of the periodic lattice structure in live neurons. To this end, we genetically fused  $\beta$ II spectrin with mMaple3, a recently developed photoactivatable fluorescent protein [220]. In neurons moderately expressing  $\beta$ II spectrin-mMaple3, the periodic pattern of  $\beta$ II spectrin-mMaple3 was readily observable in axons and the spacing of  $\sim 190$  nm was identical to that observed for endogenous  $\beta$ II spectrin in fixed neurons (Figure 4.8A). The periodic pattern was smeared in neurons with high expression levels of  $\beta$ II spectrin-mMaple3, presumably by the excess, freely diffusing  $\beta$ II spectrin-mMaple3 molecules that were not incorporated into the lattice structure.

The periodic  $\beta$ II spectrin pattern appeared to be mostly static. Fourier analysis of the patterns showed that the spatial frequency (i.e. the period) of the structure did not change over the imaging time of several minutes (Figure 4.8B). Cross-correlation analysis of the patterns taken at different time points showed no phase shift of the periodic structure during the imaging time (Figure 4.8C).

As an alternative approach to probe the stability of the structure, we used fluorescence recovery after photobleaching (FRAP). For this analysis, we transfected neurons with a  $\beta$ II spectrin-GFP fusion construct, bleached the GFP signal in local regions of axons, and measured the signal recovery rate. In neurons that exhibited moderate expression levels of  $\beta$ II spectrin, where the majority of  $\beta$ II spectrin-GFP molecules were incorporated into the periodic lattice structure (data not shown), the recovery rate was extremely slow and essentially undetectable after 30 minutes (Figure 4.8D). In contrast, the fluorescence recovery was much faster (75% recovery in 5 minutes) in neurons where the expression level of  $\beta$ II spectrin-GFP was high and the majority of  $\beta$ II spectrin-GFP molecules were not incorporated into the periodic structure (Figure 4.8E and data not shown). These data indicate that periodic lattice structure was highly stable in live neurons.

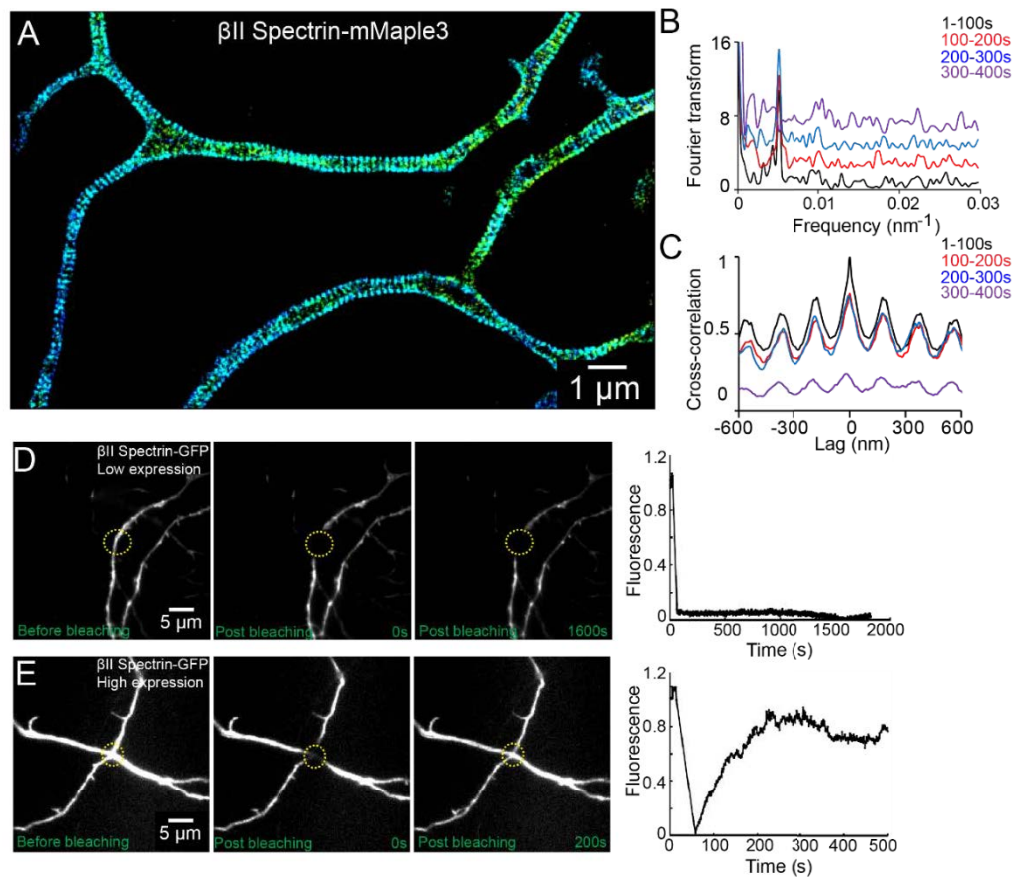


**Figure 4.8. The periodic lattice structure is stable in live neurons.** A) 3D STORM image of  $\beta$ II spectrin-mMaple3 in live neurons at DIV 10. B) The STORM movie was segregated into four different time windows. Fourier transform analysis of each time window is shown. The baseline of Fourier traces is

**Figure 4.8. (continued)** shifted manually for clear visualization. C) Cross-correlation analysis of  $\beta$ II spectrin across different time windows. The black curve is the autocorrelation of the image during 0-100 s. The color curves are the cross-correlation between 0-100 s and later time windows. Similar results were found in 6 independent experiments. D-E) FRAP analyses of  $\beta$ II spectrin in DIV 10 neurons. Neurons were transfected with  $\beta$ II spectrin-GFP at DIV 8. D) Representative neurons at a low  $\beta$ II spectrin expression level, where  $\beta$ II spectrin-GFP molecules were incorporated into the periodic structure. The images before photo-bleaching, 0 s post-bleaching, 1600 s post-bleaching and the fluorescence recovery trace is shown. E) The fluorescence recovery of representative neurons with a high  $\beta$ II spectrin expression level, where most  $\beta$ II spectrin-GFP molecules were not incorporated into the periodic structure. Similar results were found in more than 8 independent experiments.

#### 4.2.6 Microtubule dependence of the periodic membrane skeleton

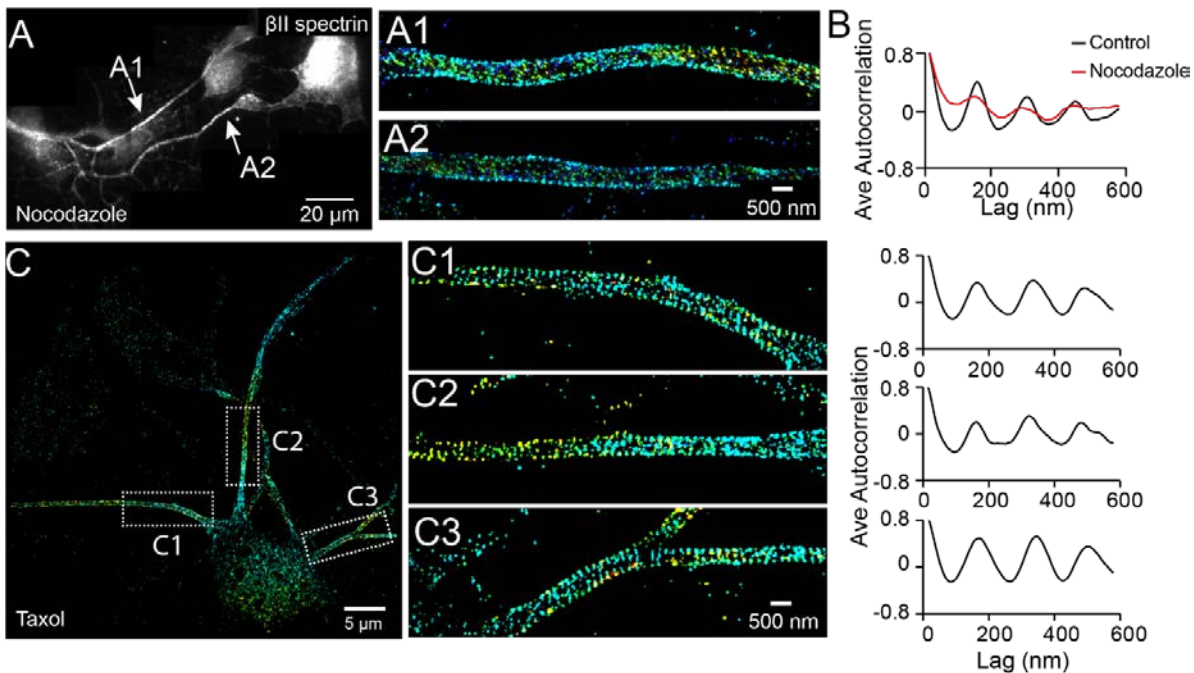


**Figure 4.9. The periodic structure of  $\beta$ II spectrin relies on intact microtubules.** A, B) DIV 4 neurons were either untreated or treated with nocodazole (50 $\mu$ M) for 1 hour, and immunostained with  $\beta$ II spectrin antibody for 3D STORM. A reconstructed neuron image from nocodazole-treated neurons, and two STORM images are shown in A. B) Average autocorrelation analyses of  $\beta$ II spectrin from multiple control and nocodazole-treated neurons ( $n = 9$  neurons for control and  $n = 8$  neurons for nocodazole-treated conditions; from 3 independent experiments for each condition). C) Neurons were treated with taxol (5 nM) at DIV 3 for three days, which induces the growth of multiple axon-like processes. A representative STORM image of a treated neuron at DIV 6, the enlarged images of the boxed regions, and the autocorrelation analyses ( $n = 10$  neurons, 4 independent experiments) are shown.

Microtubules are essential for the establishment of neuronal polarity. Local stabilization of microtubules is sufficient to induce axon formation [221]. Moreover, tubulin binds to ankyrin B, a molecule that also interacts with  $\beta$ II spectrin [222]. We thus tested whether microtubules play a role in the formation of the periodic membrane skeleton structure. In neurons treated with the microtubule-disrupting

drug nocodazole (50  $\mu$ M for 1 hour), the periodic pattern of  $\beta$ II spectrin was largely disrupted (Figure 4.9A and 4.9B). On the other hand, when microtubules were stabilized with taxol (5 nM for 3 days), a treatment that is known to induce multiple axon-like processes in neurons [221], we found that  $\beta$ II spectrin exhibited a periodic pattern in all of these axon-like processes (Figure 4.9C). We also treated neurons with SB 216763, a drug that stabilizes microtubules and promotes axonal growth by inhibiting glycogen synthase kinase-3 beta (GSK-3 $\beta$ ) [223, 224]. Similarly, in neurons treated with SB-216763, we observed that the periodic lattice structure was formed in multiple axon-like long processes (data not shown).

#### 4.2.7 Role of Ankyrin B in the periodic membrane skeleton

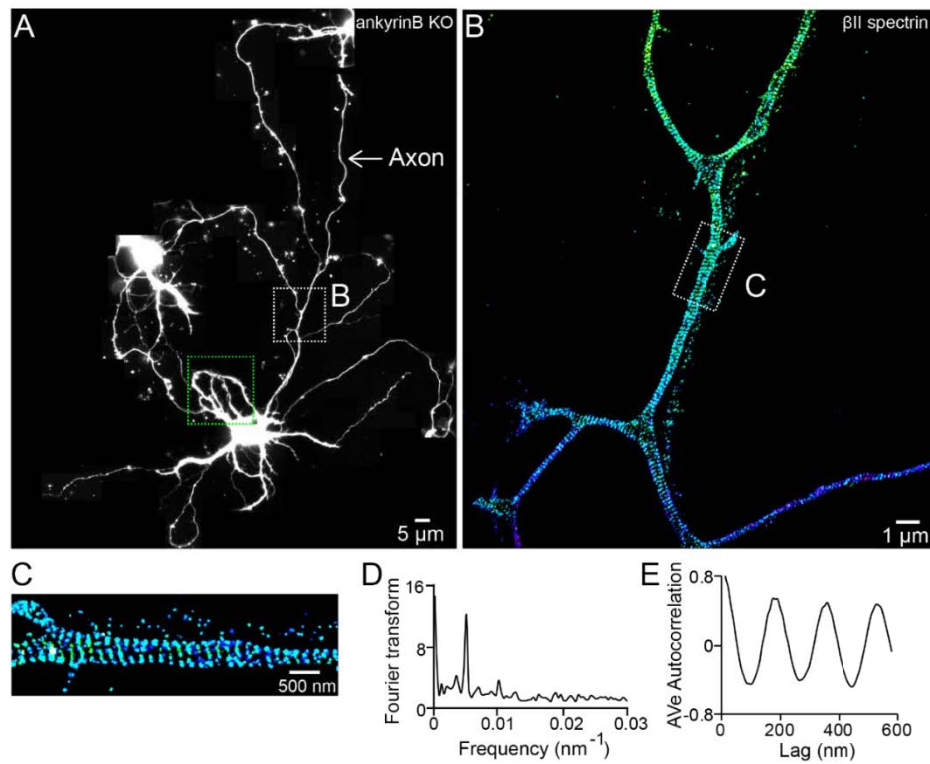


**Figure 4.10. The  $\beta$ II spectrin structure in axons of ankyrin B KO neurons.** A) Reconstructed image of an ankyrin B KO DIV 10 neuron.  $\beta$ II spectrin was subjected for 3D STORM image in both dendrites and axons. The STORM image of dendrites in green-boxed region is shown in Figure 4.11. The STORM image of axon in white-boxed region is shown in B). C) Enlarged STORM image of the boxed region in B). D-E) Fourier transform and autocorrelation analyses of the axon segment shown in C).



Given the different actin-spectrin organizations in axons and dendrites, an interesting question arises as to what molecular factors are critical for promoting the preferential formation of the highly regular, periodic lattice structure in axons. Ankyrin B (ANK 2) is a molecule that binds to  $\beta$ II spectrin [129]. It is highly enriched in axons [225-227], and recently found to be potentially linked with autism [220, 228]. We have shown previously that ankyrin B also adopts a partially periodic pattern in axons albeit with a lower regularity [149], potentially due to an incomplete occupancy of the ankyrin B binding sites on the lattice structure and the presence of ankyrin B on intracellular membranes [129]. We thus asked whether ankyrin B is involved in regulating the formation of this periodic membrane skeleton in axons.

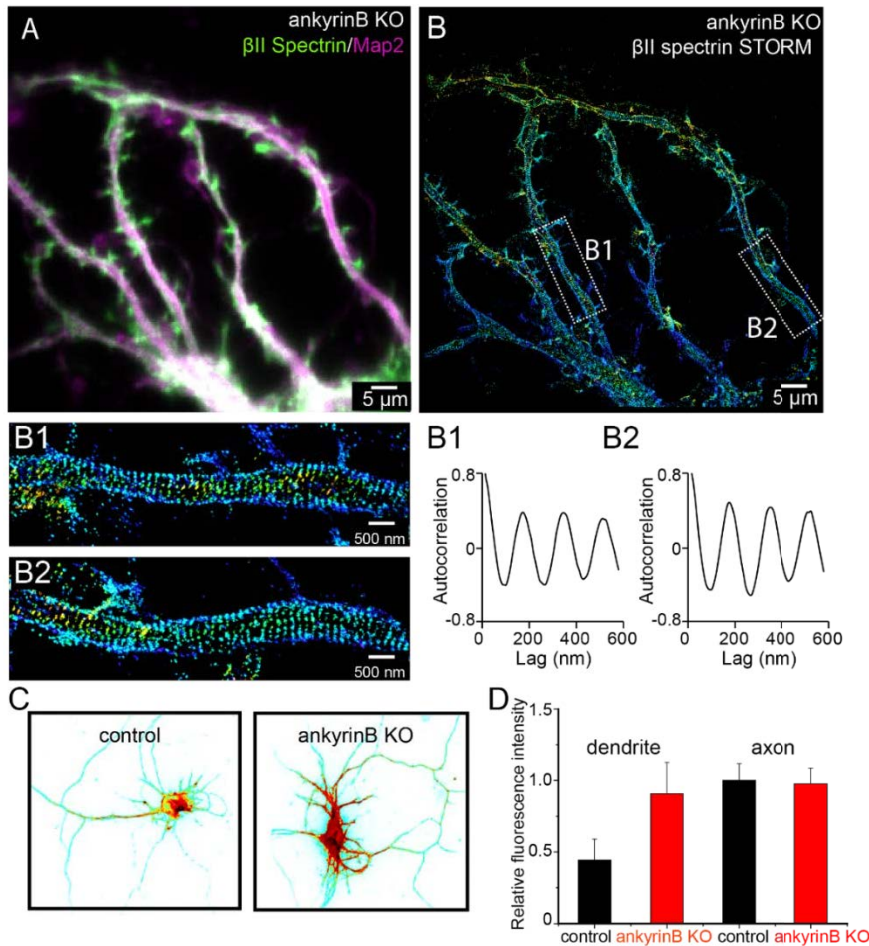


**Figure 4.11. Role of ankyrin B in the regulation of the periodic lattice structure.** A-B) DIV 10 neurons from ankyrin B knockout (KO) mice were immunostained for  $\beta$ II spectrin and a dendritic marker Map2, and imaged. (A) Conventional image of  $\beta$ II spectrin and Map2. (B) 3D STORM of  $\beta$ II spectrin.

**Figure 4.11. (continued)** The image is taken from the green-boxed region of the neuron in Figure 4.10. The enlarged STORM image and autocorrelation analyses of boxed regions are shown in B1) and B2). Similar results were found in 4 independent experiments. C) Conventional  $\beta$ II spectrin image from wild type (control) and ankyrin B KO DIV 10 neurons. The fluorescence intensity is coded by color, with red indicating higher expression. D) The relative fluorescence intensity of  $\beta$ II spectrin in dendrites and axons of wild type and ankyrin B KO neurons (n = 14 neurons for wild type and n = 13 neurons for ankyrin B KO; 3 independent experiments).

To address this question, we performed STORM imaging on dissociated hippocampal neurons from ankyrin B knockout mice [229] at DIV 10. Similar to wild type neurons, ankyrin B knockout neurons still showed enrichment of MAP2 in dendrites with similar dendritic morphology, making dendrites easy to identify in these neurons (Figure 4.10 and 4.11). The periodic pattern of  $\beta$ II spectrin in axons were not perturbed by ankyrin B deletion and appeared quantitatively similar to that observed in control wild type neurons (Figure 4.10). Surprisingly,  $\beta$ II spectrin also adopted a highly regular, periodic distribution in all dendrites, with the periodicity quantitatively similar to that observed in axons (Figure 4.11A and 4.11B). This is in contrast to what we observed in wild type neurons, where only a small fraction of dendrites have isolated patches of the periodic structure (Figure 4.3). The actin capping protein adducin also adopted a periodic distribution in dendrites of ankyrin B knockout neurons, with quantitatively similar periodicity to that of  $\beta$ II spectrin. Knocking down  $\beta$ II spectrin disrupted the periodic distribution of adducin, indicating that the periodic lattice structure in the dendrites of the ankyrin B knockout neurons also depended on  $\beta$ II spectrin (Figure 4.12). These data indicate that the formation of the periodic membrane skeleton does not require ankyrin B. Instead, ankyrin B is important for inhibiting the formation of this periodic lattice structure in dendrites.

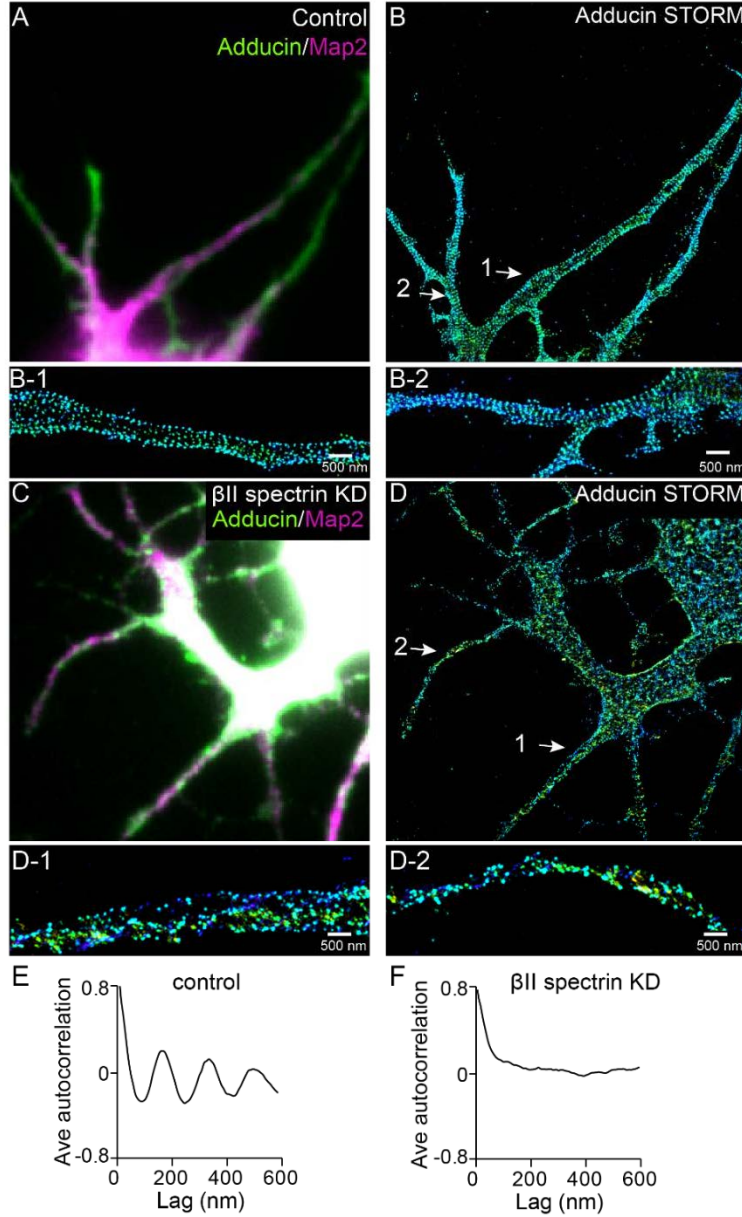


**Figure 4.12. Formation of the periodic lattice structure in dendrites of ankyrin B knockout neurons depends on  $\beta$ II spectrin.** A-B) Ankyrin B knockout neurons were immunostained for adducin (green) and MAP2 (magenta), and imaged by conventional (A) and 3D STORM (B) microscopy. Magnified STORM images of adducin for arrow-indicated regions are shown in B-1) and B-2). C-D) Ankyrin B knockout neurons were infected with  $\beta$ II spectrin-shRNA expressing adenovirus, and immunostained for adducin and MAP2, and imaged by conventional (C) and 3D STORM (D) microscopy. Infected neurons were marked by GFP signal expressed from the virus (not shown). Magnified STORM images of adducin from arrow indicated region are shown in D-1) and D-2). E) Average autocorrelation analysis of adducin distribution in dendrites of ankyrin B knockout neurons (n = 9 neurons, 4 independent experiments). F) Average autocorrelation analysis of adducin distribution in dendrites of ankyrin B knockout neurons treated with  $\beta$ II spectrin-shRNA expressing adenovirus (n = 15 neurons, 3 independent experiments).



#### **4.2.8 Local $\beta$ II spectrin concentration regulates the formation of this periodic lattice structure and ankyrin B regulates the polarized distribution of $\beta$ II spectrin in neurites**

In addition to the induction of the periodic lattice structure in dendrites, we noticed that ankyrin B knockout also induced a dramatic redistribution of  $\beta$ II spectrin in neurites. In wild type neurons, the local concentration of  $\beta$ II spectrin, as indicated by immunofluorescence intensity, was  $\sim$ 2-fold higher in axons than that in dendrites (Figure 4.11C and 4.11D), consistent with previous results [133, 134]. However, the expression level of  $\beta$ II spectrin was substantially increased in dendrites by the ankyrin B knockout to a point that the local concentration of  $\beta$ II spectrin in dendrites became indistinguishable from that in axons, and both were comparable to the  $\beta$ II spectrin concentration observed in wild type axons (Figure 4.11C and 4.11D). We thus hypothesized that the increased local concentration of  $\beta$ II spectrin caused the formation of this periodic lattice structure in dendrites.

To test this hypothesis, we increased the expression level of  $\beta$ II spectrin in all neurites by transiently transfecting neurons with a HA-tagged  $\beta$ II spectrin construct, and performed STORM imaging on  $\beta$ II spectrin in transfected neurons at DIV 11. As expected, the local concentration of  $\beta$ II spectrin in the dendrites of  $\beta$ II spectrin-HA expressing neurons was higher than that observed in control neurons that did not express  $\beta$ II spectrin-HA (Figure 4.13A-C). Remarkably, whereas a small fraction of dendrites from control neurons had isolated patches of periodic  $\beta$ II spectrin (Figure 4.13D and 4.13E), in  $\beta$ II spectrin-HA overexpressing neurons,  $\beta$ II spectrin displayed a periodic pattern in nearly all dendritic processes (Figure 4.13F and 4.13G). Autocorrelation analysis showed that the periodicity in the dendrites of overexpressing neurons was substantially enhanced compared to the dendrites of control neurons (Figure 4.13H).

Taken together, these data suggest that the local concentration of  $\beta$ II spectrin is a key determining factor for the preferential formation of the periodic membrane skeleton in axons and that ankyrin B was critical for setting the polarized distribution of  $\beta$ II spectrin in axons and dendrites.

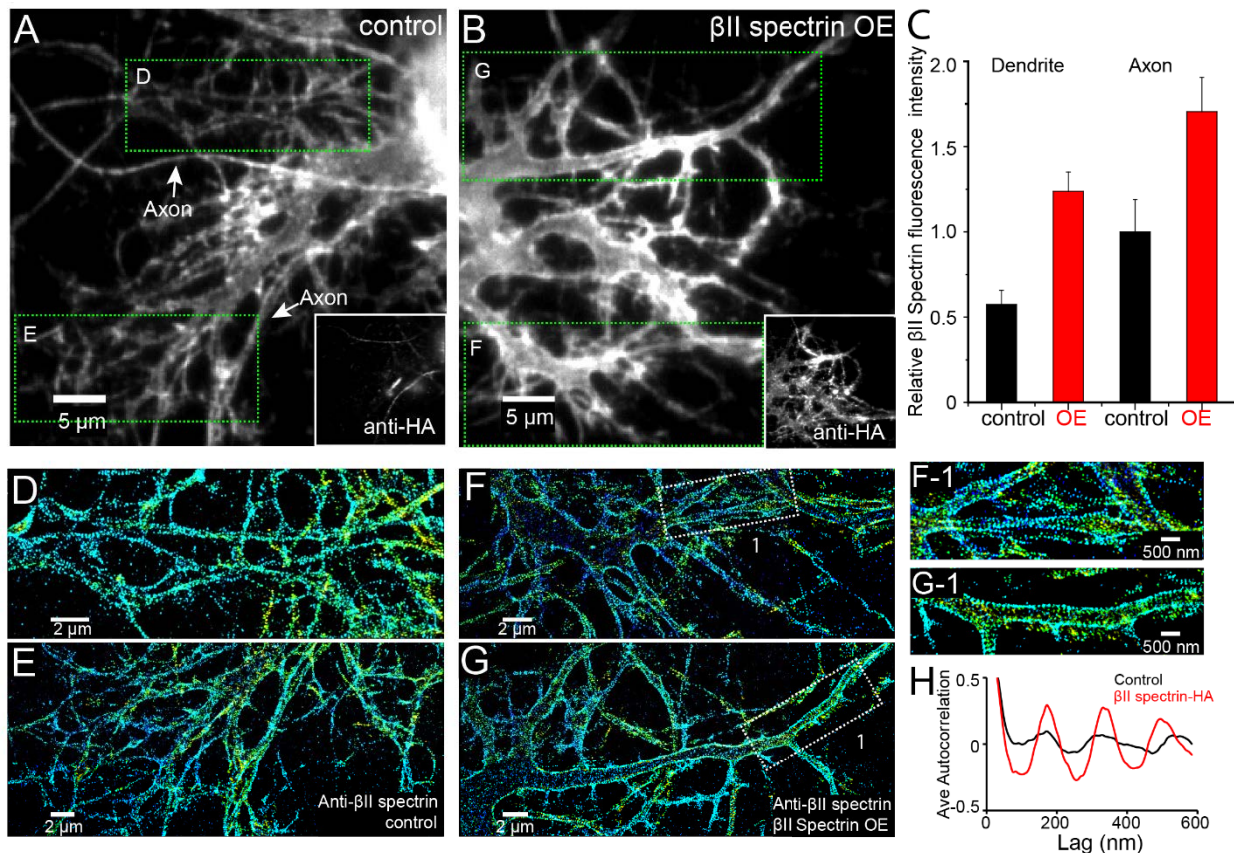


**Figure 4.13. Local  $\beta$ II spectrin concentration determines the formation of the periodic lattice structure.** DIV 9 neurons were either mock-transfected or transfected with  $\beta$ II spectrin-HA, and immunostained for HA and  $\beta$ II spectrin.  $\beta$ II spectrin were subsequently imaged by 3D STORM. A-B) Conventional images of  $\beta$ II spectrin in dendrites of a control neuron and a  $\beta$ II spectrin-HA overexpressing (OE) neuron. The HA image is shown in the insets. C) The relative fluorescence intensity for  $\beta$ II spectrin in dendrites and axons of control and  $\beta$ II spectrin-HA overexpressing neurons ( $n = 10$  neurons for control and  $n = 15$  neurons for  $\beta$ II spectrin-HA overexpressing conditions; from 3 independent experiments for each condition). D-E) STORM images of  $\beta$ II spectrin from green-boxed regions in A. F-G) STORM images of  $\beta$ II spectrin from green-boxed regions in B. F-1) and G-1) are enlarged images of the white-boxed regions in F and G respectively. H) Average autocorrelation analyses of  $\beta$ II spectrin in dendrites of control and  $\beta$ II spectrin-HA overexpressing neurons ( $n = 8$  neurons for control and  $n = 12$  neurons for  $\beta$ II spectrin-HA overexpressing conditions; from 3 independent experiments for each condition).

#### 4.3 Discussion

Actin, spectrin and associated molecules form a periodic lattice structure with long-range order preferentially underneath the axonal membrane. Many molecular components, including actin,  $\beta$ II spectrin, adducin, ankyrin B,  $\beta$ IV spectrin, ankyrin G and sodium channels, are present in this structure.

We have observed this periodic membrane skeleton with STORM imaging of fixed cultured neurons (Figure 4.1 and 4.2) and fixed brain tissue slices [149] using actin-binding phalloidin and immunolabeling

of endogenously expressed proteins, as well as in live cultured neurons using fluorescent fusion proteins (Figure 4.8). Recently, this periodic structure has also been observed in live neurons using a cell-permeable actin-binding dye and STED imaging [230]. Since a single actin filament can interact with multiple spectrin tetramers, and a single spectrin tetramer can bind to two actin filaments, one at each end of the symmetric tetramer [129], we reason that these crosslinking interactions are responsible for the formation of the lattice structure. Indeed, depolymerizing actin filaments disrupted the periodic distribution of  $\beta$ II spectrin, and knocking down of  $\beta$ II spectrin disrupted the periodic distribution of actin (data not shown). Because this lattice structure is associated with the axonal membrane, proper preservation of the membrane structure is essential for observing this structure. For example, a recent electron microscopy study of the AIS in neurons that has been subjected to detergent extraction of membrane before fixation did not show such periodic membrane skeleton [231]. Indeed when we applied the same “fixation after membrane extraction” protocol to neurons, the structure was destroyed and not observed in STORM images (data not shown). In this study, we investigated the developmental mechanism of this newly discovered axonal membrane skeleton.

We found that this periodic membrane skeleton started to form early during axon development. In stage 3 neurons at DIV 2, when one neurite just broke the symmetry and became an axon (typically several times longer than other neurites), the periodic pattern of  $\beta$ II spectrin already emerged (Figure 4.2). It originated in the proximal axon regions near the cell bodies and gradually propagated to the distal ends of axons (Figure 4.2). This spatial distribution is in contrast to most previously identified signaling molecules involved in axon differentiation and development, which are enriched and function at the growing tip of axons [123, 124, 212, 213]. After its initial appearance, the lattice structure continued to mature with the actin filaments becoming more stable, potentially because of capping by adducin (Figures 4.4, 4.5). Once matured, the structure appeared highly stable with little movement and extremely slow turnover of its molecular components was observed in live neurons (Figure 4.8). This highly stable

membrane skeleton may function to provide a stable mechanical support for axons. Indeed, deletion of  $\beta$  spectrin from *C elegans* causes axons to break when the animals move [142].

The emergence of this periodic lattice during early axon development and its origination in the proximal axon region near the cell body suggest that the periodic membrane skeleton may function as an independent mechanism for establishing or maintaining neuronal polarization in addition to the previously identified pathways that function at the distal ends of axons. However, the periodic membrane skeleton is not required for the initiation of axon differentiation because the periodic structure only started to form in stage 3, but not stage 2, a stage at which most signaling molecules for axon initiation exhibit high activity [212, 213]. Moreover, neurons depleted of  $\beta$ II spectrin are also capable of forming long axons [134], though these axons may not fully functional. Indeed, removal of  $\alpha$ II or  $\beta$ II spectrin is embryonically lethal in mice [143, 144] and AIS, the structure important for action potential generation, fails to assemble properly in neurons that are depleted of  $\beta$ II spectrin [134].

Interestingly, molecules important for the specification of AIS, ankyrin G,  $\beta$ IV spectrin, and sodium channels, were all incorporated into this periodic membrane skeleton. During the early stages of axon development, the expression levels of ankyrin G and  $\beta$ IV spectrin were low in the proximal axon region, which was instead occupied by the periodic lattice comprising  $\beta$ II spectrin (Figure 4.2). Ankyrin G and  $\beta$ IV spectrin began to enrich in the proximal axon region later during axon development, at  $\sim$ DIV 8 (data not shown), consistent with previous observations [134]. The incorporation of ankyrin G and  $\beta$ IV spectrin into the periodic lattice was observed even later, at around DIV 12, replacing  $\beta$ II spectrin from the structure in the AIS (Figure 4.6). The enrichment and periodic assembly of the AIS components appeared to depend on  $\beta$ II spectrin (Figure 4.7). Our data suggest the following developmental course for the AIS formation. Before the AIS is formed, actin and  $\beta$ II spectrin form a cohesive periodic lattice structure that covers the entire axonal shaft including the proximal axonal region. The AIS then forms by the enrichment of ankyrin G and  $\beta$ IV spectrin in the proximal axonal region and the replacement of  $\beta$ II spectrin by  $\beta$ IV spectrin in the periodic membrane skeleton. Potentially, ankyrin G, the master regulator

of AIS that recruits other AIS components [132, 217, 218], is first enriched in the proximal axon region. Ankyrin G then recruits  $\beta$ IV spectrin to the same region and causes it to be incorporated in the periodic lattice.  $\beta$ IV spectrin in turn anchors ankyrin G into a periodic pattern as well. As an adaptor, ankyrin G then places sodium channels into a periodic distribution pattern in the AIS.

Finally, we addressed the question why the cohesive, periodic lattice structure preferentially formed in axons, with a small fraction of dendrites showed isolated patches of periodic structure with much less regularity (Figure 4.3). We found multiple molecular factors participate in this regulation. The periodic lattice structure depended on intact microtubules. Treatment with a microtubule-depolymerizing drug disrupts the structure in axons, whereas treatment with microtubule-stabilizing drugs induces the formation of the lattice structure in multiple neurites (Figure 4.9). Importantly, we found that the local concentration of  $\beta$ II spectrin is a determining factor for the formation of the lattice structure. The local concentration of  $\beta$ II spectrin is  $\sim 2$  times higher in axons than in dendrites (Figure 4.11). Remarkably, increasing the dendritic concentration of  $\beta$ II spectrin by over-expression induced the formation of the periodic lattice structure in all dendrites (Figure 4.13). Interestingly, ankyrin B was critical for maintaining the polarized distribution of  $\beta$ II spectrin. Knocking out ankyrin B led to an even distribution of  $\beta$ II spectrin in dendrites and axons and the formation of a highly regular and cohesive periodic lattice structure in all dendrites (Figure 4.11). Consistent with the notion that the increased concentration of  $\beta$ II spectrin in dendrites is responsible for inducing the formation of the periodic lattice structure in dendrites, knocking down  $\beta$ II spectrin from ankyrin B knockout neurons disrupted the lattice structure (Figure 4.12). These results indicate that ankyrin B is critical for establishing a polarized distribution of  $\beta$ II spectrin in neurites with a higher concentration of  $\beta$ II spectrin in axons than in dendrites, which in turn promotes the formation of the periodic membrane skeleton in axons.

It is interesting to speculate how ankyrin B may establish such a polarized distribution of  $\beta$ II spectrin. The predominant form of ankyrin B during early neuronal development is a 440 kDa splice variant that is preferentially targeted to axons [225, 227, 232]. Given that ankyrin B specifically binds to

$\beta$ II spectrin, we speculate that the distribution of ankyrin B in axons may help establishing the enrichment of  $\beta$ II spectrin in axons during early neuronal development. Moreover, Lorenzo and colleagues recently found that ankyrin B is a major cargo adaptor for dynactin and promotes axonal transport of proteins and organelles and that disruption of ankyrin B-dynactin interaction significantly impairs the axonal transport of many proteins [233]. It is thus possible that ankyrin B may also preferentially transport  $\beta$ II spectrin into axons instead of dendrites. By maintaining a polarized distribution of  $\beta$ II spectrin in neurons, ankyrin B functions as a negative regulator for preventing the formation of the periodic membrane skeleton in dendrites. The exact mechanism by which ankyrin B maintains a polarized distribution of  $\beta$ II spectrin remains an interesting question for future investigation.

#### **4.4 Materials and Methods**

All experimental procedures were performed in accordance with the Guide for the Care and Use of Laboratory Animals of the National Institutes of Health. The protocol was approved by the Institutional Animal Care and Use Committee (IACUC) of Harvard University.

*Neuron culture.* Primary hippocampal cultures were prepared from wild type neonatal (E18) rat embryos (timed pregnant SD rats from Charles River Laboratories, Wilmington, MA) or ankyrin B knockout mice as reported previously [229]. Hippocampi were isolated and digested with 0.05% trypsin-EDTA (1x) (Invitrogen 25300-054) at 37°C for 15 minutes. The hippocampi were transferred to the Hib A solution (BrainBits HA-Ca), washed several times with the Hib A solution, and pipetted up and down until the tissues were mostly dissolved. The solution was then passed through a cell strainer (VWR 21008-949) to remove the residual undissociated tissue and collected in a 50 mL conical tube. Neurons were spun down to the bottom of the tube, resuspended with the culture media made of 96 mL Neurobasal (Life Technologies 12349-015), 2 mL B-27 Supplement (Life Technologies 17504-044), 1 mL Penicillin-Streptomycin (Life technologies 15140-122) and 1 mL Glutamax (Life technologies 35050-061), and then plated onto poly-L-lysine/laminin-coated 12-mm coverslips (BD bioscience BD354087) or poly-L-lysine coated 8-well chambers. 5  $\mu$ M cytosine-D-arabinofuranoside (Sigma C1768) was added to the culture

media to inhibit the growth of glial cells three days after plating. The neurons were fed twice a week with freshly made culture media until use.

*Reagent.* The following primary antibodies were used in this study: guinea pig anti-Map2 antibody (Synaptic Systems, 188002); mouse anti- $\beta$ II spectrin antibody (BD Biosciences, 612563); mouse anti-ankyrin G antibody (Santa Cruz, Sc-12719, epitope mapping the spectrin-binding domain of ankyrin G near the N-terminal); goat anti-ankyrin G antibody (Santa Cruz, Sc-31778, epitope mapping the C terminal of ankyrin G); rabbit anti-adducin antibody (Abcam, ab51130); rabbit anti-HA antibody (Abcam, ab9110); rabbit anti-GFP antibody (Abcam, ab290); goat anti- $\beta$ III spectrin (Santa Cruz, sc-9660). Rabbit antibodies targeting the C- or N-terminus of  $\beta$ IV spectrin were kind gifts from Dr. Matt Rasband at Baylor College of Medicine.

The following secondary antibodies were used in this study for conventional imaging: Alexa Fluor 647 donkey anti-mouse (Invitrogen, A31571), Alexa Fluor 555 donkey anti-mouse (Invitrogen, A31570), Alexa Fluor 488 donkey anti-mouse (Invitrogen, A21202), Alexa Fluor 647 donkey anti-rabbit (Invitrogen, A31573), Alexa Fluor 568 donkey anti-rabbit (Invitrogen, A10042), Alexa Fluor 488 donkey anti-rabbit (Invitrogen, A21206), Alexa Fluor 488 goat anti-guinea pig (Invitrogen, A11073), Alexa Fluor 647 donkey anti-goat (Invitrogen, A21447), Alexa Fluor 568 donkey anti-goat (Invitrogen, A11057).

For STORM imaging, secondary antibodies were custom-labeled with a photoswitchable reporter dye, Alexa Fluor 647, and an activator dye Alexa Fluor 405, which facilitates the photoswitching of the reporter dye. Donkey anti-mouse and donkey anti-rabbit secondary antibodies (Jackson ImmunoResearch) were each labeled with a mixture of amine-reactive activator and reporter dyes in a one-step reaction, as described previously [150]. In some experiments, commercial Alexa Fluor 647 conjugated donkey anti-mouse, anti-rabbit or anti-goat secondary antibodies were used.

*Transfection of neurons with fusion protein constructs.*  $\beta$ II spectrin-GFP and  $\beta$ II spectrin-HA plasmids (addgene, 31070) used in this study were reported previously, with GFP inserted at the N

terminal of  $\beta$ II spectrin, and the HA tag at the C terminal of  $\beta$ II spectrin respectively [134]. To make the  $\beta$ II spectrin-mMaple 3 construct, we replaced the HA tag sequence with the mMaple 3 sequence [220]. Plasmids were transfected into neurons using a calcium phosphate transfection kit from Invitrogen (K2780-01). The protocol for transfection was modified slightly for our neuronal cultures. Briefly, neurons were plated at a density of 40,000 cells/well in 12 well plates, and cultured for 6 to 10 days before the transfection. After changing media from original neuronal culture media to Minimum Essential Media (MEM, Life Technology, supplemented with 20 mM HEPES, pH 7.15), 100  $\mu$ l plasmid mixture was added, and neurons were incubated at 37 °C for 20 minutes. The media was subsequently aspirated, and replaced with a lower pH MEM (supplemented with 20 mM HEPES, pH 6.8) at 37 °C for 4 minutes. After dissolving all calcium phosphate crystals, we added back the original neuronal culture media. Experiments were performed 2 or 3 days after transfection.

*Knockdown with shRNA.* The  $\beta$ II spectrin shRNA adenoviral construct used in this study was a kind gift from Dr. Matt Rasband at Baylor College of Medicine, and described previously [234]. The two sense sequences of shRNA are: 5'-GCATGTCACGATGTTACAA-3' and 5'-GGATGAAATGAAGGTGCTA-3'. For assaying the effect of  $\beta$ II spectrin knockdown on actin and adducin structure, neurons were infected with the virus at DIV3 and fixed for STORM imaging at around DIV 9 or 10. For assaying the effect of  $\beta$ II spectrin knockdown on  $\beta$ IV spectrin structure, neurons were infected with the virus at DIV3 or DIV7, and fixed at DIV12 for STORM imaging of  $\beta$ IV spectrin. Infected neurons were marked by a GFP signal expressed from the adenoviral construct. The knockdown efficiency was validated through immunostaining against  $\beta$ II spectrin.

*Drug treatment of neurons.* The following chemicals were used in this study with their concentration and treatment time stated: latrunculin A (Sigma, L5163, 20  $\mu$ M, 1 hour or indicated time series), cytochalasin D (Sigma, C8273, 50 $\mu$ M, 1 hour), nocodazole (Sigma, M1404, 50 $\mu$ M, 1 hour), taxol (Sigma, T7402, 5nM), SB216763 (Sigma, S3442, 5 $\mu$ M). For taxol treatment, neurons were treated with the drug at DIV3 with the indicated concentration, and fixed at DIV6 for STORM imaging. For



SB216763 treatment, neurons were treated with the drug at DIV1 with the indicated concentration, and fixed at DIV5 for STORM imaging.

*Fluorescence labeling of neurons.* Cultured neuron were fixed at various days in vitro (DIV). For imaging of actin, we used a similar method to label actin as reported previously [149, 235]. Briefly, the samples were simultaneously fixed and extracted for 1 min using a solution of 0.3% (v/v) glutaraldehyde (GA) and 0.25% (v/v) Triton X-100 in cytoskeleton buffer (CB, 10 mM MES, pH 6.1, 150 mM NaCl, 5 mM EGTA, 5 mM glucose and 5 mM MgCl<sub>2</sub>), and then post-fixed for 15 min in 2% (v/v) GA in CB, a previously established protocol for maintaining actin ultrastructure [149, 235]. The GA-fixed samples were treated with freshly prepared 0.1% (w/v) sodium borohydride for 7 min to reduce background fluorescence caused by GA fixation. To label actin filaments, samples were labeled with Alexa Fluor 647 conjugated phalloidin (Invitrogen A22287) overnight at 4 °C or ~ 1 hour at room temperature. A concentration of ~0.5 μM phalloidin in PBS was used. To minimize the dissociation of phalloidin from actin during washing steps, actin labeling was performed after all other labeling steps (i.e. immunofluorescence of other molecular targets) were completed. The sample was washed 2-3 times with PBS and then immediately mounted for imaging.

To test whether strong membrane extraction prior to fixation [231] disrupts the membrane skeleton structure, neurons were extracted with 1% Triton X-100 in PEM buffer (100 mM Pipes-KOH, pH 6.9, 1 mM MgCl<sub>2</sub>, and 1 mM EGTA) containing 2% polyethylene glycol, 2 μM phalloidin, and 2 μM taxol for 3 min at room temperature after a quick rinse with the PEM buffer containing 2 μM taxol and subsequently fixed with 0.2% GA in PBS for at least 20 min, as described previously [231]. Fixed samples were treated with freshly prepared 0.2% (w/v) sodium borohydride for 5-10 min to reduce background fluorescence caused by GA fixation and washed in PBS. Actin labeling was performed similarly as described above.

For imaging of molecular components not including actin (MAP2, βII spectrin, βIII spectrin, βIV spectrin, ankyrin G and adducin), the samples were fixed using 4% (w/v) paraformaldehyde in phosphate

buffered saline (PBS) for 15 min. Fixed neuron samples were then permeabilized and blocked in blocking buffer (3% w/v bovine serum albumin or 10% w/v donkey serum, 0.2% v/v Triton X-100 in PBS) for 1 hour, and subsequently stained with primary antibodies in blocking buffer overnight at 4 °C. The samples were washed three times and then stained with secondary antibodies (described above) in blocking buffer for ~1 hour at room temperature.

*Fixed-cell STORM imaging.* The imaging buffer was PBS containing 100 mM cysteamine, 5% glucose, 0.8 mg/mL glucose oxidase (Sigma-Aldrich), and 40 µg/mL catalase (Roche Applied Science) for fixed neurons. To image the samples from 12-mm coverslips, approximately 4 µL of imaging buffer was dropped at the center of a freshly-cleaned, #1.5 rectangular coverslip (22 mm by 60 mm), and the sample on the 12-mm coverslip was mounted on the rectangular coverslip and sealed with nail polish or Cytoseal. To image samples from 8-well chambers, 400 µL of imaging buffer was added to the imaging chamber.

The STORM setup was based on an Olympus IX-71 inverted optical microscope as described previously [236]. 405-nm (CUBE 405-50C; Coherent), 460-nm (Sapphire 460-10; Coherent), 532-nm (GCL-200-I; CrystaLaser), and 657-nm (RCL-300-656; CrystaLaser) lasers were introduced into the sample through the back focal plane of the microscope. A translation stage allowed the laser beams to be shifted towards the edge of the objective so that the emerging light reached the sample at incidence angles slightly smaller than the critical angle of the glass-water interface, thus illuminating only the fluorophores within a few micrometers of the coverslip surface. A T660LPXR (Chroma) was used as the dichroic mirror and an ET705/72M band-pass filter (Chroma) was used as the emission filter. For 3-dimensional (3D) STORM imaging, a cylindrical lens was inserted into the imaging path so that images of single molecules were elongated in  $x$  and  $y$  for molecules on the proximal and distal sides of the focal plane (relative to the objective), respectively [112].

During imaging, continuous illumination of 657-nm laser ( $\sim 2$  kW/cm<sup>2</sup>) was used to excite fluorescence from Alexa Fluor 647 molecules and switched them into the dark state. Continuous

illumination of the 405-nm laser (when Alexa Fluor 405 was used as the activator dye) or 532-nm laser (when Cy3 was used as the activator dye) was used to reactivate the fluorophores to the emitting state. The power of the activation lasers (typical range 0-1 W/cm<sup>2</sup>) was adjusted during image acquisition so that at any given instant, only a small, optically resolvable fraction of the fluorophores in the sample were in the emitting state.

A typical STORM image was generated from a sequence of about 30,000~60,000 image frames at a frame rate of 60 Hz. The recorded STORM movie was analyzed according to previously described methods [105, 112]. The centroid positions and ellipticities of the single-molecule images provided lateral and axial positions of each activated fluorescent molecule, respectively [112]. Super-resolution images were reconstructed from the molecular coordinates by depicting each location as a 2D Gaussian peak.

*Live-cell STORM imaging.* Live cell STORM experiments were performed on the same STORM setup as described earlier [114, 236]. Neurons were initially transfected with  $\beta$ II spectrin-mMaple 3 at DIV8, and imaged in an extracellular solution containing: 128mM NaCl, 5mM KCl, 2mM CaCl<sub>2</sub>, 1mM MgCl<sub>2</sub>, 25mM HEPES, 30mM glucose, pH 7.3) at DIV10 or DIV11. Continuous illumination of the 405 nm laser was used to activate the mMaple 3 fluorescent protein. Continuous illumination of 561 nm laser was used to excite mMaple 3 and switched them to the dark state. Imaging analysis was performed as described above.

*FRAP analysis.* FRAP experiments were performed on the same STORM setup as described above. Neurons were transfected with  $\beta$ II spectrin-GFP at DIV8 and then imaged at DIV10. Directly before FRAP experiments, neuronal culture media was replaced with an extracellular solution. After recording an image before photo-bleaching, a small region of the sample was bleached by shrinking the size of iris at the excitation light path for 10 seconds with the maximum laser power. Subsequently, the sample was imaged using the same power as that of pre-bleached image. The image was recorded at a frequency of 1 Hz. We used the unbleached regions in the image to calibrate the photo-bleaching effect

during the entire recording time. The fluorescence recovery fraction was measured as the fluorescence intensity at the bleached region at indicated time versus the original intensity before photo-bleaching.

## **Chapter 5: The Prevalence of the Periodic Membrane Skeleton in Different Neuronal Types**

Work in this chapter was performed in collaboration with Dr. Ruobo Zhou, Monica Carrasco, and Zhuhao Wu.

## **5.1 Introduction**

The aforementioned studies in Chapter 4 were mostly performed in cultured hippocampal neurons or hippocampal tissue slices. Hippocampal neuronal cultures are primarily comprised of pyramidal cells, whereas the brain contains many different types of neurons with different morphologies, properties and functions. It remains unknown whether the periodic submembrane cytoskeletal structure is present in different neuronal types and different regions of the nervous system. For example, it is unclear whether the periodic structure is a specific property of excitatory neurons, such as the pyramidal cells, or whether similar structure also exists in inhibitory neurons. Similarly, it remains to be determined whether the structure is only present in central neurons or whether it also exists in peripheral neurons. With the axons of many neuronal types myelinated in the brain, it remains unclear whether myelination has any impact on the formation of periodic membrane skeleton.

In this study, we examined these important questions by super-resolution imaging of different types of cultured neurons. We found that the periodic membrane skeleton prevails in the axons of different neuronal types from central and periphery nervous system. For all the neuronal types we examined, the periodic membrane skeleton is preferentially formed in all axons, while a small fraction of dendrites also contain isolated patches of the lattice structure. Furthermore, myelination does not appear to impact the formation of this lattice structure in vitro. Altogether, our results suggest that the periodic membrane skeleton is highly prevalent in different neuronal types.

## **5.2 Results**

### **5.2.1 The periodic membrane skeleton is present in inhibitory neurons from the hippocampus**

To study how prevalent the periodic membrane skeleton is in different neuronal types, we cultured neurons from different mouse brain regions (central nervous system) or spinal cord (periphery nervous system), or used neurons derived from embryonic stem cells.  $\beta$ II spectrin, a core component of the periodic membrane skeleton [149, 207], was immunostained and visualized by stochastic optical

reconstruction microscopy (STORM) [105-107, 112]. The periodic membrane skeleton was initially observed in hippocampal neurons [149], most of which are excitatory neurons. To test whether the finding can be extended to additional neuronal types, we first decided to image the distribution of  $\beta$ II spectrin in inhibitory neurons from the hippocampus. Inhibitory neurons can be specifically marked by immunostaining of GAD65 or parvalbumin. Based on the neuronal morphology, we were able to distinguish the axons from dendrites. We focused on imaging axonal regions closer to the cell body, as these sites were where the periodic lattice structure forms earliest in excitatory neurons [207]. As shown in Figure 5.1, in axons of both GAD65+ and parvalbumin+ neurons,  $\beta$ II spectrin adopts a highly periodic structure, with a periodicity of around 190 nm, consistent with our previous findings [149, 207]. Nearly all the GAD65+ and parvalbumin+ neurons have the periodic structure formed in axons at DIV10 (days in vitro) (Figure 5.1), indicating that the periodic structure is highly prevalent in inhibitory neurons from the hippocampus. As compared to the periodic distribution in axons,  $\beta$ II spectrin is largely irregular in dendrites (Figure 5.1 A-2 and B-2), although a small fraction of dendrites also appeared to have isolated patches of the periodic structure, consistent to what we observed in excitatory neurons [207].

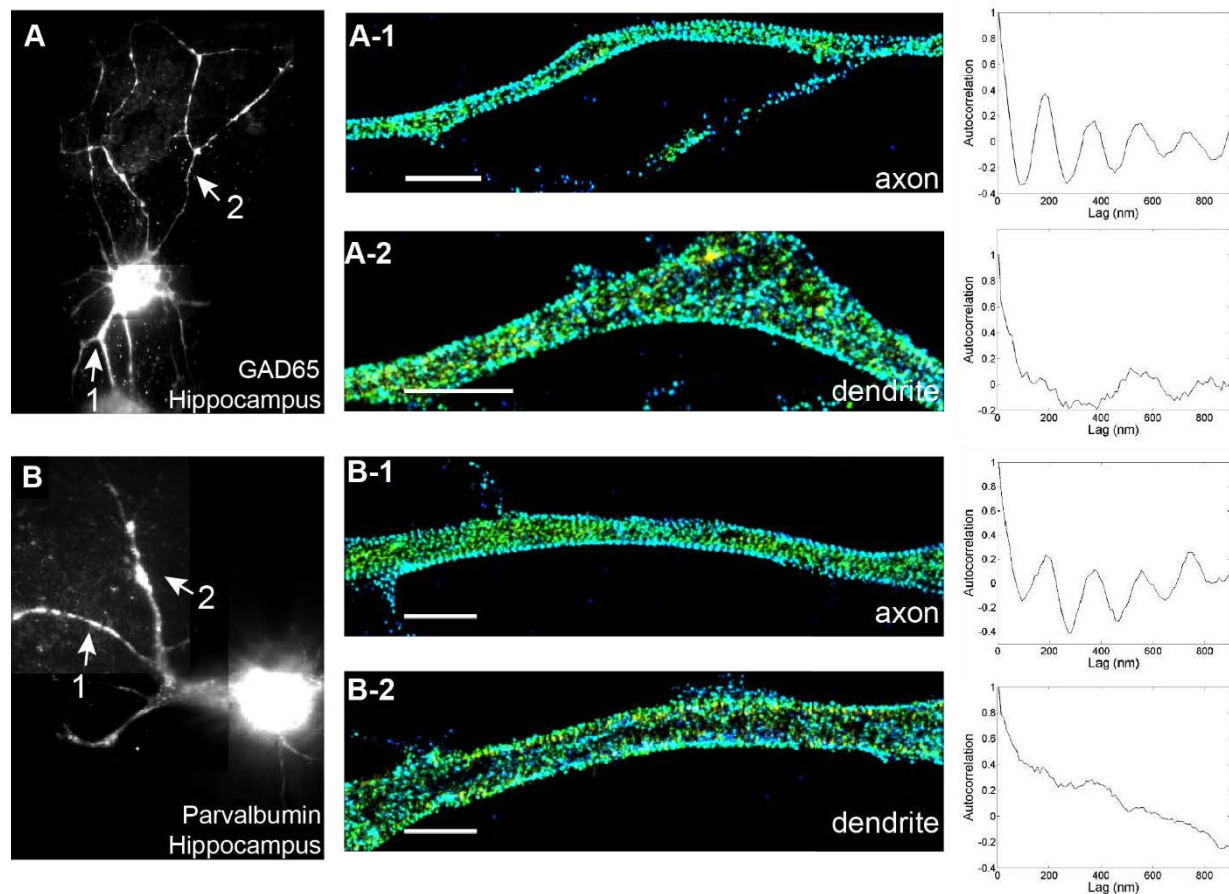


**Figure 5.1.  $\beta$ II spectrin is organized into a periodic structure in inhibitory neurons from the hippocampus.** A) Neurons from the hippocampus were cultured till DIV10 and immunostained with anti-GAD65 antibody. A reconstructed image of the neuron based on GAD65 staining is shown on the left. Axonal and dendritic regions (arrows) were chosen for STORM imaging. 3D STORM images of  $\beta$ II spectrin are shown in the middle. Autocorrelation analyses of the distribution of  $\beta$ II spectrin for each image is shown on the right. B) Similar to A) except that the neuron was stained with parvalbumin antibody.

### 5.2.2 The periodic membrane skeleton is present in neurons from central and periphery nervous system

Next, we extended our imaging to other neuronal types from different brain regions. For the cortex and middle brain regions, we used immunostaining of vGlut1, GAD65 and parvalbumin to mark the excitatory and inhibitory neurons. Though these two brain regions contain many morphologically and functionally distinct neuronal types, we reasoned that our labeling strategy would still allow us to quantify the prevalence of the periodic structure in all neuronal types from the cortex and middle brain. A representative excitatory and inhibitory neuron from the cortex and middle brain are shown in Figure 5.2.



Similar to what we observed in hippocampal neurons,  $\beta$ II spectrin in the axonal regions of these neurons exhibited a highly periodic form (Figure 5.2). We systematically quantified the degree of periodicity through autocorrelation analysis. As shown by the averaged autocorrelation curve from multiple measurements (Figure 5.2), axons of both excitatory and inhibitory neurons from the cortex and middle brain all had  $\beta$ II spectrin organized into a periodic form, whereas only a small fraction of dendrites appeared to have the periodic structure and typically in the form of isolated patches, especially in cortical neurons (arrowheads in Figure 5.2A-2). Average autocorrelation analysis indicated that the degree of periodicity in dendrites is much worse than that in axons and in short-range. These results suggest that the periodic membrane skeleton might be a general structural feature for axons in the brain.

To further test our hypothesis, we chose to image the distribution of  $\beta$ II spectrin in a few morphologically and functionally distinct neuronal types from other brain regions. Specifically, in the cerebellum, we imaged Golgi cells, Purkinje cells, and granule cells, marked by positive metabotropic glutamate receptor staining, positive calbindin staining, and negative calbindin and positive NeuN staining, respectively. Granules cells account for the majority of neurons in the brain and is known for its small cell body. Purkinje cells are large in size and have elaborate dendritic branches. Golgi cells are GABAergic interneurons that synapse on granule cells and parallel fibers [237]. In the pontine nuclei, we imaged mossy fibers, a major input to the cerebellum. Furthermore, two additional types of neurons were chosen because of their distinct neuronal transmitter type and function: dopamine neurons from basal ganglion and olfactory neurons from the olfactory bulb. For all of these neurons, we cultured them for at least 10 days, fixed them, and immunostained with  $\beta$ II spectrin for STORM imaging. As shown in Figure 5.3, all the neurons had a periodic distribution of  $\beta$ II spectrin in their axons, and the periodicity matches with that of hippocampal neurons. Quantitatively, the degree of periodicity varies among different neuronal types, with Golgi cells and Purkinje neurons having a slightly worse periodicity. This might due to a slow development process for cerebellum neurons in vitro, as observed in previous studies [238, 239]. These

data suggest that the periodic structure is highly prevalent in morphologically and functionally distinct neuronal types in the central nervous system.

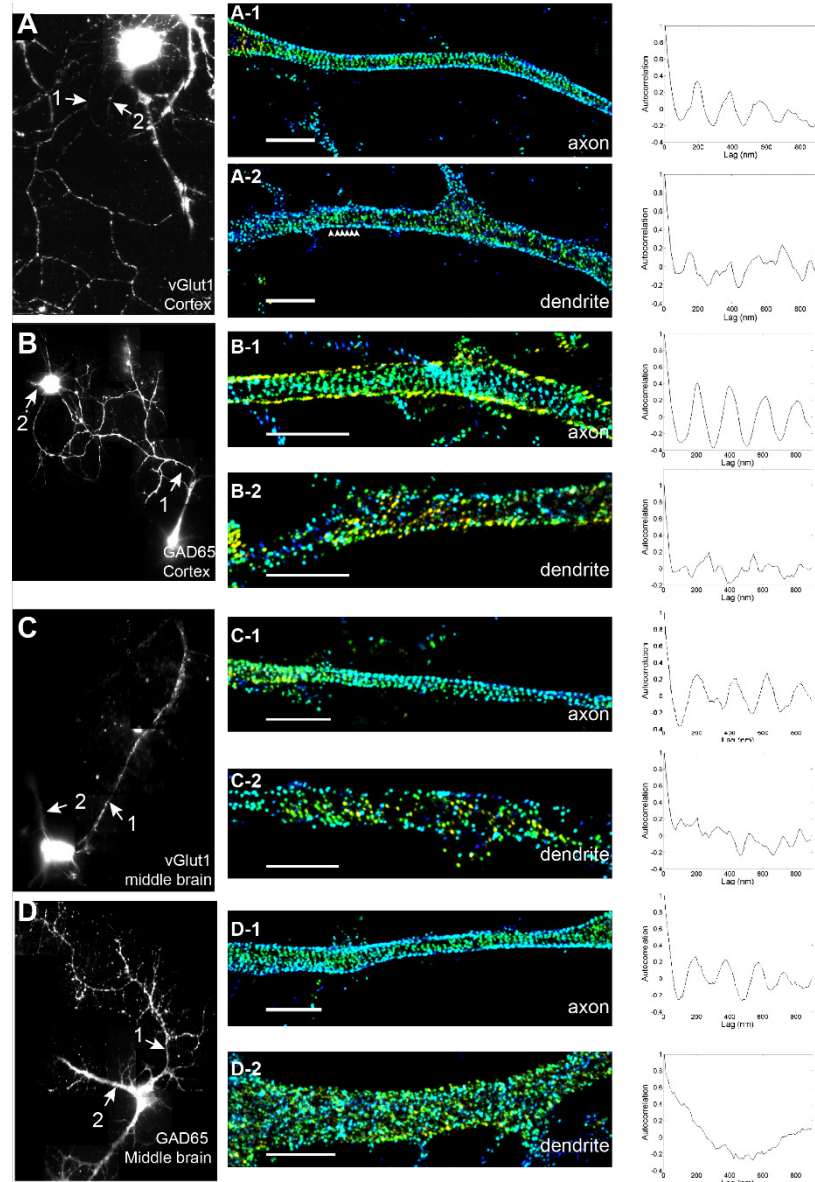


**Figure 5.2. The periodic lattice structure is present in both excitatory and inhibitory neurons from the cortex and middle brain.** Neurons from the cortex and middle brain regions were cultured till DIV 10 and immunostained with vGlut1 or GAD65 to label the excitatory and inhibitory neurons respectively. A) Left: a reconstructed image of vGlut1+ cortical neuron; middle: 3D STORM image of  $\beta$ II spectrin in the axonal and dendritic regions (arrows); right: autocorrelation analysis of the distribution of  $\beta$ II spectrin for the imaged regions. B) Similar to A) except the cortical neurons was labeled by GAD65. C) Similar to A) except the neuron was from the middle brain. D) Similar to A) except the neuron was from the middle brain and marked by GAD65.

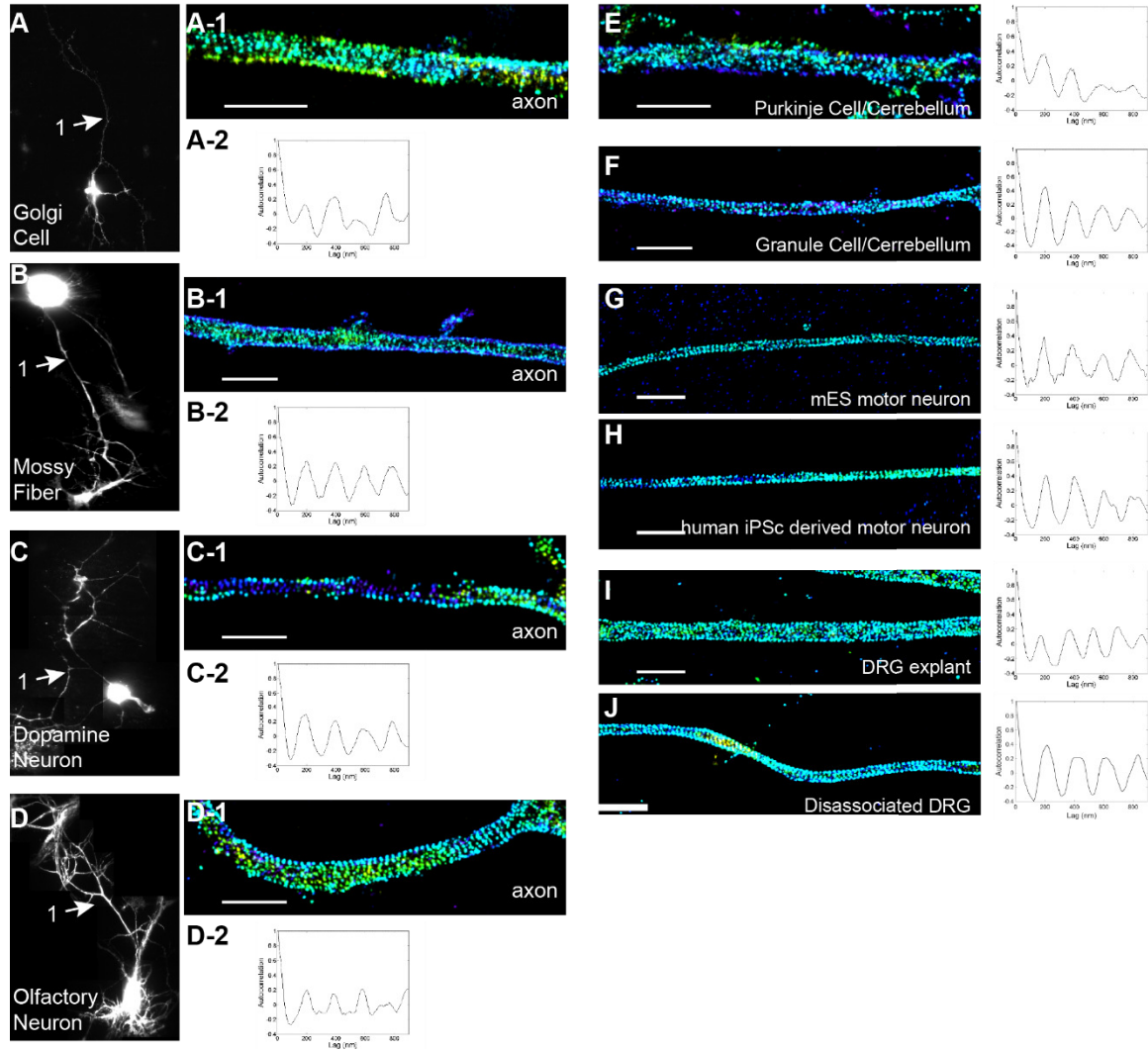


**Figure 5.3. The periodic structure is highly prevalent in different neuronal types from the central and periphery nervous system.** Neurons from the central and periphery nervous system were cultured for at least ten days and fixed for STORM imaging. A) A reconstructed image of Golgi cell from the cerebellum based on immunostaining of metabotropic glutamate receptor. 3D STORM images of  $\beta$ II spectrin and autocorrelation analyses of the distribution of  $\beta$ II spectrin in the axon were shown in A-1 and A-2. B) Similar to A) except the cell is mossy fiber from the pontine nuclei. C) Similar to A) except the cell is a dopamine neuron marked by tyrosine hydroxylase staining from the basal ganglion. D) Similar to A) except the cell is an olfactory neuron marked by OMP staining from the olfactory bulb. E) 3D STORM images of  $\beta$ II spectrin and autocorrelation analyses of the distribution of  $\beta$ II spectrin in the axon of Purkinje cells from cerebellum. F) 3D STORM images of  $\beta$ II spectrin and autocorrelation analyses of the distribution of  $\beta$ II spectrin in the axon of granule cells from cerebellum. G) 3D STORM images of  $\beta$ II spectrin and autocorrelation analyses of the distribution of  $\beta$ II spectrin in the axon of mouse embryonic stem cell-derived motor neurons. H) 3D STORM images of  $\beta$ II spectrin and autocorrelation analyses of the distribution of  $\beta$ II spectrin in the axon of human iPS cells-derived motor neurons. I) 3D STORM images of  $\beta$ II spectrin and autocorrelation analyses of the distribution of  $\beta$ II spectrin in the axon of DRG sensory neurons cultured in the explant format. J) 3D STORM images of  $\beta$ II spectrin and autocorrelation analyses of the distribution of  $\beta$ II spectrin in the axon of dissociated DRG sensory neurons.

Finally, we examined whether the periodic structure was present in periphery neurons. Two representative periphery neurons, motor neurons and DRG sensory neurons, were cultured, fixed and immunostained against  $\beta$ II spectrin for STORM imaging. The results for DRG neurons were obtained in collaboration with Dr. Marc Tessier-Lavigne's group in Rockefeller University, while the results for motor neurons were obtained in collaboration with Dr. Tom Maniatis's group in Columbia University. Motor neurons were either generated from mouse embryonic stem cells, or from human iPS cells. DRG sensory neurons were cultured either in an explant format, or dissociated form. Consistent with what we observed in central nervous system, we found that the periodic form of  $\beta$ II spectrin is evident for both motor neurons and DRG sensory neurons (Figure 5.3G-5.3J).

Altogether, these results indicate that the periodic structure is present in neurons from both the central and periphery nervous system. Given that the group of selected neurons are morphologically and functionally different, and were dissociated from distinct locations, these results suggest that the periodic membrane skeleton is highly prevalent in different neuronal types.

### **5.2.3 The structural organization of $\beta$ II spectrin in glia cells**

The high prevalence of the periodic structure in different neuronal types prompted us to wonder whether the lattice structure is unique to neurons, or whether other cells with long tubular neurite-like processes may have the periodic structure. To this end, we imaged the distribution of  $\beta$ II spectrin in four different types of glia cells: microglia, oligodendrocytes, astrocytes, NG2 glia cells and Schwann cells [237]. All these cells have thin processes protruding from the cell body and express  $\beta$ II spectrin. However, as compared to the distribution of  $\beta$ II spectrin in neurons, we failed to detect the periodic structure in long range order in these glia cells (Figure 5.4). Under rare circumstances, isolated patches of periodic  $\beta$ II spectrin can be observed in these processes, mostly evident in astrocytes, similar to what we observed in dendrites of neurons.

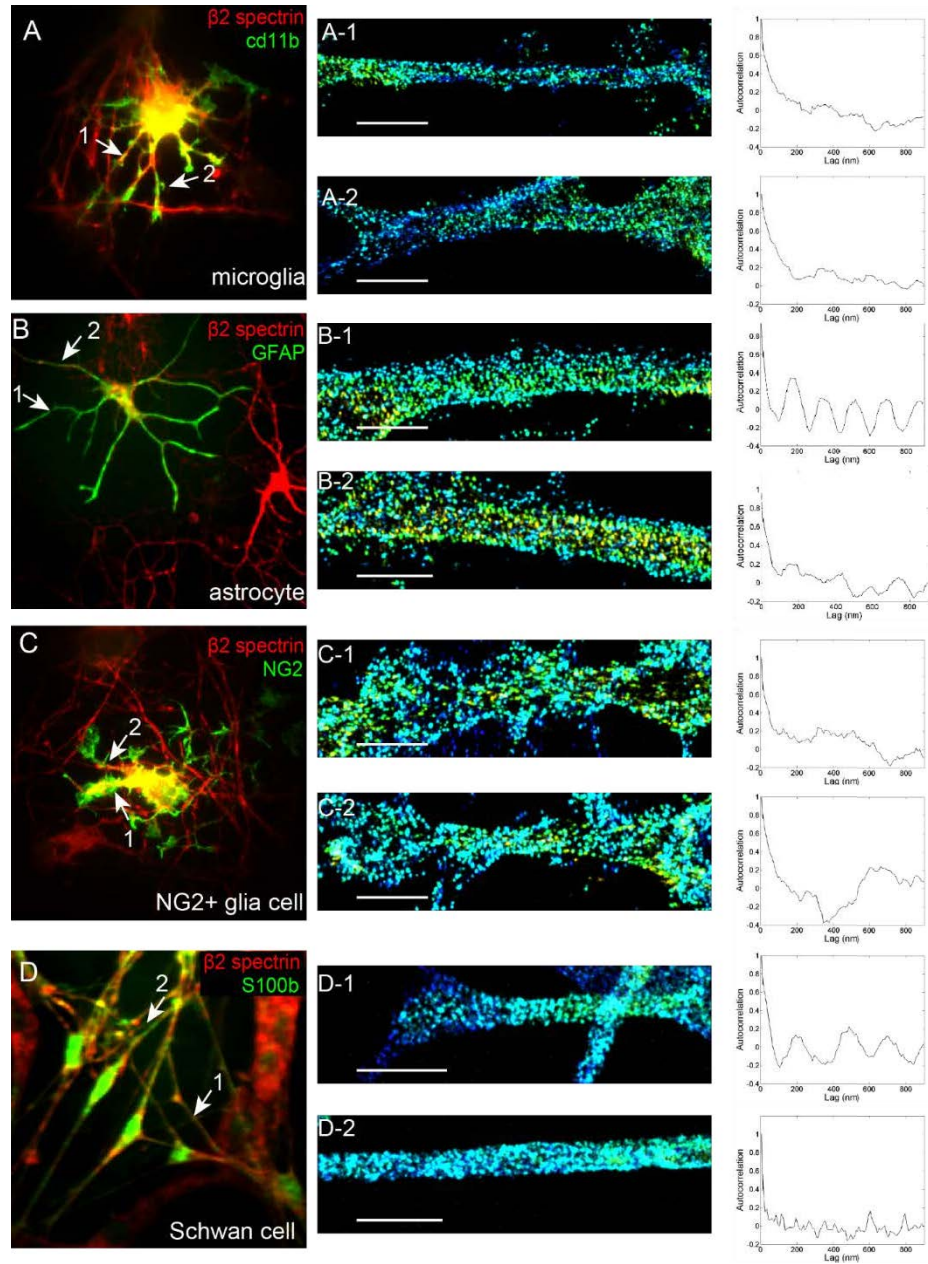


**Figure 5.4.  $\beta$ II spectrin is largely irregular in the processes of different glia cells.** A) Left: a microglia cell stained with microglia marker CD11b (green) and  $\beta$ II spectrin (red); middle: 3D STORM images of  $\beta$ II spectrin in two processes from the microglia (arrows); right: autocorrelation analyses of the distribution of  $\beta$ II spectrin from the imaged regions. B) Similar to A) except an astrocyte was labeled by astrocyte marker GFAP (green) and  $\beta$ II spectrin. C) Similar to A) except a NG2+ glia cell was labeled by NG2 (green) and  $\beta$ II spectrin. D) Similar to A) except a Schwann cell was labeled by Schwann cell marker S100b (green) and  $\beta$ II spectrin.

#### 5.2.4 Myelination does not affect the formation of the periodic structure in cultured neurons

As neurons in the body are heavily myelinated, we next sought to examine whether myelination had any effect on the formation of this periodic membrane skeleton. A co-culture system was used to induce myelination on hippocampal neurons, as previously reported [240]. Briefly, hippocampal neurons were cultured for two weeks before seeding with glia cells from the cerebellum. After about six weeks, the cells were fixed, and immunostained against  $\beta$ II spectrin, Map2 and MBP (myelination marker). Under conventional imaging, segments of axons wrapped by the sheath of oligodendrocytes were evident by the specific MBP staining (Figure 5.5A). We used STORM to image the distribution of  $\beta$ II spectrin in myelinated axons as well as unmyelinated regions. As shown in Figure 5.5B,  $\beta$ II spectrin still adapts a highly periodic form in myelinated regions, with a periodicity of around 180 nm. Because the axon has unmyelinated regions, we were able to compare the degree of periodicity between myelinated and unmyelinated regions on the same axon. As shown by the autocorrelation analysis (Figure 5.5C), there is no significant difference between the autocorrelation amplitude, indicating that myelination does not impact the formation of the periodic membrane skeleton, at least in our in vitro co-culture system.



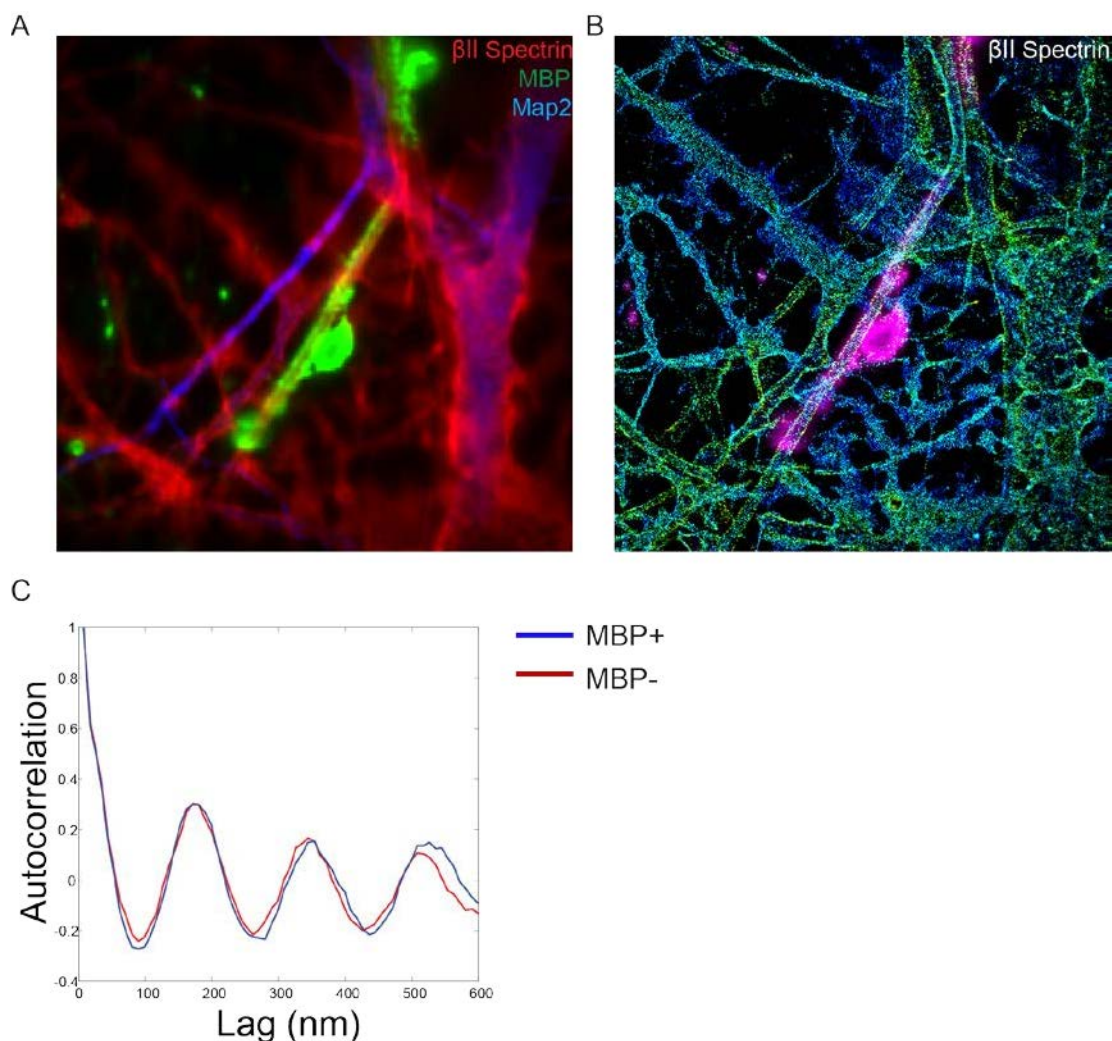


**Figure 5.5. Myelination does not affect the formation of the periodic membrane skeleton.**

Hippocampal neurons were cultured for two weeks before adding the glia cells. After co-culturing for six weeks, the cells were fixed and immunostained with  $\beta$ II spectrin (red), Map2 (dendritic marker, blue) and MBP (myelination marker, green). A) A conventional image of the myelinated axon. The green tube in the middle marks a myelinated axon. B) 3D STORM image of  $\beta$ II spectrin from A). The myelin sheath was shown in magenta. As shown in the image,  $\beta$ II spectrin adopts a highly periodic structure in the myelinated as well as unmyelinated regions along the axon. C) Average autocorrelation analyses of the distribution of  $\beta$ II spectrin from the MBP+ and MBP- regions from the same axon. The periodicity appears similar in the myelinated and unmyelinated regions. Average from at least 7 neurons.

### 5.3 Discussion

Actin, spectrin and associated molecules organize into a submembrane periodic lattice structure around the circumference of axons. The initial observation was primarily made in hippocampal neurons [149]. In this study, we extended this observation to multiple neuronal types in the central nervous system

and periphery nervous system. Excitatory neurons, inhibitory neurons in the hippocampus, cortex, and middle brain regions, granule cells, Golgi cells, Purkinje cells from cerebellum, mossy fibers from the pontine nuclei, dopamine neurons from basal ganglion, olfactory neurons from the olfactory bulb, mouse embryonic-derived motor neurons, human iPS cell-derived motor neurons, and mouse DRG sensory neurons, myelinated hippocampal neurons all appear to have the periodic membrane skeleton in their axons. These many neuronal types are morphologically and functionally different, and came from distinct origins. Although we couldn't exclude the possibility that some neuronal types may not have the lattice structure because we didn't image all the neuronal types in the body, given the high prevalence of the periodic structure, it is highly likely that the periodic membrane skeleton is a general feature for all the neurons. In addition to the observation of the periodic lattice structure in cultured cells, the Zhuang lab has also previously observed the presence of the lattice structure in the tissue slice of cortex and hippocampus [149]. The periodic actin-spectrin lattice structure has also been observed in the axons of hippocampal neurons and nodes of Ranvier of myelinated sciatic nerve by the Hell lab [215].

Initially, the periodic membrane skeleton was only observed in axons, whereas dendrites predominantly contains long actin filaments and irregular distributions of  $\beta$ II spectrin [149]. Two subsequent studies found that in matured neurons, the periodic structure can be observed in a small fraction of dendrites as well typically appearing as isolated patches [207, 215]. To systematically determine the distribution of  $\beta$ II spectrin in dendrites of different neurons, we also imaged the dendritic distribution of  $\beta$ II spectrin from different neuronal types in this study. For all the different neuronal types we imaged, we either did not detect the periodic structure in dendrites or only detected such structure in a small fraction of dendrites. Within these dendrites, the periodic structure didn't exist in long-range order, but typically in the form of isolated patches. This is consistent to what we and the Hell lab observed in hippocampal neurons [207, 215].

The above results indicate that the polarized distribution of the periodic membrane skeleton in neurites might be a general feature across different neuronal types.



Actin is an evolutionally conserved cytoskeletal protein and essentially present in all eukaryotic cells. On the other hand, spectrin is a relatively late invention in evolution and only starts to appear from metazoans [129, 241]. An actin, spectrin-based cytoskeleton exist in neurons from *C. elegans* and *Drosophila melanogaster*, and was found to be important to be crucial for the mechanical stability for axons [142] and protecting axon from mechanical stress [145] in *C. elegans*, and for axon path finding [208], for the stabilization of presynaptic terminals [209] in the flies. However, it remains unknown whether actin, spectrin and associated molecules also organize into a periodic form, or whether other structural organization exist in neurons from these species. In this study, we found that the periodic membrane skeleton exists in mouse and human iPS-cell derived neurons. It will be interesting to determine when the periodic lattice structure evolve evolutionally in the future.

#### **5.4 Materials and Methods**

All experimental procedures were performed in accordance with the Guide for the Care and Use of Laboratory Animals of the National Institutes of Health. The protocol was approved by the Institutional Animal Care and Use Committee (IACUC) of Harvard University.

*Neuron culture.* For culturing neurons from hippocampus, cortex, middle brain, pontine nuclei, cerebellum, basal ganglion, olfactory bulb, the indicated brain regions were dissociated from the brain of wild type neonatal (E18) rat embryos (timed pregnant SD rats from Charles River Laboratories, Wilmington, MA), as reported previously [229]. Briefly, the brain tissues were isolated and digested with 0.05% trypsin-EDTA (1x) (Invitrogen 25300-054) at 37°C for 15 minutes, washed in HBSS solution several times, and then transferred to the culture media. After washing it once with the culture media, the tissues were pipetted up and down in the fresh culture media until the tissues were mostly dissolved. For hippocampal, cortex, middle brain, pontine nuclei, basal ganglion, cerebellum and olfactory bulb cultures, the neurons were resuspended with the culture media made of 96 mL Neurobasal (Life Technologies, 12349-015), 2 mL B-27 Supplement (Life Technologies, 17504-044), 1 mL Penicillin-Streptomycin (Life technologies, 15140-122) and 1 mL Glutamax (Life technologies, 35050-061), and then plated onto poly-

L-lysine/laminin-coated 18-mm coverslips (neuVtro, GG-18-pdl). The cerebellum culture could also be maintained in DMEM/F-12 media (Life Technologies, 11330-057) supplemented with 100 mM putrescine (Sigma-Aldrich, P7505), 30 nM Na<sub>2</sub>SeO<sub>3</sub> (Sigma-Aldrich, S5261), 1.4 mM L-glutamine (Sigma-Aldrich, 1294808), and 10 mg/ml gentamicin (Sigma-Aldrich, G1397), and we observed modest increase of survival rate for Purkinje cells when cultured in this media, as reported previously [238].

The co-culturing protocol for inducing myelination on hippocampal neuron is modified from a previously reported procedure [240]. Briefly, hippocampal neurons from E18 rat brains were dissociated and seeded as described above. Two weeks after plating, we harvested glia cells from the cerebellum of E18 rat by the same dissociation procedure. About 100,000 glia cells were seeded with 60,000 hippocampal neurons on the 18-mm coverslips. The co-cultured neurons were maintained in the culture media: for 40 ml media, the components include 19.5 ml Neurobasal media (Life Technologies, 12349-015), 19.5ml DMEM-high glucose media (Life Technologies, 11965-082), 400 µl Glutamax (Life technologies, 35050-061), 400 µl 100 mM sodium pyruvate (Life Technologies, 11360-070), 400 µl 0.5mg/ml insulin (Sigma-Aldrich, I6634), 400 µl 100X Sato, 400 µl 100X T3, 800 µl B-27(Life Technologies, 17504-044), 40 µl 5mg/ml N-acetyl cysteine (Sigma-Aldrich, A8199), 40 µl 10 µg/ml biotin(Sigma-Aldrich, B4639), 40 µl 1000X Cellgro Trace Element B(Life Technologies, MT99-175-C1). The neurons were fed twice a week with freshly made culture media until use.

*Reagents.* The following primary antibodies were used in this study: guinea pig anti-Map2 antibody (Synaptic Systems, 188004); mouse anti-βII spectrin antibody (BD Biosciences, 612563); rabbit anti-adducin antibody (Abcam, ab51130); rabbit anti-GFP antibody (Abcam, ab290); guinea pig anti-vGlut1 antibody(Synaptic Systems, 135304); rabbit anti-calbindin antibody (Swant, CB38); rabbit anti-tyrosine hydroxylase antibody (Abcam, ab6211); rabbit anti-GAD65 antibody(Synaptic Systems, 198103); goat anti-parvalbumin antibody (Santa Cruz, sc-7449); rabbit anti-metabotropic glutamate receptor antibody (Abcam, ab6438); rat anti-MBP antibody (Millipore, Mab386); rabbit anti-OMP antibody (Santa Cruz, sc-67219); goat anti-ChAT antibody (Millipore, AB144P); rabbit anti-NG2 antibody (Millipore,

AB5320); rabbit anti-CD11b (Novus Biologicals, NB110-89474); rabbit anti-S100b (Abcam, ab41548); rabbit anti-GFAP (Encor, RPCA-GFAP), rabbit anti-NeuN (Millipore, MABN140). The following secondary antibodies were used in this study: Alexa Fluor 647 donkey anti-mouse (Invitrogen, A31571), Alexa Fluor 647 donkey anti-rabbit (Invitrogen, A31573), Alexa Fluor 568 donkey anti-rabbit (Invitrogen, A10042), Alexa Fluor 488 donkey anti-rabbit (Invitrogen, A21206), Alexa Fluor 488 goat anti-guinea pig (Invitrogen, A11073), Alexa Fluor 568 donkey anti-goat (Invitrogen, A11057). For STORM imaging, Alexa Fluor 647 donkey anti-mouse (Invitrogen, A31571) or secondary antibodies custom-labeled with Alexa Fluor 647 and Alexa Fluor 405 [150] were used.

*Immunofluorescence of neurons.* Cultured neurons were fixed at various days in vitro (DIV) using 4% (w/v) paraformaldehyde in phosphate buffered saline (PBS) for 15 min. Fixed neuron samples were then permeabilized with 0.2% v/v Triton X-100 in PBS for 5 minutes and blocked in blocking buffer (3% w/v bovine serum albumin in PBS) for 1 hour, and subsequently stained with primary antibodies in blocking buffer overnight at 4 °C. The samples were washed three times and then stained with secondary antibodies (described above) in blocking buffer for ~1 hour at room temperature.

*STORM imaging.* The STORM setup was based on an Olympus IX-71 inverted optical microscope as described previously [236]. 405-nm (CUBE 405-50C; Coherent), 460-nm (Sapphire 460-10; Coherent), 532-nm (GCL-200-I; CrystaLaser), and 657-nm (RCL-300-656; CrystaLaser) lasers were introduced into the sample through the back focal plane of the microscope. A translation stage allowed the laser beams to be shifted towards the edge of the objective so that the emerging light reached the sample at incidence angles slightly smaller than the critical angle of the glass-water interface, thus illuminating only the fluorophores within a few micrometers of the coverslip surface. A T660LPXR (Chroma) was used as the dichroic mirror and an ET705/72M band-pass filter (Chroma) was used as the emission filter. For 3-dimensional (3D) STORM imaging, a cylindrical lens was inserted into the imaging path so that images of single molecules were elongated in *x* and *y* for molecules on the proximal and distal sides of the focal plane (relative to the objective), respectively [112].

Before imaging, the sample was supplemented with the imaging buffer: PBS containing 100 mM cysteamine, 5% glucose, 0.8 mg/mL glucose oxidase (Sigma-Aldrich), and 40  $\mu$ g/mL catalase (Roche Applied Science). During imaging, continuous illumination of 657-nm laser ( $\sim 2$  kW/cm<sup>2</sup>) was used to excite fluorescence from Alexa Flour 647 molecules and switched them into the dark state. Continuous illumination of the 405-nm laser was used to reactivate the fluorophores to the emitting state. The power of the activation lasers (typical range 0-1 W/cm<sup>2</sup>) was adjusted during image acquisition so that at any given instant, only a small, optically resolvable fraction of the fluorophores in the sample were in the emitting state.

A typical STORM image was generated from a sequence of about 20,000~40,000 image frames at a frame rate of 60 Hz. The recorded STORM movie was analyzed according to previously described methods [105, 112]. The centroid positions and ellipticities of the single-molecule images provided lateral and axial positions of each activated fluorescent molecule, respectively [112]. Super-resolution images were reconstructed from the molecular coordinates by depicting each location as a 2D Gaussian peak.

## **Chapter 6: Discussion and Future Directions**

Fluorescence imaging has become an indispensable tool to study biological processes and has generated many important insights in modern biology. One feature that makes fluorescence imaging so powerful is its ability to achieve molecule-specific visualization for targets of interest. With the development of many staining methods, fluorescent imaging also allows researchers to easily probe different biological processes in fixed or live conditions. In this dissertation, I present the use of conventional fluorescence imaging to study the role of host factors in influenza virus infection, as well as the use of super-resolution imaging to characterize the developmental mechanism of a novel periodic membrane skeleton.

## **6.1 Host Factors in Influenza Virus Infection**

As an obligatory pathogen that only encodes 13 proteins, influenza virus must co-opt host cell machinery to harbor infection and to produce progeny viruses [15]. The life cycle of virus infection involves extensive intracellular trafficking of viral components. In order to characterize the virus-host cell interactions, several genome-wide siRNA screens and proteomic analyses have been performed to identify host factors involved in influenza virus infection [63-68]. Hundreds of candidate host factors have been identified, though the exact functional role for many of these host factors remains to be elucidated. In Chapter 2 and 3, I present the study of CD81 and COPI complex, two top candidates identified in multiple siRNA screens and proteomic analyses, and their role in influenza virus infection.

In Chapter 2, my colleagues and I used siRNA to knockdown CD81 and examined the effect of CD81 depletion on the major steps of influenza infection. We report a dual function of CD81 in influenza virus infection by regulating two major steps: virus fusion during viral entry and virus budding during viral egress. Specifically, during viral entry, more than half of internalized virus particles were trafficked into a specific CD81-positive endosomal population for virus uncoating. Depleting CD81 led to a significant defect in viral uncoating and infection. During viral egress, CD81 was recruited to virus assembly site, and incorporated into individual virions at specific sub-viral locations. For spherical and slightly elongated influenza virus, CD81 was localized at both the growing tip and the budding neck of

the progeny viruses. CD81 depletion resulted in virions that failed to detach from the plasma membrane and a marked decrease in progeny virus production. In filamentous virus, CD81 was distributed at multiple sites along the viral filament. Taken together, these results demonstrate important roles of CD81 in both entry and budding stages of the influenza infection cycle.

In Chapter 3, my colleagues and I used siRNA and pharmacological inhibitors to dissect the effect of COPI depletion or disruption on influenza infection. Knocking down COPI using siRNA led to a significant defect for virus internalization and virus trafficking from early to intermediate/late endosomes. The entry block was not limited to influenza virus, but also for other cargoes (Tfn, EGF, and dextran) that internalize through either clathrin-mediated endocytosis or macropinocytosis. Because of the large defect in viral entry during prolonged siRNA treatment, we also used pharmacological inhibitors to acutely disrupt the COPI complexes. With the inhibitor treatment, we found that disruption of functional COPI complexes directly inhibited viral membrane protein expression, assembly of viral components at the plasma membrane, and production of infectious progeny virus. Our findings suggest that COPI complexes likely function indirectly in influenza virus entry but play direct roles in viral membrane protein expression and assembly.

As exemplified by these two studies, fluorescence imaging is a versatile tool that allows us to probe the influenza infection in either fixed or live cells. Virtually every step along the infection cycle can be examined by imaging-based assays [28]. Particularly, by labeling individual virions with a fluorescent dye and tracking the movements of viruses during viral entry, we were able to capture each step during viral entry from virus binding, to virus internalization, trafficking to endosomes and virus fusion [28]. This allowed us to study in real time how influenza viruses interact with host factors, and to examine the specific role of host factors during each entry step. Similarly, the assays developed for the study of post-entry steps are mostly based on fixed cell fluorescence imaging as well. Complementary to the traditional biochemical approaches, these imaging-based methods not only provide detailed quantification for viral

replication, viral protein translation and transport, but also the spatiotemporal information on the functional role of host proteins during virus infection.

Importantly, the assays presented in these two studies can be easily extended to the characterization of functional roles for other host factors in influenza virus infection, or more generally, infection cycle of other viruses. Over the past few years, many genome-wide studies have been performed to identify host dependency and susceptibility proteins involved in the infection cycle of different viruses [242]. Given that viruses exploit a variety of cellular machineries to enter cells, these assays will undoubtedly provide invaluable insights for dissecting the dynamic roles of these identified host proteins in viral entry. With the extended list of candidate proteins involved in virus infection, it should be minded that live cell imaging is a relatively low throughput assay. Development of high-throughput and high-content live cell imaging methods for analyzing the large body of data will tremendously abet future work.

On the other hand, it is important to note that viruses are generally small in size, while the interactions between virus and cellular factors occur at the nanometer scale [15]. Under conventional light microscopy, the precise localization of host or viral proteins is blurred by the diffraction limit of light. For instance, during viral entry, initiation of clathrin-mediated endocytosis by influenza virus leads to a highly specific, well-orchestrated and ordered cellular protein distribution within the clathrin-coated pit [243]. However, such detailed spatial orchestration information is often missing from conventional imaging. The recent development of super-resolution techniques that overcome the diffraction limit and provide nanometer-scale image resolution will open up a window for more detailed investigation of virus-cell interactions [98-101]. Future studies on virus and host cell interaction will undoubtedly benefit from the use of super-resolution imaging.

Altogether, my studies elucidated the role of several essential host factors in the influenza life cycle, and would potentially offer important insights in restricting influenza spread. The exciting discoveries made possible by fluorescence imaging represent just the tip of iceberg of what we know about virus-host cell interaction. With the development of new technologies and discovery of novel



biological processes, future imaging studies on virus-host cell interaction will undoubtedly further enrich our understanding on virology and basic cellular biology.

## **6.2 The periodic membrane skeleton in neurons**

In the nervous system, the information typically flows from the axons of output neurons to the dendrites of receiving neurons. This directional transmission of information depends critically on the polarization of neurons, namely the differentiation between axons and dendrites. The cytoskeleton plays critical roles in determining the shape and mechanical properties of the cell, as well as in supporting many cellular functions, including cell motility, cell division, and intracellular transport [117-120]. In neurons, cytoskeletal structures are essential for the establishment of neuronal polarity, the growth and stabilization of axons and dendrites, the trafficking of cargos to specific neurites, as well as the plasticity of synapses [117-120]. The Zhuang labs recently discovered a strikingly ordered submembrane cytoskeleton structure that is predominantly present in axons [149]. Three molecular components of this novel cytoskeleton structure were identified, including actin, spectrin and adducin. Actin filaments form a ring-like structure that wraps around the circumference of the axons. These actin rings were evenly spaced along the axon shafts with a highly regular periodicity, forming a quasi-one-dimensional lattice structure with a long-range order. Actin filaments in the rings were capped by adducin and adjacent actin rings were connected by spectrin tetramers. The periodic lattice also organizes the axonal membrane by placing important membrane proteins, such as the voltage-gated sodium channels, into a periodic distribution [149].

In Chapter 4, my colleagues and I used super-resolution imaging to study the developmental process of this periodic membrane skeleton, and the molecular mechanism underlying its specific formation in axons. We found that the periodic membrane skeleton forms early during neuronal development, and originates from axonal regions closer to the cell body, and propagates toward distal axon ends. The lattice structure continues to mature by recruiting additional molecular components during neuronal development, and once matured, it appears to be highly stable.

We found that a small fraction of dendrites also have the periodic structure during later developmental stages. In these dendrites, the periodic lattice structure often appeared as isolated patches and not throughout the entire dendrites [207]. Recently, D'Este and colleagues used SiR-Actin, a newly developed fluorescent probe, to label actin, and imaged the periodic structure in live neurons through STED imaging. Consistent with our findings, they reported that the lattice structure was identified in all axons but only in ~25% of the dendrites [215]. Altogether, the data suggest that the periodic membrane skeleton preferentially forms in axons, though a small fraction of dendrites have this lattice structure.

We further found that the formation of this periodic membrane skeleton is regulated by the local concentration of  $\beta$ II spectrin, which is higher in axons than in dendrites. Increasing the concentration of  $\beta$ II spectrin by overexpression or by knocking down ankyrin B induces the formation of the periodic structure in dendrites, demonstrating that the spectrin concentration is a key determinant in the preferential development of this structure in axons and that ankyrin B is critical for the polarized distribution of  $\beta$ II spectrin in neurites.

In Chapter 5, my colleagues and I studied the prevalence of this periodic membrane skeleton in different neuronal types. We found that this periodic structure is highly prevalent in many morphologically and functionally distinct neurons from the central and periphery nervous system. On the other hand, glia cells do not appear to contain this periodic skeleton in long range order. Furthermore, we found that myelination does not impact the formation of this periodic structures in vitro.

In red blood cells, the submembrane cytoskeleton is comprised of a large number of protein species in addition to actin, spectrin and adducin, including ankyrin, tropomyosin, band 4.1, dematin, tropomodulin [129, 222]. Although the ultrastructural organization of the axonal submembrane cytoskeleton is highly distinct from that of the red blood cells, the microscopic molecular interactions appear to be similar. It is highly likely that the periodic membrane skeleton in neurons contains many more molecular components. To obtain a complete picture of how the periodic membrane skeleton is organized in neurons, it is crucial to further determine the molecular composition of this novel structure.

Indeed, recent unpublished studies in the Zhuang lab have substantially expanded the molecular component list of this periodic lattice structure.

As mentioned above, the lattice structure places sodium channels into a periodic pattern along the axon initial segments. Recent unpublished results in the Zhuang lab revealed additional, important membrane proteins on this structure. Together, these studies suggest the ability of this submembrane cytoskeleton to organize molecular components of the axonal membrane, which is critical for action potential generation and propagation, and other signaling pathways [149]. Additionally, mutant *C. elegans* lacking spectrin exhibits substantially lower axon stability, suggesting that the periodic lattice structure is essential for supporting mechanical stability of the axons [142]. Moreover, the actin-spectrin lattice structure appears to be in a pre-stressed state in *C. elegans* axons, protecting the axons from buckling during animal movement, and such pre-stressed state is important for mechanosensation [145]. These observations suggest important functional roles of this periodic membrane skeleton. In the future, it will be of particular interest to investigate whether dysfunction in this membrane skeletal structure has implications in neurological diseases.

## References

1. Jones, E.G., *Neuroanatomy: Cajal and after Cajal*. Brain Res Rev, 2007. **55**(2): p. 248-55.
2. Vale, R.D., et al., *Direct observation of single kinesin molecules moving along microtubules*. Nature, 1996. **380**(6573): p. 451-3.
3. Lichtman, J.W. and J.A. Conchello, *Fluorescence microscopy*. Nat Methods, 2005. **2**(12): p. 910-9.
4. Yuste, R., *Fluorescence microscopy today*. Nat Methods, 2005. **2**(12): p. 902-4.
5. Petty, H.R., *Fluorescence microscopy: established and emerging methods, experimental strategies, and applications in immunology*. Microsc Res Tech, 2007. **70**(8): p. 687-709.
6. Johnson, I., *Fluorescent probes for living cells*. Histochem J, 1998. **30**(3): p. 123-40.
7. Fernandez-Suarez, M. and A.Y. Ting, *Fluorescent probes for super-resolution imaging in living cells*. Nat Rev Mol Cell Biol, 2008. **9**(12): p. 929-43.
8. Zhang, J., et al., *Creating new fluorescent probes for cell biology*. Nat Rev Mol Cell Biol, 2002. **3**(12): p. 906-18.
9. Jing, C. and V.W. Cornish, *Chemical tags for labeling proteins inside living cells*. Acc Chem Res, 2011. **44**(9): p. 784-92.
10. Giepmans, B.N., et al., *The fluorescent toolbox for assessing protein location and function*. Science, 2006. **312**(5771): p. 217-24.
11. Spence, M.T.Z. and I.D. Johnson, *The molecular probes handbook : a guide to fluorescent probes and labeling technologies*. 11th ed. 2010, Carlsbad, CA: Live Technologies Corporation. xiv, 1160 p.
12. Michalet, X., et al., *Quantum dots for live cells, in vivo imaging, and diagnostics*. Science, 2005. **307**(5709): p. 538-44.
13. Bao, G., W.J. Rhee, and A. Tsourkas, *Fluorescent probes for live-cell RNA detection*. Annu Rev Biomed Eng, 2009. **11**: p. 25-47.
14. Tyagi, S., *Imaging intracellular RNA distribution and dynamics in living cells*. Nat Methods, 2009. **6**(5): p. 331-8.
15. Fields, B.N., D.M. Knipe, and P.M. Howley, *Fields virology*. 5th ed. 2007, Philadelphia: Wolters Kluwer Health/Lippincott Williams & Wilkins.
16. Flint, S.J. and American Society for Microbiology., *Principles of virology*. 3rd ed. 2009, Washington, DC: ASM Press.
17. Ruthardt, N., D.C. Lamb, and C. Brauchle, *Single-particle Tracking as a Quantitative Microscopy-based Approach to Unravel Cell Entry Mechanisms of Viruses and Pharmaceutical Nanoparticles*. Molecular Therapy, 2011. **19**(7): p. 1199-1211.
18. Kukura, P., et al., *High-speed nanoscopic tracking of the position and orientation of a single virus*. Nature Methods, 2009. **6**(12): p. 923-U85.

19. Jaqaman, K., et al., *Robust single-particle tracking in live-cell time-lapse sequences*. Nature Methods, 2008. **5**(8): p. 695-702.
20. Katayama, Y., et al., *Real-time nanomicroscopy via three-dimensional single-particle tracking*. Chemphyschem, 2009. **10**(14): p. 2458-64.
21. Vaughan, J.C., et al., *Rapid Actin-Dependent Viral Motility in Live Cells*. Biophysical Journal, 2009. **97**(6): p. 1647-1656.
22. Lehmann, M.J., et al., *Actin- and myosin-driven movement of viruses along filopodia precedes their entry into cells*. Journal of Cell Biology, 2005. **170**(2): p. 317-325.
23. Ewers, H., et al., *Single-particle tracking of murine polyoma virus-like particles on live cells and artificial membranes*. Proceedings of the National Academy of Sciences of the United States of America, 2005. **102**(42): p. 15110-15115.
24. Mercer, J. and A. Helenius, *Vaccinia virus uses macropinocytosis and apoptotic mimicry to enter host cells*. Science, 2008. **320**(5875): p. 531-535.
25. Schelhaas, M., et al., *Human papillomavirus type 16 entry: Retrograde cell surface transport along actin-rich protrusions*. Plos Pathogens, 2008. **4**(9).
26. Collier, K.E., et al., *RNA Interference and Single Particle Tracking Analysis of Hepatitis C Virus Endocytosis*. Plos Pathogens, 2009. **5**(12).
27. Dixit, R., V. Tiwari, and D. Shukla, *Herpes simplex virus type 1 induces filopodia in differentiated P19 neural cells to facilitate viral spread*. Neuroscience Letters, 2008. **440**(2): p. 113-118.
28. Sun, E., J. He, and X. Zhuang, *Live cell imaging of viral entry*. Curr Opin Virol, 2013. **3**(1): p. 34-43.
29. Cureton, D.K., et al., *Vesicular Stomatitis Virus Enters Cells through Vesicles Incompletely Coated with Clathrin That Depend upon Actin for Internalization*. Plos Pathogens, 2009. **5**(4).
30. Johannsdottir, H.K., et al., *Host Cell Factors and Functions Involved in Vesicular Stomatitis Virus Entry*. J Virol, 2009. **83**(1): p. 440-453.
31. Ehrlich, M., et al., *Endocytosis by random initiation and stabilization of clathrin-coated pits*. Cell, 2004. **118**(5): p. 591-605.
32. Rust, M.J., et al., *Assembly of endocytic machinery around individual influenza viruses during viral entry*. Nature Structural & Molecular Biology, 2004. **11**(6): p. 567-573.
33. Cureton, D.K., et al., *The length of vesicular stomatitis virus particles dictates a need for actin assembly during clathrin-dependent endocytosis*. Plos Pathogens, 2010. **6**(9): p. e1001127.
34. van der Schaar, H.M., et al., *Dissecting the cell entry pathway of dengue virus by single-particle tracking in living cells*. Plos Pathogens, 2008. **4**(12): p. e1000244.
35. Damm, E.M., et al., *Clathrin- and caveolin-1-independent endocytosis: entry of simian virus 40 into cells devoid of caveolae*. Journal of Cell Biology, 2005. **168**(3): p. 477-488.
36. Pelkmans, L., J. Kartenbeck, and A. Helenius, *Caveolar endocytosis of simian virus 40 reveals a new two-step vesicular-transport pathway to the ER*. Nature Cell Biology, 2001. **3**(5): p. 473-83.

37. Liebl, D., et al., *Mouse polyomavirus enters early endosomes, requires their acidic pH for productive infection, and meets transferrin cargo in Rab11-positive endosomes.* J Virol, 2006. **80**(9): p. 4610-22.
38. Aleksandrowicz, P., et al., *Ebola virus enters host cells by macropinocytosis and clathrin-mediated endocytosis.* J Infect Dis, 2011. **204** Suppl 3: p. S957-67.
39. Coyne, C.B., et al., *Coxsackievirus entry across epithelial tight junctions requires occludin and the small GTPases Rab34 and Rab5.* Cell Host & Microbe, 2007. **2**(3): p. 181-92.
40. Mercer, J., et al., *Vaccinia virus strains use distinct forms of macropinocytosis for host-cell entry.* Proceedings of the National Academy of Sciences of the United States of America, 2010. **107**(20): p. 9346-9351.
41. Mercer, J. and A. Helenius, *Virus entry by macropinocytosis.* Nature Cell Biology, 2009. **11**(5): p. 510-520.
42. Kalin, S., et al., *Macropinocytotic uptake and infection of human epithelial cells with species B2 adenovirus type 35.* J Virol, 2010. **84**(10): p. 5336-50.
43. Nanbo, A., et al., *Ebolavirus Is Internalized into Host Cells via Macropinocytosis in a Viral Glycoprotein-Dependent Manner.* Plos Pathogens, 2010. **6**(9).
44. de Vries, E., et al., *Dissection of the Influenza A Virus Endocytic Routes Reveals Macropinocytosis as an Alternative Entry Pathway.* Plos Pathogens, 2011. **7**(3).
45. Cureton, D.K., R. Burdeinick-Kerr, and S.P. Whelan, *Genetic Inactivation of COPI Coatomer Separately Inhibits Vesicular Stomatitis Virus Entry and Gene Expression.* Journal of Virology, 2012. **86**(2): p. 655-66.
46. Kolokoltsov, A.A., et al., *Small interfering RNA profiling reveals key role of clathrin-mediated endocytosis and early endosome formation for infection by respiratory syncytial virus.* J Virol, 2007. **81**(14): p. 7786-7800.
47. Vonderheit, A. and A. Helenius, *Rab7 associates with early endosomes to mediate sorting and transport of semliki forest virus to late endosomes.* Plos Biology, 2005. **3**(7): p. 1225-1238.
48. Lakadamyali, M., et al., *Visualizing infection of individual influenza viruses.* Proceedings of the National Academy of Sciences of the United States of America, 2003. **100**(16): p. 9280-9285.
49. Lozach, P.Y., et al., *Entry of Bunyaviruses into Mammalian Cells.* Cell Host & Microbe, 2010. **7**(6): p. 488-499.
50. Lakadamyali, M., M.J. Rust, and X.W. Zhuang, *Ligands for clathrin-mediated endocytosis are differentially sorted into distinct populations of early endosomes.* Cell, 2006. **124**(5): p. 997-1009.
51. Arhel, N., et al., *Quantitative four-dimensional tracking of cytoplasmic and nuclear HIV-1 complexes.* Nature Methods, 2006. **3**(10): p. 817-24.
52. Brandenburg, B. and X. Zhuang, *Virus trafficking - learning from single-virus tracking.* Nat Rev Microbiol, 2007. **5**(3): p. 197-208.
53. Wiley, D.C. and J.J. Skehel, *The structure and function of the hemagglutinin membrane glycoprotein of influenza virus.* Annu Rev Biochem, 1987. **56**: p. 365-94.
54. Matlin, K.S., et al., *Infectious entry pathway of influenza virus in a canine kidney cell line.* J Cell Biol, 1981. **91**(3 Pt 1): p. 601-13.

55. Sieczkarski, S.B. and G.R. Whittaker, *Influenza virus can enter and infect cells in the absence of clathrin-mediated endocytosis*. Journal of Virology, 2002. **76**(20): p. 10455-10464.
56. Rust, M.J., et al., *Assembly of endocytic machinery around individual influenza viruses during viral entry*. Nat Struct Mol Biol, 2004. **11**(6): p. 567-73.
57. Rossman, J.S., G.P. Leser, and R.A. Lamb, *Filamentous Influenza Virus Enters Cells via Macropinocytosis*. Journal of Virology, 2012. **86**(20): p. 10950-60.
58. Whittaker, G.R., M. Kann, and A. Helenius, *Viral entry into the nucleus*. Annu Rev Cell Dev Biol, 2000. **16**: p. 627-651.
59. Mercer, J., M. Schelhaas, and A. Helenius, *Virus entry by endocytosis*. Annu Rev Biochem, 2010. **79**: p. 803-33.
60. Rossman, J.S. and R.A. Lamb, *Influenza virus assembly and budding*. Virology, 2011. **411**(2): p. 229-36.
61. Chen, C. and X.W. Zhuang, *Epsin 1 is a cargo-specific adaptor for the clathrin-mediated endocytosis of the influenza virus*. Proc Natl Acad Sci U S A, 2008. **105**(33): p. 11790-11795.
62. Lakadamyali, M., M.J. Rust, and X. Zhuang, *Ligands for clathrin-mediated endocytosis are differentially sorted into distinct populations of early endosomes*. Cell, 2006. **124**(5): p. 997-1009.
63. Hao, L., et al., *Drosophila RNAi screen identifies host genes important for influenza virus replication*. Nature, 2008. **454**(7206): p. 890-3.
64. Brass, A.L., et al., *The IFITM proteins mediate cellular resistance to influenza A H1N1 virus, West Nile virus, and dengue virus*. Cell, 2009. **139**(7): p. 1243-54.
65. Shapira, S.D., et al., *A physical and regulatory map of host-influenza interactions reveals pathways in H1N1 infection*. Cell, 2009. **139**(7): p. 1255-67.
66. Karlas, A., et al., *Genome-wide RNAi screen identifies human host factors crucial for influenza virus replication*. Nature, 2010. **463**(7282): p. 818-22.
67. Konig, R., et al., *Human host factors required for influenza virus replication*. Nature, 2010. **463**(7282): p. 813-7.
68. Hutchinson, E.C., et al., *Conserved and host-specific features of influenza virion architecture*. Nat Commun, 2014. **5**: p. 4816.
69. Shaw, M.L., et al., *Cellular proteins in influenza virus particles*. Plos Pathogens, 2008. **4**(6): p. e1000085.
70. Hemler, M.E., *Tetraspanin functions and associated microdomains*. Nat Rev Mol Cell Biol, 2005. **6**(10): p. 801-11.
71. Levy, S. and T. Shoham, *The tetraspanin web modulates immune-signalling complexes*. Nat Rev Immunol, 2005. **5**(2): p. 136-48.
72. Xu, C.F., et al., *CD82 endocytosis and cholesterol-dependent reorganization of tetraspanin webs and lipid rafts*. Faseb Journal, 2009. **23**(10): p. 3273-3288.
73. Stipp, C.S., T.V. Kolesnikova, and M.E. Hemler, *Functional domains in tetraspanin proteins*. Trends Biochem Sci, 2003. **28**(2): p. 106-12.

74. Yanez-Mo, M., et al., *Tetraspanin-enriched microdomains: a functional unit in cell plasma membranes*. Trends Cell Biol, 2009. **19**(9): p. 434-46.
75. Berditchevski, F. and E. Odintsova, *Tetraspanins as regulators of protein trafficking*. Traffic, 2007. **8**(2): p. 89-96.
76. Richardson, M.M., L.K. Jennings, and X.A. Zhang, *Tetraspanins and tumor progression*. Clin Exp Metastasis, 2011. **28**(3): p. 261-70.
77. Zhang, X.A. and C. Huang, *Tetraspanins and cell membrane tubular structures*. Cell Mol Life Sci, 2012. **69**(17): p. 2843-52.
78. Martin, F., et al., *Tetraspanins in viral infections: a fundamental role in viral biology?* Journal of Virology, 2005. **79**(17): p. 10839-51.
79. Pileri, P., et al., *Binding of hepatitis C virus to CD81*. Science, 1998. **282**(5390): p. 938-41.
80. Zhang, J., et al., *CD81 is required for hepatitis C virus glycoprotein-mediated viral infection*. Journal of Virology, 2004. **78**(3): p. 1448-1455.
81. Flint, M., et al., *Diverse CD81 proteins support hepatitis C virus infection*. Journal of Virology, 2006. **80**(22): p. 11331-11342.
82. Ploss, A. and M.J. Evans, *Hepatitis C virus host cell entry*. Curr Opin Virol, 2012. **2**(1): p. 14-9.
83. Sharma, N.R., et al., *Hepatitis C Virus Is Primed by CD81 Protein for Low pH-dependent Fusion*. Journal of Biological Chemistry, 2011. **286**(35): p. 30361-30376.
84. Montpellier, C., et al., *Interacting Regions of CD81 and Two of Its Partners, EWI-2 and EWI-2wint, and Their Effect on Hepatitis C Virus Infection*. Journal of Biological Chemistry, 2011. **286**(16): p. 13954-13965.
85. Nydegger, S., et al., *Mapping of tetraspanin-enriched microdomains that can function as gateways for HIV-1*. Journal of Cell Biology, 2006. **173**(5): p. 795-807.
86. Beck, R., et al., *The COPI system: molecular mechanisms and function*. FEBS Lett, 2009. **583**(17): p. 2701-9.
87. Hsu, V.W. and J.S. Yang, *Mechanisms of COPI vesicle formation*. Febs Letters, 2009. **583**(23): p. 3758-3763.
88. Popoff, V., et al., *COPI Budding within the Golgi Stack*. Cold Spring Harbor Perspectives in Biology, 2011. **3**(11).
89. Lippincott-Schwartz, J. and W. Liu, *Insights into COPI coat assembly and function in living cells*. Trends Cell Biol, 2006. **16**(10): p. e1-4.
90. Aniento, F., et al., *An endosomal beta COP is involved in the pH-dependent formation of transport vesicles destined for late endosomes*. Journal of Cell Biology, 1996. **133**(1): p. 29-41.
91. Whitney, J.A., et al., *Cytoplasmic coat proteins involved in endosome function*. Cell, 1995. **83**(5): p. 703-13.
92. Daro, E., et al., *Inhibition of endosome function in CHO cells bearing a temperature-sensitive defect in the coatomer (COPI) component epsilon-COP*. Journal of Cell Biology, 1997. **139**(7): p. 1747-1759.



93. Gabriely, G., R. Kama, and J.E. Gerst, *Involvement of specific COPI subunits in protein sorting from the late endosome to the vacuole in yeast*. Molecular and Cellular Biology, 2007. **27**(2): p. 526-540.
94. Gu, F., et al., *Functional dissection of COP-I subunits in the biogenesis of multivesicular endosomes*. Journal of Cell Biology, 1997. **139**(5): p. 1183-1195.
95. Guo, Q., E. Vasile, and M. Krieger, *Disruptions in Golgi Structure and Membrane Traffic in a Conditional-Lethal Mammalian-Cell Mutant Are Corrected by Epsilon-Cop*. Journal of Cell Biology, 1994. **125**(6): p. 1213-1224.
96. Abbe, E., *Beitrage zur Theorie des Mikroskops und der mikroskopischen Wahrnehmung*. Arc. F. Mikr. Anat, 1873. **9**: p. 8.
97. Pawley, J.B., *Handbook of biological confocal microscopy*. 3rd ed. 2006, New York, NY: Springer. xxviii, 985 p.
98. Huang, B., H. Babcock, and X. Zhuang, *Breaking the diffraction barrier: super-resolution imaging of cells*. Cell, 2010. **143**(7): p. 1047-58.
99. Huang, B., M. Bates, and X. Zhuang, *Super-resolution fluorescence microscopy*. Annu Rev Biochem, 2009. **78**: p. 993-1016.
100. Lippincott-Schwartz, J. and S. Manley, *Putting super-resolution fluorescence microscopy to work*. Nat Methods, 2009. **6**(1): p. 21-3.
101. Hell, S.W., *Far-field optical nanoscopy*. Science, 2007. **316**(5828): p. 1153-8.
102. Hell, S.W. and J. Wichmann, *Breaking the diffraction resolution limit by stimulated emission: stimulated-emission-depletion fluorescence microscopy*. Opt Lett, 1994. **19**(11): p. 780-2.
103. Klar, T.A. and S.W. Hell, *Subdiffraction resolution in far-field fluorescence microscopy*. Opt Lett, 1999. **24**(14): p. 954-6.
104. Gustafsson, M.G., *Nonlinear structured-illumination microscopy: wide-field fluorescence imaging with theoretically unlimited resolution*. Proc Natl Acad Sci U S A, 2005. **102**(37): p. 13081-6.
105. Rust, M.J., M. Bates, and X. Zhuang, *Sub-diffraction-limit imaging by stochastic optical reconstruction microscopy (STORM)*. Nat Methods, 2006. **3**(10): p. 793-5.
106. Betzig, E., et al., *Imaging intracellular fluorescent proteins at nanometer resolution*. Science, 2006. **313**(5793): p. 1642-5.
107. Hess, S.T., T.P. Girirajan, and M.D. Mason, *Ultra-high resolution imaging by fluorescence photoactivation localization microscopy*. Biophys J, 2006. **91**(11): p. 4258-72.
108. Thompson, R.E., D.R. Larson, and W.W. Webb, *Precise nanometer localization analysis for individual fluorescent probes*. Biophys J, 2002. **82**(5): p. 2775-83.
109. Gelles, J., B.J. Schnapp, and M.P. Sheetz, *Tracking kinesin-driven movements with nanometre-scale precision*. Nature, 1988. **331**(6155): p. 450-3.
110. Dempsey, G.T., et al., *Evaluation of fluorophores for optimal performance in localization-based super-resolution imaging*. Nature Methods, 2011. **8**(12): p. 1027-36.

111. Bates, M., et al., *Multicolor super-resolution imaging with photo-switchable fluorescent probes*. Science, 2007. **317**(5845): p. 1749-53.
112. Huang, B., et al., *Three-dimensional super-resolution imaging by stochastic optical reconstruction microscopy*. Science, 2008. **319**(5864): p. 810-3.
113. Jones, S.A., et al., *Fast, three-dimensional super-resolution imaging of live cells*. Nature Methods, 2011. **8**(6): p. 499-508.
114. Shim, S.H., et al., *Super-resolution fluorescence imaging of organelles in live cells with photoswitchable membrane probes*. Proc Natl Acad Sci U S A, 2012. **109**(35): p. 13978-83.
115. Xu, K., H.P. Babcock, and X. Zhuang, *Dual-objective STORM reveals three-dimensional filament organization in the actin cytoskeleton*. Nat Methods, 2012. **9**(2): p. 185-8.
116. Vaughan, J.C., S. Jia, and X. Zhuang, *Ultrabright photoactivatable fluorophores created by reductive caging*. Nat Methods, 2012. **9**(12): p. 1181-4.
117. Pollard, T.D. and J.A. Cooper, *Actin, a central player in cell shape and movement*. Science, 2009. **326**(5957): p. 1208-12.
118. Fojo, A.T., *The role of microtubules in cell biology, neurobiology, and oncology*. Cancer drug discovery and development. 2008, Totowa, NJ: Humana Press. xviii, 587 p.
119. Nixon, R.A. and A. Yuan, *Cytoskeleton of the nervous system*. Advances in neurobiology,. 2011, New York: Springer. xv, 774 p.
120. Lodish, H.F., *Molecular cell biology*. 7th ed. 2013, New York: W.H. Freeman and Co. xxxiii, 1154, 58 p.
121. Luo, L., *Actin cytoskeleton regulation in neuronal morphogenesis and structural plasticity*. Annu Rev Cell Dev Biol, 2002. **18**: p. 601-35.
122. Dent, E.W. and F.B. Gertler, *Cytoskeletal dynamics and transport in growth cone motility and axon guidance*. Neuron, 2003. **40**(2): p. 209-27.
123. Barnes, A.P. and F. Polleux, *Establishment of Axon-Dendrite Polarity in Developing Neurons*. Annual Review of Neuroscience, 2009. **32**: p. 347-381.
124. Stiess, M. and F. Bradke, *Neuronal Polarization: The Cytoskeleton Leads the Way*. Developmental Neurobiology, 2011. **71**(6): p. 430-444.
125. Kapitein, L.C. and C.C. Hoogenraad, *Which way to go? Cytoskeletal organization and polarized transport in neurons*. Molecular and Cellular Neuroscience, 2011. **46**(1): p. 9-20.
126. Cingolani, L.A. and Y. Goda, *Actin in action: the interplay between the actin cytoskeleton and synaptic efficacy*. Nat Rev Neurosci, 2008. **9**(5): p. 344-56.
127. Siegel, G.J., *Basic neurochemistry : molecular, cellular, and medical aspects*. 7th ed. 2006, Amsterdam ; Boston: Elsevier. xxiv, 992 p.
128. Bennett, V. and A.J. Baines, *Spectrin and ankyrin-based pathways: metazoan inventions for integrating cells into tissues*. Physiol Rev, 2001. **81**(3): p. 1353-92.
129. Bennett, V. and D.N. Lorenzo, *Spectrin- and ankyrin-based membrane domains and the evolution of vertebrates*. Curr Top Membr, 2013. **72**: p. 1-37.

130. Liu, S.C., L.H. Derick, and J. Palek, *Visualization of the hexagonal lattice in the erythrocyte membrane skeleton*. J Cell Biol, 1987. **104**(3): p. 527-36.
131. Byers, T.J. and D. Branton, *Visualization of the protein associations in the erythrocyte membrane skeleton*. Proc Natl Acad Sci U S A, 1985. **82**(18): p. 6153-7.
132. Jenkins, S.M. and V. Bennett, *Ankyrin-G coordinates assembly of the spectrin-based membrane skeleton, voltage-gated sodium channels, and L1 CAMs at Purkinje neuron initial segments*. J Cell Biol, 2001. **155**(5): p. 739-46.
133. Riederer, B.M., I.S. Zagon, and S.R. Goodman, *Brain spectrin(240/235) and brain spectrin(240/235E): two distinct spectrin subtypes with different locations within mammalian neural cells*. J Cell Biol, 1986. **102**(6): p. 2088-97.
134. Galiano, M.R., et al., *A distal axonal cytoskeleton forms an intra-axonal boundary that controls axon initial segment assembly*. Cell, 2012. **149**(5): p. 1125-39.
135. Stankewich, M.C., et al., *A widely expressed betaIII spectrin associated with Golgi and cytoplasmic vesicles*. Proc Natl Acad Sci U S A, 1998. **95**(24): p. 14158-63.
136. Sakaguchi, G., et al., *A novel brain-specific isoform of beta spectrin: isolation and its interaction with Munc13*. Biochem Biophys Res Commun, 1998. **248**(3): p. 846-51.
137. Gao, Y., et al., *beta-III spectrin is critical for development of purkinje cell dendritic tree and spine morphogenesis*. J Neurosci, 2011. **31**(46): p. 16581-90.
138. Bennett, V., J. Davis, and W.E. Fowler, *Brain spectrin, a membrane-associated protein related in structure and function to erythrocyte spectrin*. Nature, 1982. **299**(5879): p. 126-31.
139. Korobova, F. and T. Svitkina, *Molecular architecture of synaptic actin cytoskeleton in hippocampal neurons reveals a mechanism of dendritic spine morphogenesis*. Mol Biol Cell, 2010. **21**(1): p. 165-76.
140. Bradke, F. and C.G. Dotti, *The role of local actin instability in axon formation*. Science, 1999. **283**(5409): p. 1931-4.
141. Dent, E.W., S.L. Gupton, and F.B. Gertler, *The growth cone cytoskeleton in axon outgrowth and guidance*. Cold Spring Harb Perspect Biol, 2011. **3**(3).
142. Hammarlund, M., E.M. Jorgensen, and M.J. Bastiani, *Axons break in animals lacking beta-spectrin*. J Cell Biol, 2007. **176**(3): p. 269-75.
143. Tang, Y., et al., *Disruption of transforming growth factor-beta signaling in ELF beta-spectrin-deficient mice*. Science, 2003. **299**(5606): p. 574-7.
144. Stankewich, M.C., et al., *Cell organization, growth, and neural and cardiac development require alphaII-spectrin*. J Cell Sci, 2011. **124**(Pt 23): p. 3956-66.
145. Krieg, M., A.R. Dunn, and M.B. Goodman, *Mechanical control of the sense of touch by beta-spectrin*. Nat Cell Biol, 2014. **16**(3): p. 224-33.
146. Ikeda, Y., et al., *Spectrin mutations cause spinocerebellar ataxia type 5*. Nat Genet, 2006. **38**(2): p. 184-90.
147. Writzl, K., et al., *Early onset West syndrome with severe hypomyelination and coloboma-like optic discs in a girl with SPTAN1 mutation*. Epilepsia, 2012. **53**(6): p. e106-10.

148. McMurray, C.T., *Neurodegeneration: diseases of the cytoskeleton?* Cell Death Differ, 2000. **7**(10): p. 861-5.
149. Xu, K., G. Zhong, and X. Zhuang, *Actin, spectrin, and associated proteins form a periodic cytoskeletal structure in axons.* Science, 2013. **339**(6118): p. 452-6.
150. He, J., et al., *Dual function of CD81 in influenza virus uncoating and budding.* PLoS Pathog, 2013. **9**(10): p. e1003701.
151. Harris, A., et al., *Influenza virus pleiomorphy characterized by cryoelectron tomography.* Proc Natl Acad Sci U S A, 2006. **103**(50): p. 19123-7.
152. Chu, C.M., I.M. Dawson, and W.J. Elford, *Filamentous forms associated with newly isolated influenza virus.* Lancet, 1949. **1**(6554): p. 602.
153. Roberts, P.C., R.A. Lamb, and R.W. Compans, *The M1 and M2 proteins of influenza A virus are important determinants in filamentous particle formation.* Virology, 1998. **240**(1): p. 127-137.
154. Nayak, D.P., et al., *Influenza virus morphogenesis and budding.* Virus Res, 2009. **143**(2): p. 147-61.
155. Rossman, J.S., et al., *Influenza Virus M2 Ion Channel Protein Is Necessary for Filamentous Virion Formation.* Journal of Virology, 2010. **84**(10): p. 5078-5088.
156. Shapiro, G.I., T. Gurney, and R.M. Krug, *Influenza-Virus Gene-Expression - Control Mechanisms at Early and Late Times of Infection and Nuclear-Cytoplasmic Transport of Virus-Specific Rnas.* Journal of Virology, 1987. **61**(3): p. 764-773.
157. McClure, M.O., et al., *The pH independence of mammalian retrovirus infection.* J Gen Virol, 1990. **71** ( Pt 4): p. 767-73.
158. Kolokoltsov, A.A., et al., *Small interfering RNA profiling reveals key role of clathrin-mediated endocytosis and early endosome formation for infection by respiratory syncytial virus.* Journal of Virology, 2007. **81**(14): p. 7786-800.
159. Lakadamyali, M., et al., *Visualizing infection of individual influenza viruses.* Proc Natl Acad Sci U S A, 2003. **100**(16): p. 9280-5.
160. Chen, B.J., et al., *Influenza virus hemagglutinin and neuraminidase, but not the matrix protein, are required for assembly and budding of plasmid-derived virus-like particles.* Journal of Virology, 2007. **81**(13): p. 7111-23.
161. Bourmakina, S.V. and A. Garcia-Sastre, *Reverse genetics studies on the filamentous morphology of influenza A virus.* J Gen Virol, 2003. **84**(Pt 3): p. 517-27.
162. Burleigh, L.M., et al., *Influenza A viruses with mutations in the M1 helix six domain display a wide variety of morphological phenotypes.* Journal of Virology, 2005. **79**(2): p. 1262-1270.
163. Rust, M.J., M. Bates, and X.W. Zhuang, *Sub-diffraction-limit imaging by stochastic optical reconstruction microscopy (STORM).* Nature Methods, 2006. **3**(10): p. 793-795.
164. Huang, B., et al., *Three-dimensional super-resolution imaging by stochastic optical reconstruction microscopy.* Science, 2008. **319**(5864): p. 810-813.
165. Blanchard, E., et al., *Hepatitis C virus entry depends on clathrin-mediated endocytosis.* Journal of Virology, 2006. **80**(14): p. 6964-72.

166. Farquhar, M.J., et al., *Hepatitis C virus induces CD81 and claudin-1 endocytosis*. Journal of Virology, 2012. **86**(8): p. 4305-16.
167. Gordon-Alonso, M., et al., *Tetraspanins CD9 and CD81 modulate HIV-1-induced membrane fusion*. J Immunol, 2006. **177**(8): p. 5129-37.
168. Sato, K., et al., *Modulation of human immunodeficiency virus type 1 infectivity through incorporation of tetraspanin proteins*. Journal of Virology, 2008. **82**(2): p. 1021-1033.
169. Piper, R.C. and D.J. Katzmann, *Biogenesis and function of multivesicular bodies*. Annu Rev Cell Dev Biol, 2007. **23**: p. 519-47.
170. Jolly, C. and Q.J. Sattentau, *Human immunodeficiency virus type 1 assembly, budding, and cell-cell spread in T cells take place in tetraspanin-enriched plasma membrane domains*. Journal of Virology, 2007. **81**(15): p. 7873-7884.
171. Khurana, S., et al., *Human immunodeficiency virus type 1 and influenza virus exit via different membrane Microdomains*. Journal of Virology, 2007. **81**(22): p. 12630-12640.
172. Ruiz-Mateos, E., et al., *CD63 is not required for production of infectious human immunodeficiency virus type 1 in human macrophages*. Journal of Virology, 2008. **82**(10): p. 4751-61.
173. Kremontsov, D.N., et al., *Tetraspanins regulate cell-to-cell transmission of HIV-1*. Retrovirology, 2009. **6**.
174. Weng, J., et al., *Formation of Syncytia Is Repressed by Tetraspanins in Human Immunodeficiency Virus Type 1-Producing Cells*. Journal of Virology, 2009. **83**(15): p. 7467-7474.
175. Grigorov, B., et al., *A role for CD81 on the late steps of HIV-1 replication in a chronically infected T cell line*. Retrovirology, 2009. **6**.
176. Rossman, J.S., et al., *Influenza virus M2 protein mediates ESCRT-independent membrane scission*. Cell, 2010. **142**(6): p. 902-13.
177. Vonderheit, A. and A. Helenius, *Rab7 associates with early endosomes to mediate sorting and transport of Semliki forest virus to late endosomes*. PLoS Biol, 2005. **3**(7): p. e233.
178. Sun, E., J. He, and X. Zhuang, *Dissecting the Role of COPI Complexes in Influenza Virus Infection*. Journal of Virology, 2013. **87**(5): p. 2673-85.
179. Skehel, J.J., et al., *Changes in the conformation of influenza virus hemagglutinin at the pH optimum of virus-mediated membrane fusion*. Proc Natl Acad Sci U S A, 1982. **79**(4): p. 968-72.
180. Doms, R.W., A. Helenius, and J. White, *Membrane-Fusion Activity of the Influenza-Virus Hemagglutinin - the Low Ph-Induced Conformational Change*. Journal of Biological Chemistry, 1985. **260**(5): p. 2973-2981.
181. Whittaker, G.R., M. Kann, and A. Helenius, *Viral entry into the nucleus*. Annual Review of Cell and Developmental Biology, 2000. **16**: p. 627-651.
182. Gu, F. and J. Gruenberg, *Biogenesis of transport intermediates in the endocytic pathway*. FEBS Lett, 1999. **452**(1-2): p. 61-66.
183. Johannsdottir, H.K., et al., *Host Cell Factors and Functions Involved in Vesicular Stomatitis Virus Entry*. Journal of Virology, 2009. **83**(1): p. 440-453.

184. Matlin, K.S., et al., *Pathway of vesicular stomatitis virus entry leading to infection*. J Mol Biol, 1982. **156**(3): p. 609-31.
185. Superti, F., et al., *Entry Pathway of Vesicular Stomatitis-Virus into Different Host-Cells*. Journal of General Virology, 1987. **68**: p. 387-399.
186. Sun, X.J., et al., *Role of clathrin-mediated endocytosis during vesicular stomatitis virus entry into host cells*. Virology, 2005. **338**(1): p. 53-60.
187. White, J., K. Matlin, and A. Helenius, *Cell fusion by Semliki Forest, influenza, and vesicular stomatitis viruses*. Journal of Cell Biology, 1981. **89**(3): p. 674-9.
188. Randall, R.E. and S. Goodbourn, *Interferons and viruses: an interplay between induction, signalling, antiviral responses and virus countermeasures*. Journal of General Virology, 2008. **89**: p. 1-47.
189. Stegmann, T., et al., *Fusion of influenza virus in an intracellular acidic compartment measured by fluorescence dequenching*. Biochim Biophys Acta, 1987. **904**(1): p. 165-70.
190. Sigismund, S., et al., *Clathrin-independent endocytosis of ubiquitinated cargos*. Proc Natl Acad Sci U S A, 2005. **102**(8): p. 2760-5.
191. Chen, H. and P. De Camilli, *The association of epsin with ubiquitinated cargo along the endocytic pathway is negatively regulated by its interaction with clathrin*. Proceedings of the National Academy of Sciences of the United States of America, 2005. **102**(8): p. 2766-2771.
192. Jiang, X. and A. Sorkin, *Epidermal growth factor receptor internalization through clathrin-coated pits requires Cbl RING finger and proline-rich domains but not receptor polyubiquitylation*. Traffic, 2003. **4**(8): p. 529-43.
193. Macia, E., et al., *Dynasore, a cell-permeable inhibitor of dynamin*. Developmental Cell, 2006. **10**(6): p. 839-50.
194. Doherty, G.J. and H.T. McMahon, *Mechanisms of endocytosis*. Annu Rev Biochem, 2009. **78**: p. 857-902.
195. Lakadamyali, M., M.J. Rust, and X. Zhuang, *Endocytosis of influenza viruses*. Microbes Infect, 2004. **6**(10): p. 929-36.
196. Kobayashi, T., et al., *A lipid associated with the antiphospholipid syndrome regulates endosome structure and function*. Nature, 1998. **392**(6672): p. 193-7.
197. Mossessova, E., R.A. Corpina, and J. Goldberg, *Crystal structure of ARF1\*Sec7 complexed with Brefeldin A and its implications for the guanine nucleotide exchange mechanism*. Mol Cell, 2003. **12**(6): p. 1403-11.
198. Saenz, J.B., et al., *Golgicide A reveals essential roles for GBF1 in Golgi assembly and function*. Nat Chem Biol, 2009. **5**(3): p. 157-65.
199. Misselwitz, B., et al., *RNAi screen of Salmonella invasion shows role of COPI in membrane targeting of cholesterol and Cdc42*. Molecular Systems Biology, 2011. **7**.
200. Razi, M., E.Y.W. Chan, and S.A. Tooze, *Early endosomes and endosomal coatome are required for autophagy*. Journal of Cell Biology, 2009. **185**(2): p. 305-321.
201. Huotari, J. and A. Helenius, *Endosome maturation*. EMBO J, 2011. **30**(17): p. 3481-500.

202. Zhang, C.J., et al., *Expression of a dominant allele of human ARF1 inhibits membrane traffic in vivo*. Journal of Cell Biology, 1994. **124**(3): p. 289-300.
203. Guo, Y., et al., *Functional genomic screen reveals genes involved in lipid-droplet formation and utilization*. Nature, 2008. **453**(7195): p. 657-661.
204. Collinet, C., et al., *Systems survey of endocytosis by multiparametric image analysis*. Nature, 2010. **464**(7286): p. 243-9.
205. Sun, Q.M., et al., *Rubicon controls endosome maturation as a Rab7 effector*. Proceedings of the National Academy of Sciences of the United States of America, 2010. **107**(45): p. 19338-19343.
206. Vaughan, J.C., et al., *Rapid actin-dependent viral motility in live cells*. Biophys J, 2009. **97**(6): p. 1647-56.
207. Zhong, G., et al., *Developmental mechanism of the periodic membrane skeleton in axons*. Elife, 2014. **3**.
208. Hulsmeier, J., et al., *Distinct functions of alpha-Spectrin and beta-Spectrin during axonal pathfinding*. Development, 2007. **134**(4): p. 713-22.
209. Pielage, J., R.D. Fetter, and G.W. Davis, *Presynaptic spectrin is essential for synapse stabilization*. Curr Biol, 2005. **15**(10): p. 918-28.
210. Susuki, K. and M.N. Rasband, *Spectrin and ankyrin-based cytoskeletons at polarized domains in myelinated axons*. Exp Biol Med (Maywood), 2008. **233**(4): p. 394-400.
211. Pielage, J., et al., *A presynaptic giant ankyrin stabilizes the NMJ through regulation of presynaptic microtubules and transsynaptic cell adhesion*. Neuron, 2008. **58**(2): p. 195-209.
212. Arimura, N. and K. Kaibuchi, *Neuronal polarity: from extracellular signals to intracellular mechanisms*. Nat Rev Neurosci, 2007. **8**(3): p. 194-205.
213. Cheng, P.L. and M.M. Poo, *Early events in axon/dendrite polarization*. Annu Rev Neurosci, 2012. **35**: p. 181-201.
214. Dotti, C.G., C.A. Sullivan, and G.A. Banker, *The establishment of polarity by hippocampal neurons in culture*. J Neurosci, 1988. **8**(4): p. 1454-68.
215. D'Este, E., et al., *STED nanoscopy reveals the ubiquity of subcortical cytoskeleton periodicity in living neurons*. Cell Rep, 2015. **10**(8): p. 1246-51.
216. Kuhlman, P.A., et al., *A new function for adducin. Calcium/calmodulin-regulated capping of the barbed ends of actin filaments*. J Biol Chem, 1996. **271**(14): p. 7986-91.
217. Zhou, D.X., et al., *Ankyring is required for clustering of voltage-gated Na channels at axon initial segments and for normal action potential firing*. Molecular Biology of the Cell, 1998. **9**: p. 37a-37a.
218. Yang, Y., et al., *beta IV spectrin is recruited to axon initial segments and nodes of Ranvier by ankyrinG*. Journal of Cell Biology, 2007. **176**(4): p. 509-519.
219. Susuki, K., et al., *Schwann cell spectrins modulate peripheral nerve myelination*. Proc Natl Acad Sci U S A, 2011. **108**(19): p. 8009-14.
220. Iossifov, I., et al., *The contribution of de novo coding mutations to autism spectrum disorder*. Nature, 2014. **515**(7526): p. 216-21.

221. Witte, H., D. Neukirchen, and F. Bradke, *Microtubule stabilization specifies initial neuronal polarization*. J Cell Biol, 2008. **180**(3): p. 619-32.
222. Bennett, V. and J. Davis, *Erythrocyte ankyrin: immunoreactive analogues are associated with mitotic structures in cultured cells and with microtubules in brain*. Proc Natl Acad Sci U S A, 1981. **78**(12): p. 7550-4.
223. Jiang, H., et al., *Both the establishment and the maintenance of neuronal polarity require active mechanisms: Critical roles of GSK-3 beta and its upstream regulators*. Cell, 2005. **120**(1): p. 123-135.
224. Yoshimura, T., et al., *GSK-3beta regulates phosphorylation of CRMP-2 and neuronal polarity*. Cell, 2005. **120**(1): p. 137-49.
225. Kunimoto, M., *Neuron-specific isoform of brain ankyrin, 440-kD ankyrin(B), is targeted to the axons of rat cerebellar neurons*. Journal of Cell Biology, 1995. **131**(6): p. 1821-1829.
226. Engelhardt, M., et al., *Ankyrin-B structurally defines terminal microdomains of peripheral somatosensory axons*. Brain Struct Funct, 2013. **218**(4): p. 1005-16.
227. Chan, W., E. Kordeli, and V. Bennett, *440-Kd Ankyrin(B) - Structure of the Major Developmentally-Regulated Domain and Selective Localization in Unmyelinated Axons*. Journal of Cell Biology, 1993. **123**(6): p. 1463-1473.
228. De Rubeis, S., et al., *Synaptic, transcriptional and chromatin genes disrupted in autism*. Nature, 2014. **515**(7526): p. 209-15.
229. Scotland, P., et al., *Nervous system defects of AnkyrinB (-/-) mice suggest functional overlap between the cell adhesion molecule L1 and 440-kD AnkyrinB in premyelinated axons*. J Cell Biol, 1998. **143**(5): p. 1305-15.
230. Lukinavicius, G., et al., *Fluorogenic probes for live-cell imaging of the cytoskeleton*. Nat Methods, 2014. **11**(7): p. 731-3.
231. Jones, S.L., F. Korobova, and T. Svitkina, *Axon initial segment cytoskeleton comprises a multiprotein submembranous coat containing sparse actin filaments*. J Cell Biol, 2014. **205**(1): p. 67-81.
232. Kunimoto, M., E. Otto, and V. Bennett, *A New 440-Kd Isoform Is the Major Ankyrin in Neonatal Rat-Brain*. Journal of Cell Biology, 1991. **115**(5): p. 1319-1331.
233. Lorenzo, D.N., et al., *A PIK3C3-ankyrin-B-dynactin pathway promotes axonal growth and multiorganelle transport*. J Cell Biol, 2014. **207**(6): p. 735-52.
234. Hedstrom, K.L., Y. Ogawa, and M.N. Rasband, *AnkyrinG is required for maintenance of the axon initial segment and neuronal polarity*. J Cell Biol, 2008. **183**(4): p. 635-40.
235. Koestler, S.A., et al., *Differentially oriented populations of actin filaments generated in lamellipodia collaborate in pushing and pausing at the cell front*. Nat Cell Biol, 2008. **10**(3): p. 306-13.
236. Jones, S.A., et al., *Fast, three-dimensional super-resolution imaging of live cells*. Nat Methods, 2011. **8**(6): p. 499-508.
237. Kandel, E.R., *Principles of neural science*. 5th ed. 2013, New York: McGraw-Hill. 1, 1709 p.



- 238. Tabata, T., et al., *A reliable method for culture of dissociated mouse cerebellar cells enriched for Purkinje neurons*. J Neurosci Methods, 2000. **104**(1): p. 45-53.
- 239. Furuya, S., A. Makino, and Y. Hirabayashi, *An improved method for culturing cerebellar Purkinje cells with differentiated dendrites under a mixed monolayer setting*. Brain Res Brain Res Protoc, 1998. **3**(2): p. 192-8.
- 240. Gardner, A., P. Jukkola, and C. Gu, *Myelination of rodent hippocampal neurons in culture*. Nat Protoc, 2012. **7**(10): p. 1774-82.
- 241. Bennett, V. and A.J. Baines, *Spectrin and ankyrin-based pathways: Metazoan inventions for integrating cells into tissues*. Physiological Reviews, 2001. **81**(3): p. 1353-1392.
- 242. Kilcher, S. and J. Mercer, *Next generation approaches to study virus entry and infection*. Curr Opin Virol, 2014. **4**: p. 8-14.
- 243. McMahon, H.T. and E. Boucrot, *Molecular mechanism and physiological functions of clathrin-mediated endocytosis*. Nat Rev Mol Cell Biol, 2011. **12**(8): p. 517-33.